

MICROSTRUCTURE, NANO-, AND MACRO-INDENTATION CHARACTERIZATION OF AISI 302 STEEL AFTER HIGH-TEMPERATURES AGING

 **Omar Ben Lenda**^{a,*},  **Hajar El Ganich**^b,  **El Madani Saad**^a

^a *Laboratory of Physical-Chemistry of Processes and Materials, Faculty of Sciences and Technology Settat, Hassan 1st University, Settat, Morocco*

^b *Hassan First University of Settat, High Institute of Health Sciences, Laboratory of Sciences and Health Technologies, BP 555, 26000, Settat, Morocco*

*Corresponding Author e-mail: o.benlenda@uhp.ac.ma

Received August 2, 2023; revised September 18, 2023; accepted September 19, 2023

The structural and mechanical studies of the AISI 302 steel aim to design a correct heat treatment in order to optimize its mechanical properties. In this study, we investigated the influence of temperature and time of aging on the structural and mechanical characteristics of the AISI 302 steel. The steel was aged at temperatures of 1100°C and 1200°C and for times ranging from 0 to 6000 minutes. The structural and mechanical characterization techniques used were the metallurgical microscope, nanoindentation technique, and macro-hardness test. At the microstructural level, an increase in the time or temperature of the aging contributed to an increase in the austenite grains size of AISI 302 steel. This microstructural change led to a decrease in the nanohardness and a drop in the macro-hardness between the unaged and aged conditions of AISI 302 steel.

Keywords: AISI 302 Steel; Aging; Microstructure; Austenite; Grain growth; Nanohardness; Nanoindentation; Macro-hardness

PACS: 81.05.Bx; 81.40.Cd; 81.70.Bt; 81.70.Fy

1. INTRODUCTION

In terms of annual production, austenitic stainless steels are the largest group of stainless steels [1]. The AISI 300 steel series are Chromium-Nickel alloys [2], which are essentially developed from steel composed of 18 wt% (percentage by weight) of Chromium and 8 wt% of Nickel [3]. They exhibit good mechanical properties, manufacturability, and corrosion resistance [1]. They are typically used in high-temperatures and food contact applications [4].

Owing to their importance at the industrial level, steels have been extensively studied to understand their metallurgical behavior [5–10]. In the literature, the phenomenon of austenite grain growth and its relationship with the temperature and time of the aging treatment have gained great interest [11–13]. D. Dong et al. [11], Z. Li et al. [12] and S. Benmaziane et al. [13] found that the austenite grain size of the steels increases considerably by increasing the treatment temperature. For a fixed temperature, they also reported that the grain growth rate decreases with increasing treatment time. The mechanism of grain growth has been elucidated in several studies [12, 14–16]. As shown in the work of R.C. Chen et al. [15], the growth of austenite grain in 300 M steel results from the grain boundaries migrating by incrementing temperature from 900°C to 1150°C and time from 5 to 120 minutes. For the GCr15 bearing steel cast billet treated at a temperature range of 1000–1250°C and a holding time interval of 30–180 minutes, Z. Li et al. [12] explained that grain boundaries migrating process decrease the driving force for grain growth.

Studies have sought to determine the effect of the size of austenite grains on the nano- and macro-mechanical properties of steels [17–20]. S. Li et al. [18], G. Liu et al. [19], and our previous work [20] reported the thermal aging behavior of the micro-constituents of various stainless-steel grades. For the austenite, at temperatures below 800°C and for prolonged holding times, the measurements showed that nanohardness after aging was slightly influenced [18–20]. The paper results of Y. Su et al. [17] have shown that the increase of the austenite grains size contributed to the decrease in the strength and ductility of Novel 20LH5 austenitic stainless steel.

Several metallurgical studies have been conducted on AISI 302 steel; however, only limited research has been performed on the evolution of the nanohardness of austenite as a function of time at high-temperatures. The structural and mechanical studies of the AISI 302 steel help to determine a heat treatment correctly to optimize its mechanical performance. In this paper, the aging mechanism and microstructural variations of AISI 302 steel at temperatures 1100°C and 1200°C up to 6000 minutes were investigated. Herein, the microstructure of AISI 302 steel under different heat treatment conditions was visualized using metallurgical microscope. Mechanical characterization of the AISI 302 steel before and after aging was carried out using the nanoindentation technique and macro-hardness tests.

2. MATERIALS AND METHODS

2.1. Chemical Composition

The chemical composition (in wt%) of the as-received AISI 302 steel is shown in Table 1 [21]. The AISI 302 steel was obtained from a steel plant located in the city of Casablanca, Morocco. At the industrial level, the AISI 302

commercial steel was produced in an electric arc furnace and hot-rolled to 10 mm thick plates. The AISI 302 steel samples used in the present study were rectangular in shape and had dimension of 25×25×10 mm³.

Table 1. Chemical composition of AISI 302 steel

Element	Fe	Cr	C	Ni	Si	Mn	P
Percentage by weight (wt%)	72.81	18	0.15	8	0.4	0.61	0.03

2.2. Aging Treatments

The AISI 302 steel samples were aged using a SELECTA air furnace at a heating rate of 20°C per minute and temperature control with an accuracy of ± 1°C. First, the steel was aged at two temperatures 1100°C and 1200°C and for the following durations: 0 (unaged condition of the AISI 302 steel), 60, 600, 1000, and 6000 minutes. Then, the quenching of the samples was carried out in water up to a temperature of ~ 25°C (room temperature).

2.3. Metallurgical Observations

Prior to the metallurgical observations, the samples of AISI 302 steel were mechanically polished using abrasive papers with grain sizes of 320, 600, 1200, and 4000. The polishing was completed using diamond pastes with particle sizes of 1, 3, and 6 µm and suspended in distilled water. This mechanical preparation made it possible to remove the oxide layers formed during heat treatments and to obtain a mirror-polished surface.

The structure of AISI 302 stainless steel was visualized by chemical etching with dilute aqua regia solution (mixture of 5 mL HNO₃, 15 mL HCl, and 100 mL H₂O) and the rinsing was performed with bi-distilled water [22]. The structure of the AISI 302 steel was examined using an OPTIKA brand metallurgical microscope coupled with a high-resolution AIPTEK camera. The average grain size was measured by using the linear intercept method.

2.4. Nanoindentation Technique

Nanoindentation tests were performed using a Nanoindenter XP (CSM Instruments) tester with a Berkovich indenter of B-O 45 series (pyramidal diamond tip with a nominal angle of 65.3° between the vertical axis and each face) [23]. Nanoindentations were performed under a maximum load of 50000 µN and a dwell time of 5 seconds.

Analysis of the loading-unloading curves of the samples was performed using the method of Oliver and Pharr [24, 25]. Figure 1 shows a typical loading–unloading curve with an indication of the parameters used in this method. The h_c is the contact depth and can be calculated as follows:

$$h_c = h_{max} - \varepsilon \times \left(\frac{P_{max}}{S} \right) \tag{1}$$

Where P_{max} is the peak load, h_{max} is the indenter maximum penetration on the sample flat surface, ε is a constant (equal to 0.75 for Berkovich indenter), and S is the unloading curve tangent slope.

A_c is the contact projection area and can be expressed as follows:

$$A_c = 24.5 \times h_c^2 + \sum_{i=0}^7 C_i \times h_c^{1/2^i} \tag{2}$$

Where C_1, C_2, \dots, C_7 are constants. The first term of equation (2) describes the perfect shape of the Berkovich indenter, and the second term describes deviations from Berkovich geometry due to the blunting tip.

H_{IT} is the nanohardness and expressed as follows:

$$H_{IT} = P_{max}/A_c \tag{3}$$

Another parameter used in the evaluation of loading-unloading curves is h_r which refers to the indenter residual penetration. The value of the h_r parameter is the intersection of the unloading curve with the horizontal axis (see Figure 1).

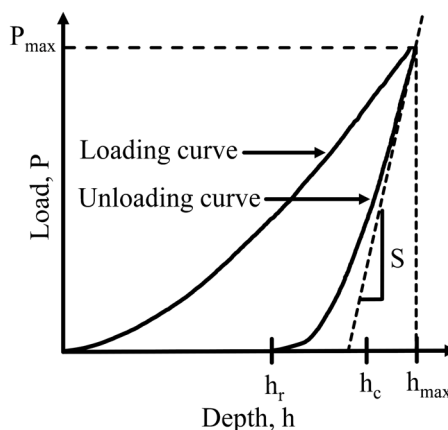


Figure 1. The typical loading-unloading curve of nanoindentation test

2.5. Macro-Hardness Test

Macro-hardness measurements were effectuated using a TESTWELL Durometer. The macro-hardness of the AISI 302 steel samples was evaluated using the ROCKWELL C method (diamond indenter with a total load of 150 Kgf) [26]. To assure repeatability, each macro-hardness value corresponded to the average of 10 indentations well distributed on the flat surface of each sample.

3. RESULTS AND DISCUSSIONS

3.1. Metallurgical Study

Figure 2 shows the phase fraction versus temperature diagram computed using the JMatPRO (version 7.0) software for the steel composition shown in Table 1 and for a temperature range of 1000 – 1500°C. As illustrated in Figure 2, the microstructure of AISI 302 steel was composed of 100 wt% of austenite for the two temperatures studied 1100°C and 1200°C.

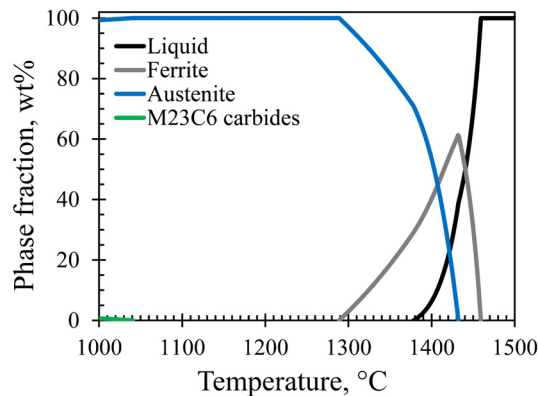


Figure 2. Phase diagram of the AISI 302 steel calculated using JMatPro (Version 7) software

Figure 3 shows micrographs of the microstructure of the AISI 302 steel aged at 1100 °C for 0, 60, 600, 1000, and 6000 minutes. According to the images obtained, the equiaxed grains size of the AISI 302 steel increased by increasing the aging time from 0 to 6000 minutes. The grains growth contributes to a reduction in the number of grains per unit volume, and therefore a decrease in the total area of grain boundaries [27]. At high-temperatures, these microstructural changes are caused by the grain boundaries migrating process [15–16].

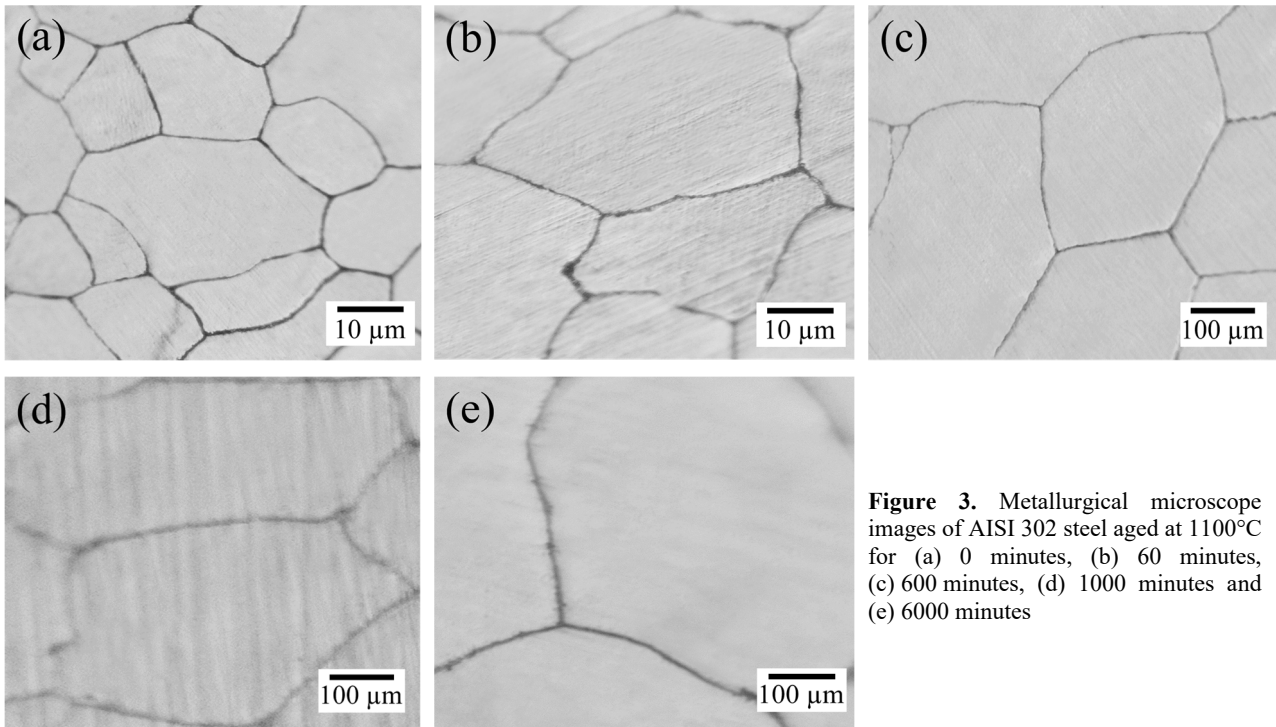


Figure 3. Metallurgical microscope images of AISI 302 steel aged at 1100°C for (a) 0 minutes, (b) 60 minutes, (c) 600 minutes, (d) 1000 minutes and (e) 6000 minutes

Figure 4 shows the austenite grain size as a function of the temperature and time of aging. As can be observed, for a fixed temperature, the austenite grain growth behavior can be divided into two stages: rapid growth stage for times below 1000 minutes, and relatively slow growth stage for times up to 6000 minutes. In other words, the majority of grain

growth occurred within 1000 minutes, and as the aging time increased, the grain growth rate slowed down. We can conclude that grain growth kinetics are reduced by increasing the aging time, which is linked to a decrease in the driving force for grain growth [28].

Several scientific papers have discussed the effect of the temperature and time of treatment on the austenite grain growth rate. The grain growth rate (dD/dt) can be quantitatively described as follows [12, 28-31]:

$$\frac{dD}{dt} = M_0 \exp\left(-\frac{Q_b}{RT}\right) \frac{A\gamma}{D} \quad (4)$$

Where M_0 is the pre-exponential coefficient, Q_b is the grain boundary activation energy, R is the gas constant (8.314 J/mol/K), T is the temperature, A is a constant, γ is the grain boundary energy, and D is the austenite grain size. According to equation 4, the austenite growth rate increases with the increase of temperature and decreases with the increase of austenite grain size. These conclusions are in good agreement with the grain size measurements of AISI 302 steel under different conditions (see Figure 4).

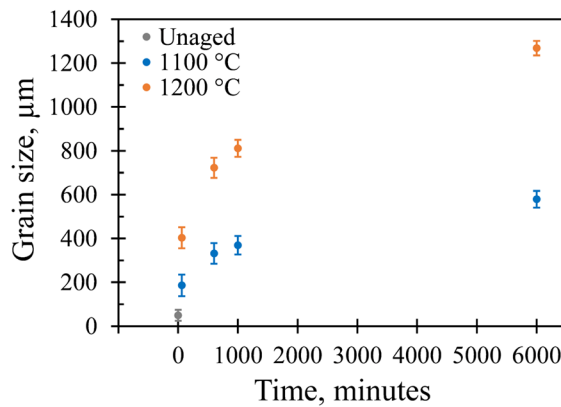


Figure 4. The austenite grain size of austenite aged at 1100°C and 1200°C for 0 (unaged), 60, 600, 1000, and 6000 minutes

3.2. Nanoindentation Technique

Figure 5 shows the nanoindentation curves of the austenite aged at 1100 °C and 1200°C for 0, 60, 600, 1000, and 6000 minutes. The nanoindentation measurements were categorized according to the aging temperature; Figure 5(a) for 1100°C and Figure 5(b) for 1200°C. The applied load (P) was plotted as a function of the penetration depth of the indenter (h) on the flat surfaces of the samples. For the different aging treatments, the mechanical behavior of the austenite was nearly identical. Nanoindentation curves did not exhibit discontinuities during the complete loading-unloading cycle [32, 33]. For all nanoindentation curves obtained, the unloading part was linear with a low slope. The plotted nanoindentation curves correspond to ductile materials [34].

We plotted the nanoindentation curve of the austenite aged for 0 minutes in Figure 5(a) and Figure 5(b) in order to visualize the effect of thermal aging time. At a given temperature, the nanoindentation curves shifted to the right by incrementing the aging time. According to Figure 5, the difference in displacement between the austenite curves was small for times greater than 60 minutes at two temperatures 1100°C and 1200°C.

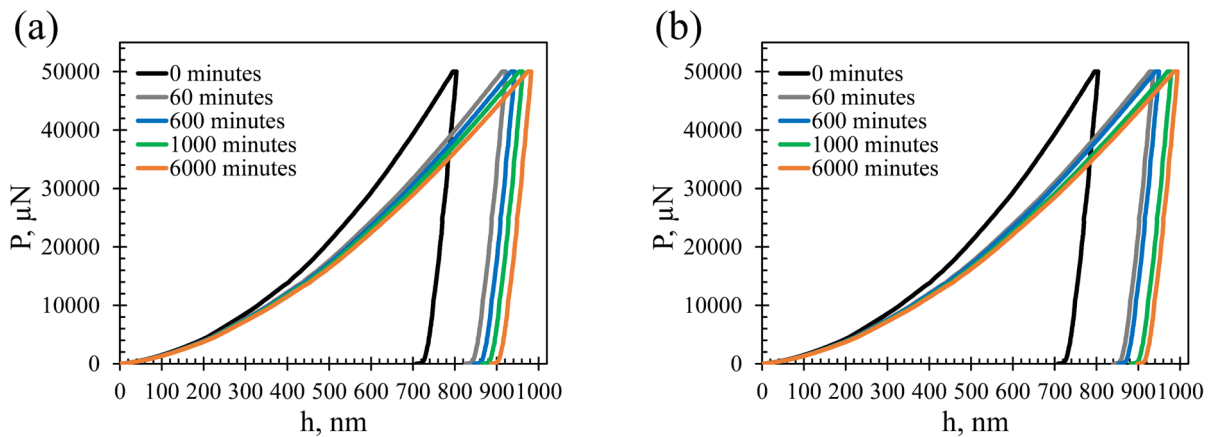


Figure 5. The loading-unloading curves of the AISI 302 steel aged at (a) 1100°C and (b) 1200°C for 0 (unaged), 60, 600, 1000, and 6000 minutes

The nano-mechanical behavior of the austenite can also be evaluated from the parameters extracted from the P-h curves and which are h_{max} and h_r . Table 2 shows the values of the parameters h_{max} and h_r as a function of the

temperature and time of the aging. Compared to the austenite aged for 0 minutes, the values of h_{\max} and h_r increased by increasing one of the aging treatment parameters (time or temperature).

Table 2. Parameters extracted from the loading-unloading curves of austenite aged at 1100°C and 1200°C for 0 (unaged), 60, 600, 1000, and 6000 minutes

Aging time (minutes)	Maximum indenter penetration depth (h_{\max} (nm))		Residual indenter penetration depth (h_r (nm))	
	1100°C	1200°C	1100°C	1200°C
0 (unaged)	803.99		707.79	
60	921.71	936.15	825.51	839.95
600	942.81	949.62	846.61	853.42
1000	961.93	978.54	865.73	882.34
6000	982.36	994.10	886.16	897.90

Table 3 shows the variation in the elastic deformation work (W_e), plastic deformation work (W_p), and total work (W_t) performed by the Berkovich indenter in the austenite phase as a function of the temperature and time of the aging. The W_e corresponds to the area surrounded between the unloading curve and the horizontal axis. The W_p corresponds to the area between the loading and unloading curves and the horizontal axis. The W_t is the sum of the W_e and W_p . As can be seen from this table, the W_e decreased while the W_t and W_p increased by incrementing the temperature or time of the aging. These results indicated an increase in the plastic deformation of the austenite aged at temperatures 1100°C and 1200°C for the longest holding time of 6000 minutes.

Table 3. The elastic deformation work, plastic deformation work and total deformation work carried out by the Berkovich indenter at aging temperatures 1100°C and 1200°C for 0 (unaged), 60, 600, 1000, and 6000 minutes.

Aging time (minutes)	Elastic work deformation carried out by the indenter (W_e (PJ))		Plastic work deformation carried out by the indenter (W_p (PJ))		Total work deformation carried out by the indenter (W_t (PJ))	
	1100°C	1200°C	1100°C	1200°C	1100°C	1200°C
0 (unaged)	1869.49		12454.95		14324.44	
60	1723.60	1709.22	15401.94	16202.61	16725.54	17911.83
600	1704.09	1699.53	16465.45	16671.93	18169.54	18371.46
1000	1698.71	1678.84	16984.51	17256.79	18683.22	18935.63
6000	1661.42	1654.74	17322.82	17952.25	18984.24	19606.99

The nanohardness values of the austenite as a function of the temperature and time of the aging are summarized in Table 4. For a given aging time, the nanohardness at 1200°C was lower than that at 1100°C. For the two temperatures explored, the nanohardness of the austenite decreased for aging times between 0 and 60 minutes. By contrast, the nanohardness of the austenite remained nearly constant over an aging time interval ranging from 60 to 6000 minutes. Several scientific studies have also shown that the nano-hardness of the aged austenite is almost constant at temperatures between 350°C and 800°C, and for prolonged holding times up to 20000 h [35-37].

Table 4. Nano-hardness of the austenite aged at 1100°C and 1200°C for 0 (unaged), 60, 600, 1000, and 6000 minutes.

Aging time (min)	Nanohardness (H_{IT} (GPa))	
	1100°C	1200°C
0 (unaged)	3.69 ± 0.30	
60	2.75 ± 0.25	2.66 ± 0.30
600	2.62 ± 0.25	2.58 ± 0.25
1000	2.51 ± 0.15	2.42 ± 0.20
6000	2.40 ± 0.10	2.34 ± 0.15

3.3. Macro-Hardness Test

Figure 6 shows the macro-hardness evolution of the AISI 302 steel aged at 1100°C and 1200°C for 0, 60, 600, 1000, and 6000 minutes. Regardless of the aging temperature, this mechanical property reduced significantly by incrementing the treatment time.

As shown in Figure 6, the thermal aging behavior of AISI 302 steel was almost identical for the two temperatures studied. The aging behavior of the AISI 302 steel exhibited a decreasing trend with two-softening stages and it can be described as follows: the macro-hardness decreased sharply in the first stage (0–1000 minutes) and it continued to decrease but slightly in the second stage (1000–6000 minutes). The error bars represent the standard deviation of the macro-hardness measurements. In the second stage, the variation of the macro-hardness standard deviation fluctuated very little compared with the first stage.

The significant loss of the steel macro-hardness can be explained mainly by the austenite grains growth and reduction in the area of grain boundaries per unit volume [14,27,38]. The Hall-Petch equation [39–41] also confirms the relationship between the variation in the macro-hardness (H) and the change in the microstructure. It can be written as follows:

$$H = f \times \left(H_0 + k / \frac{1}{d^2} \right) + (1 - f) \times H_{GB}. \quad (5)$$

In which f is the volume fraction of the grains and $(1-f)$ is the volume fraction of the grain boundaries, H_0 and k are material-specific constants, d is the average grain diameter, and H_{GB} is the hardness of the grain boundaries.

For the two temperatures investigated, the two stages of the macro-hardness variation as a function of time are due to the decrease of the grain growth rate by incrementing the treatment time [11, 12].

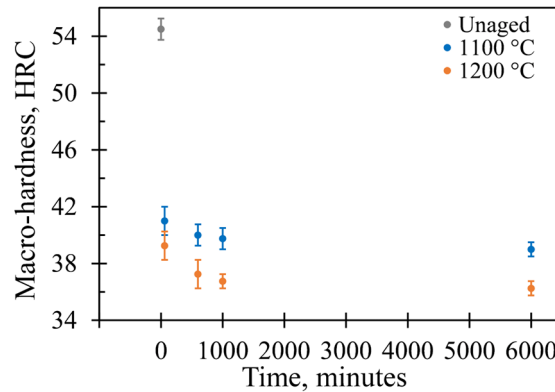


Figure 6. Macro-hardness variation of the AISI 302 steel aged at 1100°C and 1200°C for 0 (unaged), 60, 600, 1000, and 6000 minutes

4. CONCLUSIONS

In this study, the influence of thermal aging on the microstructural changes, nanoindentation responses, and macro-hardness evolution of the AISI 302 steel was investigated. The main conclusions drawn from this study were as follows:

1. According to metallurgical observations, the increase in the temperature or time of aging leads to an increase in the grains size. The austenite grain size aged for 0 minutes was $49.23 \pm 25 \mu\text{m}$ and after 6000 minutes, it changed significantly to 581.71 ± 38.25 and $1268.10 \pm 33.45 \mu\text{m}$ for the temperatures 1100°C and 1200°C, respectively.
2. At a fixed aging temperature, the nanohardness of the austenite decreased by incrementing the aging time from 0 to 6000 minutes. The nanohardness of the austenite aged at 0 minutes was equal to 3.69 ± 0.30 GPa, and after 6000 minutes of aging, it was equal to 2.40 ± 0.10 and 2.34 ± 0.15 GPa for the temperatures 1100°C and 1200°C, respectively.
3. For the temperatures explored, the macro-hardness property dropped significantly with incrementing the thermal aging time. The macro-hardness of AISI 302 steel aged at 0 minutes was equal to 54.5 ± 0.75 HRC and after 6000 minutes of aging, it was equal to 39 ± 0.5 and 36.25 ± 0.5 HRC for the temperatures 1100°C and 1200°C, respectively.

ORCID

©Omar Ben Lenda, <https://orcid.org/0009-0008-1979-5508>; ©Hajar El Ganich, <https://orcid.org/0000-0003-3303-607X>
 ©El Madani Saad, <https://orcid.org/0000-0003-3621-1339>

REFERENCES

- [1] J.K.L. Lai, C.H. Shek, and K.H. Lo, *Stainless steels: An introduction and their recent developments*, (Bentham Science Publishers, Beijing, China, 2012), pp. 23. <https://doi.org/10.1007/978-1-84628-669-8>
- [2] J.R. Davis, *Alloy digest sourcebook: stainless steels*, (ASM international, Materials Park, Ohio, USA, 2000), p. 7.
- [3] S.L. Chawla, *Materials selection for corrosion control*, (ASM international, Materials Park, Ohio, USA, 1993), p. 117.
- [4] F. Cardarelli, *Materials Handbook: A Concise Desktop Reference*, 2nd ed. (Springer Science & Business Media, London, UK, 2008), p. 102. <https://doi.org/10.1007/978-1-84628-669-8>
- [5] N.A. Savinkov, O.M. Bulanchuk, and A.A. Bizyukov, *East Eur. J. Phys.* **3**, 102 (2021). <https://doi.org/10.26565/2312-4334-2021-3-16>
- [6] I. Kolodiy, O. Kalchenko, S. Karpov, V. Vovodin, M. Tikhonovsky, O. Velikodnyi, G. Tolmachova, R. Vasilenko, and G. Tolstolutska, *East Eur. J. Phys.* **2**, 105 (2021). <https://doi.org/10.26565/2312-4334-2021-2-07>
- [7] V. Vovodin, M. Tikhonovsky, G. Tolstolutska, H. Rostova, R. Vasilenko, O. Kalchenko, N. Andrievska, and O. Velikodnyi, *East Eur. J. Phys.* **3**, 93 (2020). <https://doi.org/10.26565/2312-4334-2020-3-12>
- [8] N. Filonenko, A. Babachenko, and G. Kononenko, *East Eur. J. Phys.* **2**, 46 (2019). <https://doi.org/10.26565/2312-4334-2019-2-07>
- [9] V.A. Belous, Yu.A. Zadneprovskiy, N.S. Lomino, I.S. Domnich, and T.I. Bevs, *East Eur. J. Phys.* **4**, 98 (2018). <https://doi.org/10.26565/2312-4334-2018-4-12>
- [10] O. Ben Lenda, S. Benmaziane, A. Tara, and E. Saad, *E3S Web Conf.* **297**, (2021). <https://doi.org/10.1051/e3sconf/202129701044>
- [11] D. Dong, F. Chen, and Z. Cui, *J. Mater. Eng. Perform.* **25**, 152 (2016). <https://doi.org/10.1007/s11665-015-1810-9>
- [12] Z. Li, Z. Wen, F. Su, R. Zhang, and Z. Li, *J. Mater. Res.* **31**, 2105 (2016). <https://doi.org/10.1557/jmr.2016.248>
- [13] S. Benmaziane, O. Ben Lenda, S. Saissi, L. Zerrouk, and E. Saad, *Recent Pat. Mech. Eng.* **15**, 486 (2022). <http://dx.doi.org/10.2174/2212797615666220816123154>
- [14] Z. B. Liu, X. Tu, X. H. Wang, J. X. Liang, Z. Y. Yang, Y. Q. Sun, and C. J. Wang, *J. Iron Steel Res. Int.* **27**, 732 (2020). <https://doi.org/10.1007/s42243-020-00429-6>

- [15] R.C. Chen, C. Hong, J.J. Li, Z.Z. Zheng, and P.C. Li, *Procedia Eng.* **207**, 663 (2017), <https://doi.org/10.1016/j.proeng.2017.10.1038>
- [16] C. Yue, L. Zhang, S. Liao, and H. Gao, *J. Mater. Eng. Perform.* **19**, 112 (2010), <https://doi.org/10.1007/s11665-009-9413-y>
- [17] Y. Su, R. Song, T. Wang, H. Cai, J. Wen, and K. Guo, *Mater. Lett.* **260**, 1 (2020), <https://doi.org/10.1016/j.matlet.2019.126919>
- [18] S. Li, Y. Wang, S. Li, H. Zhang, F. Xue, and X. Wang, *Mater. Des.* **50**, 886 (2013), <https://doi.org/10.1016/j.matdes.2013.02.061>
- [19] G. Liu, Y. Wang, S. Li, and X. Wang, *J. Mater. Eng. Perform.* **27**, 4714 (2018), <https://doi.org/10.1007/s11665-018-3540-2>
- [20] O. Ben Lenda, E. Saad, A. Tara, and O. Jbara, *Adv. Mater. Process. Technol.* **8**, 3859 (2022), <https://doi.org/10.1080/2374068X.2022.2036443>
- [21] H.S. Khatak, and B. Raj, *Corrosion of Austenitic Stainless Steels: Mechanism, Mitigation and Monitoring* (Woodhead Publishing, Cambridge, UK, 2002), p. 6
- [22] G.F. Vander Voort, *Metallography, Principles and Practice* (ASM International, Materials Park, Ohio, USA, 1999), p. 649
- [23] M. Yovanovich, in: *Proceedings of the 44th AIAA Aerospace Sciences Meeting and Exhibit* (American Institute of Aeronautics and Astronautics, Reno, Nevada, 2006), pp. 1-28.
- [24] W.C. Oliver, and G.M. Pharr, *J. Mater. Res.* **7**, 1564 (1992). <https://doi.org/10.1557/JMR.1992.1564>
- [25] G.M. Pharr, W.C. Oliver, and F.R. Brotzen, *J. Mater. Res.* **7**, 613 (1992). <https://doi.org/10.1557/JMR.1992.0613>
- [26] E. Broitman, *Tribol. Lett.* **65**, 1 (2017), <https://doi.org/10.1007/s11249-016-0805-5>
- [27] G.E. Dieter, H.A. Kuhn, and S.L. Semiatin, *Handbook of Workability and Process Design* (ASM international, Materials Park, Ohio, USA, 2003), pp. 250-251
- [28] Y. Xu, J. Liu, Y. Zhao, and Y. Jiao, *Philos. Mag.* **101**, 77 (2021). <https://doi.org/10.1080/14786435.2020.1821113>
- [29] M. Militzer, E.B. Hawbolt, and T.R. Meadowcroft, *Metall. Mater. Trans. A*, **27**, 3399 (1996). <https://doi.org/10.1007/BF02595433>
- [30] S.H. Mohamadi Azghandi, V. Ghanooni Ahmadabadi, and A. Zabet, *Philos. Mag.* **94**, 2758 (2014). <https://doi.org/10.1080/14786435.2014.932460>
- [31] B.R. Patterson, and Y. Liun, *Metall. Trans. A*. **23**, 2481 (1992). <https://doi.org/10.1007/BF02658051>
- [32] T.H. Ahn, C.S. Oh, K. Lee, E.P. George, and H.N. Han, *J. Mater. Res.* **27**, 39 (2012), <https://doi.org/10.1557/jmr.2011.208>
- [33] N.K. Mukhopadhyay, and P. Paufler, *Int. Mater. Rev.* **51**, 209 (2006), <https://doi.org/10.1179/174328006X102475>
- [34] O. Ben Lenda, A. Tara, F. Lazar, O. Jbara, A. Hadjadj, and E. Saad, *Strength Mater.* **52**, 71 (2020). <https://doi.org/10.1007/s11223-020-00151-4>
- [35] S.L. Li, Y.L. Wang, and X.T. Wang, *Mater. High Temp.* **32**, 524 (2015). <https://doi.org/10.1179/1878641314Y.0000000040>
- [36] G. Liu, Y. Wang, S. Li, K. Du, and X. Wang, *Mater. High Temp.* **33**, 15 (2016). <https://doi.org/10.1179/1878641315Y.0000000014>
- [37] S.L. Li, Y.L. Wang, H.L. Zhang, S.X. Li, K. Zheng, F. Xue, and X.T. Wang, *J. Nucl. Mater.* **433**, 41 (2013). <https://doi.org/10.1016/j.jnucmat.2012.09.004>
- [38] J. Choi, C.S. Seok, S. Park, and G. Kim, *J. Mater. Res. Technol.* **8**, 2011 (2019). <https://doi.org/10.1016/j.jmrt.2018.11.017>
- [39] E.O. Hall, *Proc. Phys. Soc. B*, **64**, 747 (1951). <https://doi.org/10.1088/0370-1301/64/9/303>
- [40] N.J. Petch, *J. Iron Steel Inst.* **174**, 25 (1953)
- [41] A.M. Glezer, and I.E. Permyakova, *Melt-Quenched Nanocrystals* (CRC Press, Boca Raton, Florida, USA, 2013).

ХАРАКТЕРИСТИКА МІКРОСТРУКТУРИ, НАНО- ТА МАКРОІНДЕНТАЦІЇ СТАЛІ AISI 302 ПІСЛЯ ВИСОКОТЕМПЕРАТУРНОГО СТАРІННЯ

Омар Бен Ленда^а, Хаджар Ель Ганіч^б, Ель Мадані Саад^а

^аПерший університет Хасана в Сетаті, лабораторія фізико-хімії процесів та матеріалів факультету наук та технологій, Сетат, Марокко

^бПерший університет Хасана в Сеттаті, вищий інститут медичних наук, лабораторія наук та технологій охорони здоров'я, BP 555, 26000, Сетат, Марокко

Структурні та механічні дослідження сталі AISI 302 спрямовані на розробку правильної термообробки з метою оптимізації її механічних властивостей. У цьому дослідженні ми досліджували вплив температури та часу старіння на структурно-механічні характеристики сталі AISI 302. Сталь старіли при температурах 1100°C і 1200°C протягом часу від 0 до 6000 хвилин. Методами структурної та механічної характеристики, які використовувалися, були металургійний мікроскоп, метод наноіндентування та тест на макротвердість. На мікроструктурному рівні збільшення часу або температури старіння сприяло збільшенню розміру зерен аустеніту сталі AISI 302. Ця зміна мікроструктури призвела до зниження нанотвердості та падіння макротвердості між нестареним і старим станом сталі AISI 302.

Ключові слова: сталь AISI 302; старіння; мікроструктура; аустеніт; зростання зерна; нанотвердість; наноіндентування; макротвердість

INFLUENCE OF APERTURE OF RADIATING STRIP STRUCTURE ON ELECTRODYNAMIC CHARACTERISTICS OF PATCH ANTENNA

✉Sergey A. Pogarsky*, ✉Dmitry V. Mayboroda, Serhii M. Mykhaliuk

V.N. Karazin Kharkiv National University, 4, Svobody Sq., Kharkiv, Ukraine, 61022

*Corresponding Author e-mail: spogarsky@gmail.com

Received September 3, 2023; revised September 19, 2023; accepted September 22, 2023

The paper presents the results of numerical modeling of the electrodynamic characteristics of a Vivaldi type patch antenna based on a circular disk resonator. The modeling was carried out using the semi-open resonator model by the finite element method (FEM) implemented in the HFFS package. The antenna was fed using a coplanar line segment. The antenna elements were placed over a grounded plane. The influence of design parameters and the function determining the curvature of the exponentially expanding slot discontinuity on the frequency, energy and polarization characteristics was investigated. It was established that with a certain selection of variable parameters, such an antenna can be matched with external circuits in the range from 7.03 GHz to 20 GHz with a level of VSWR values not exceeding 1.92. In the amplitude-frequency characteristic, fairly wide frequency bands with almost perfect matching are observed. The choice of the type of excitation element in the form of a section of the coplanar line made it possible to exclude additional elements inherent in Vivaldi antennas, namely, a section of the auxiliary strip line and a balancing resonator. This kind of antenna allows to form radiation patterns of various shapes from single-sided to cosecant quadrate. At the same time, in some intervals of observation angles, the formed fields turn out to be elliptically polarized with an ellipticity coefficient close to unity. The combination of the obtained results makes it possible to predict the use of this kind of antennas for operation with broadband signals.

Keywords: Ring resonator; Antenna Vivaldi; Coplanar line; Matching; Frequency characteristics; Energy characteristics

PACS: 84.40.Ba; 84.40.Dc

Small-size strip-type antennas with various radiating apertures have long been an integral part of radio engineering systems for various purposes. The bibliography, which reflects possible variants of aperture, can be found in a large number of publications [1-3]. The purpose of this or that type of aperture is determined by the need to solve certain radio engineering problems. If such a single antenna had to have a maximum (or very high compared to an isotropic radiator) gain, the designs described in [4, 5] were used. If it was necessary to be able to operate with arbitrary polarization of the radiated or received fields, other designs were used [6, 7]. Structural (topological) solutions for both one and another case have both general principles of construction of structures and presence of elements, which lead to fundamental differences both in circuit solutions and in approaches, methods of modeling and determination of parameters of such complex-composition systems [8].

A special place is occupied by planar single antennas (or antenna arrays based on them), which are used for transmission (reception) of ultra-wideband signals. Such kind of radiating structures should have as significantly wider operating band (or several separate bands) in comparison with "standard" technical solutions, acceptable gain and acceptable level of matching with external circuits. Quite a large number of designs and technical solutions are known that satisfy such requirements [9-11]. In addition, there are a number of other factors (e.g., antenna location in space) that can significantly complicate the application of known designs or require their substantial modernization.

One of the most important elements of any microwave design is the element of feeding (in fact, the method of feeding) of a certain (given) spectrum of oscillations. Among the most widespread methods of feeding in the microwave range we can point out the planar ones - it is feeding by means of sections of various types of strip lines [12], sections of coaxial line [13], and in the high-frequency part of the microwave range (above 20 GHz) - sections of standard metal or dielectric waveguides [14].

Any of the known feeding methods has both known advantages and disadvantages. For example, the planar method of feeding allows to preserve the overall planarity of the structure. At the same time, taking into account the possibility of existence of higher types of waves (under certain conditions), the process of simulation the parameters of such a structure becomes much more complicated. When using multi-element stripline systems for feeding (for example, coplanar or multiconductor), it is necessary to take into account a wide enough spectrum of possible natural waves. The use of the feeding method using a coaxial line segment basically violates the planarity of the structure. In addition, under certain conditions, this method of feeding can lead to the need to search for non-standard design solutions. At the same time, due to the peculiarities of the coaxial line itself, the spectrum of the considered natural waves existing in the radiating structure is limited in the low-frequency part when modeling the characteristics.

Considering all these factors, it is relevant to study the influence of the radiating aperture of a planar antenna on its characteristics at a given method of feeding.

In this paper we consider an antenna with an exponentially varying aperture opening (Vivaldi type antenna) and the effect of different parameters on the frequency, energy and polarization characteristics of the antenna.

STRUCTURE UNDER STUDY

We will consider an electrodynamic structure, which is a disk-strip resonator having an exponentially expanding slot. Antennas with this kind of slot inhomogeneity are called "Vivaldi antennas" in the known literature [15, 16]. A disk-shaped strip resonator, or patch resonator, is placed on a thin dielectric substrate. This entire structure is placed over an infinitely extended, infinitely conducting metallic plane (Fig. 1). It should be noted that such an electrodynamic model is as close as possible to real antenna designs for various purposes. In Fig. 1 the following designations are used: 1 - metallic plane, 2 - dielectric substrate, 3 - patch element, 4 - coplanar line elements.

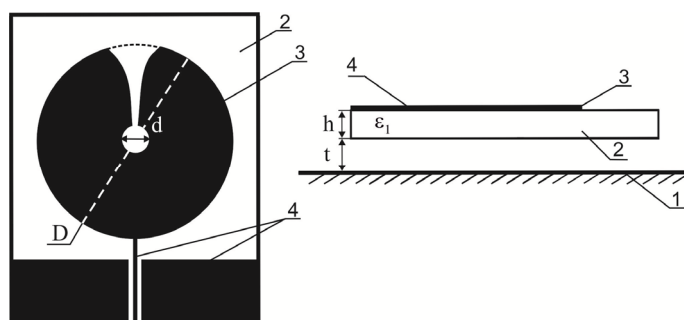


Figure 1. The structure geometry and notations

In known designs, feeding of the slot discontinuity is carried out by means of a strip line segment located under the slot discontinuity. A symmetrizing strip resonator is an obligatory element. All this complicates the design and affects the antenna characteristics quite strongly. In the proposed design, the feeding is carried out using a disk slot discontinuity. Due to the fact that this discontinuity feeds axially symmetric types of oscillations (due to a certain choice of geometric dimensions of the structure in comparison to the resonant frequencies), there is no need to use an auxiliary strip resonator, in addition, all elements of the structure are located in one plane.

Geometric dimensions and material constants were chosen based on the assumption that the antenna is designed to operate in the microwave frequency range. The following values of parameters were chosen: external diameter of the patch element $D = 13.5$ mm; internal diameter $d = 2$ mm; thickness of dielectric substrate $h = 0.5$ mm; the values ϵ , t are variant values. The infinity of the dimensions of the metal plane allows not to take into account the edge diffraction effects.

RESULTS OF NUMERICAL SIMULATION

The construction of a rigorous electrodynamic model of such a structure is rather difficult and, as it seems, practically impossible in the near future. Numerical simulation can be realized within the framework of the well-known model of a semi-open resonator. The model assumes, the resonator is formed by two elements – a patch element and a grounded base. Under the assumption that the metal of the elements is ideal, the classical boundary condition of zero equality of the tangential component of the electric field is satisfied on the elements. Another element of the resonator is the cylindrical surface, which is defined by the projection of the patch element onto the grounded plane. The magnetic wall condition is satisfied on this surface.

Based on the chosen ratio of the structure parameters and imposing certain restrictions on the parameter t , we can say that if the thickness of the dielectric substrate and the distance to the grounded base are significantly smaller than the resonant length in the resonator λ_r , the electric field vector will not have variations along the coordinate system ort perpendicular to the plane of the structure. In this case, the spectrum of oscillations excited in the resonator will include only oscillations of the $E_{mn0} (TM_{mn0})$ type.

Numerical simulations have been carried out using the finite element method (FEM) implemented within the commercial ANSOFT HFSS package [17]. As it is obvious, the dependencies of the main frequency and energy parameters are multi-parametric. For this reason, a multi-criteria optimization was carried out, first of all, of the return loss value $|S_{11}|$ using the above-mentioned variational parameters.

As it is known, the return loss value $|S_{11}|$ and the associated VSWR (voltage standing wave ratio) value determine the degree of matching of the device with external circuits. This parameter is important both from the point of view of minimal impact on the source that excites oscillations, and from the point of view of effective transfer of oscillation energy to the final device. The dependencies of both quantities are multi-parametric on the antenna geometric dimensions and material constants. For this reason, the evaluation of the matching level by only one parameter is not an absolute criterion for the overall performance. Nevertheless, the study of partial dependencies of return loss on any of

the parameters allows us to determine the frequency bands within which effective operation is possible (in this case, it is effective radiation).

Analysis of known designs using strip, microstrip, slot and coplanar structures shows that an integral part is a dielectric substrate, on which the patch elements are placed. The dielectric substrate is thus an important structural element, but, at the same time, the substrate is involved in the formation of a certain field structure, affecting the value of the input impedance (i.e., affecting the value of the matching of the device as a whole). Thus, the substrate parameters thickness h and dielectric constant value ϵ_r are important parameters. Moreover, the dielectric substrate thickness is a decisive factor for eliminating the possibility of excitation of surface waves in the dielectric substrate. In this regard, a priori the substrate thickness h is chosen "thin" in comparison with the resonance lengths of oscillations that are excited in the structure, and in comparison, with the operating wavelength ($h \ll \lambda_r, h \ll \lambda$). We limit the operating frequency range to the value of $F = 20$ GHz, because above this frequency, higher types of waves and slot waves may exist in the feed coplanar line. The value of the thickness is chosen to be $h = 0.5$ mm, which is significantly smaller than the minimum operating wavelength $\lambda = 1.5$ cm for the $F = 20$ GHz frequency.

Fig. 2 shows the dependences of the return loss value $|S_{11}|$ in a given frequency range when the dielectric constant of the substrate varies. Values of dielectric permittivity are chosen from a number of values that are used in real devices.

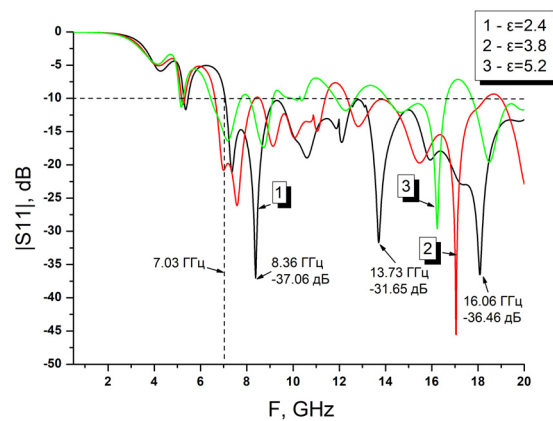


Figure 2. Dependencies of $|S_{11}|$ vs frequency with ϵ_r variation

The analysis of dependencies shows that all dependencies have oscillatory character regardless of the value of ϵ_r . The frequency range (from 0.5 to 3 GHz) is clearly seen, within which a complete reflection is observed, i.e., matching is not possible in principle. In the vicinity of 5 GHz, a not wide local band with an acceptable level of return loss is observed. For the dielectric substrate with the value of $\epsilon_r = 2.4$, starting from the $F = 7.03$ GHz frequency, an ultra-wide band opens up with a broadband coefficient of $\xi \approx 2.84$. This value of ϵ_r should be considered optimal. And, although within this band there are certain oscillations of the value of $|S_{11}|$, the absolute level of return loss does not exceed the value of -10 dB (corresponding to the value of $VSWR \approx 1.92$). In addition, near the frequencies 8.36 GHz, 13.73 GHz, 16.06 GHz local frequency bands are observed, within which there is almost perfect matching with a level less than -30 dB, which corresponds to $VSWR < 1.06$ and direct losses of -0.004 dB. Near these frequencies, the effective radiation pattern of the antenna can be predicted. However, other antenna characteristics may not have maximum values at other frequencies in the range of return loss levels less than -10 dB.

Another important antenna design parameter is the parameter t . It is the distance from the patch element to the ground plane. From the point of view of electrodynamics, this parameter is important for two reasons. First, it determines the size of the region where the energy of excited oscillations is concentrated. Second, this parameter will ultimately influence the value of the resonant frequency of the structure. And thus, the combination of these two factors will determine on the energy characteristics of the antenna (gain, pattern, polarization characteristics).

Fig. 3 shows the dependence $|S_{11}|$ vs the frequency with variation of the parameter t .

The analysis of the above dependencies shows that in the considered frequency range all dependencies have a sharply oscillatory character. Especially noticeable are the drops of $|S_{11}|$ values at a small value of the parameter t ($t = 1.5$ mm, curve 1). This is explained by the factor that at close location of the screen to the coplanar line elements it passes from the class of isolated coplanar lines to the class of grounded coplanar lines, which are characterized by a strong dispersion dependence. Increasing this distance leads to a decrease in this dependence, while a decrease in ripples is observed.

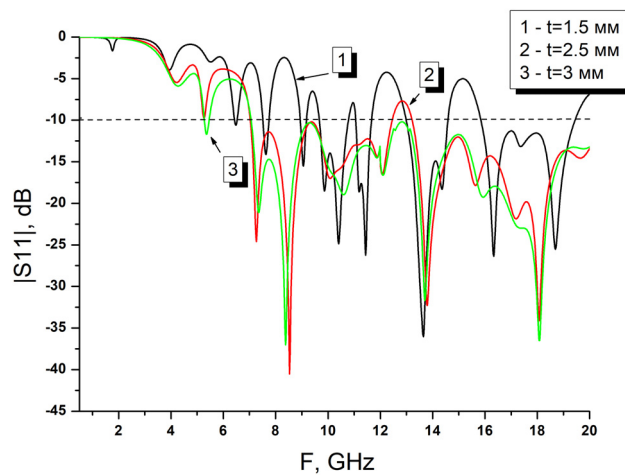


Figure 3. Dependencies of $|S_{11}|$ vs frequency with variation t

By using the optimization procedure, a value of the parameter $t = 3$ mm (curve 3) is obtained at which the ripple of $|S_{11}|$ does not exceed the value of -10 dB. Further increase of the parameter t does not lead to reduction of the ripple level, and from the structural point of view the structure itself loses one of its main advantages it is planarity.

The classical version of the Vivaldi type strip antenna for excitation involves the use of a strip line segment with a symmetric resonator. The functional purpose of the symmetric resonator is to equalize the phases of the currents flowing along opposite sections of the slot discontinuity. The option of using for such an antenna actually a ring resonator allows to simplify the design considerably. Fig. 4 shows the distribution of current density lines on the disk patch element and the ground plane.

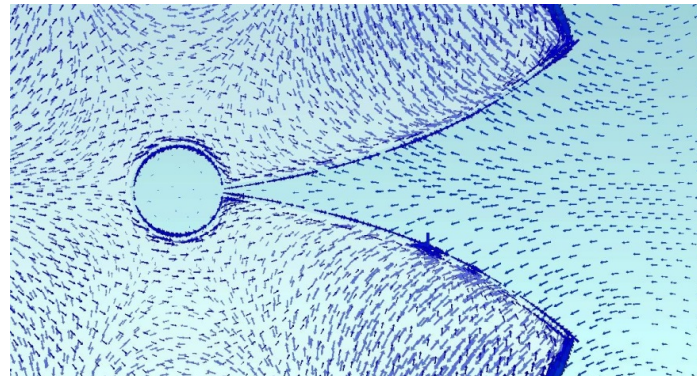


Figure 4. Structure of current density lines on the antenna elements

The image analysis shows that the internal slot resonator is excited on one of the lowest axially symmetric oscillation type E_{020} . And the currents that come to the beginning of the exponential slot discontinuity come in the same phase. For this reason, it can be assumed that the radiation pattern will have a single-lobe shape. The currents on the ground plane are in anti-phase with respect to the currents on the patch element.

The topology of the exponential slot discontinuity (actually the opening angle) has a significant influence not only on the magnitude of $|S_{11}|$, but also determines the antenna gain. Fig. 5 shows two dependences of the gain on frequency for two different topologies defined by the functions: curve 1 - $2 \cdot \exp(-0.3 \cdot x) + 0.1$; curve 2 - $8 \cdot \exp(-0.123 \cdot x) - 1$ for the optimized value of the parameter $t = 3$ mm and the value of the relative dielectric constant of the substrate $\epsilon_r = 2.4$. x is a linear coordinate along the exponential slot. The gain dependencies are plotted with respect to the gain of an isotropic radiator (IEEE classification in dBi).

As it is obvious both dependences have oscillatory character. However, in the case of a larger opening (curve 2) the scatter of values is smaller and amounts $\approx 34\%$ to 6.67 dBi from the mean value compared to a smaller opening where the scatter amounts $\approx 47\%$ to 6.16 dBi from the mean value. Both dependencies have an absolute maximum, but these maxima are quite strongly shifted in frequency relative to each other. These maxima are much higher than the "standard" value of patch antenna gain (in general it is 5...6). But, if in known designs such values are achieved only at some fixed frequencies (in some cases in the band of 1...2% reduced to the center frequency of this range), then, focusing on the value of 6 dBi, the band in this case is $\Delta F = 6.8$ GHz (reduced to the center frequency - 86%). That is, in this band it is possible to work with wideband signals.

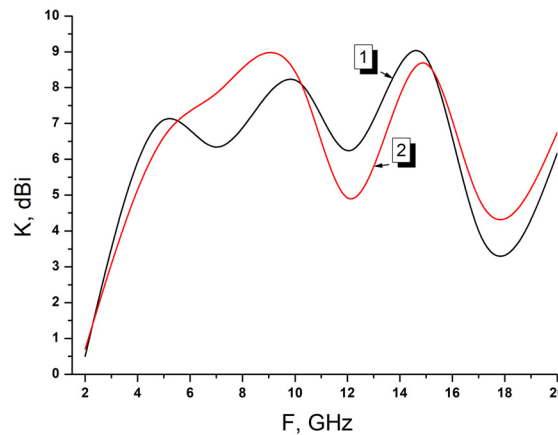


Figure 5. Dependences of the gain coefficient vs frequency at variation of the slot discontinuity opening function

Since the energy and polarization characteristics are multi-parametric dependencies, it is possible to synthesize antennas with given parameters using various optimization procedures. As an example, in Fig. 6 one can find the normalized radiation patterns in the azimuthal plane (as with any traveling wave antenna) at two frequencies $F = 7$ GHz and $F = 8.38$ GHz for an antenna with optimized values of the parameters ϵ_r and t . The frequencies are chosen based on the specific use of the antenna. These two frequencies correspond to two minima in the low-frequency part of the considered range near the minima of the $|S_{11}|$ function values.

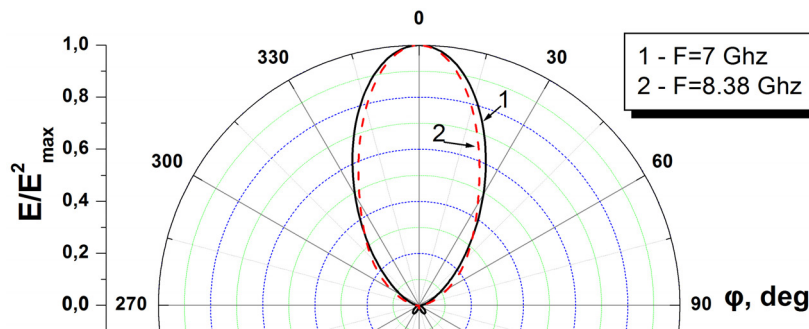


Figure 6. Directional patterns in azimuthal plane with optimized set of parameters

It is obvious that at both frequencies the directivity patterns are single-lobe, symmetric with respect to the direction of the axis of the exponential slot inhomogeneity, the maximum of the main lobe of the pattern is observed in the direction of this axis. The level of the rear lobes at the $F = 7$ GHz frequency does not exceed -18 dB. The width of the diagram at 0.707 level depends on the topology of the slot heterogeneity (actually the maximum opening), which is determined by the curvature change function. In this case, the diagram is given for the function (wide opening) and the width is 35° . By varying the parameters t, ϵ_r and the curvature change function, it is possible to form directional diagrams of other shapes (double-lobe, cosecant quadrate, etc.).

In most cases, planar patch antennas form linearly polarized radiated fields, unless the design uses various auxiliary elements that change the distribution of surface currents on the surface of the patch elements (e.g., short-circuits), or uses multiport feeding with a certain phase shift. In the antenna under consideration, over the entire operating frequency range, relatively narrow intervals of angles are observed within which elliptical polarization of the radiated fields can be obtained. These frequencies are usually coincident (or very close) to the natural resonant frequencies of the types of oscillations excited in the resonating volume. However, at some frequencies in the antenna without using known techniques it is possible to obtain radiated fields elliptically polarized with an ellipticity coefficient close to zero (according to the IEEE criterion in dB). Fig. 7 shows the angular-local polarization characteristic of the antenna at $F = 8.38$ GHz. Near this frequency, a rather deep minimum with a level up to -37 dB is observed on the amplitude-frequency characteristics (with parameter variation t, ϵ_r) (the VSWR level of 1.029 and direct loss of -0.001 dB are provided).

As one can see from the graph above, in the range of observation angles from 78.5° to 109.9° the ellipticity coefficient does not exceed the value of 3 dB, i.e. polarization is close to circular. At the observation angle $\theta = 91.85^\circ$ the value of the ellipticity coefficient is $\eta = 0.053$ dB. In other ranges of angle variation, linear polarization is observed. By varying the parameters ϵ_r and t the opening angle, the ellipticity coefficient can be achieved, but other important characteristics can be significantly degraded.

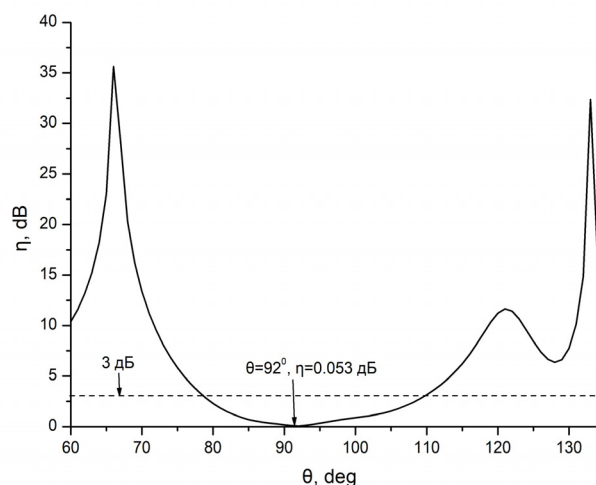


Figure 7. Polarization characteristic at the $F = 8.38$ GHz frequency

CONCLUSION

The paper presents the results of numerical modeling of the parameters of the Vivaldi type patch antenna. The antenna excitation was carried out by means of a coplanar line segment. The antenna and exciter elements were placed on a dielectric substrate and were "suspended" above a grounded base. The presence of a sufficiently large number of variable parameters allows control of frequency, energy and polarization parameters in a sufficiently wide frequency band. The antenna is sufficiently well matched with external circuits in a wide enough frequency range and has a sufficiently high gain in comparison with known designs based on various planar structures. The totality of the obtained results allows us to predict the use of this kind of antennas for operation with broadband signals.

ORCID

©Sergey A. Pogarsky, <https://orcid.org/0000-0003-0833-1421>; ©Dmitry V. Mayboroda, <https://orcid.org/0000-0002-9564-2369>

REFERENCES

- [1] K.-L. Wong, *Compact and Broadband Microstrip Antennas*, (John Wiley & Sons, 2002). <https://doi.org/10.1002/0471221112>
- [2] G. Kumar, and K.P. Ray, *Broadband microstrip antennas*, (Artech House, 2003). <http://read.pudn.com/downloads150/ebook/652719/Broadband%20microstrip%20antennas.pdf>
- [3] J. Liu, Q. Xue, H. Wong, H.W. Lai, and Y. Long, "Design and analysis of a low-profile and broadband microstrip monopolar patch antenna," *IEEE Trans. Antennas Propag.*, **61**, 11-18, (2013). <https://doi.org/10.1109/TAP.2012.2214996>
- [4] Z. Wang, L. Juhua, and L. Yunliang, "A simple wide-bandwidth and high-gain microstrip patch antenna with both sides shorted," *IEEE Antennas and Wireless Propagation Lett.* **18.6**, 1144-1148, (2019). <https://doi.org/10.1109/LAWP.2019.2911045>
- [5] F. Xue, H. Wang, Y. Wang, and L. Zhang, "Broadband and high efficiency single-layer reflectarray using circular ring attached two sets of phase-delay lines," *PIER M.* **66**, 193-202, (2018). <https://doi.org/10.2528/PIERM18010916>
- [6] Nasimuddin, Z.N. Chen, and X. Qing, "Slotted microstrip antennas for circular polarization with compact size," *IEEE Antennas and Propag. Magazine*, **55**, 127-134, (2013). <https://doi.org/10.1109/MAP.2013.6529322>
- [7] E.S. Angelopoulos, A.Z. Anastopoulos, D.I. Kaklamani, A.A. Alexandridis, F. Lazarakis, and K. Dangakis, "Circular and Elliptical CPW-Fed Slot and Microstrip-Fed Antennas for Ultra-wideband Applications," *IEEE Antennas and Wireless Propag. Lett.*, **5**, 294-297, (2006). <https://doi.org/10.1109/LAWP.2006.878882>
- [8] D.V. Maiboroda, and S.A. Pogarsky, "On the choice of optimal topology of a reflecting module based upon the circular microstrip structure," *Telecom. and Radio Eng.* **73**(19), 1713-1726 (2014). <https://doi.org/10.1615/TelecomRadEng.v73.i19.20>
- [9] Y.-J. Ren, and K. Chang, "An Annual Ring Antenna for UWB Communications", *IEEE Antennas and Wireless Propag. Lett.* **5**, 274-276, (2006). <http://dx.doi.org/10.1109/LAWP.2006.875897>
- [10] Z. Niang, and X.M. Qing, "Research and development of planar UWB antennas", *IEEE APMC 2005 Proceedings*, (2005). <https://doi.org/10.1109/APMC.2005.1606190>
- [11] F. Geran, G. Dashzadeh, M. Fardis, N. Hojjat, and A. Ahmadi, "Rectangular slot with a novel triangle ring microstrip feed for UWB applications," *J. of Electromagnetic Waves and Appl.* **21**(3), 387-396 (2007). <http://dx.doi.org/10.1163/156939307779367341>
- [12] S.A. Pogarsky, L.M. Lytvynenko, D.V. Mayboroda, and A.V. Poznyakov, "Influence of excitation method on the integral characteristics of circular patch monopole antennas," *Telecommunications and Radio Eng.* **77**(17), 1485-1495 (2018). <https://doi.org/10.1615/TelecomRadEng.v77.i17.10>
- [13] G. Kumar, and K.P. Ray, *Broadband microstrip antennas*, (Artech House Inc. Boston, London, 2003).
- [14] S.A. Pogarsky, and D.V. Mayboroda, UA Patent No. 151703, (31 August, 2022).
- [15] S. Lin, "Development of a novel UWB Vivaldi antenna array using SIW technology," *Progress in Electr. Res.* **90**, 369-384 (2009). <http://dx.doi.org/10.2528/PIER09020503>
- [16] J. Shan, A. Xu, and J. Lin, "A Parametric Study of Microstrip-Fed Vivaldi Antenna", in: *Proc. of 2017 3rd IEEE Intern. Conf. on Computer and Communications (ICCC)*, (2017), pp. 1099-1103. <https://doi.org/10.1109/comppcomm.2017.8322713>
- [17] Ansoft HFSS /ANSYS Academic Research HF (5 tasks): 1 task(s) Permanent with TECS expiring 01-May-2020 Customer #1076710.

ВПЛИВ АПЕРТУРИ ВИПРОМНОЧОЇ СМУЖКОВОЇ СТРУКТУРИ НА ЕЛЕКТРОДИНАМІЧНІ ХАРАКТЕРИСТИКИ ПАТЧ АНТЕНИ

Сергій О. Погарський, Дмитро В. Майборода, Сергій М. Михалюк

Харківський національний університет імені В.Н. Каразіна, майдан Свободи, 4, Харків, Україна, 61022

У статті представлено результати чисельного моделювання електродинамічних характеристик патч-антени типу Вівальді на основі кільцевого дискового резонатора. Моделювання здійснено з використанням моделі напіввідкритого резонатора методом кінцевих елементів (МКЕ), реалізованого в пакеті ANSOFT HFSS. Збудження антени здійснювалося за допомогою відрізка копланарної лінії. Елементи антени розміщувалися над заземленою площиною. Досліджено вплив конструктивних параметрів і функції, що визначає кривизну щільної неоднорідності, яка експоненціально розширюється, на частотні, енергетичні та поляризаційні характеристики. Встановлено, що за певного вибору варіативних параметрів таку антену вдається узгодити із зовнішніми ланцюгами в діапазоні від 7.03 ГГц до 20 ГГц з рівнем значень КСВН, що не перевищують величину 1.92. В амплітудно-частотній характеристиці спостерігаються досить широкі частотні смуги з практично ідеальним узгодженням. Вибір типу елемента збудження у вигляді відрізка копланарної лінії дозволив виключити додаткові елементи, притаманні антенам типу Вівальді, а саме, відрізок допоміжної смужкової лінії та симетруючий резонатор. Такого роду антена дозволяє формувати діаграми спрямованості різної форми від однопелюсткової до косеканс квадратної. При цьому в деяких інтервалах кутів спостереження поля, що формуються, виявляються еліптично поляризованими з коефіцієнтом еліптичності близьким до одиниці. Сукупність отриманих результатів дозволяє прогнозувати використання такого роду антен для роботи з широкосмуговими сигналами.

Ключові слова: *кільцевий резонатор; антена Вівальді; копланарна лінія; узгодження; частотні характеристики; енергетичні характеристики*

THE COMPUTER MODEL OF A THERMAL DELAYED NEUTRON FLUXES FORMING SYSTEM FOR NUCLEAR MEDICINE

Sergey P. Gokov^{a*}, Viktor M. Horbach^b, Valentin I. Kasilov^a, Ludmila N. Kolpakova^b,
Olena A. Lyukhtan^b, Evgen V. Tsiats'ko^a

^a NSC "Kharkiv Institute of Physics and Technology", Kharkiv, Ukraine

^b V.N. Karazin Kharkiv National University, Kharkiv, Ukraine

*Corresponding author e-mail: gokovsp@kipt.kharkov.ua

Received October 5, 2023; revised November 2, 2023; accepted November 15, 2023

In the work the computer model of a cell of a system for generating fluxes of therapeutic beams of delayed neutrons, based on the use of delayed fission neutrons, was developed in the Geant 4 environment. The principle of such a neutron source is that when a powerful electron beam interacts with a combined tungsten target and a target containing fissile material, a fission reaction occurs; as a result of which neutrons are emitted. If we move a target activated in this way several tens of meters into a neutron flux generation system consisting of a heater, protection, collimator and reflector, we will obtain a compact neutron source for nuclear medicine. A significant advantage of such a neutron source is the absence of gamma background from the electron accelerator and the combined target, and a bulky protection system is not required. In the Geant 4 environment, the geometry of this cell was developed and a series of experiments were carried out with 10^7 neutrons. The QGSP BIC HP physical sheet was used. A study of neutron energy spectra showed that more than half of the neutrons whose fluxes are formed using such a cell of the formation system have an energy <100 keV, which is suitable for use for therapeutic purposes. Analysis of the data obtained in a computer experiment made it possible to develop a modified cell of the system for generating streams of therapeutic beams of delayed neutrons, which differs from the basic one by the presence of a solid polyethylene moderator with holes for activated targets and a graphite reflector. Analysis of the data obtained showed that in this case the number of thermal neutrons hitting the detector increases 10 times compared to the base cell, and the energy of 80% of the particles does not exceed 5 keV, which is much better suited for therapeutic purposes.

Keywords: *Therapeutic beams; Delayed neutrons; Electron accelerator; Computer model; Neutron capture therapy*

PACS: 29.20.-c; 28.90.+

INTRODUCTION

As you know, cancer is one of the most common diseases in the world. According to the American Cancer Society, more than 10,000,000 people have been diagnosed with cancer worldwide in 2022, only there were approximately 1.9 million new cancer cases in the United States, including 609,360 deaths. Despite the fact that great progress has been made in medicine, humanity still needs to invent improved cancer therapy. One of the key challenges is the use of nuclear medicine.

In nuclear medicine, high-energy electrons from electron accelerators are traditionally used to treat superficial tumors. X-ray radiation and gamma therapy are used for deep-lying affected tissue areas. Other particles - protons, alpha particles, neutrons - are used much less frequently in accordance with the characteristics and nature of the disease. The main disadvantage of existing methods used in radiation therapy is the lack of sufficient selectivity of the effect of radiation on malignant tumors. When exposed to ionizing radiation, both healthy and damaged tissues are affected, especially in cases where the tumor has a complex shape or is located in several places. An alternative for the treatment of such diseases may be neutron therapy, in particular neutron capture therapy.

In 1936, Gordon Locher has proposed the concept of neutron capture therapy (NCT) [1]. It was proposed to inject boron, lithium, or gadolinium compounds into the cancerous tumor, followed by irradiation with slow neutrons. NCT was originally intended to be used to treat brain tumors. However, the results obtained over the past 10-15 years have shown new opportunities for the use of neutron capture therapy, in particular for the treatment of melanoma. Clinical studies have shown [2-4] that NCT may be an effective treatment for many other diseases, such as cancer of the colon and rectum, prostate, breast, lung, oral cavity, thyroid gland and other. Thus, modern technologies using neutrons are one of the most effective methods of treatment malignant tumors, therefore the need for sources of thermal neutrons with energy $E < 0.5$ eV, epithermal in the energy range $0.5 \text{ eV} < E < 10 \text{ keV}$ and fast neutrons $E > 10 \text{ keV}$ in the world are continuously growing.

For many years, traditional neutron sources based on nuclear reactors [2-5] and charged particle accelerators, including neutron sources with a subcritical assembly controlled by a pulsed electron accelerator beam, have been and are still being used for neutron and neutron capture therapy [6,7]. The removal of neutrons from the core of such sources is usually carried out using a neutron channel on which a slow-neutron beam former was installed.

To generate therapeutic neutrons for neutron capture therapy application, we have developed concept proposes to use delayed fission neutrons [8,9]. They can be formed under high-power electron beam interaction with a combined target from a tungsten and uranium dioxide. Under the photo- neutron interaction with uranium dioxide, a fission

reaction is taken place, as a result, both prompt and delayed fission neutrons are emitted. The number of delayed neutrons is about 1% of the total number of produced ones. If we move a target activated in this way several tens of meters into a neutron flux generation system consisting of a heater, protection, collimator and reflector, we will obtain a compact neutron source for nuclear medicine. A significant advantage of such a neutron source is the absence of gamma background from the electron accelerator and the combined target, and a bulky protection system is not required.

The scheme of activated target transportation is shown in Figure 1. Activated targets are delivered to the shaper using a conveyor. As a result, concentrated flux of therapeutic neutrons is formed on the irradiated object. After the emission of delayed neutrons in the shaper, the uranium dioxide targets are returned to the core of the electron accelerator for reactivation. Thus, targets are transported cyclically as many times as necessary to reach a therapeutic dose when the object is irradiated. Proposed construction of the shaper is presented in Figure 2 in detail.

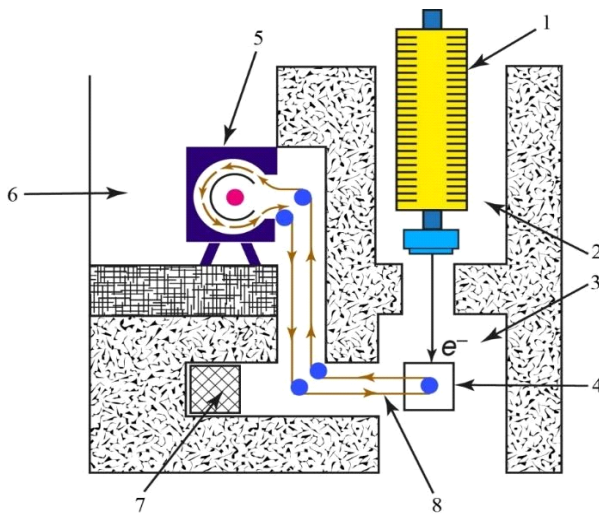


Figure 1. View of system for transporting activated targets: 1 - Electron accelerator; 2, 3 - Accelerator bunker; 4 - Active zone; 5 - Shaper; 6 - Radiation therapy room; 7 - Radioactive waste repository; 8 - Conveyor

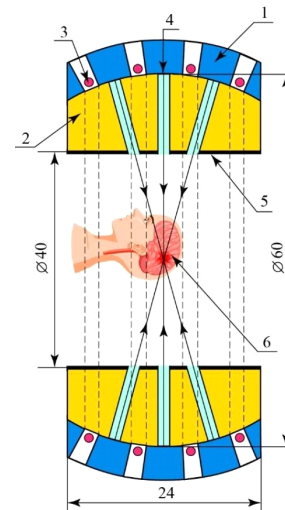


Figure 2. The design of the shaper of the concentrated therapeutic neutron flux (without a graphite reflector): 1 - Moderator; 2 - Radiation protection; 3 - Activated target; 4 - Channel of collimator; 5 - Cadmium layer; 6 - Irradiated object. All dimensions are in cm

After activation is completed, the target delivered to the shaper emits delayed fission neutrons with an average energy of 0.5 MeV, as well as gamma rays caused by induced radioactivity in the target. The radiation is isotropically distributed in all directions, including the direction of the irradiated object. Delayed neutrons passing through the moderator (1) change their energy close to epithermal range value (from 0.5 eV to 10 keV). They are directed to a therapeutic beam formed and focused by multi collimator system to the irradiated object located in the center of the shaper. To suppress induced gamma radiation and fast neutrons from the source in the direction of the irradiated object, combined blocking protection is provided.

DESCRIPTION OF THE COMPUTER MODEL OF THE CELL OF THE SYSTEM FOR FORMING CONCENTRATED SLOW NEUTRON FLUXES

In the work, a computer model of the cell of the system for generating concentrated slow neutron fluxes on delayed fission neutrons for nuclear medicine was developed in the Geant4 and PhysList QGSP BERT HP [10]. The hadronic part of this physics list consists of elastic, inelastic, capture and fission processes. Each process is built from a set of cross section sets and interaction models which provide the detailed physics implementation. The scheme of model the basic cell of the system for generating concentrated slow neutron fluxes is shown in Figure 3.

The basic cell, presented in Figure 3 comprises the two-point isotropic neutron sources (activated samples with uranium) with an energy of 0.5 MeV (1), a polyethylene neutron moderator (2), a protective layer of borated polyethylene 10 cm thick to reduce the flux of fast neutrons (3), a neutron detector with an area of 1 cm² (4).

The computer model of basic cell of the neutron source is presented in Figure 4. Using a computer model, a series of experiments was carried out with 10⁷ neutrons per source. In the work we investigated the change in the number of neutrons hitting on the detector when the size of the moderator is changed. This dependence is presented in Figure 5. As can be seen from the Figure5, the optimal size of a cubic moderator from the point of view of the formation of therapeutic neutron fluxes is 3-4 cm.

In the work also we also determine the dependence of the number of neutrons that enter the detector on the position of the sources relative to the moderator and protection made of borated polyethylene. It is presented in Figure 6. From Figure 6 it can be seen that the optimal location of neutron sources is the angle formed by the edge of the moderator and the plane of protection made of borated polyethylene. That is, close to the moderator and protection made of borated polyethylene.

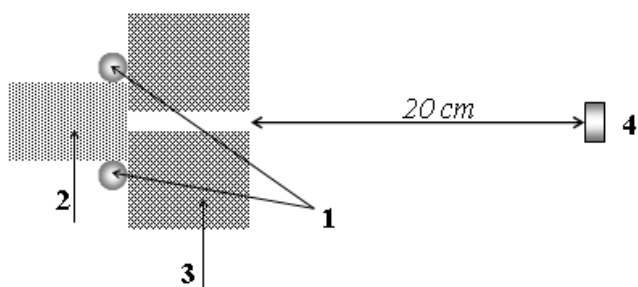


Figure 3. The basic cell of the neutron source

1-The two-point isotropic neutron sources (activated samples with uranium) with an energy of 0.5 MeV, 2- Polyethylene neutron moderator, 3- The protective layer of borated polyethylene 10 cm, 4- Thea neutron detector with an area of 1 cm²

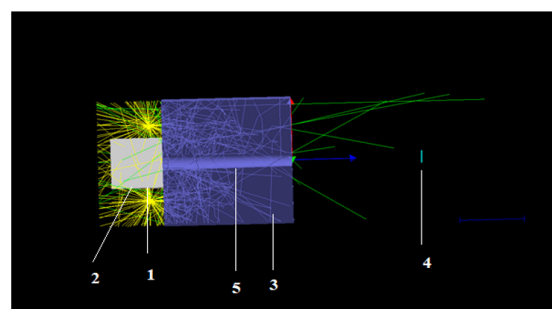


Figure 4. The computer model of basic cell of the neutron source

1-The two-point isotropic neutron sources (activated samples with uranium) with an energy of 0.5 MeV, 2- Polyethylene neutron moderator, 3- The protective layer of borated polyethylene 10 cm, 4- The neutron detector with an area of 1 cm², 5 - Collimator

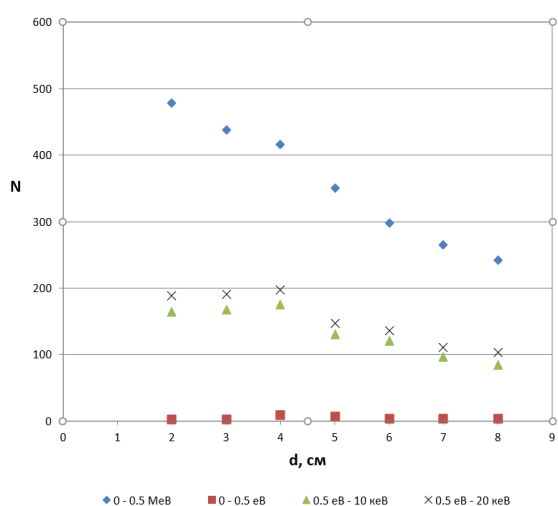


Figure 5. Dependence of the number of neutrons on the size of the moderator

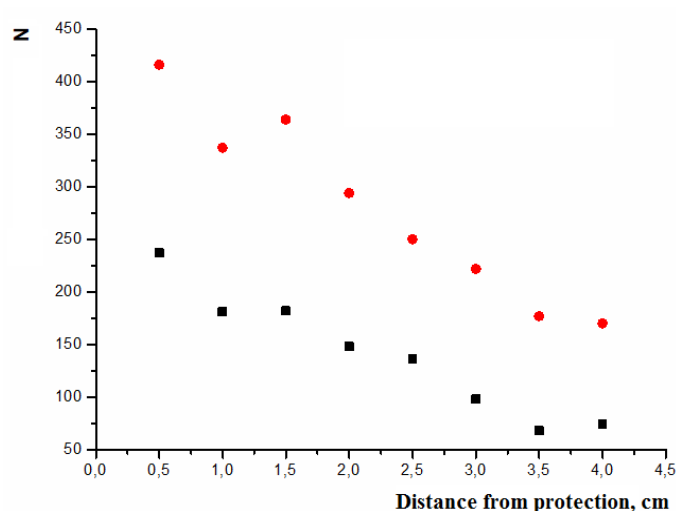


Figure 6. Dependence of the number of neutrons on the distance from protection

In the work we involved calculating the energy distribution of neutrons that enter the detector from the base cell of the shaper. The resulting spectrum is shown in Figure 7. The average statistical error was determined as the square root of the number of registered events. A study of neutron energy spectra showed that more than half of the neutrons whose fluxes are formed using such a cell of the formation system have an energy <100 keV, which is suitable for use for therapeutic purposes.

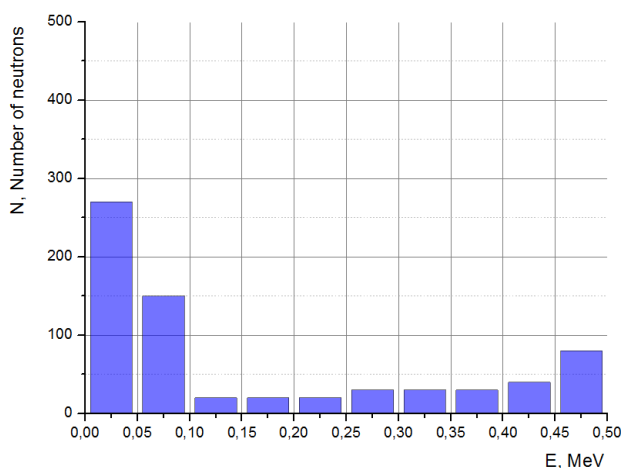


Figure 7. Neutron spectra from basic cell

In the process of working with a computer model based on the basic cell of the neutron flux generation system, a modernized cell was developed in order to increase the number of thermal neutrons that reach the detector. It differs from the basic cell in the reduced thickness of the polyethylene protection in front of the boron-free detector, the presence of a solid polyethylene moderator with holes for activated targets, as well as a 10 cm thick graphite reflector.

The modernized cell, presented in Figure 8 comprises the two-point isotropic neutron sources (activated samples with uranium) with an energy of 0.5 MeV (1), a polyethylene neutron moderator (2), a protective layer of polyethylene without boron 5 cm thick (3), a neutron detector with an area of 1 cm² (4), graphite reflector (5).

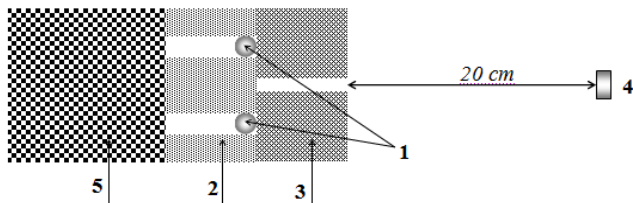


Figure 8. The modernized cell of the neutron source
 1-The two-point isotropic neutron sources (activated samples with uranium) with an energy of 0.5 MeV, 2- Polyethylene neutron moderator, 3- The protective layer of polyethylene 5 cm, 4- neutron detector with an area of 1 cm², graphite reflector

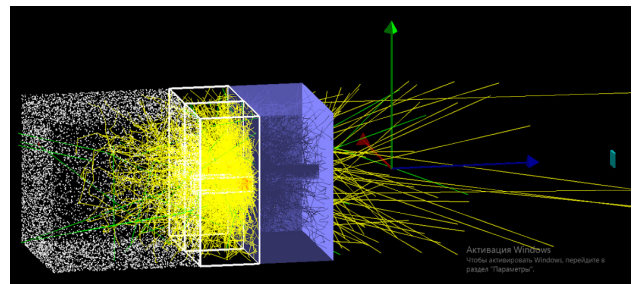


Figure 9. The computer model of modernized cell of the neutron source

In the work computer experiments using a model for a modified cell with 10⁷ neutrons per neutron source were also carried out. Analysis of the data obtained showed that in this case the number of thermal neutrons hitting the detector increases 10 times compared to the base cell, and the energy of 80% of the particles does not exceed 5 keV, which is much better suited for therapeutic purposes. Neutron spectra are presented in Figure 10 and 11.

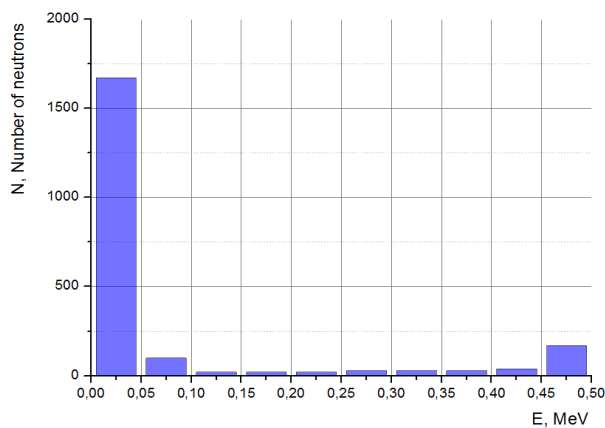


Figure 10. Neutron spectra from modernized cell

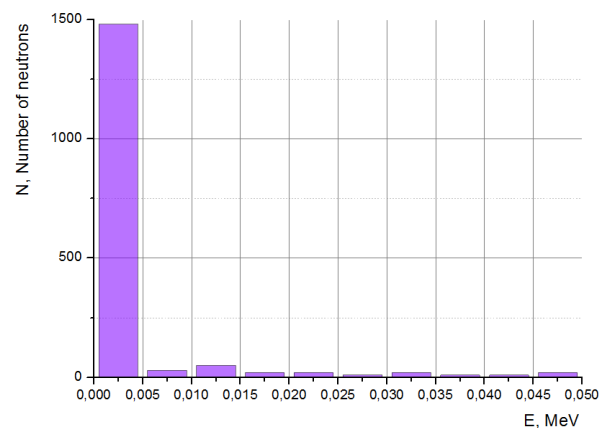


Figure 11. Neutron spectra from modernized cell, E < 5 keV

CONCLUSIONS

In the work the computer model of a cell of a system for generating fluxes of therapeutic beams of delayed neutrons, based on the use of delayed fission neutrons, was developed in the Geant 4 environment. The basic cell of our neutron source consists of a cubic polyethylene moderator, fast neutron protection made of borated polyethylene with a conical collimator, a detector and two isotropic neutron sources with an energy of 0.5 MeV. A study of the dependence of the number of neutrons hitting the detector on the size of the moderator face showed that the optimal size would be 3-4 cm.

A study of neutron energy spectra showed that more than half of the neutrons whose fluxes are formed using such a cell of the formation system have an energy <100 keV, which is suitable for use for therapeutic purposes.

Analysis of the data obtained in a computer experiment made it possible to develop a modified cell of the system for generating streams of therapeutic beams of delayed neutrons, which differs from the basic one by the presence of a solid polyethylene moderator with holes for activated targets and a graphite reflector. Analysis of the data obtained showed that in this case the number of thermal neutrons hitting the detector increases 10 times compared to the base cell, and the energy of 80% of the particles does not exceed 5 keV, which is much better suited for therapeutic purposes. Thus, the computer model developed in the work of a cell of a system for generating flows of therapeutic slow-neutron beams allows not only to calculate the parameters of neutron flows incident on the detector, but also to improve the design of the device itself to obtain optimal characteristics for medical irradiation.

ORCID

- ©Sergey P. Gokov, <https://orcid.org/0000-0002-3656-3804>; ©Ludmila N. Kolpakova, <https://orcid.org/0009-0004-0704-5954>
 ©Vikor M. Horbach, <https://orcid.org/0000-0002-1889-2903>; ©Olana A. Lyukhtan, <https://orcid.org/0009-0001-4367-7201>
 ©Valentin I. Kasilov, <https://orcid.org/0000-0002-1355-311X>

REFERENCES

- [1] G.L. Locher, Am. J. Roentgenol. Radium. Ther. **36**, 1 (1936). https://ia904501.us.archive.org/30/items/sim_ajr-american-journal-of-roentgenology_1936-07_36_1_0/sim_ajr-american-journal-of-roentgenology_1936-07_36_1_0.pdf

- [2] A.M. Hughes, and N. Hu, *Cancers*, **15**(16), 4091 (2023). <https://doi.org/10.3390/cancers15164091>
- [3] A. Wittig, and W.A.G. Sauerwein, *Cancer Biother. Radiopharm.* **38**(3), 195 (2023). <https://doi.org/10.1089/cbr.2022.0074>
- [4] X. Cheng, F. Li, and L. Liang, *Current Oncology*, **29**(10), 7868 (2022). <https://doi.org/10.3390/curroncol29100622>
- [5] L.-W. Wang, Y.-W.H. Liu, and F.-I. Chou, *Cancer Communications*, **38**, 1 (2018). <https://doi.org/10.1186/s40880-018-0295-y>
- [6] L. Porra, T. Seppälä, L. Wendland, H. Revitzer, H. Joensuu, P. Eide, H. Koivunoro, et al., *Acta Oncologica*, **61**(2), 269 (2021). <https://doi.org/10.1080/0284186X.2021.1979646>
- [7] L. Porra, L. Wendland, T. Seppälä, H. Koivunoro, H. Revitzer, J. Tervonen, L. Kankaanranta, et al., *Cancer Biother. Radiopharm.* **38**(3), 184 (2023). <https://doi.org/10.1089/cbr.2022.0059>
- [8] V. Kasilov, S. Gokov, S. Kalenik, S. Kochetov, L. Saliy, V. Tsyats'ko, E. Tsyats'ko, and O. Shopen, *East European Journal of Physics*, (4), 160-163 (2021). <https://doi.org/10.26565/2312-4334-2021-4-21>
- [9] S.P. Gokov, S.H. Karpus, V.I. Kasilov, G.D. Kovalenko, and S.S. Kochetov, *Problems of Atomic Science and Technology*, **3**(145), 133 (2023). <https://doi.org/10.46813/2023-145-133>
- [10] Geant4 Collaboration, *Physics Reference Manual*, <https://geant4-userdoc.web.cern.ch/UsersGuides/ForApplicationDeveloper/BackupVersions/V10.6c/fo/BookForApplicationDevelopers.pdf>

**КОМП'ЮТЕРНА МОДЕЛЬ СИСТЕМИ ФОРМУВАННЯ ПОТОКІВ ТЕПЛОВИХ
ЗАПІЗНИЛИХ НЕЙТРОНІВ ДЛЯ ЯДЕРНОЇ МЕДИЦИНИ**
**Сергій П. Гоков^a, Віктор М. Горбач^b, Валентин Й. Касілов^a, Людмила М. Колпакова^b,
Олена А. Люхтан^b, Євген В. Цяцько^a**

^a ННЦ "Харківський фізико-технічний інститут", Харків, Україна

^b Харківський національний університет імені В.Н. Каразіна, Харків, Україна

В роботі в середовищі Geant 4 була розроблена комп'ютерна модель осередку системи формування потоків терапевтичних пучків сповільнених нейтронів, яка заснована на використанні запізнених нейтронів поділу. Сутність такого джерела нейтронів полягає в тому, що при взаємодії потужного електронного пучка з комбінованою мішенню з вольфраму та мішенню яка містить подільний матеріал, відбувається реакція поділу; в результаті якої випромінюються нейтрони. Якщо перенести активовану таким чином мішень на декілька десятків метрів в систему формування потоків нейтронів, яка складається з тепловача, захисту, коліматора та відбивача, ми отримаємо компактне джерело нейтронів для ядерної медицини. Вагомою перевагою такого джерела нейтронів є відсутність гама фону від прискорювача електронів та комбінованої мішені, при цьому буде непотрібна громіздка система захисту. В середовищі Geant 4 була розроблена геометрія цього осередку та проведена низка експериментів на 10^7 нейтронів. При цьому використовувався фізичний лист QGSP BIC HP. Дослідження енергетичних спектрів нейтронів довело, що більше половини нейтронів, потоки яких формуються за допомогою такого осередку системи формування мають енергію < 20 кеВ, яка є придатною для використання в терапевтичних цілях. Аналіз отриманих в комп'ютерному експерименті даних дав можливість розробити модифікований осередок системи формування потоків терапевтичних пучків сповільнених нейтронів, який відрізняється від базового, наявністю цільного тепловача з поліетилену з отворами для активованих мішеней, та відбивача з графіту. Аналіз отриманих даних довів, що в цьому разі кількість теплових нейтронів, які потрапляють на детектор зростає у 10 разів в порівнянні з базовим осередком, а енергія 80% частинок не перевищує 5 кеВ, що значно краще підходить для терапевтичних цілей.

Ключові слова: *терапевтичні пучки; запізнелі нейтрони; прискорювач електронів; комп'ютерна модель; нейтрон-захватна терапія*

ENHANCED HEAT TRANSFER ANALYSIS ON MHD HYBRID NANOFLUID FLOW OVER A POROUS STRETCHING SURFACE: AN APPLICATION TO AEROSPACE FEATURES

R. Chandra Sekhar Reddy,  Gunisetty Ramasekhar*

*Department of Mathematics, Rajeev Gandhi Memorial College of Engineering and Technology (Autonomous),
Nandyal 518501, Andhra Pradesh, India*

*Corresponding Author e-mail: gunisettyrama@gmail.com

Received October 1, 2023; revised October 24, 2023; accepted November 6, 2023

The advancement of aircraft technology has presented manufacturers with new criteria and problems for the functioning of their devices. It is essential that, in order to guarantee the secure operation of aerospace machinery, the failure mechanisms be identified, and the operational durability of critical structural components be improved as quickly as possible. New aviation materials have been developed in the modern years. In an aviation engine, engine oil lubricates, cools, washes, maintains against rust, decreases sound, and accelerates. The most important is lubrication. All mechanical components would burn out if not maintained. The aim of this work is to minimize costs by extending the operational life of aircraft components (mechanical and motor parts) and enhancing fuel mileage and flying distance. Based on the importance of the inspiration on magnetohydrodynamic Aluminum Oxide-Cobalt hybrid nanofluid flow over a stretching surface in the existence of a porous medium, thermal radiation is investigated. In this model, we used Engine oil mixed with Aluminum Oxide and Cobalt nanoparticles. By using the suitable self-similarity variables, the PDE is transformed into ODEs. After that, the dimensionless equations are solved by using the Maple built-in BVP Midrich scheme. Graphs and tables explain how the operational factors affect fluid flow efficiency. Compared to nanofluids, hybrid nanofluids have a better heat transfer rate.

Keywords: *BVP Midrich scheme; MHD; Thermal radiation; Porous medium; Hybrid nanofluid*

PACS: 44.05.+e, 44.30.+v, 44.40.+a, 47.10.ad

INTRODUCTION

The movement of heat from one location to another is a critical step in the process of either central heating or central cooling an item. The considerable heat that is generated must be reduced to a reasonable level or dissipated in order for a device or system to function at its highest possible standard. In order to minimize heat on equipment such as processors and in a number of sectors such as automotive and technology, fluid refrigerants have historically been employed [1]. However, traditional liquid refrigerants have a weak heat transfer [2]. Because of this, there is a greater potential for creativity and technological improvement in the field of cooling. The use of nanofluid, which is a fluid that includes nanoparticles, is one of the methods that has been established to improve the efficiency of heat transfer in liquid refrigeration systems [3], [4]. The issue with fluid containing dispersed nano meter particles is coagulation, deposition, and flow line blockage. The aforementioned issues might be partly addressed by employing nanomaterials embedded as micro particles. Nanofluids are extensively employed in semiconductors, automotive, power, and universal healthcare industries, among others, owing to their appealing high - temperature, visual, and electromagnetic characteristics [5]–[7].

An innovative approach of mixing two or three kinds of metallic nanoparticles within the base fluid to boost thermal performance has been developed. Hybrid nanofluid mixes metallic nanoparticles in base fluid. Using hybrid nanofluids to chill or warm machines enhances heat transmission [8], [9]. Many researchers have studied nanoparticle combinations in base fluids to create a refrigerant with superior thermal conductivity. Temperature distribution and heat capacity of hybrid nanofluid are influenced by particle diameter, volume fraction, thermal efficiency, and viscosity [10]. Nanofluid improves material impact energy and is an excellent refrigerant. Among the several metals that are used in the study of nanofluids, Alumina, due to its chemical stability and increased mechanical power, is often employed in the investigation of hybrid nanofluids. Other types of cobalt alloys are put to use in devices like jet turbines, which need high hardness. Electroplating is sometimes performed using cobalt metal because of its excellent standards, high level of hardness, and excellent corrosion resistance.

Magnetohydrodynamics, reduced as (MHD), is the study of fluids that have associated electric currents and are placed in a magnetic field. Magneto-fluid dynamics is the term that describes this process. Examples of magneto-fluids include plasmas, ions, seawater, and liquid crystals. Hannes Alfvén was given the Nobel Prize in Physics that year, which was granted in 1970 for his ground-breaking work in the field of MHD. The magneto-nanofluid combines the characteristics of magnets and liquids into a single substance. The magnetic impacts not only radicalize the particles in the liquid system but also create a modification in heat transfer. Additionally, the magnetic effects cause the absorption to be reconstructed. Because they contain more viscous body cells than non-malignant nanoparticles and because the cells improve blood circulation, magnetic nanoparticles are used in the biomedical industry [11]–[13]. MHD has received a lot of attention in astronomy, healthcare, optical transplants, metal processing, geophysical disciplines, and petrochemical engineering [14].

Engine oil is used in power turbines, motor engines, and machines, including cars. Contact between shifting gears in mechanical systems reduces efficiency by heating dynamic energy. Oil’s primary function is to reduce contact between moving components. The engine oil may cool contacting parts, however. Heat transfer and thickness of engine oil are important for mechanical cooling and lubrication. The viscosity influences pumping force and oil circulation. This study also considers cobalt and aluminium oxide. Cobalt-based fantastic alloys are recycled in jet machines, with military warrior planes, owing to their immovability at high temperatures. Al₂O₃ is a great ceramic oxide by a varied range of uses, with aerospace manufacturing, and additional high-modernization arenas [15], [16].

MOTIVATION OF THE PROPOSED MODEL

According to the current literature, no research has been done to analyse the concept of magnetohydrodynamic (MHD) over a stretching surface with the presence of porous medium and linear thermal radiation. The equations that are created are in the form of PDE. To convert the PDE into ODEs, a self-similarity transformation is used. After applying transformations, for the graphical purpose, we have used the Maple built in BVP Midrich scheme. In this study we employ the Engine oil as a base fluid and Aluminium Oxide - Cobalt are hybrid nanofluids. This model plays an essential role in aerospace machinery, nuclear reactor cooling, and vehicles. In the results and discussion section, graphs for different physical significance are given. As a result, the researchers are confident that the new study is unique, will have a considerable influence in the domains of engineering and mathematics, and has the opportunity to encourage new investigators.

MATHEMATICAL FORMULATION

In addition to a stretched surface, a two-dimensional heat transfer representation is examined in a mixed-heat-dispersal (MHD) aluminium oxide–cobalt hybrid nanofluid. Within the framework of the energy and temperature equation, thermal radiation is taken into account. As can be seen in Table 1, two distinct kinds of nanoparticles, namely Al₂O₃ and cobalt, are suspended in the base fluid engine oil. The velocity components *u* and *v* are measured along the *x*-axis and the *y*-axis, respectively; the velocity is written as *u_w* = *ax*. Furthermore, the temperature of the sheet as well as the temperature of the free stream is represented by the symbols *T_w*, *T_∞*, which is demonstrated in Figure 1, respectively.

Table 1. Thermophysical properties of Engine oil, Al₂O₃-Cobalt hybrid nanofluid [19].

Property	Engine oil	Al ₂ O ₃	Cobalt
Density ρ (kgm^{-3})	863	3970	8900
Specific heat C_p ($Jkg^{-1}K^{-1}$)	2048	765	420
Heat conductivity k_f ($Wm^{-1}K^{-1}$)	0.1404	40	100
Electrical conductivity σ (Ωm) ⁻¹	55×10^{-6}	1×10^{-10}	1.602×10^7
Pr	6450		

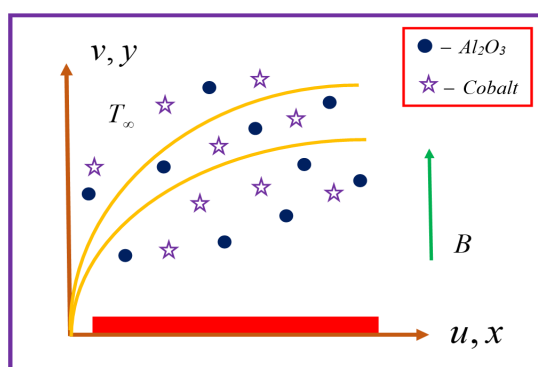


Figure 1. Geometry of the problem.

The governing flow equations are constructed as [17], [18]

$$\frac{\partial u}{\partial x} + \frac{\partial u}{\partial y} = 0, \tag{1}$$

$$u \frac{\partial u}{\partial x} + v \frac{\partial u}{\partial y} = \frac{\mu_{hnf}}{\rho_{hnf}} \left(\frac{\partial^2 u}{\partial y^2} \right) - \frac{\mu_{hnf}}{\rho_{hnf}} \frac{u}{K^*} - \frac{\sigma_{hnf}}{\rho_{hnf}} (B^2 u), \tag{2}$$

$$u \frac{\partial T}{\partial x} + v \frac{\partial T}{\partial y} = \frac{k_{hnf}}{(\rho c_p)_{hnf}} \left(\frac{\partial^2 T}{\partial y^2} \right) - \frac{1}{(\rho c_p)_{hnf}} \left(\frac{\partial q_r}{\partial y} \right) + \frac{\sigma_{hnf} B^2}{(\rho c_p)_{hnf}} u^2. \tag{3}$$

By Rosseland approach, we have

$$q_r = -\frac{4\sigma^*}{3k^*} \frac{\partial T^4}{\partial y}. \tag{4}$$

By applying the Taylor's series expansion of T^4 about T_∞ and neglecting terms having higher order, we obtain

$$T^4 = 4T_\infty^3 T - 3T_\infty^4. \tag{5}$$

Putting Eq. (5) in Eq. (3), we get

$$u \frac{\partial T}{\partial x} + v \frac{\partial T}{\partial y} = \frac{k_{hnf}}{(\rho c_p)_{hnf}} \left(\frac{\partial^2 T}{\partial y^2} \right) - \frac{1}{(\rho c_p)_{hnf}} \frac{16T_\infty^3}{3k^*} \frac{\partial^2 T}{\partial y^2} + \frac{\sigma_{hnf} B^2}{(\rho c_p)_{hnf}} u^2. \tag{6}$$

The corresponding boundary conditions are:

$$\begin{aligned} u = u_w(x) = ax, v = 0, k_{hnf} \frac{\partial T}{\partial y} = h_f (T_f - T), \quad & \text{at } y = 0 \\ u \rightarrow 0, T \rightarrow T_\infty \quad & \text{as } y \rightarrow \infty. \end{aligned} \tag{7}$$

The following suitable self-similarity transformations are defined as:

$$u = axf'(\eta), v = -\sqrt{av_f} f(\eta), \theta(\eta) = \frac{T - T_\infty}{T_f - T_\infty}, \eta = y \sqrt{\frac{a}{v_f}}. \tag{8}$$

Thermophysical properties of hnf are

$$\begin{aligned} K_1 &= \frac{\mu_{hnf}}{\mu_f}, K_2 = \frac{\rho_{hnf}}{\rho_f}, K_3 = \frac{(\rho c_p)_{hnf}}{(\rho c_p)_f}, K_4 = \frac{k_{hnf}}{k_f}, K_5 = \frac{\sigma_{hnf}}{\sigma_f} \\ K_1 &= \frac{1}{(1-\phi_1)^{2.5} (1-\phi_2)^{2.5}}, \\ K_2 &= \left\{ (1-\phi_2) \left[(1-\phi_1) + \phi_1 \left(\frac{\rho_{s_1}}{\rho_f} \right) \right] + \phi_2 \frac{\rho_{s_2}}{\rho_f} \right\}, \\ K_3 &= (1-\phi_2) \left[(1-\phi_1) + \phi_1 \left(\frac{(\rho c_p)_{s_1}}{(\rho c_p)_f} \right) \right] + \phi_2 \frac{(\rho c_p)_{s_2}}{(\rho c_p)_f}, \\ K_4 &= \frac{k_{s_1} + 2k_{bf} - 2\phi_2(k_{bf} - k_{s_2})}{k_{s_2} + 2k_{bf} + \phi_2(k_{bf} - k_{s_2})} \times \frac{k_{s_1} + 2k_f - 2\phi_1(k_f - k_{s_1})}{k_{s_1} + 2k_f + \phi_1(k_f - k_{s_1})}, \\ K_5 &= \frac{\sigma_{s_2} + 2\sigma_{nf} - 2\phi_2(\sigma_{nf} - \sigma_{s_2})}{\sigma_{s_2} + 2\sigma_{nf} + \phi_2(\sigma_{nf} - \sigma_{s_2})} \times \frac{\sigma_{s_1} + 2\sigma_f - 2\phi_1(\sigma_f - \sigma_{s_1})}{\sigma_{s_1} + 2\sigma_f + \phi_1(\sigma_f - \sigma_{s_1})}. \end{aligned} \tag{9}$$

In order to create the following dimensionless ODEs, Eqs. (2) and (6) are transformed using the ideal technique indicated in Eq (8).

$$\frac{K_1}{K_2} f''' + K_2 (ff'' - (f')^2) - \frac{K_1}{K_2} Kf' - \frac{K_5}{K_2} Mf' = 0, \tag{10}$$

$$\theta'' \left(K_4 + \frac{4}{3} Rd \right) + K_3 Prf\theta' + \frac{K_5}{K_3} MEc(f')^2 = 0. \tag{11}$$

The boundaries of the change are described as:

$$\begin{aligned} f(0) = 0, f'(0) = 1, K_4\theta'(0) = -Bi(1 - \theta(0)) \\ f'(\infty) = 0, \theta'(\infty) = 0. \end{aligned} \tag{12}$$

Note that $M = \frac{\sigma_f B^2}{\rho_f a}$ is the magnetic field parameter, $Pr = \frac{\mu_f (c_p)_f}{k_f}$ is the Prandtl number, $Rd = \frac{4\sigma^* T_\infty^3}{k^* k_f}$ is the

Radiation parameter, $Bi = \frac{h_f}{k_f} \sqrt{\frac{v_f}{a}}$ is the Biot number, $Ec = \frac{a^2 x^2}{c_p (T_f - T_\infty)}$ is the Eckert number, and $K = \frac{v_f}{aK^*}$ is the

porosity parameter.

The dimensional form of skin-friction coefficient, and Nusselt numbers are expressed as

$$C_f = \frac{\tau_w}{\rho_f u_w^2} \tag{13}$$

Where shear stress τ_w is $\tau_w = \mu_{hmf} \left. \frac{\partial u}{\partial y} \right|_{y=0}$

$$Nu = \frac{xq_w}{k_f (T_w - T_\infty)} \tag{14}$$

Where heat flux q_w is $q_w = -k_{hmf} \left. \frac{\partial T}{\partial y} \right|_{y=0}$

The Non-dimensional form of Eqs. (13–14) converts are

$$Re_r^{1/2} C_f = Cf = K_1 f''(0), \tag{15}$$

$$Re_r^{-1/2} Nu_r = Nu = -K_4 \theta'(0). \tag{16}$$

Where Re_r is the local Reynolds number.

SOLUTION METHODOLOGY

The nature of the ODE system (10–11) with BCs (12) is extremely nonlinear in its characteristics. For the purpose of dealing with these equations, we adopt a computational approach known as the BVP Midrich method. Using Maple, we are able to solve the control problem. The midway method's standard operating procedure is laid out in detail below. The following is a demonstration of the overall algorithm for the technique of midpoint collocation

$$\bar{Z}'(x) = F(x, \bar{Z}(x)), \quad \bar{Z}(x_0) = \bar{Z}_0, \tag{17}$$

In the explicit midpoint approach, also known as the Modified Euler method, the formula looks like this

$$\bar{Z}_{n+1} = \bar{Z}_n + hF\left(x_n + \frac{h}{2}, \bar{Z}_n + \frac{h}{2}F\left(x_n, \bar{Z}_n\right)\right), \tag{18}$$

The above equation h represents the step size and $x_n = (x_0 + nh)$.

The strategy that takes into account the implicit midpoint may be described as

$$\bar{Z}_{n+1} = \bar{Z}_n + hF\left(x_n + \frac{h}{2}, \bar{Z}_n + \frac{1}{2}\left(\bar{Z}_n, \bar{Z}_{n+1}\right)\right), \quad n = 0, 1, 2, \dots \tag{19}$$

At each step size, the technique for locating the midpoint has a local error of order $O(h^3)$ whereas the global error is of order $O(h^2)$. When dealing with algorithms that are more quantifiable demanding, the algorithm-error decreases at a quicker rate as $h \rightarrow 0$ progresses, and the result gets more dependable.

RESULTS AND DISCUSSION

The non-dimensional controlling flow model (10) – (11), which are subject to the boundary conditions (12), may be solved numerically with the assistance of Maple built in BVP Midrich scheme. We took the values of non-dimensional parameters and evaluated. The precise solutions are obtained from Table 2, which demonstrations the variations in skin friction coefficient. The findings of both investigations were determined to be fairly accurate. Figure 2 shows that the numerical process for BVP Midrich technique.

Table 2. Comparison table for various Prandtl numbers of the current study.

Pr	Ali et al. [17]	Present results
0.7	0.4560	0.45532
2.0	0.9113	0.91032

The effect of M on the velocity sketch is seen in Figure 3. It can be seen that the velocity profile has a decreasing trend for higher M values, which indicates that the value of M is increasing. Physically speaking, an increase in M causes a Lorentz force to be produced, which retards the movement of the liquid. As a consequence of the fact that the Lorentz force is antagonistic to the motion of fluids, the flow velocity decreases as a consequence of the increased resistance, which in turn leads to a drop in the velocity field. When increases the K values improves the velocity outline, which is demonstrated in Figure 4, physically by raising the K values, a porous substance becomes more difficult to flow across, retarding the flow of fluids. As a direct and immediate consequence of this, the dimension of the outermost boundary layer is decreased.

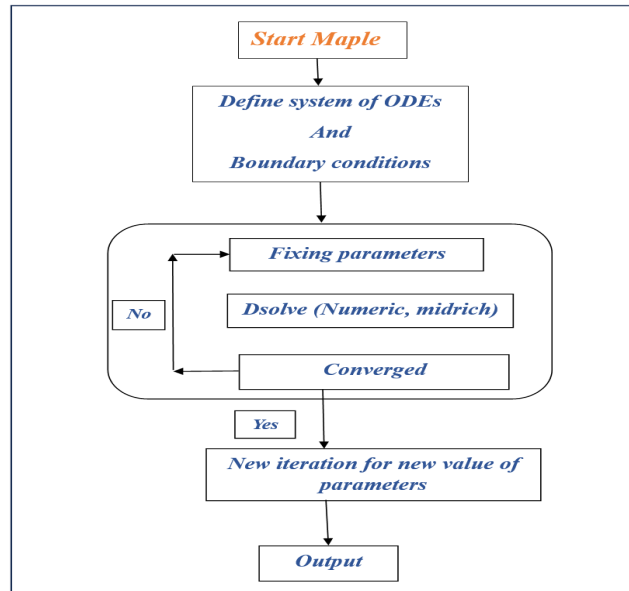


Figure 2. A flow chart pictogram of BVP Midrich technique.

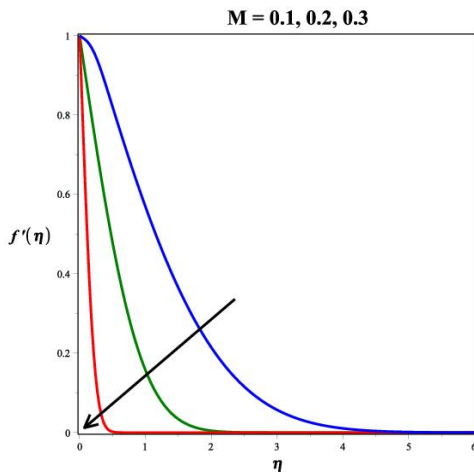


Figure 3. Pictogram of M on $f'(\eta)$.

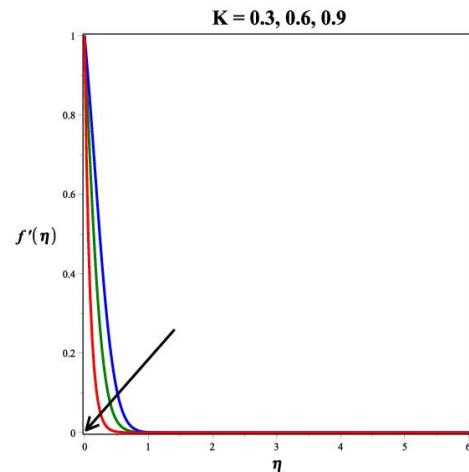


Figure 4. Pictogram of K on $f'(\eta)$.

The influence of magnetic field on temperature profile is seen in Figure 5. It states that growing the M parameter increased the energy outline. This enhancement is due to the fact that the addition of a M into an electrically conducting material produces a resistive Lorentz force. This kind of force has the ability to raise the fluids temperature. So, this reason the temperature profile enhances. Figure 6 shows the radiation parameter temperature profile features. Physically, thermal radiation is the radiant energy released by all generators above zero. Electromagnetic radiation from heated surfaces rotates atoms in matter, generating kinetic energy. The graph demonstrates how increasing radiation enhances heat transmission. When Rd is raised, more heat is transmitted into the liquid, strengthening the thermal barrier. Since the mean absorption coefficient drops as radiation grows, temperature also increases. The effect of Eckert number on energy profile is seen in Figure 7. It states that growing the Ec values are increased the temperature outline. Physically, Ec generates the frictional forces which cause to increase the fluid temperature. The influence of Pr on energy profile is seen in Figure 8. It states that increasing the Pr values are enhanced the temperature outline. The thermal dissipation of the liquid essentially reduces, resulting in a decrease in temperature outline.

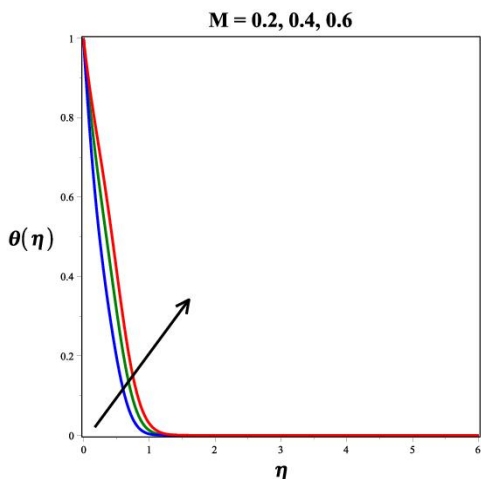


Figure 5. Pictogram of M on $\theta(\eta)$.

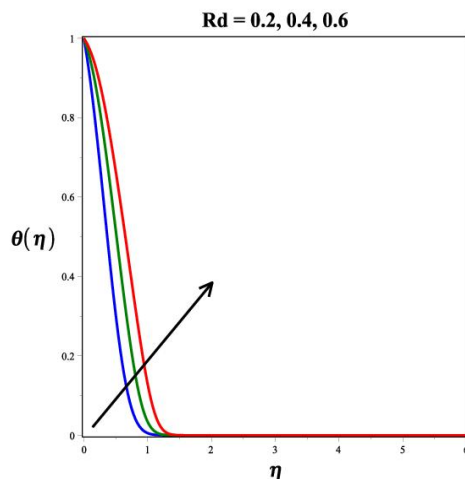


Figure 6. Pictogram of Rd on $\theta(\eta)$.

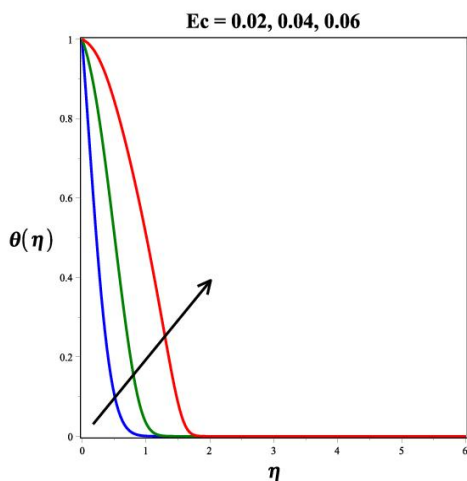


Figure 7. Pictogram of Ec on $\theta(\eta)$.

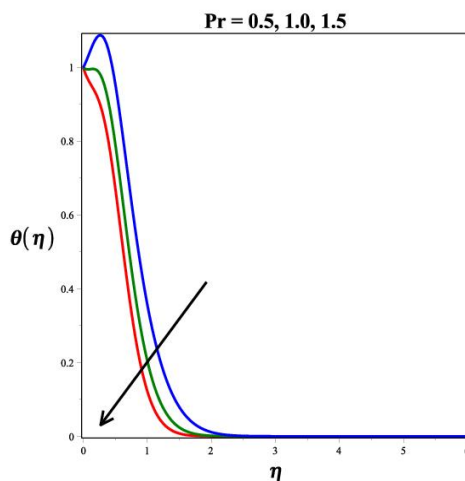


Figure 8. Pictogram of Pr on $\theta(\eta)$.

Figure 9 and 11 displays the influence of the K and M on the Cf . It shows that the skin friction factor is decreasing for the greater values of K and M , while the reverse nature we observed on Figure 11. Figure 10 and 12 demonstrate the inspiration of the Rd and magnetic field on the Nu profile. It shows that the Nu is enhancing in all cases of the greater values of Rd and magnetic field. Figures 13 and 14 exhibit magnetic parameter for various values of $M = 0.5, 1.0$ influences on streamlines plots. Magnetic parameter strength draws electrical conductivity molecules more towards to the main stream.

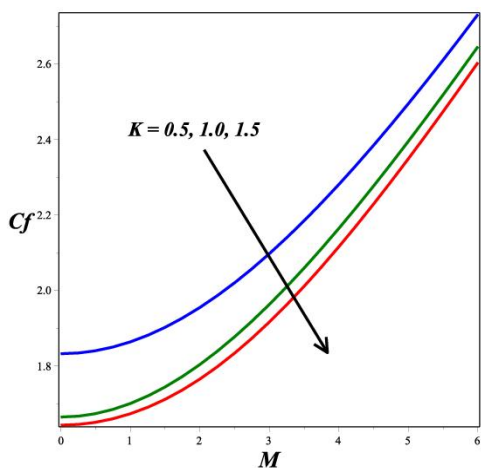


Figure 9. Sway of K and M on Cf .

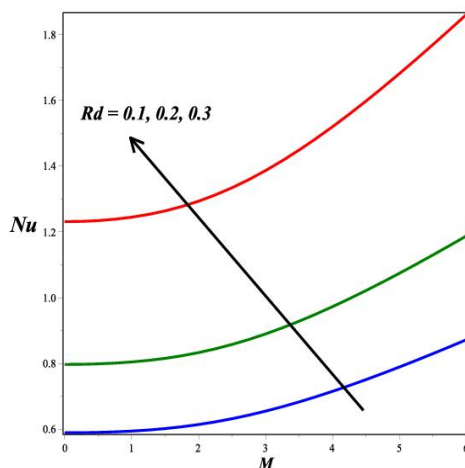


Figure 10. Sway of Rd and M on Nu .

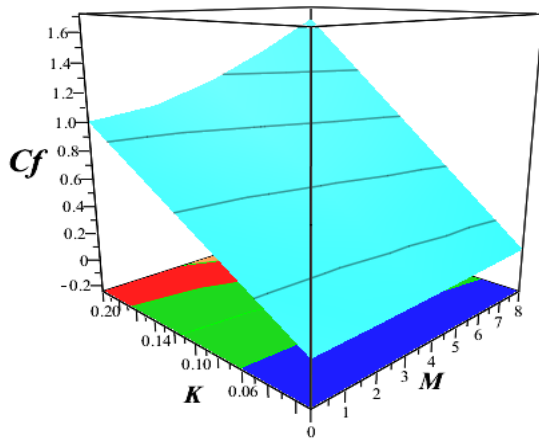


Figure 11. Sway of K and M on C_f .

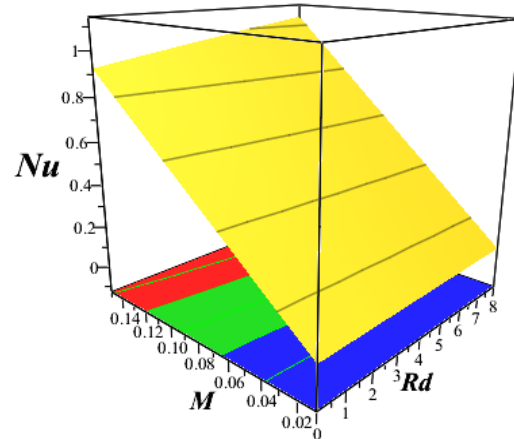


Figure 12. Sway of M and Rd on Nu .

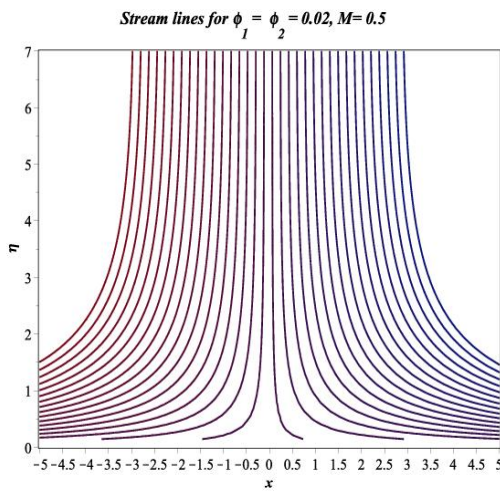


Figure 13. Stream lines for $M = 0.5$.

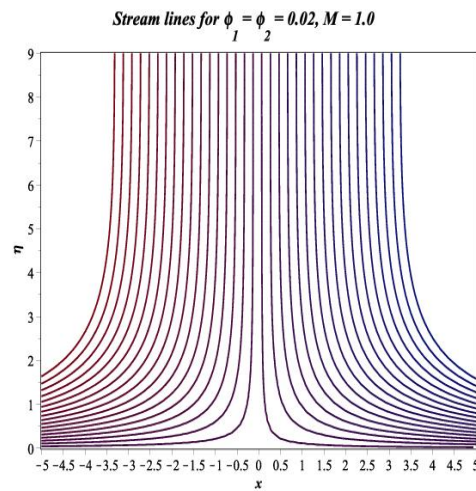


Figure 14. Stream lines for $M = 1.0$.

CONCLUSIONS

The current research study explored the numerical solution for MHD of Al_2O_3 -Cobalt/Engine oil hybrid nanofluid over a Stretching surface. The Numerical method (BVP Midrich scheme) was used to solve the issue of velocity, temperature and the outcome was truly solution to the model. The results are presented in a variety of graphical formats, including a two-dimensional plot, 3D surface plots, and streamlines.

The research produced a number of interesting findings, which are listed below:

- Velocity profile decreases for the increasing values of the magnetic field and porosity parameter values.
- The temperature profile improved with an improvement in the radiation parameter.
- The skin friction factor slowly increased for the larger values of the porous parameter.
- The Nu profile enhanced, for the increasing values of the M and Rd .
- Streamlines have an oscillating character, which is necessary for magnifying the magnetic field parameter.

ORCID

©Gunisetty Ramasekhar, <https://orcid.org/0000-0002-3256-3145>

REFERENCES

- [1] M. Sheikholeslami, *Application of control volume based finite element method (CVFEM) for nanofluid flow and heat transfer*, (Elsevier Science, 2018).
- [2] S. Das, S.U. S. Choi, and H.E. Patel, "Heat transfer in nanofluids - a review," *Heat Transfer Engineering*, **27**(10), 3–19 (2007). <https://doi.org/10.1080/01457630600904593>
- [3] B.A. Bhanvase, D.P. Barai, S.H. Sonawane, N. Kumar, and S.S. Sonawane, "Intensified Heat Transfer Rate With the Use of Nanofluids," in: *Intensified heat transfer rate with the use of nanofluids*, (Elsevier, 2018). pp. 739-750. <https://doi.org/10.1016/B978-0-12-813351-4.00042-0>
- [4] S.R.R. Reddy, P. Bala Anki Reddy, and A.M. Rashad, "Activation Energy Impact on Chemically Reacting Eyring–Powell Nanofluid Flow Over a Stretching Cylinder," *Arab. J. Sci. Eng.* **45**(7), 5227–5242 (2020). <https://doi.org/10.1007/s13369-020-04379-9>

- [5] M. Gupta, V. Singh, R. Kumar, and Z. Said, "A review on thermophysical properties of nanofluids and heat transfer applications," *Renewable and Sustainable Energy Reviews*, **72**, 638-670 (2017). <https://doi.org/10.1016/j.rser.2017.02.073>
- [6] B. Mehta, D. Subhedar, H. Panchal, and Z. Said, "Synthesis, stability, thermophysical properties and heat transfer applications of nanofluid – a review," *J. Mol. Liq.* **364**, 120034 (2022). <https://doi.org/10.1016/J.MOLLIQ.2022.120034>
- [7] S.U.S. Choi, and J.A. Eastman, "Enhancing Thermal Conductivity of Fluid with Nanoparticles," *ASME Fluids Engineering Division, Scientific Research Publishing*, **231**, 99-105 (1995). https://ecotert.com/pdf/196525_From_unt-edu.pdf
- [8] S. Jakeer, and P.B.A. Reddy, "Entropy generation on the variable magnetic field and magnetohydrodynamic stagnation point flow of Eyring – Powell hybrid dusty nanofluid: Solar thermal application," *Proc. Inst. Mech. Eng. Part C J. Mech. Eng. Sci.*, **236**(13), (2022). <https://doi.org/10.1177/09544062211072457>
- [9] N.S.M. Hanafi, W.A.W. Ghopa, R. Zulkifli, S. Abdullah, Z. Harun, and M.R.A. Mansor, "Numerical simulation on the effectiveness of hybrid nanofluid in jet impingement cooling application," *Energy Reports*, **8**, 764–775 (2022). <https://doi.org/10.1016/J.EGYR.2022.07.096>
- [10] Azmi, et al. "A review on thermo-physical properties and heat transfer applications of single and hybrid metal oxide nanofluids," *Journal of Mechanical Engineering and Sciences*, **13**(2), 5182-5211 (2019). <https://doi.org/10.15282/JMES.13.2.2019.28.0425>
- [11] S. Arulmozhi, K. Sukkiramathi, S.S. Santra, R. Edwan, U. Fernandez-Gamiz, and S. Noeiaghdam, "Heat and mass transfer analysis of radiative and chemical reactive effects on MHD nanofluid over an infinite moving vertical plate," *Results Eng.* **14**, 100394 (2022). <https://doi.org/10.1016/J.RINENG.2022.100394>
- [12] S.R.R. Reddy, and P.B. Anki Reddy, "Thermal radiation effect on unsteady three-dimensional MHD flow of micropolar fluid over a horizontal surface of a parabola of revolution," *Propuls. Power Res.* **11**(1), 129–142 (2022). <https://doi.org/10.1016/J.JPPR.2022.01.001>
- [13] S. Jakeer, and B.A.R. Polu, "Homotopy perturbation method solution of magneto-polymer nanofluid containing gyrotactic microorganisms over the permeable sheet with Cattaneo–Christov heat and mass flux model," *Proc. Inst. Mech. Eng. Part E J. Process Mech. Eng.* **236**(2), 525–534 (2022). <https://doi.org/10.1177/09544089211048993>
- [14] S. Jakeer, and P.B.A. Reddy, "Entropy generation on EMHD stagnation point flow of hybrid nanofluid over a stretching sheet: Homotopy perturbation solution," *Phys. Scr.* **95**(12), 125203 (2020). <https://doi.org/10.1088/1402-4896/abc03c>
- [15] X. Zhang, Y. Chen, and J. Hu, "Recent advances in the development of aerospace materials," *Prog. Aerosp. Sci.* **97**, 22–34 (2018). <https://doi.org/10.1016/J.PAEROSCI.2018.01.001>
- [16] H. Xia, P.G. Tucker, and W.N. Dawes, "Level sets for CFD in aerospace engineering," *Prog. Aerosp. Sci.* **46**(7), 274–283 (2010). <https://doi.org/10.1016/J.PAEROSCI.2010.03.001>
- [17] M. Ramzan, F. Ali, N. Akkurt, A. Saeed, P. Kumam, and A. M. Galal, "Computational assesment of Carreau ternary hybrid nanofluid influenced by MHD flow for entropy generation," *J. Magn. Magn. Mater.* **567**, 170353 (2023). <https://doi.org/10.1016/j.jmmm.2023.170353>
- [18] G. Ramasekhar, and P.B.A. Reddy, "Entropy generation on EMHD Darcy-Forchheimer flow of Carreau hybrid nano fluid over a permeable rotating disk with radiation and heat generation : Homotopy perturbation solution," *Proc. Inst. Mech. Eng. Part E: J. Process Mech. Eng.* **237**(4), 1179-1191 (2023). <https://doi.org/10.1177/09544089221116575>
- [19] A. Divya, and P.B.A. Reddy, "Aerospace aspects of electromagnetohydrodynamic dusty fl ow of hybrid nano fl uid with entropy generation over a rotating disk," *Proc. Inst. Mech. Eng. Part E: J. Process Mech. Eng.* **237**(2), 196-206 (2023). <https://doi.org/10.1177/09544089221102417>

РОЗШИРЕНИЙ АНАЛІЗ ТЕПЛОБМІНУ МГД-ГІБРИДНОГО ПОТОКУ НАНОРІДИНИ НАД ПОРИСТОЮ ПОВЕРХНЕЮ, ЩО РОЗТЯГУЄТЬСЯ: ЗАСТОСУВАННЯ ДЛЯ АЕРОКОСМІЧНИХ ХАРАКТЕРИСТИК

Р. Чандра Секар Редді, Гунісетті Рамасекар

*Факультет математики, Меморіальний коледж інженерії та технологій імені Раджива Ганді (автономний),
Nandyal 518501, Андхра-Прадеш, Індія*

Розвиток авіаційної техніки поставив перед виробниками нові критерії та проблеми для функціонування їхніх пристроїв. Важливо, щоб для гарантування безпечної роботи аерокосмічного обладнання було якнайшвидше визначено механізми відмови та покращено експлуатаційну довговічність критичних структурних компонентів. У сучасності були розроблені нові авіаційні матеріали. В авіаційних двигунах моторне масло змащує, охолоджує, промиває, захищає від іржі, знижує шум і прискорює. Метою даної роботи є мінімізація витрат за рахунок продовження терміну експлуатації компонентів літака (механічних і моторних частин) і збільшення запасу палива і дальності польоту. Виходячи з важливості натхнення щодо магнітогідродинамічного потоку гібридної нанофлюїду оксиду алюмінію та кобальту над поверхнею, що розтягується (SS) і існуванні пористого середовища, досліджено теплове випромінювання. У цій моделі ми використовували моторне масло, змішане з оксидом алюмінію та наночастинками кобальту. Використовуючи відповідні змінні самоподібності, PDE перетворюється в ODE. Після цього безрозмірні рівняння розв'язуються за допомогою схеми Maple, вбудованої в схему BVP Midrich. Графіки та таблиці пояснюють, як робочі фактори впливають на ефективність потоку рідини. Порівняно з нанофлюїдами гібридні нанофлюїди мають кращу швидкість теплопередачі.

Ключові слова: *схема BVP Midrich; МГД; теплове випромінювання; пористе середовище; гібридний нанофлюїд*

SURFACE ELECTROMAGNETIC TE-WAVES TOTAL INTERNAL REFLECTION

✉ Viktor Galaydych^a, ✉ Mykola Azarenkov^{a,b}

^a V.N. Karazin Kharkiv National University, 4, Svoboda Sq., Kharkiv, 61022, Ukraine

^b Institute of Solid State Physics, Materials Science and Technologies, National Science Center Kharkiv Institute of Physics and Technology, 1 Akademichna St, Kharkiv, 61108, Kharkiv, Ukraine.

*Corresponding Author e-mail: viktor.galaydych@gmail.com

Received July, 13, 2023; revised September 15, 2023; accepted November 6, 2023

We have considered the refraction of surface electromagnetic waves (SEW) at the heterogeneous metasurface. The considered structure consists of three regions: mu-negative metamaterial, ordinary magnetic, and vacuum. The boundaries between considered media are planar. A phenomenological approach was used; media were assumed to be lossless and isotropic. In this paper, we show the possibility of total internal reflection effect for SEW of TE-polarization that can propagate along such heterogeneous metasurface. The value of the angle of total internal reflection decreases for higher frequency waves from the interval under consideration. The presented result may help design both research and industry complex systems.

Keywords: *mu-negative metamaterial; Metasurface; Electromagnetic surface wave; Total internal reflection*

PACS: 52.35g, 52.50.Dg

1. INTRODUCTION

Artificially created composite materials called metamaterials are intensively researched [1]–[4]. Great interest in metamaterials is caused by the presence of such combinations of the electrodynamic characteristics that are not found in natural materials. The study of surface electromagnetic waves in metamaterials began with work [5]. To date, many articles have been published that studied the properties of surface electromagnetic waves in the structures metamaterials involved [6]–[8]. Most of research deal with a double-negative media, i.e. both dielectric permittivity and magnetic permeability are negative.

But creating a metamaterial that only has a negative magnetic permeability is significantly easier [9]. Recently were published the papers [10]–[12] in which study the surface electromagnetic waves at the interface between mu-negative medium and ordinary mu-positive medium. Aim of present work is to determine how the transition from one interface between such media to another interface formed by a different pair of media will affect the propagation of such surface waves.

2. PROBLEM STATEMENT AND RESULTS

The geometry of the structure to be considered is as follows. The lower half-space ($Z < 0$) filled by the negative permeability medium (mu-negative medium). The upper half-space ($Z > 0$), in its turn, consists of two halves. One half ($Z > 0, X > 0$) is vacuum, another ($Z > 0, X < 0$) is filled with a conventional magnetic material (see Fig. 1). The plane surface electromagnetic waves propagates in the plane ($Z = 0$) along interface between the negative permeability medium and a conventional magnet. Its wave vector k_1 inclines to the normal to the plane ($X = 0$) at an angle θ_i . In addition to the reflection of this wave from the plane $X = 0$ separating the magnetic material from the vacuum, a refracted plane surface wave propagates in the half-space $X > 0$ along the plane interface 'the mu-negative medium/vacuum'. Its wave vector k_2 lies in the plane $X = 0$ and inclines to the normal at an angle θ_r .

Maxwell's equations admit solutions in the form of the surface wave disturbances (1–3) of TE-polarization, e.g. with an electric $\vec{E} = \{0; E_y; 0\}$ and magnetic fields $\vec{H} = \{H_x; 0; H_z\}$ [12]:

$$E_{y1,2} = E_{y01,2} \exp[-\kappa_{1,2}|z| + i(\vec{k}_{1,2}\vec{r} - \omega t)], \quad (1)$$

$$H_{z1,2} = \left(\frac{k_{1,2}}{k\mu_{1,2}}\right) (\exp[-\kappa_{1,2}|z| + i(\vec{k}_{1,2}\vec{r} - \omega t)]), \quad (2)$$

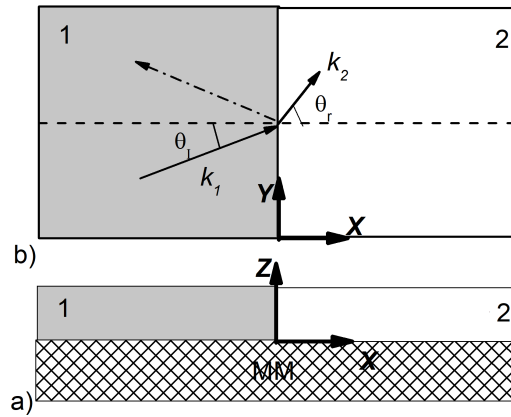


Figure 1. The geometry of structure: shaded – mu-negative metamaterial, grey – magnetic material, white – vacuum; a)-side view, b)-top view

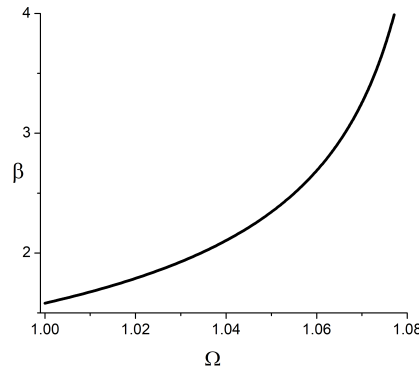


Figure 2. The normalized wavenumber versus the normalized frequency for surface electromagnetic TE-wave

$$H_{x1,2} = \left(-\frac{\kappa_{1,2}}{k\mu_{1,2}}\right)(\exp[-\kappa_{1,2}|z| + i(\vec{k}_{1,2}\vec{r} - \omega t)], \tag{3}$$

where $k = \omega/c$ and κ_1 and κ_2 are the skin depth in ordinary magnet and vacuum

$$\kappa_1 = \sqrt{k_1^2 - \epsilon_1\mu_1k^2}, \kappa_2 = \sqrt{k_2^2 - \epsilon_2\mu_2k^2}, \tag{4}$$

and $k_{1,2}$ are the wavenumbers of TE-modes, directed by the boundaries 'mu-negative/magnet' and 'mu-negative/vacuum', accordingly:

$$k_{1,2} = (\omega/c)\sqrt{\mu(\omega)\mu_{1,2}/(\mu(\omega) + \mu_{1,2})}, \tag{5}$$

here indexes 1,2 refer to the regions including magnet $X < 0$, ($\epsilon_1 = 1, \mu_1 = 2.5$) and vacuum $X > 0$ ($\epsilon_2 = \mu_2 = 1$), accordingly. Vectors \vec{r} lie in a plane $Z = 0$. For mu-negative metamaterial we can assume that its dielectric permittivity equal 1, and negative magnetic permeability has a form [5]:

$$\mu(\omega) = 1 - a\omega^2/(\omega^2 - \omega_0^2), \tag{6}$$

$a = 0.56, \omega_0/2\pi = 4GHz$.

It's easy from the well-known condition of equality of wavevector tangential components:

$$k_1 \sin \theta_i = k_2 \sin \theta_r \tag{7}$$

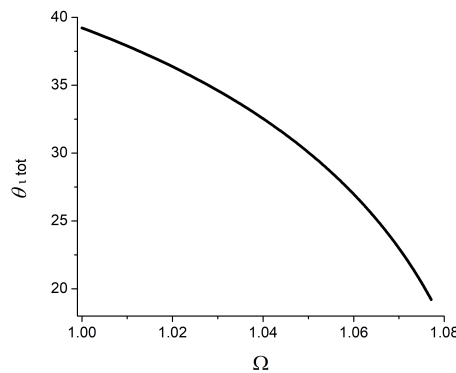


Figure 3. Values of the total internal reflection angle versus the normalized frequency for surface TE-wave

and $\sin\theta_r = 1$ to obtain value for angle of total internal reflection θ_{itot} :

$$\theta_{itot} = \arcsin \sqrt{1 + (\mu_1 - 1)/(1 + \mu(\omega))} / \sqrt{\mu_1} \tag{8}$$

Results of calculation presented the Fig. 2,3 were obtained for normalized wavenumber $\beta = ck_1/\omega_0$ and normalized frequency $\Omega = \omega/\omega_0$. In Fig. 2 it presents the dispersion of surface electromagnetic TE-waves in the quite narrow frequency, in which magnetic permeability of metamaterial is less 0.

$$\frac{\kappa_1}{\mu_1} + \frac{\kappa(\omega)}{\mu(\omega)} = 0, \tag{9}$$

here $\kappa(\omega) = \sqrt{k_1^2 - \mu(\omega)k^2}$ is a penetration depth of electromagnetic surface wave energy into mu-negative metamaterial.

As can see, this wave is slow (its phase velocity is less the speed of light in vacuum) and forward (the directions of phase and group velocities coincide) [11].

In Fig. 3 presents dependence value of critical angle θ_{itot} vs normalized frequency Ω . At higher frequencies to penetrate into the area covered by the vacuum can only waves with wavevector inclined to the normal at the angles of incidence $\theta_i < 20^\circ$.

Certain part of energy of surface electromagnetic waves cannot escape from the mu-negative medium, because the angle of incidence is bigger than the critical angle of total internal reflection. By choosing the ratio of parameters of the mu-negative metamaterial and the magnetic material, it is possible to reduce the critical angle, which will give a higher percentage of total reflection from the vacuum boundary.

This phenomenon can be used both in waveguides and resonators. Very likely to use the effect of frustrated total internal reflection in research and diagnostics. We hope that obtained results will expand the capabilities of the element base of modern devices. The area of possible applications are: transmission and control of signals, charged particles movement control, photovoltaic and much more. More detailed study of this phenomenon will be published in short time.

We would like to acknowledge financial support by the Ministry of Education and Science of Ukraine, under the Project 2-13-21.

ORCID

 Viktor Galaydych, <https://orcid.org/0000-0002-2255-9716>;  Mykola Azarenkov, <https://orcid.org/0000-0002-4019-4933>

REFERENCES

[1] B. Cappello, and L. Matekovits, in: *2020 IEEE International Symposium on Antennas and Propagation and North American Radio Science Meeting*, 2020, pp. 813–814, <https://doi.org/10.1109/IEEECONF35879.2020.9329662>
 [2] I.V. Shadrivov, M. Lapine, and Y.S. Kivshar, editors *Nonlinear, tunable and active metamaterials*, (Springer, 2015). <https://link.springer.com/book/10.1007/978-3-319-08386-5>
 [3] J.A. Girón-Sedas, O.N. Oliveira Jr., and J.R. Mejía-Salazar, *Superlattices and Microstructures*, **117**, 423 (2018). <https://doi.org/10.1016/j.spmi.2018.03.062>

- [4] A.V. Zayats, I.I. Smolyaninov, and A.A. Maradudin, *Physics Reports*. **408**(3), 131 (2005). <https://doi.org/10.1016/j.physrep.2004.11.001>
- [5] R. Ruppin, *Physics Letters A* **277**, 61, (2000). [https://doi.org/10.1016/S0375-9601\(00\)00694-0](https://doi.org/10.1016/S0375-9601(00)00694-0)
- [6] V.K. Galaydych, N.A. Azarenkov, V.P. Olefir, and A.E. Sporov, *Problems of Atomic Science and Technology*, **1**, 96 (2017). https://vant.kipt.kharkov.ua/ARTICLE/VANT_2017_1/article_2017_1_96.pdf
- [7] S. Lee, D.-H. Kim, H. Kim, C. Song, S. Kong, J. Park, et al., *IEEE Transactions on Electromagnetic Compatibility*, **60**, 4 1001 (2018). <https://doi.org/10.1109/TEMC.2017.2751595>
- [8] B.R. Lavoie, P.M. Leung, and B.C. Sanders, *Photonics and Nanostructures: Fundamentals and Applications*, **10**(4), 602–614 (2012). <https://doi.org/10.1016/j.photonics.2012.05.010>
- [9] J.B. Pendry, A.J. Holden, D.J. Robbins, and W.J. Stewart, *IEEE Trans. MTT-47*, **2075**, (1999). <https://doi.org/10.1109/22.798002>
- [10] A.A. Maradudin, and T.A. Leskova, *Physica B: Condensed Matter*, **405**(14), 2972 (2010). <https://doi.org/10.1016/j.physb.2010.01.016>
- [11] V. Galaydych, and M. Azarenkov, *Applied Physics B*, **128**, 132 (2022). <https://doi.org/10.1007/s00340-022-07854-3>
- [12] V. Galaydych, and M. Azarenkov, *Applied Physics A*, **129**, 466 (2023). <https://doi.org/10.1007/s00339-023-06751-6>

ПОВНЕ ВНУТРІШНЄ ВІДБИТТЯ ПОВЕРХНЕВИХ ЕЛЕКТРОМАГНІТНИХ ТЕ-ХВИЛЬ

Віктор Галайдич^a, Микола Азаренков^{a,b}

^a Харківський національний університет ім. В.Н. Каразіна, майдан Свободи, 4, 61022, Харків, Україна

^b Національний науковий центр «Харківський фізико-технічний інститут», 61108, Харків, Україна

Досліджено заломлення поверхневих електромагнітних хвиль (ПЕХ) на неоднорідній метаповерхні. Структура, що розглядається, містить три області: мю-негативного метаматеріалу, звичайного магнетика та вакууму. Межі між середовищами, що розглядаються, є плоскими. Було використано феноменологічний підхід, також вважалось, що всі середовища є ізотропними та в них немає втрат енергії хвиль. У цьому повідомленні показано можливість ефекту повного внутрішнього відбиття для поверхневих електромагнітних хвиль ТЕ-поляризації, що можуть поширюватись вздовж такої неоднорідної метаповерхні. Значення кута повного внутрішнього відбиття зменшується для більш високочастотних хвиль з інтервалу, що розглядається. Представлений результат може допомогти в проектуванні як дослідницьких, так і промислових складних систем.

Ключові слова: мю-негативний метаматеріал; метаповерхня; електромагнітна поверхнева хвиля; повне внутрішнє відбиття

OPTICAL PARAMETERS OF ALUMINUM ALLOY SAMPLES IRRADIATED BY HIGH CURRENT RELATIVISTIC ELECTRON BEAMS

 **Mykola O. Azarenkov**^{a,c},  **Oleksii A. Haluza**^b,  **Alexander V. Gapon**^{c*},  **Volodymyr V. Lytvynenko**^d

^a National Science Center Kharkiv Institute of Physics and Technology, Institute of Solid-State Physics, Materials Science and Technologies, 1, Akademicheskaya St., Kharkiv, 61108, Ukraine

^b National Technical University "Kharkiv Polytechnic Institute", 2 Kyrpychova St., Kharkiv, 61002, Ukraine

^c V.N. Karazin Kharkiv National University, 4, Svobody Sq., Kharkiv, 61020, Ukraine

^d Institute of Electrophysics and Radiation Technologies NAS of Ukraine, Chernyshevsky St., 28, 61002 Kharkiv, Ukraine

*Corresponding author e-mail: gapon@karazin.ua

Received October 1, 2023; revised November 7, 2023; accepted November 17, 2023

The aluminum alloys D16, D16AT are widely used as construction materials in the aircraft industry. Questions connected with the enhancement of the properties of the construction elements made of the alloys through surface modification are of great interest now. The objects of the study in our paper are the samples of the aluminum alloy D16AT subjected to irradiation by high-current relativistic electron beams. Leaving aside the material science aspects, in this work we focused on modeling the optical properties of the samples. The problem is relevant because optical methods for surface analysis have become widespread due to their versatility and efficiency. Through the treatment of the preliminary measured ellipsometry data, we obtain the optical constants of the samples and their dispersion in the visible region of wavelength. The method used consists of an approximation of the reflection coefficient calculated from the ellipsometry data by finding the values of the parameters in the model. The last is performed by the least squares method. The reflection coefficient is assumed to correspond to the semibounded uniaxial medium with the optical axis perpendicular to the interface between the medium and the homogeneous and dielectric ambient medium. The dielectric function of the semibounded medium is approximated by the Drude-Lorentz model. The possibility of birefringence of the samples caused by the irradiation with electron beams is discussed.

Keywords: Electron beam treatment, Aluminum alloy, Optics of metals, Ellipsometry

PACS: 07.60 Fs, 61.80.Fe

INTRODUCTION

The electron beam techniques are interesting for processing and modification of a wide range of materials and possess such useful features as energy effectivity, versatility and short technological process time.

Irradiation by electron beams becomes the widespread and effective technology used for modification of a metal surface. In particular, hardness, wear and chemical resistivity can be improved due to changes followed the electron beam impact, such as refinement of grain structure and solid phase transformation. Investigations in this field are intensively continued. Comprehensive reviews of the studies are [1], [2]. Besides traditional applications for structural materials, it can be pointed out to the studies of electron beams for the treatment of textile materials [3] and food [4]. The paper [5] gives a survey of the applications in the rapidly growing additive manufacturing. The paper [6] reports enhancing a film of organic-inorganic hybrid perovskite by electron beam irradiation to use it in LED applications. In [7] the influence of an electron beam surface treatment on the dislocational substructure of high-entropy alloys was investigated.

In addition, combined technologies acquire widespread use. It is worthwhile to mention sprayed coating and electron beam remelting treatments in the first wall of nuclear fusion devices [8], and a combined treatment of a porosity polyamide coating by the laser and electron beams to make it waterproof [9].

The methods of the analysis and the process control have great importance for the technology. In the framework of the simple model of a semibounded medium, we analyze rotating analyzer ellipsometry (RAE) data [10] to study D16AT alloy samples exposed to high current relativistic electron beams.

THEORETICAL MODEL

We consider a linear absorbing medium characterized by a dielectric function ε . The refraction coefficient is expressed via the dielectric function as follows:

$$n = \nu - i\kappa = \sqrt{\varepsilon}, \quad (1)$$

where ν and κ are the real and imaginary parts of the refraction coefficient. The dielectric function of metals in the visible and infrared wavelength ranges is satisfied well with the Drude-Lorentz model and can be approximated as

$$\varepsilon = 1 - \frac{f_0 \omega_p^2}{\omega(\omega - i\Gamma_0)} - \sum_j \frac{f_j \omega_p^2}{\omega(\omega - i\Gamma_j) - \omega_j^2}. \quad (2)$$

In fact, the medium response is presented here as the sum of the impacts of the non-interacting oscillators, in which ω is the wave frequency; f_0, f_j are the strengths of the oscillators; ω_p is the free electrons plasma frequency; ω_j are the frequencies of the oscillators; and Γ_0, Γ_j are the inverse lifetimes of the oscillators [11]. We assume that the expressions (1) and (2) are also acceptable for the ordinary and extraordinary refraction coefficients n_o and n_e of a birefringent uniaxial medium. This is the case when the principal axes of the permittivity tensor coincide with those of the conductivity tensor of the medium.

The Jones vector determines a fully polarized beam uniquely. It is formed from the complex electric field components parallel (E_p) and perpendicular (E_s) to the incidence plane. In the general case, a reflection of the polarized beam from the surface of the birefringent medium can be described by the reflection coefficients $r_{pp}, r_{ps}, r_{sp}, r_{ss}$, combined in the Jones matrix of the reflected surface:

$$\begin{pmatrix} E_{ip} \\ E_{is} \end{pmatrix} = \begin{pmatrix} r_{pp} & r_{ps} \\ r_{sp} & r_{ss} \end{pmatrix} \begin{pmatrix} E_{rp} \\ E_{rs} \end{pmatrix}. \tag{3}$$

The indexes “i” and “r” mark the incident and reflected waves, correspondingly. In ellipsometry, however, only relative values of the reflection coefficients are considered. Usually, the coefficients are referenced to the coefficient r_{ss} . Denoting these normalized values through $\rho_{pp}, \rho_{ps}, \rho_{sp}$, we can rewrite the expression (3) as:

$$\begin{pmatrix} E_{ip} \\ E_{is} \end{pmatrix} = r_{ss} \begin{pmatrix} \rho_{pp} & \rho_{ps} \\ \rho_{sp} & 1 \end{pmatrix} \begin{pmatrix} E_{rp} \\ E_{rs} \end{pmatrix}, \tag{4}$$

In the study, we assume that the optical axis of the birefringent sample is perpendicular to the surface. Then, the r_{ps} and r_{sp} coefficients drop out, while the diagonal elements are [12]:

$$r_{ss} = \frac{E_{rs}}{E_{is}} = \frac{\cos \varphi - (n_o^2 - \sin^2 \varphi)^{1/2}}{\cos \varphi + (n_o^2 - \sin^2 \varphi)^{1/2}}, \tag{5}$$

$$r_{pp} = \frac{E_{rp}}{E_{ip}} = \frac{n_o n_e \cos \varphi - (n_e^2 - \sin^2 \varphi)^{1/2}}{n_o n_e \cos \varphi + (n_e^2 - \sin^2 \varphi)^{1/2}}, \tag{6}$$

$$\rho_{pp} = r_{pp} / r_{ss}, \tag{7}$$

where φ is the angle of incidence and n_o, n_e are the refraction indexes regarding the ambient medium. Therefore, only one coefficient, ρ_{pp} , encapsulates all the ellipsometry data in this case. When the birefringence of the sample vanishes, the values r_{ss} and r_{pp} tend to the r_s and r_p of the isotropic medium as the refractive indexes n_o, n_e tends to the isotropic refraction index n . Then the coefficient ρ_{pp} reads as follows:

$$\rho_{pp}^0 = \frac{\sin^2 \varphi - \cos \varphi (n^2 - \sin^2 \varphi)^{1/2}}{\sin^2 \varphi + \cos \varphi (n^2 - \sin^2 \varphi)^{1/2}}. \tag{8}$$

ROTATING ANALYZER ELLIPSOMETRY

Let us consider the typical diagram of the RAE instrument shown in Figure 1. The beam emitted by the source passes through the polarizer **P** to obtain linear polarization, reflects from the sample surface, passes the analyzer **A**, and is photometrized. The angle of incidence of the beam φ can vary.

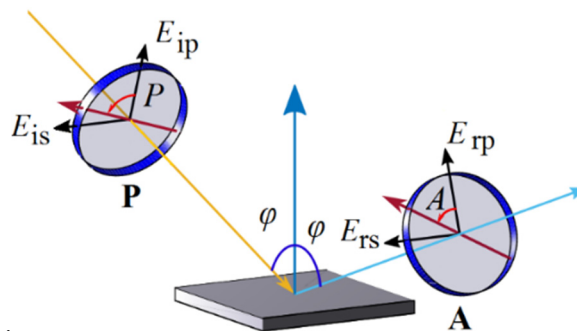


Figure 1. The sketch of the typical rotating analyzer ellipsometry instrument

In addition, the spectral analysis of the beam is performed, which allows to determine the dependence of the ellipsometry parameters on the wavelength. The detector output $I(t)$ varies with the time t as

$$I(t) = I_0(1 + \alpha \cos 2\alpha t + \beta \sin 2\alpha t), \tag{9}$$

where $A=\omega t$ is the rotating analyzer turn angle. The values α and β give the ellipsometry parameters ψ and Δ :

$$\tan \psi = \sqrt{\frac{1+\alpha}{1-\alpha}} |\tan P|, \quad \cos \Delta = \frac{\beta}{\sqrt{1-\alpha^2}}. \quad (10)$$

To extract the reflection coefficient ρ_{pp} only valid in our case, we can set the polarization azimuth P of the polarizer to 45° , so modules of the complex amplitudes E_{ip} and E_{is} of the incident beam become equal. In this condition

$$\tan \psi e^{i\Delta} = \frac{E_{rp}}{E_{rs}} = \frac{E_{rp}/E_{ip}}{E_{rs}/E_{is}} = \frac{r_{pp}}{r_{ss}} = \rho_{pp}. \quad (11)$$

In contrast, for an arbitrary orientation of the optical axis of the sample, when the Jones matrix of the reflected surface is off-diagonal, we should change the azimuth P of the polarizer to obtain at least three pairs of (ψ, Δ) determining the coefficients $\rho_{pp}, \rho_{ps}, \rho_{sp}$.

Expressions (11), (7) and (8) set the interrelation between the measured ellipsometry parameters ψ, Δ and the constants of the optically uniaxial medium n_o, n_e . Obviously, to determine the set of four unknowns, consisting the real and imaginary parts of n_o and n_e , we need at least two different measurements of the set of two ellipsometry parameters (ψ, Δ) . They are made by the incident angle φ changing. As experimental data contain measurement errors, all the points $(\psi, \Delta)_k$ corresponded to the different incident angles φ_k should be considered to extract the values of the refractive coefficients. By the least squares method, we find the values of refractive indexes n_o, n_e , for which the objective function f reaches its minimum:

$$f = \sum_k |\rho_{pp}(\varphi_k) - \tan \psi_k \exp(i\Delta_k)|^2 \rightarrow \min. \quad (12)$$

SAMPLES STUDIED

This work deals with the samples made from the D16AT aluminum alloy obtained during the wide investigations performed to study a modification of the surface of a metal target by the high current pulsed relativistic electron beams.

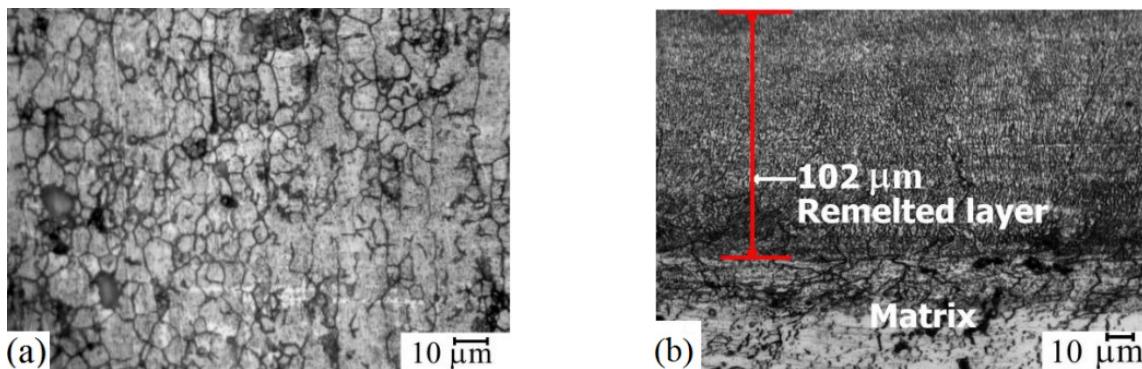


Figure 2. The D16AT aluminum alloy microstructure before (a) and after (b) the irradiation [14].

Details of the preparation, processing, and postprocessing of the samples are presented in the works [13], [14], and [15]. Generally, the interaction of the beams with metal targets represents a rather complex sequence of processes, initiated by radiation and ionization energy losses of particles. This leads to a change in the essential operational properties of the surface layer of irradiated samples, such as plasticity, corrosion and erosion resistance, hardness, etc. Exposure to the electron impact results in the refinement of the grain structure down to nanoscale sizes [14], the redistribution of elements at grain boundaries [15], etc. Figure 2 shows the changes in the surface layer of the D16AT alloy sample due to the electron beam impact. In Figure 2(b), the remelted layer about 100 microns in depth is visible, which is characterized by the modified structure and phase composition. Particularly, the average grain size is reduced from $11 \mu\text{m}$ to $0.8 \mu\text{m}$, concentrations of the alloy dopes rise by 1–3 wt% compared to the matrix values, and the dislocation density becomes eight times greater.

High levels of pressure and temperature gradients during short-term ($\sim 1 \mu\text{s}$) processing suggest that the sample surface layer can obtain properties of an optically uniaxial medium. The model of a semibounded uniaxial medium should be acceptable due to the smallness of the skin depth of metals in the visible region in comparison with the layer depth. Figure 3 shows the angular dependencies of the ellipsometry parameters of three samples denoted as K1, K2 and K3 [10]. Sample K1 was not subjected to any radiation effects; sample K2 was irradiated with the electron beam incident perpendicular to the surface; and sample K3 was irradiated at an angle of 45° to the surface. All the samples were made from the same workpiece and polished in the same way.

We tried both isotropic and uniaxial models to approximate the data. It turns out that the minimum of the objective function (12) achieved in the assumption of $n_o = n_e = n$ can be improved in the framework of the uniaxial model. For

now, we have only the ellipsometry data reconstructed from the experimental graphs, which are out of the instrumental accuracy of $10'$ [10]. It makes the results ambiguous, and then the uniaxiality of the samples remains under question. Figures 3(a), 3(b) show the angular dependencies of the ellipsometry parameters, measured at the wavelength of 633 nm. The curves corresponding to the two models nearly coincide on such large-scale plots, so the curves for the isotropic model are presented. The approximation of the angular dependencies gives the following isotropic refractive index values for samples K1, K2 and K3, respectively: 1.03 - 4.51i, 1.23 - 4.33i, 1.31 - 4.25i. The approximation of the spectral dependencies shown in figures 3(c), 3(d) gives information about the parameters of the Lorentz-Drude model (2), presented in Table 1. The data was measured with the fixed incident angle of 72° .

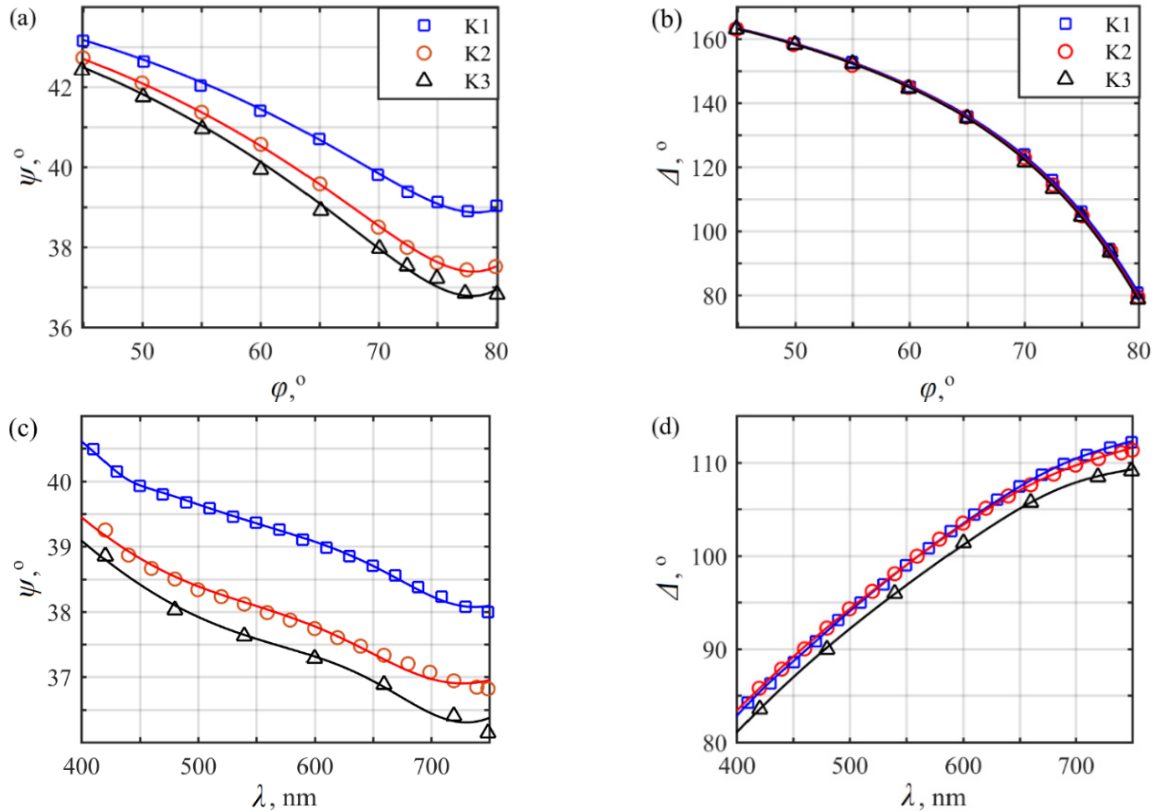


Figure 3. Angular (a), (b), and spectral (c), (d) dependencies of the ellipsometry parameters.

Table 1. Parameters of the Lorentz–Drude model (2) for the different samples. Column *Al* contains parameters for aluminum [12]; columns K1, K2, K3 contain parameters for corresponding samples of D16AT alloy. Calculations were performed in the isotropic approximation. The frequencies ω_p , ω_j and inverse lifetimes Γ_0 , Γ_j are presented in the energetic units.

	<i>Al</i>	K1	K2	K3
$\hbar\omega_p$ (eV)	14.98	9.269	6.215	5.608
f_0	0.523	0.158	0.312	0.915
$\hbar\Gamma_0$ (eV)	0.047	0.093	2.709	0.035
f_1	0.227	0.439	0.134	0.226
$\hbar\Gamma_1$ (eV)	0.333	0.493	1.026	0.568
$\hbar\omega_1$ (eV)	0.162	0.153	1.706	0.185
f_2	0.050	0.149	1.683	1.120
$\hbar\Gamma_2$ (eV)	0.312	2.355	1.283	2.799
$\hbar\omega_2$ (eV)	1.544	2.031	1.684	1.521
f_3	0.166	0.007	1.132	0.001
$\hbar\Gamma_3$ (eV)	1.351	0.860	2.106	0.007
$\hbar\omega_3$ (eV)	1.808	2.885	2.907	2.615
f_4	0.030	0.024	0.172	0.035
$\hbar\Gamma_4$ (eV)	3.382	0.546	4.067	0.468
$\hbar\omega_4$ (eV)	3.473	1.701	0.258	1.723
f_5	0.523	0.158	6.215	5.608
$\hbar\Gamma_5$ (eV)	0.047	0.093	0.312	0.915
$\hbar\omega_5$ (eV)	0.227	9.269	2.709	0.035

CONCLUSION

The semibounded medium model suits pretty well for the RAE data of the samples of D16AT alloy irradiated by high current pulsed relativistic beams. We calculate the optical constants of the samples and obtain parameters for the dispersion Lorentz-Drude model of the samples. The birefringence of samples induced by the irradiation was supposed but not proved due to the insufficient accuracy of the available data.

Acknowledgments

This work was supported by the Simons Foundation Program: Presidential Discretionary-Ukraine Support Grants, Award No 1030287.

ORCID

Mykola O. Azarenkov, <https://orcid.org/0000-0002-4019-4933>; Alexander V. Gapon, <https://orcid.org/0000-0003-4362-8060>
Oleksii A. Haluza, <https://orcid.org/0000-0003-3809-149X>; Volodymyr V. Lytvynenko, <https://orcid.org/0000-0003-4850-2555>

REFERENCES

- [1] S. Valkov, M. Ormanova, and P. Petrov, *Metals*, **10**, 1219 (2020). <https://doi.org/10.3390/met10091219>.
- [2] Y.F. Ivanov, V.E. Gromov, D.V. Zagulyaev, S.V. Konovalov, and Yu.A. Rubannikova, *Steel Transl.* **52**, 71 (2022). <https://doi.org/10.3103/S0967091222010120>.
- [3] T. Abou Elmaaty, S. Okubayashi, H. Elsis, and E. Abouelenin, *J. Polym. Res.* **29**, 117 (2022). <https://doi.org/10.1007/s10965-022-02952-4>.
- [4] G. Wang, D. Wang, and M. Huang, *Food Biophysics* **18**, 470 (2023). <https://doi.org/10.1007/s11483-023-09787-6>.
- [5] V. Sonkamble, and N. Phafat, *Discover Mechanical Engineering* **2**, 1 (2023). <https://doi.org/10.1007/s44245-022-00008-x>.
- [6] B. Jin, D. Zhao, F. Liang, L. Liu, D. Liu, P. Wang, and M. Qiu, *AAAS Research*, Article ID 9797058 (2021). <https://doi.org/10.34133/2021/9797058>.
- [7] K.A. Osintsev, V.E. Gromov, S.V. Vorob'ev, Yu.F. Ivanov, and I.A. Panchenko, *Steel Transl.* **52**, 375 (2022). <https://doi.org/10.3103/S0967091222040106>.
- [8] W.B. Liao, Z.Y. Liu, M.J. He, C. Feng, F. Wang, and J. Huang, *J. Therm. Spray. Tech.* **30**, 2128 (2021). <https://doi.org/10.1007/s11666-021-01281-0>.
- [9] J. Kim, D.M. Chun, H.W. Park, and J. Kim, *Int. J. of Precis. Eng. and Manuf.-Green Tech.* **10**, 71 (2023). <https://doi.org/10.1007/s40684-022-00420-4>.
- [10] A.I. Belyaeva, A.A. Galuza, V.F. Klepikov, V.V. Litvinenko, A.G. Ponomarev, M.A. Sagajdachny, K.A. Slatin, et al., *PAST*, **2**(93), 191 (2009). https://vant.kipt.kharkov.ua/ARTICLE/VANT_2009_2/article_2009_2_191.pdf
- [11] A.D. Rakic, A.B. Djuric, J.M. Elazar, and M.L. Majewski, *Appl. Opt.* **37**(22), 5271-83 (1998). <https://doi.org/10.1364/ao.37.005271>
- [12] H. Fujiwara, *Spectroscopic Ellipsometry: Principles and Applications* (Wiley, 2007), p 369.
- [13] S.E. Donets, V.V. Litvinenko, Yu. B. Poltoratskiy, A.G. Ponomarev, and V.T. Uvarov, *East Eur. J. Ent. Tech.* **4/5**(52), 14 (2011). <https://journals.urau.ua/cejte/article/view/1398/1296>
- [14] V.V. Bryukhovetsky, V.V. Lytvynenko, D.E. Myla, Yu. F. Lonin, A.G. Ponomarev and V.T. Uvarov, *J. Nano. Electr. Phys.* **13**, 06025 (2021). [https://doi.org/10.21272/jnep.13\(6\).06025](https://doi.org/10.21272/jnep.13(6).06025)
- [15] V.V. Arsenyuk, M.I. Bazaleev, S.E. Donets, V.F. Klepikov, V.V. Lytvynenko, Yu.B. Poltoratskiy, A.G. Ponomarev, et al., *PAST*, **6**(91), 124 (2007), https://vant.kipt.kharkov.ua/ARTICLE/VANT_2007_6/article_2007_6_124.pdf

ОПТИЧНІ ПАРАМЕТРИ ЗРАЗКІВ АЛЮМІНІЄВОГО СПЛАВУ, ОПРОМІНЕНИХ СИЛЬНОСТРУМНИМИ РЕЛЯТИВІСТЬСЬКИМИ ЕЛЕКТРОННИМИ ПУЧКАМИ

Микола О. Азаренков^{a,c}, Олексій А. Галуза^b, Олександр В. Гапон^b, Володимир В. Литвиненко^d

^a Національний науковий центр «Харківський фізико-технічний інститут» вул. Академічна, 1, Харків, 61108, Україна

^b Національний технічний університет «Харківський політехнічний інститут», вул. Кирпичова, 2, Харків, 61002, Україна

^c Харківський національний університет імені В.Н. Каразіна, м. Свободи, 4, Харків, 61020, Україна

^d Інститут Електрофізики та Радіаційних технологій НАН України, вул. Чернишевська, 28, 61002, Харків, Україна

Алюмінієві сплави Д16, Д16АТ широко використовуються як конструкційні матеріали в авіабудуванні. Питання, пов'язані з покращенням властивостей елементів конструкцій зі сплавів шляхом модифікації поверхні, зараз викликають великий інтерес. Об'єктами дослідження в нашій роботі є зразки алюмінієвого сплаву Д16АТ, опромінені сильнострумовими релятивістськими електронними пучками. Залишаючи осторонь матеріалознавчі аспекти, у цій роботі ми зосередилися на моделюванні оптичних властивостей зразків. Актуальність проблеми пов'язана з тим, що оптичні методи аналізу поверхні набули широкого поширення завдяки своїй універсальності та ефективності. Завдяки обробці попередньо вимірних даних еліпсометрії ми отримуємо оптичні константи зразків та їх дисперсію у видимій області довжин хвиль. Використаний метод полягає в апроксимації коефіцієнта відбиття, розрахованого з даних еліпсометрії шляхом знаходження значень параметрів у моделі методом найменших квадратів. Вважається, що коефіцієнт відбиття відповідає напівобмеженому однобічному середовищу з оптичною віссю, перпендикулярною межі розділу середовища з однорідним і діелектричним навколишнім середовищем. Діелектрична функція напівобмеженого середовища апроксимується моделлю Друде-Лоренца. Обговорюється можливість подвійного променезаломлення зразків, викликаного опроміненням електронними променями.

Ключові слова: електронно-променева обробка; алюмінієвий сплав; оптика металів; еліпсометрія

CAPACITIVE SPECTROSCOPY OF DEEP LEVELS IN SILICON WITH SAMARIUM IMPURITY

✉ Sharifa B. Utamuradova*, ✉ Khojakbar S. Daliev, ✉ Shakhrukh Kh. Daliev, Uktam K. Erugliev

Institute of Semiconductor Physics and Microelectronics at the National University of Uzbekistan, Tashkent, Uzbekistan

*Corresponding Author e-mail: sh-utamuradova@yandex.ru

Received October 1, 2023; revised October 24, 2023; accepted November 8, 2023

The effect of thermal treatment on the behavior of samarium atoms introduced into silicon during the growth process was studied using the method of transient capacitive deep-level spectroscopy (DLTS). It has been shown that various high-temperature treatments lead to the activation of samarium atoms in the bulk of n-Si and the formation of deep levels. The energy spectrum of deep levels arising during heat treatments has been determined. The dependence of the efficiency of formation of these levels in n-Si<Sm> on the processing temperature has been studied. It was found that the higher the content of samarium atoms in the bulk of silicon at the same high-temperature treatment temperature, the higher the concentration of the deep level $E_C-0.39$ eV. From this we can conclude that the $E_C-0.39$ eV level is associated with the activation of samarium atoms in the n-Si<Sm> volume.

Keywords: *Capacitive spectroscopy; DLTS; Silicon; Doping; Samarium; Heat Treatment; Energy Spectrum; Deep Level; Formation Efficiency*

PACS: 71.20. – b, 71.28. + d

INTRODUCTION

It is known that the atoms of rare-earth elements introduced into the silicon lattice from the melt during growth, possessing high chemical activity and propensity to complexation, are present in silicon in an electrically inactive state [1-6]. The atoms of these rare earth elements in silicon can be activated by various external influences, such as heat treatment or irradiation [7-9].

In connection with the search for semiconductor materials with special properties (increased thermal stability, radiation resistance, etc.), interest in silicon doped with rare-earth elements has recently increased due to their essential role in the formation of silicon properties [10-12]. The world practice shows that during the technological processing of semiconductor wafers in the production of various structures and devices, various interactions of defects with each other occur, which are determined primarily by uncontrolled and specially introduced point defects characterized by maximum mobility in the lattice [13-16]. Therefore, the processes of defect structure formation of the crystal must be related to them.

In this work, the influence of various high-temperature treatments on the properties of silicon doped with samarium atoms during the growth process is investigated.

MATERIALS AND METHODS

Studies of the energy spectrum of deep levels (DL) appearing in samarium-doped silicon after various high-temperature treatments in the temperature range 900-1250 °C were carried out using the DLTS method on Schottky barriers created on the basis of initial and heat-treated samples of silicon with samarium impurity. The methods of measurement and processing of DLTS spectra, as well as the technology of Schottky barriers fabrication are described in [17-18].

The concentration of deep levels in n-Si<Sm> samples and control samples were determined from the maximum of DLTS peaks, as well as using volt-farad characteristics [18-21].

Measurements of DLTS spectra in the original n-Si<Sm> samples, (not subjected to high temperature treatments) showed that no deep levels were observed in appreciable concentration as well as in the original n-Si control samples. At the same time, additional studies by neutron activation analysis indicate the presence of Sm atoms in rather high concentrations (from 10^{15} to 10^{17} cm⁻³) in the n-Si<Sm> volume.

These facts confirm the assumption of the authors [22,23] about electroneutrality of Sm atoms in Si. According to the same authors, the presence of Sm atoms has a noticeable effect on the thermal stability of Si.

In order to study the role of samarium in the processes of thermal defect formation in silicon and possible activation of samarium atoms under thermal effects, we carried out high-temperature treatments in the temperature range 900÷1200°C for 5÷10 h. Under the same conditions ($T = 900\div 1200^\circ\text{C}$, $t = 5\div 10$ h) thermal annealing and control samples of n-Si (without samarium) were carried out in parallel.

RESULTS AND DISCUSSION

Fig. 1 shows DLTS spectra of n-Si<Sm> and n-Si samples heat-treated at 1200°C for 2 h followed by sharp quenching. The spectra were measured in constant voltage mode ($U_{\text{samp.}} = 8$ V) in the temperature range 77-300 K at $t_1 = 10$ ms and $t_2 = 60$ ms.

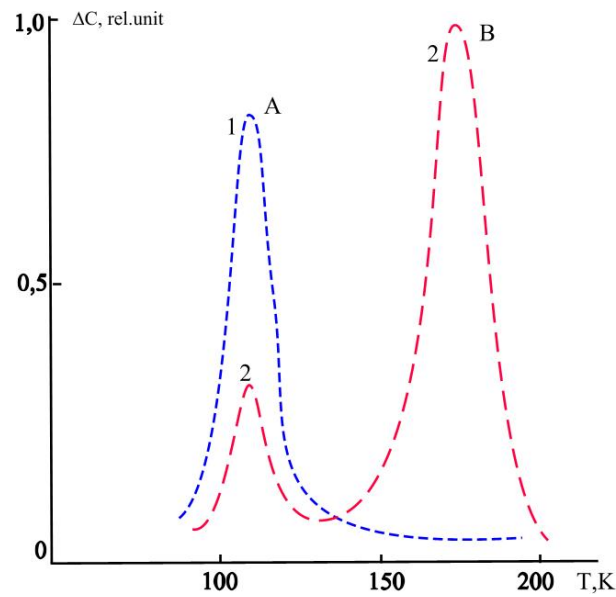


Figure 1. Typical DLTS spectra of n-Si control samples (curve 1) and n-Si<Sm> samples (curve 2) heat-treated at T = 1200°C

The dependences $\lg(\theta) = f(10^3/T)$, the so-called Arrhenius plots [24], obtained from the DLTS spectra by comparing them with the calculated curve $\Delta C/\Delta C_{\max}$ are shown in Fig. 2. These measurements showed that two peaks with maxima at $T_{\max} = 110$ K (peak A) and $T_{\max} = 180$ K (peak B) are observed in the DLTS spectra of silicon samples doped with samarium during growth and subjected to high-temperature treatment.

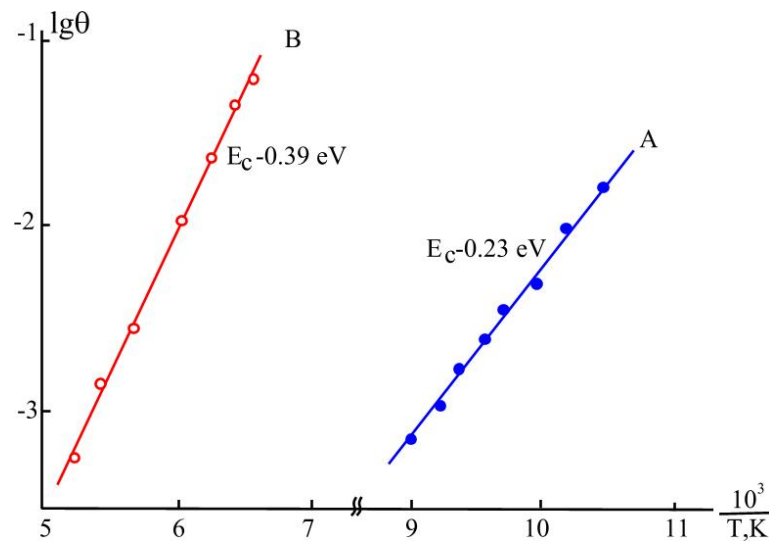


Figure 2. Temperature dependences of the recharge time constant of deep levels in n-Si<Sm> samples subjected to thermal treatment

From the slope of the dependences $\lg(\theta) = f(10^3/T)$ for each of the DLTS peaks, it is obtained that the DLs occurring in the upper half of the forbidden zone of n-Si<Sm> samples (Fig.1, curve 2) as a result of high-temperature treatment have fixed ionization energies $E_C - 0.23$ eV and $E_C - 0.39$ eV and electron capture cross sections equal to $\sigma_n \sim 4 \cdot 10^{-17}$ and $1.2 \cdot 10^{-15}$ cm², and the concentrations of these levels after high-temperature treatment at T= 1200 °C are $3.9 \cdot 10^{13}$ cm⁻³ and $1.2 \cdot 10^{14}$ cm⁻³, respectively.

The DLTS spectra of the heat-treated control samples of n-Si, which underwent the same heat treatment as n-Si<Sm>, show one deep level with ionization energy $E_C - 0.23$ eV, electron capture cross section $\sigma_n \sim 4 \cdot 10^{-17}$ and concentration $1.0 \cdot 10^{14}$ cm⁻³ (Fig.1, curve 1).

Analysis of DLTS spectra shows that the concentrations of the observed levels in n-Si<Sm> samples strongly depend on the treatment temperature: the concentrations of DL $E_C - 0.23$ eV and $E_C - 0.39$ eV after high-temperature treatment at 1100°C (Fig.3, curve 1) have values of $5.7 \cdot 10^{13}$ cm⁻³ and $8.6 \cdot 10^{13}$ cm⁻³, respectively, and after high-temperature treatment at 1200 °C (Fig.3, curve 2) their values are $3.9 \cdot 10^{13}$ cm⁻³ and $1.2 \cdot 10^{14}$ cm⁻³, respectively.

In the heat-treated control n-Si samples, the concentration of $E_C - 0.23$ eV level was $7.9 \cdot 10^{13}$ cm⁻³ (at T= 1100°C, Fig. 3, curve 3) and $1.0 \cdot 10^{14}$ cm⁻³ (at T= 1200 °C, Fig.3, curve 4).

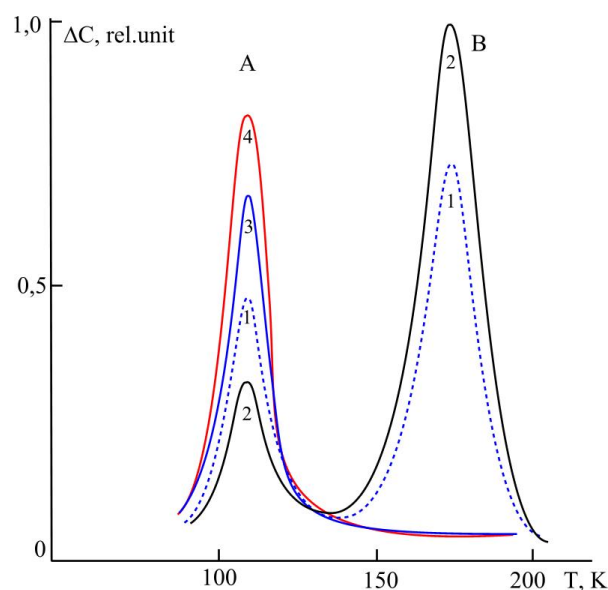


Figure 3. Typical DLTS spectra of heat-treated n-Si<Sm> (curves 1 and 2) and n-Si (curves 3 and 4) samples
T, °C: 1100 - curves 1 and 3, 1200 - curves 2 and 4

Comparison of the obtained results shows that the higher the temperature of high-temperature treatment, the greater the concentration of the deep level $E_C-0.39$ eV. On the contrary, the concentration of the level $E_C-0.23$ eV in n-Si<Sm>, which is also observed in the control samples, decreases markedly with increasing high-temperature treatment temperature. Note that at the same processing temperatures, the concentration of this deep level in the n-Si<Sm> samples, is much smaller than in the control n-Si samples (see Table 1).

In addition, it is found that the higher the content of samarium atoms in the silicon volume at the same temperature of high-temperature processing, the greater the concentration of the deep level $E_C-0.39$ eV. Hence, it can be concluded that the level $E_C-0.39$ eV is associated with the activation of samarium atoms in the n-Si<Sm> volume.

Table 1. Deep level concentrations of samples at different temperatures

Samples	T_{HTT} , °C	DL concentration, cm^{-3}	
		$E_C-0.23$ eV	$E_C-0.39$ eV
n-Si<Sm>	1100	$5.7 \cdot 10^{13}$	$8.6 \cdot 10^{13}$
n-Si<Sm>	1200	$3.9 \cdot 10^{13}$	$1.2 \cdot 10^{14}$
n-Si, control	1100	$7.9 \cdot 10^{13}$	--
n-Si, control	1200	$1.0 \cdot 10^{14}$	--

CONCLUSIONS

Thus, the analysis of the obtained results shows that samarium atoms introduced into the silicon lattice from the melt during the growth process are in the silicon volume in an electrically inactive state. High-temperature treatment in the range $T = 900 \div 1200^\circ C$ during $t = 5 \div 10$ h. leads to the formation of deep levels, probably associated with the activation of samarium atoms. The dependence of the efficiency of formation of deep levels $E_C - 0.39$ eV on the samarium content and processing temperature provides additional evidence that the observed deep levels are due to samarium atoms.

The level $E_C - 0.23$ eV is probably a defect of heat treatment, since it is observed in the control samples (heat treated without samarium).

It should be noted that the fact that the concentration of deep levels $E_s - 0.23$ eV in samples of samarium-doped silicon is smaller than in control samples suggests that samarium atoms reduce the efficiency of formation of thermal defects in silicon.

ORCID

©Sharifa B. Utamuradova, <https://orcid.org/0000-0002-1718-1122>; ©Khojakbar S. Daliev, <https://orcid.org/0000-0002-2164-6797>
©Shakhrukh Kh. Daliev, <https://orcid.org/0000-0001-7853-2777>

REFERENCES

- [1] O.V. Alexandrov, A.O. Zakhar'in, N.A. Sobolev, and Y.A. Nikolaev, Semiconductors, **36**(3), 379 (2002). <https://doi.org/10.1134/1.1461417>
- [2] Kh.S. Daliev, Sh.B. Utamuradova, O.A. Bozorova, and Sh.Kh. Daliev, Applied Solar Energy, **(41)**(1), 80 (2005). <https://www.scopus.com/record/display.uri?eid=2-s2.0-33344466989&origin=resultslist&sort=plf-f>
- [3] X. Chuanyun, J. Blundell, F. Hagelberg, and A. William, International Journal of Quantum Chemistry, **96**(4), 416 (2004). <https://doi.org/10.1002/qua.10735>

- [4] Kh.S. Daliev, Sh.B. Utamuradova, I.K. Khamidzhonov, A.Z. Akbarov, I.K. Mirzairova, and Z. Akimova, *Inorganic Materials*, **37**(5), 436 (2001). <https://doi.org/10.1023/A:1017556212569>
- [5] Sh.B. Utamuradova, Kh.S. Daliev, E.K. Kalandarov, and Sh.Kh. Daliev, *Technical Physics Letters*, **32**(6), 469 (2006). <https://doi.org/10.1134/S1063785006060034>
- [6] S.B. Utamuradova, and D.A. Rakhmanov, *Annals of the University of Craiova, Physics*, **32**, 132 (2022). https://cis01.central.ucv.ro/pauc/vol/2022_32/15_PAUC_2022_132_136.pdf
- [7] S.Z. Zainabidinov, Kh.S. Daliev, K.P. Abdurakhmanov, Sh.B. Utamuradova, I.Kh. Khomidjonov, and I.A. Mirzamurodov, *Modern Physics Letters B*, **11**(20), 909 (1997). <https://doi.org/10.1142/S0217984997001110>
- [8] R.L. Satet, M.J. Hoffmann, and R.M. Cannon, *Materials Science and Engineering: A*, **422**(1-2), 66 (2006). <http://dx.doi.org/10.1016%2Fj.msea.2006.01.015>
- [9] C. Gross, G. Gaetano, T.N. Tucker, and J.A. Baker, *Journal of the Electrochemical Society*, **119**(7), 926 (1972). <https://doi.org/10.1149/1.2404370>
- [10] S.I. Vlasov, D.E. Nazyrov, A.A. Iminov, and S.S. Khudaiberdiev, *Technical Physics Letters*, **26**(4), 328 (2000). <https://doi.org/10.1134/1.1262833>
- [11] Sh.B. Utamuradova, Sh.Kh. Daliev, S.A. Muzafarova, and K.M. Fayzullaev. *East European Journal of Physics*, **3**, 385 (2023). <https://doi.org/10.26565/2312-4334-2023-3-41>
- [12] Sh.B. Utamuradova, Sh.Kh. Daliev, E.M. Naurzalieva, and X.Yu. Utemuratova, *East European Journal of Physics*, **3**, 430 (2023). <https://doi.org/10.26565/2312-4334-2023-3-47>
- [13] N.A. Turgunov, E.Kh. Berkinov, and R.M. Turmanova, *East European Journal of Physics*, **3**, 287 (2023). <https://doi.org/10.26565/2312-4334-2023-3-26>
- [14] G. Gulyamov, S.B. Utamuradova, M.G. Dadamirzaev, N.A. Turgunov, M.K. Uktamova, K.M. Fayzullaev, A.I. Khudayberdiyeva, and A.I. Tursunov, *East European Journal of Physics*, **2**, 221 (2023). <https://doi.org/10.26565/2312-4334-2023-2-24>
- [15] Sh.B. Utamuradova, S.A. Muzafarova, A.M. Abdugafurov, K.M. Fayzullaev, E.M. Naurzalieva, and D.A. Rakhmanov, *Applied Physics*, **4**, 81(2021). <https://doi.org/10.51368/1996-0948-2021-4-81-86>
- [16] X. Lan, J. Gao, K. Xue, H. Xu, and Z. Guo, *Separation and Purification Technology*, **293**, 121121 (2022). <https://doi.org/10.1016/j.seppur.2022.121121>
- [17] K.P. Abdurakhmanov, Sh.B. Utamuradova, Kh.S. Daliev, S.G. Tadjy-Aglaeva, and R.M. Ergashev, *Semiconductors*, **32**(6), 606 (1998). <https://doi.org/10.1134/1.1187448>
- [18] Sh.B. Utamuradova, Kh.I. Kalandarov, and J.J. Khamdamov, *Semiconductor Physics and Microelectronics*, **2**(2), 9 (2020). <https://www.dropbox.com/s/7ykbddvwwiq3q8v/ON%20INTERACTION%20OF%20MANGANESE%20AND%20ZINC%20MPURITIES%20IN%20SILICON.pdf?dl=0> (in Russian)
- [19] Kh.S. Daliev, *Natural and technical sciences, RAS*, **2**(40), 22 (2009). <https://naukarus.com/vliyanie-primesi-gadoliniya-na-harakteristiki-kremnievyh-mdp-struktur> (in Russian)
- [20] L.S. Berman, and A.A. Lebedev, *Capacitance spectroscopy of deep centers in semiconductors*, Science, (Nauka, Leningrad, 1981). (in Russian)
- [21] Kh.T. Igamberdiyev, A.T. Mamadalimov, and P.K. Khabibullaev, *Journal of Engineering Physics*, **57**(4), 1220 (1989). <https://doi.org/10.1007/BF00871143>
- [22] S. Zainabidinov, D.E. Nazyrov, and M.I. Bazarbaev, *Electronic Materials Processing*, **4**, 90 (2006). <https://cyberleninka.ru/article/n/diffuziya-rastvorimost-i-elektricheskie-svoystva-samariya-i-itterbiya-v-kremnii/pdf> (in Russian)
- [23] K.H. Goh, A.S. Haseeb, and Y.H. Wong, *Journal of Alloys and Compounds*, **722**, 729 (2017). <https://doi.org/10.1016/j.jallcom.2017.06.179>
- [24] D.V. Lang, *Journal of Applied Physics*, **45**, 3023 (1974). <http://dx.doi.org/10.1063/1.1663719>

ЄМНІСНА СПЕКТРОСКОПІЯ ГЛИБОКИХ РІВНІВ У КРЕМНІЇ З ДОМІШКОЮ САМАРІЮ †

Шаріфа Б. Утамурадова, Ходжакбар С. Далієв, Шахрух Х. Далієв, Уктам К. Єруглієв

Інститут фізики напівпровідників і мікроелектроніки Національного університету Узбекистану, Ташкент, Узбекистан
Методом перехідної ємнісної глибокорівневої спектроскопії (DLTS) досліджено вплив термічної обробки на поведінку атомів самарію, введених у кремній у процесі росту. Показано, що різні високотемпературні обробки призводять до активації атомів самарію в об'ємі n-Si та утворення глибоких рівнів. Визначено енергетичний спектр глибоких рівнів, що виникають під час термічних обробок. Досліджено залежність ефективності утворення цих рівнів в n-Si<Sm> від температури обробки. Виявлено, що чим вищий вміст атомів самарію в об'ємі кремнію при однаковій температурі високотемпературної обробки, тим вища концентрація глибокого рівня EC-0,39 eV. З цього можна зробити висновок, що рівень EC-0,39 eV пов'язаний з активацією атомів самарію в об'ємі n-Si<Sm>.

Ключові слова: ємнісна спектроскопія; DLTS; кремній; легування; самарій; термообробка; енергетичний спектр; глибокий рівень; ефективність формування

TO THE THEORY OF DIMENSIONAL QUANTIZATION IN NARROW-GAP CRYSTALS

Sharifa B. Utamuradova^a, Rustam Y. Rasulov^b, Voxob R. Rasulov^b,
Kamolakhon K. Urinova^b, Kakhramon M. Fayzullaev^{a*}

^a Institute of Semiconductor Physics and Microelectronics at the National University of Uzbekistan, Tashkent, Uzbekistan

^b Fergana State University, Fergana, Uzbekistan

*Corresponding Author e-mail: qahramonfayzullaev8@gmail.com

Received October 7, 2023; revised November 13, 2023; accepted November 15, 2023

This article discusses studies of size quantization phenomena in zero-, one-, and two-dimensional semiconductor structures. The main attention is paid to the mechanisms of photon-kinetic effects in these structures. Despite many studies of the physical properties of low-dimensional systems of current carriers, the size quantization of energy spectra in narrow-gap semiconductors and the associated photonic-kinetic effects are still insufficiently studied. Therefore, this study focuses on the quantum mechanical study of size quantization in certain cases using Kane's multiband model. The insolvability of the 8×8 matrix Schrödinger equation in the Kane model for a potential well of arbitrary shape is analyzed. The dependence of the energy spectrum on the two-dimensional wave vector is studied for various cases. In particular, the energy spectra for InSb and GaAs semiconductors are considered, depending on the band parameters and the size of the potential well. Conclusions are presented on the analysis of various cases of size quantization in narrow-gap crystals with cubic or tetrahedral symmetry in the three-band approximation. It is shown that the energy spectrum corresponds to a set of size-quantized levels that depend on the Rabi parameter, band gap, and well size. The size-quantized energy spectra of electrons and holes in InSb and GaAs semiconductors are analyzed in a multiband model.

Keywords: Dimensional Quantization; Narrow-Gap; Crystal; Kane model; Schrödinger equation; Electron; Subband; Nanoelectronics; Heterostructure; Energy spectrum

PACS: 71.20. – b, 71.28. + d

INTRODUCTION

Modern achievements in the field of nanoelectronics and nanotechnology have made it possible to observe and study new unique phenomena occurring in zero-, one-, and two-dimensional semiconductor structures [1-5]. The creation of such structures contributes to the study of the mechanisms of photon-kinetic effects occurring in them [6-9].

Although many works [10-14] are devoted to the study of physical properties of low-dimensional systems of current carriers, but dimensional quantization of energy spectra in narrow-gap semiconductors and related photon-kinetic effects are rather poorly investigated. Therefore, this paper quantum-mechanically investigates dimensional quantization in specific cases. The calculations are carried out in the multizone Kane model [3, 15, 16].

THE SCHRÖDINGER EQUATION AND ANALYSIS OF ITS SOLUTIONS FOR VARIOUS CASES

In the first part of this paper, it is shown that in the approximation of the multizone Kane model the matrix Schrödinger equation is analytically unsolvable for a potential well of arbitrary shape. Therefore, it investigates the dependence of the energy spectrum of the two-dimensional wave vector perpendicular to the direction of dimensional quantization (on the Oz axis) for various cases differing in the region of current carrier energy values. As in the first part, for simplification of calculations we will restrict ourselves to linear in terms of the summands in the Kane Hamiltonian, \vec{k} – the wave vector of current carriers. Then the Schrödinger equation in the Kane model can be represented as:

$$\frac{\partial^2 \varphi_{1,2}}{\partial z^2} - \kappa_1^2 \varphi_{1,2} = 0, \quad (1)$$

whose solution is found in the form

$$\varphi_{1,2}(z) = c_1 e^{i\kappa_1 z} + c_2 e^{-i\kappa_1 z} \text{ or } \varphi_{1,2}(z) = d_1 \cos(\kappa_1 z) + d_2 \sin(\kappa_1 z), \quad (2)$$

where c_1, c_2 - integration constants

$$\kappa_1^2 = -\frac{\Lambda_0}{\Lambda_2} = \frac{\frac{3}{P^2} \varepsilon_V \varepsilon_{gv}^2 + \left(2\varepsilon_{gV} + \frac{\varepsilon_{gV}^2}{\varepsilon_{g\Delta V}}\right) \cdot k_1^2}{\left(2\varepsilon_{gV} + \frac{\varepsilon_{gV}^2}{\varepsilon_{g\Delta V}}\right) + \left(2 + \frac{\varepsilon_{gV}^2}{\varepsilon_{g\Delta V}}\right) V_0} \quad (3)$$

and at $U_0 = 0$

$$\kappa_1^2 = \frac{3}{P^2} \frac{E(E+E_g)^2}{\left(2(E+E_g) + \frac{(E+E_g)^2}{E+E_g+\Delta}\right)} - k_{\perp}^2. \tag{4}$$

If in expression (2) we take into account the condition of continuity of wave functions at the interface of the heterostructure: $\varphi_{1,2}(z = 0) = \varphi_{1,2}(z = a) = 0$, then the size quantization of the energy spectrum of current carriers can be analyzed for the following cases:

1-case. When a particle moves in the field of a potential well ($U_0 = 0$), then the dependence of the energy spectrum on the two-dimensional wave vector is determined by the relation:

$$k_{\perp, n_1}^2(E) = \frac{3}{P^2} \frac{E(E+E_g)^2}{\left(2(E+E_g) + \frac{(E+E_g)^2}{E+E_g+\Delta}\right)} - \left(\frac{\pi n_1}{a}\right)^2, \tag{5}$$

Figures 1 and 2 show the energy spectra for *InSb* and *GaAs*, calculated according to (5) for three size-quantized subbands. In the calculations, the following values were chosen: for the *InSb* crystal $m_{el} = 0.0143m_0$ - effective mass of electrons, $a = 50 \cdot 10^{-10}m$ (Fig. 1 a), $a = 75 \cdot 10^{-10}m$ (Fig. 1 b) - potential well width, $E_g = 0,18eV$ - band gap, $\Delta = 0.803 eV$ - spin-orbit splitting energy, and for *GaAs*: $m_{el} = 0.063m_0$ - effective electron mass, $a = 50 \cdot 10^{-10}m$ (Fig. 2 a), $a = 75 \cdot 10^{-10}m$ (Fig. 2 b), $E_g = 1.52eV$, $\Delta = 0,341 eV$, $P = \frac{\hbar}{2} \sqrt{\frac{3E_g}{m_{el}}}$ - Kane parameter.

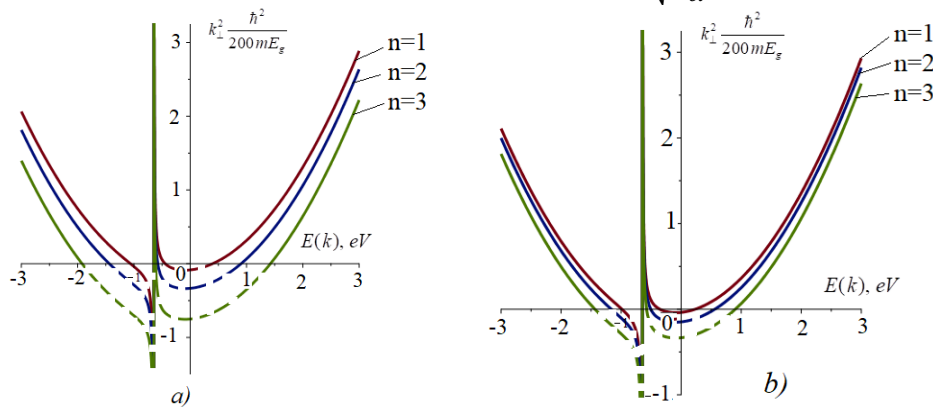


Figure 1. Size-quantized energy spectrum of electrons in InSb

In these figures, the region of negative values of the squared wave vector corresponds to the region of forbidden energies, represented by dashed lines, which represent the bandgap width and the spin-orbit splitting zone. From Fig. 1 and 2 it is clear that with increasing width of the potential well, the width of the band gap decreases (due to a shift in the energy spectrum due to size quantization) and the energy distance between close states of size quantization levels (since the energy spectrum of size quantization is inversely proportional to the width of the well).

Therefore, the energy states of electrons in the conduction band (solid line in the region of positive energy values (see Fig. 2)) and the subband of light holes in the valence band (solid line in the region of negative energy values in Fig. 2) are quantized depending on the size of the potential well, and the heavy hole subband of the valence band corresponds to a vertical line, since in Kane's approximation it does not depend on the hole wave vector. In the calculations, the minimum value of the conduction band was chosen as the energy reference point, so the electron energy is positive and the hole energy is negative.

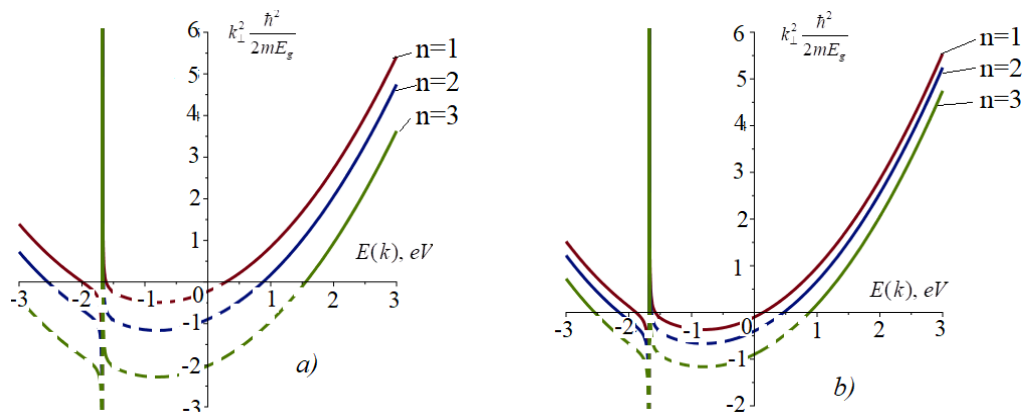


Figure 2. Size-quantized energy spectrum of electrons in GaAs

2-case. When the particle moves along the direction of dimensional quantization (in this case $k_x = 0, k_y = 0$), then the energy spectrum corresponds to a set of dimensionally quantized levels, depending on the zone parameters and the size of the hole and is described by the expression

$$\frac{\frac{3}{p^2}(E-U_0)(E+E_g-U_0)^2}{\left(2(E+E_g-U_0)+\frac{(E+E_g-U_0)^2}{E+E_g+\Delta-U_0}\right)+\left(2+\frac{(E+E_g-U_0)^2}{E+E_g+\Delta-U_0}\right)U_0} = \left(\frac{\pi n_1}{a}\right)^2, \tag{6}$$

In both - above-mentioned cases the expressions of dimensional quantization can be simplified in the following way:

(a) The energy region of current carriers satisfying the condition $E + E_g \ll \Delta$ is defined as

$$k_{\perp, n_1}^2(E) = \frac{3}{p^2}E(E + E_g) - \left(\frac{\pi n_1}{a}\right)^2, \tag{7}$$

from which we have an expression for the energy spectrum having two branches dimensionally quantized, which correspond to the dimensional quantization of subzones of electrons in the conduction zone (sign "+") and light holes (sign "-")

$$E_{\pm}(k_{\perp}) = \frac{E_g}{2} \left\{ -1 \pm \sqrt{1 + \frac{4P^2}{3E_g^2} \left[\left(\frac{\pi n_1}{a}\right)^2 + k_{\perp}^2 \right]} \right\}. \tag{8}$$

Here and below $n_1 = 1, 2, \dots$;

(b) at $E + E_g - U_0 \ll \Delta$ the dimensionally quantized levels are defined by the relation

$$\left(\frac{\pi n_1}{a}\right)^2 = \frac{1}{p^2} \frac{(E-U_0)(E+E_g-U_0)^2}{(E+E_g)}; \tag{9}$$

(c) Under the condition $E + E_{g0} \gg \Delta$ the dependence of the current carrier energy on the two-dimensional wave vector is defined as

$$k_{\perp, n_1}^2(E) = \frac{1}{p^2}E(E + E_g) - \left(\frac{\pi n_1}{a}\right)^2, \tag{10}$$

from which we obtain the expression for the size-quantized energy spectrum of electrons (sign "+") and light holes (sign "-")

$$E_{\pm}(k_{\perp}) = \frac{E_g}{2} \left\{ -1 \pm \sqrt{1 + \frac{4P^2}{E_g^2} \left[\left(\frac{\pi n_1}{a}\right)^2 + k_{\perp}^2 \right]} \right\} \tag{11}$$

The energy spectrum of electron size quantization calculated for InSb by expression (11) is shown in Fig. 3, where a) for the two-dimensional case; b) for the three-dimensional case. The above values of physical quantities are chosen in the calculations;

(d) under the condition $E + E_g - U_0 \ll \Delta$ there appear the dimensionally quantized levels defined by the relation

$$\left(\frac{\pi n_1}{a}\right)^2 = \frac{3}{2P^2} \frac{(E-U_0)(E+E_g-U_0)^2}{E+E_g}, \tag{12}$$

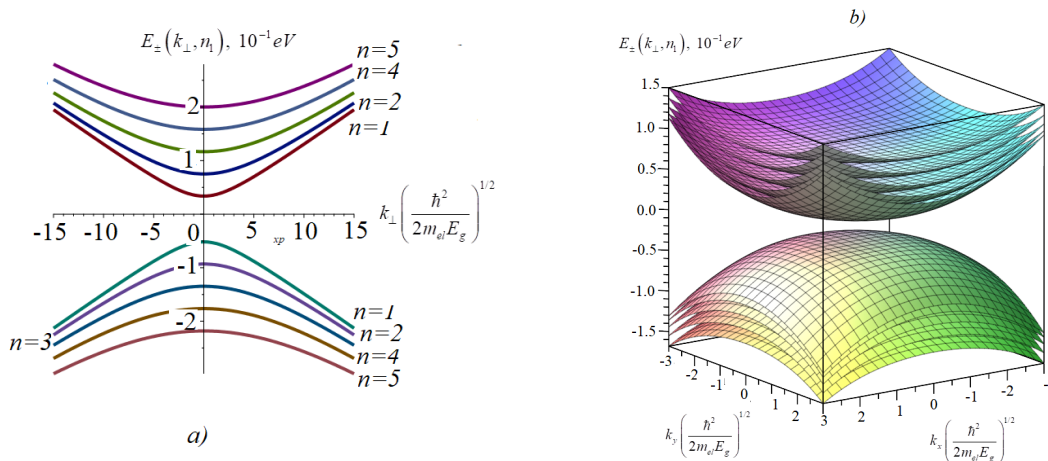


Figure 3. Size-quantized energy spectrum of electrons in InSb: a) two-dimensional; b) three-dimensional case

CONCLUSIONS

Thus, various cases of dimensional quantization in narrow-gap crystals of cubic or tetrahedral symmetry in the three-gap Kane approximation have been analyzed.

Expressions are obtained for the energy spectrum depending on the two-dimensional wave vector when electrons move both in the field of a potential well, directed along the interface of the heterostructure, and in the direction of size quantization. It is shown that in this case the energy spectrum corresponds to a set of dimensionally quantized levels, depending on the Rabi parameter, the band gap and the size of the well.

The size-quantized energy spectrum of electrons in the conduction band and holes in the subband of light holes in InSb and GaAs semiconductors was analyzed in the three-band Kane model, where the mass of heavy holes is considered infinite [15].

ORCID

©Sharifa B. Utamuradova, <https://orcid.org/0000-0002-1718-1122>; ©Rustam Y. Rasulov, <https://orcid.org/0000-0002-5512-0654>
©Voxob R. Rasulov, <https://orcid.org/0000-0001-5255-5612>; ©Kakhramon M. Fayzullaev, <https://orcid.org/0000-0001-7362-1439>

REFERENCES

- [1] V.E. Borisenko, and A.I. Vorobyova, *Nanoelectronics, Part 2*. (BSUIR, Minsk, 2003), p.76. (In Russian).
- [2] L.E. Vorobyov, S.N. Danilov, E.L. Ivchenko, I.M. Levinshstein, D.A. Firsov, and V.A. Shalygin, *Kinetic and optical phenomena in strong electric fields in semiconductors and nanostructures*, (Nauka, St. Petersburg, 2000), p.324. (In Russian).
- [3] S.A. Tarasenko, Ph.D. dissertation, St. Petersburg University, 2008. (In Russian).
- [4] G. Gulyamov, S.B. Utamuradova, M.G. Dadamirzaev, N.A. Turgunov, M.K. Uktamova, K.M. Fayzullaev, A.I. Khudayberdiyeva, et al., *East European Journal of Physics*, **2**, 221(2023). <https://doi.org/10.26565/2312-4334-2023-2-24>
- [5] Sh.B. Utamuradova, Sh.Kh. Daliev, S.A. Muzafarova, and K.M. Fayzullaev, *East European Journal of Physics*, **3**, 385 (2023). <https://doi.org/10.26565/2312-4334-2023-3-41>
- [6] E.L. Ivchenko, *Optical spectroscopy of semiconductor nanostructures*, (Alpha Science, Harrow, UK, 2005), p.350.
- [7] V.A. Shalygin, Ph.D. dissertation, St. Petersburg University, 2013. (In Russian)
- [8] D. Nematov, Kh. Kholmurodov, A. Stanchik, K. Fayzullaev, V. Gnatovskaya, and T. Kudzoev, *Trends in Sciences*, **20**(2), 4058 (2023). <https://doi.org/10.48048/tis.2023.4058>
- [9] S.A. Muzafarova, Sh.B. Utamuradova, A.M. Abdugafurov, K.M. Fayzullaev, E.M. Naurzalieva, and D.A. Rakhmanov, *Applied Physics*, **4**, 81 (2021). <https://applphys.orion-ir.ru/appl-21/21-4/PF-21-4-81.pdf> (in Russian)
- [10] I.A. Akimov, D.N. Mirlin, V.I. Perel, and V.F. Sapega, *Semiconductors*. **35**(6), 1584 (1982). <http://journals.ioffe.ru/articles/viewPDF/38563> (in Russian)
- [11] V.K. Dugaev, and P.P. Petrov, *Semiconductors*, **22**(3), 519 (1988). <http://journals.ioffe.ru/articles/viewPDF/29170> (in Russian)
- [12] E.L. Ivchenko, and G.E. Pikus, *Superlattices and other heterostructures. Symmetry and optical phenomena*, (Springer, Berlin, 1995), p. 370.
- [13] M.M. Glazov, Ph.D. dissertation, St. Petersburg University, 2012. (In Russian).
- [14] D. Nematov, Kh. Kholmurodov, A. Stanchik, K. Fayzullaev, V. Gnatovskaya, and T. Kudzoev. *Letters in Applied NanoBioScience*, **12**(3), 67 (2023). <https://doi.org/10.33263/LIANBS123.067>
- [15] G.L. Beer, and G.E. Pikus, *Symmetry and deformation effects in semiconductors*, (Media, Moscow, 2012), p. 584. (In Russian).
- [16] E.L. Ivchenko, and R.Ya. Rasulov. *Symmetry and real band structure of semi-conductors*, (Fan, Tashkent, 1989). p.126. (In Russian).
- [17] I. Vurgaftman, J.R.M. Meyer, and J.R. Ram-Mohan, *J. Appl. Phys.* **89**, 5815 (2001). <http://dx.doi.org/10.1063/1.1368156>

ДО ТЕОРІЇ РОЗМІРНОГО КВАНТУВАННЯ У ВУЗЬКОЦІЛИННИХ КРИСТАЛАХ

Шаріфа Б. Утамурадова^а, Рустам Ю. Расулов^б, Воксоб Р. Расулов^б,
Камолахон К. Урінова^б, Кахрамон М. Файзуллаєв^а

^аІнститут фізики напівпровідників і мікроелектроніки Національного університету Узбекистану, Ташкент, Узбекистан
^бФерганський державний університет, Фергана, Узбекистан

У цій статті розглядаються дослідження явищ розмірного квантування в нуль-, одно- та двовимірних напівпровідникових структурах. Основну увагу приділено механізму фотонно-кінетичних ефектів у цих структурах. Незважаючи на численні дослідження фізичних властивостей низькорозмірних систем носіїв струму, розмірне квантування енергетичних спектрів у вузькозонних напівпровідниках і пов'язані з ним фотоніко-кінетичні ефекти ще недостатньо вивчені. Таким чином, це дослідження зосереджено на квантово-механічному дослідженні розмірного квантування в певних випадках з використанням багатозонної моделі Кейна. Проаналізовано нерозв'язність матричного рівняння Шредінгера 8×8 у моделі Кейна для потенційної ями довільної форми. Досліджено залежність енергетичного спектра від двовимірного хвильового вектора для різних випадків. Зокрема, розглянуто енергетичні спектри напівпровідників InSb та GaAs залежно від параметрів зони та розміру потенційної ями. Подано висновки щодо аналізу різних випадків розмірного квантування у вузькозонних кристалах з кубічною або тетраедричною симетрією в тризонному наближенні. Показано, що енергетичний спектр відповідає набору розмірно-квантованих рівнів, які залежать від параметра Рабі, забороненої зони та розміру ями. Розмірно квантовані енергетичні спектри електронів і дірок у напівпровідниках InSb і GaAs проаналізовано в багатозонній моделі.

Ключові слова: вимірне квантування; вузька щілина; кристал; модель Кейна; рівняння Шредінгера; електрон; підзона; наноелектроніка; гетероструктура; енергетичний спектр

NON-RELATIVISTIC CALCULATION OF EXCITED-STATE IONIZATION POTENTIALS FOR LI-LIKE IONS USING WEAKEST BOUND ELECTRON POTENTIAL MODEL THEORY

Muhammad Rameez Mateen^a, Roohi Zafar^b, Ahmad Ali Rajput^a,

 Shafiq Ur Rehman^{a*}, Muhammad Mustaqeem Zahid^a

^a Department of Physics, University of Karachi, Pakistan

^b Department of Physics, NED University of Engineering and Technology, Karachi, Pakistan

*Corresponding Author e-mail: shafiqrehman5472@gmail.com

Received September 28, 2023; revised October 15, 2023; accepted November 17, 2023

In this study, a well-known Weakest Bound Electron Potential Model (WBEPM) was used to determine the excited-state ionization potential of lithium-like elements for different iso-spectrum series such as $1s^2 2p^1 P_{1/2}$, $1s^2 3s^2 S_{1/2}$, $1s^2 3d^2 D_{1/2}$, $1s^2 4s^2 S_{1/2}$, $1s^2 4p^2 P_{1/2}$, and $1s^2 4d^2 D_{1/2}$ having nuclear charges from $Z = 3$ to $Z = 18$. On the other hand, to utilize relativistic correction, Breit-Pauli approximation has also been applied to the ionization potential using a fourth-order polynomial expression in the nuclear charge Z . The deviation within the range of 0.1% has been observed between estimated and experimental values that are quite remarkable. Furthermore, new ionization potentials were proposed for iso-series with Z ranging from 19 to 30.

Keywords: non-relativistic ionization potential; Ionization Potentials; Breit-Pauli approximation; Weakest bound electron potential model (WBEPMT); nuclear charges

PACS: 31.10.+z, 31.15.-p, 31.15.Ct, 31.90.+s, 32.30.-r

INTRODUCTION

The application and properties of excited states of many electron systems have great implications in many fields of research. The spectroscopic data signify research areas in both theoretical and experimental fields like fine structure, transition probabilities, Rydberg levels, ionization potentials, etc. In 2022 the full core plus correlation and the Rayleigh-Ritz variation methods were used to study the non-relativistic energies wave functions and fine structures of high-angular-momentum states of lithium-like ions by Xin Liu and Jingchao Zhang [1]. In 2019 V. Malyshev and his group use quantum electrodynamics theory to developed a technique to calculate the two-electron recoil contributions for the $1s^2$ state in helium (He) like ions and the $1s^2 2s$ and $1s^2 2p_{1/2}$ states in lithium (Li) like ions [2]. In 2018 Shabaev et al. evaluated nuclear recoil effect on the g factor of highly charged Li-like ions by using $1/Z$ perturbation theory [3]. In 2017 by using relativistic configuration interaction (CI) method V.A. Yerokhin and his team calculated energy levels of the $1s^2 2l$ and $1s 2l 2l'$ states of Li like ions for $Z=6-17$, their theory is more accurate for the core excited states [4]. In 2016 V. A. Yerokhin et.al. reported a method to calculate more accurate value for fine structure constant α by employing the weighted difference of the g factors of the H- and Li-like ions (light element) [5]. In order to gain insight into the electronic structure of various systems, accurate determination of ionization potentials has been the subject of considerable research efforts in physics, chemistry and related fields. Reliable data on the ionization potentials for the lithium-like sequence is particularly important as it facilitates the interpretation of physical and chemical processes. To calculate ionization potentials for ionic or atomic systems, several methods have been employed, such as the 'R-matrix method', 'relativistic configuration interaction (CI) method', 'multi-configuration Hartree Fock (MCHF) method', 'multi-configuration Dirac Fock (MCDF) methods' and 'relativistic many-body perturbation theory (MBPT)' [6-13]. In recent past, a new method has been introduced by Zheng et al. known as the weakest bound electron potential model theory (WBEPMT) for ionization potential, transition probabilities, life time, quantum defects etc. The group also reported transition probability of Lithium atom and lithium like ions by using the same theory [14-19]. In 2022, R. Siddiq et al. studied the four series of Li, by using WBEPMT they calculated energies and transition probabilities of the series [20]. Saeed et al. evaluated transition probabilities and lifetimes of the lithium levels, and found new lifetimes using polynomial of each of the ns, np, nd and nf series [21]. In 2007, Yildiz et al. reported excited state ionization potential for Li by using the same theory [22]. In this work, WBEPMT, Breit-Pauli approximation and the concept of iso-spectrum-level series have been used for the precise extrapolation of ionization potentials as a function of the nuclear charge Z . The calculated ionization potential has been compared to Yildiz's findings, and it was discovered that they are in satisfactory conformity. This study is a continuation of Yildiz's work. Overall, these calculations are important in understanding the behavior of atoms and their properties.

THEORY

In this work, weakest bound electron potential model theory was used, that were developed on the basis of separation of weakest bound electron (WBE) and non-weakest bound electron (NWBE). In atomic and ionic system innermost electrons containing multiple electrons or atomic core electrons are NWBE, and others that are less tightly or outermost

electrons are known as WBE [17 new 18]. By using this model many electron systems reduce to Li-like atom, which have a single electron in their outermost shell as WBE and the core with combination of nucleus and inner electrons become NWBE. The electronic configuration is identical for all atomic or ionic terms within an iso-electronic series. However, this concept alone cannot accurately determine the ionization potentials of excited states. To address this limitation, the iso-electronic series concept is used to calculate ionization potentials. This series consists of energy levels that share the same level symbol within a known iso-electronic series. The electronic configuration, spectrum terms, and energy levels are all identical in this concept, except for the variable of nuclear charge Z [15].

The total energy of atomic and ionic systems can be calculated as the sum of relativistic energy and non-relativistic energy [15-17].

$$I(Z) = I_r(Z) + I_{nr}(Z). \tag{1}$$

The symbol $I(Z)$ is used for total energy of atomic and ionic systems, $I_r(Z)$ for relativistic energy and symbol $I_{nr}(Z)$ for non-relativistic energy. For calculation of non-relativistic energy WBEPMT is used, likewise Breit-Pauli approximation is used for relativistic energy.

NON-RELATIVISTIC IONIZATION POTENTIAL $I_{nr}(Z)$

According to WBEPM theory [18] the weakest electron under the non-relativistic condition moves in an orbit that has a larger period, due to which the coupling between WBE and NWBE reduces to Schrodinger equation of the weakest electron in a similar way as the hydrogen atom. The Schrodinger equation of the i^{th} weakest electron can be written as

$$\left[-\frac{1}{2}\nabla_i^2 + V(r_i)\right]\varphi_i = E_i\varphi_i, \tag{2}$$

$$V(r_i) = \frac{d(d+1)+2dl}{2r_i^2} + \left(-\frac{Z^*}{r_i}\right). \tag{3}$$

The first term in equation (3) represents polarization potential which is formed due to dipole formation of ionic core and WBE, and the second term is Columbic potential. Z^* is the effective nuclear charge and defined as:

$$Z^* = \sqrt{(Z - \sigma)^2 + g(Z - Z_0)} \tag{4}$$

Here Z_0 is nuclear charge, σ is screening constant and symbol g is used for relative increase factor. The ionization potential of an atom or ion can be calculated using equation (5) [16-18]:

$$I_{nr} = \frac{Z^*}{2n^{*2}} = \frac{(Z-\sigma)^2+g(Z-Z_0)}{2n^{*2}} \tag{5}$$

Here n^* is the effective principal quantum number and can be calculated by using quantum defect.

RELATIVISTIC IONIZATION POTENTIAL $I_r(Z)$

To calculate the relativistic effect the Breit-Pauli approximation is applied. The relativistic corrections of the iso-spectrum-level series could be determined by fitting fourth-order polynomial in nuclear charge. The method used to calculate $I_r(Z)$ is the same as in [16]:

$$I_r = \sum_{i=0}^4 a_i Z^i \tag{6}$$

The Value of Z^i is used in the computation of the relativistic contribution and effective nuclear charge of an atom. The parameters a_i can be determined by using the experimental values of ionization potential I_{exp} and non-relativistic ionization potential I_{nr} by using equation (1). The value of I_{exp} is obtained from NIST (National Institute of Standards and Technology) website [23]. Now the total ionization potential of the iso-spectrum-level series is given by equation number (7).

$$I = \frac{(Z-\sigma)^2+g(Z-Z_0)}{2n^2} + \sum_{i=0}^4 a_i Z^i \tag{7}$$

RESULT AND DISCUSSION

The excited state ionization potential for a range of lithium-like series, including $1s^2 2p^1 P_{1/2}$, $1s^2 3s^2 S_{1/2}$, $1s^2 3d^2 D_{1/2}$, $1s^2 4s^2 S_{1/2}$, $1s^2 4p^2 P_{1/2}$, and $1s^2 4d^2 D_{1/2}$ have been determined by using WBEPM theory, and the Breit-Pauli approximation for $n = 3$ to $n = 30$ energy levels. It is found that values of ionization potential of Lithium-Like ions are very close to the results available in NIST [23]. WBEPM is used to calculate non relativistic ionization potential I_{nr} , equation (5). To obtain more fine results of Ionization potential, relativistic effect is introduced in the ionization potential using Breit-Pauli approximation, equation (6). In addition to determine total ionization potential, equation (7) is

utilized that is the combination of both relativistic and non-relativistic effect. Since the relativistic effect generally depends on nuclear charge Z of an atom, therefore atoms like lithium to neon the relativistic effects have little impact to total energies [24-25]. The major relativistic contributions to the ionization potential increases up to the fourth power of nuclear charge Z of the iso-spectrum level series [26]. Different parameters of potential, in which the weakest bound electron travels given by equation (3) is reported in Table I. In Table II(a)-II(c) the calculated non relativistic ionization potential is compared with experimental [23] and Yildiz [19] values. First column shows nuclear charge (Z), second column shows experimental ionization Potential (I_{exp}), third column shows Yildiz ionization potential (I_{yildiz}), column IV shows calculated non-relativistic ionization Potential (I_{nr}) and fifth column shows the difference between I_{exp} and I_{nr} . Figure I-III shows the graphs between nuclear charge (Z) and non-relativistic ionization potential for different series. The red curve shows the work of Yildiz [22], the blue curve an extension of red curve shows the ionization potential calculated in this work. The two curves in all series perfectly overlap

Table I. The parameters required to calculate the ionization potential of Lithium-Like Sequence by Computer Program

	1 st series $1s^2 2p^2 P_{1/2}$	2 nd series $1s^2 3s^2 S_{1/2}$	3 rd series $1s^2 3d^2 D_{1/2}$	4 th series $1s^2 4s^2 S_{1/2}$	5 th series $1s^2 4p^2 P_{1/2}$	6 th series $1s^2 4d^2 D_{1/2}$
σ	1.9998552	1.998069833	2.000027255	2.000272688	2.000034471	2.000033207
n^*	1.9905805	2.992304883	2.999200319	3.992108353	3.991755353	3.998513662
g	0.1830223	0.51920133	0.002941923	0.386424563	0.096351577	0.000799136
a_0	12.401682	4.45E+00	6.04E+00	2.74E+00	3.24E+00	3.40E+00
a_1	-1.33E+01	-5.37E+00	-6.05E+00	-3.12E+00	-3.35E+00	-3.40E+00
a_2	3.43E+00	1.52E+00	1.51E+00	8.54E-01	8.54E-01	8.51E-01
a_3	1.67E-08	-2.37E-07	3.14E-08	6.90E-08	-1.54E-07	1.14E-07
a_4	1.14E-13	5.84E-09	-2.36E-10	-1.46E-09	3.39E-09	-3.05E-09

Table II (a). A Comparison between non-relativistic values of ionization potential with other results for series $1s^2 2p^2 P_{1/2}$ and $1s^2 3s^2 S_{1/2}$

1st series ($1s^2 2p^2 P_{1/2}$)					2nd series ($1s^2 3s^2 S_{1/2}$)				
Z	I_{exp} [20]	I_{yildiz} [19]	I_{nr} (eV)	$I_{\text{exp}} - I_{\text{nr}}$	Z	I_{exp}	I_{yildiz} [19]	I_{nr} (eV)	$I_{\text{exp}} - I_{\text{nr}}$
3	3.54344	3.54344	3.543443	-2.79E-06	3	2.01833	2.01833	2.018324	5.70E-06
4	14.25066	14.32546	14.32546	-2.09E-06	4	7.27085	7.28714	7.287146	-5.95E-06
5	31.93084	31.97487	31.97487	3.62E-06	5	15.58641	15.59502	15.59503	-7.10E-06
6	56.49166	56.49166	56.49166	4.32E-06	6	26.94195	26.94197	26.94197	2.24E-06
7	87.90269	87.87583	87.87583	2.95E-08	7	41.33234	41.32797	41.32797	2.07E-06
8	126.15448	126.12739	126.1274	7.35E-07	8	58.75740	58.75303	58.75303	2.40E-06
9	171.24633	171.24633	171.2463	-3.56E-06	9	79.21710	79.21715	79.21715	3.22E-06
10	223.18138	223.23266	223.2327	-2.85E-06	10	102.71914	102.7203	102.7203	4.54E-06
11	281.96689	282.08638	282.0864	2.85E-06	11	129.25182	129.2626	129.2626	-3.65E-06
12	347.61269	347.80748	347.8075	3.56E-06	12	158.84802	158.8439	158.8439	-1.35E-06
13	420.12125	420.39596	420.396	-7.36E-07	13	191.47027	191.4642	191.4642	1.44E-06
14	499.54365	499.85183	499.8518	-2.90E-08	14	227.20910	227.1236	227.1236	-5.27E-06
15	585.84889	586.17508	586.1751	-4.32E-06	15	265.95539	265.8221	265.8221	-1.48E-06
16	679.10256	679.36572	679.3657	-3.62E-06	16	307.72651	307.5597	307.5596	2.79E-06
17	779.27514	779.42375	779.4237	2.09E-06	17	352.60836	352.3362	352.3362	-2.43E-06
18	886.40532	886.34916	886.3492	2.79E-06	18	400.57306	400.1519	400.1519	2.83E-06
19			1000.142		19			451.0066	
20			1120.802		20			504.9004	
21			1248.33		21			561.8332	
22			1382.725		22			621.8051	
23			1523.987		23			684.8161	
24			1672.117		24			750.8661	
25			1827.114		25			819.9551	
26			1988.978		26			892.0833	
27			2157.71		27			967.2505	
28			2333.309		28			1045.457	
29			2515.776		29			1126.702	
30			2705.11		30			1210.986	

Table II(b). A Comparison between non-relativistic values of ionization potential with other results for series $1s^23d^2D_{1/2}$ and $1s^24s^2S_{1/2}$

3rd series ($1s^23d^2D_{1/2}$) [19]					4th series ($1s^24s^2S_{1/2}$) [19]				
Z	$I_{exp}[20]$	I_{yildiz}	I_{nr} (eV)	$I_{exp} - I_{nr}$	Z	$I_{exp}[20]$	I_{yildiz}	I_{nr} (eV)	$I_{exp} - I_{nr}$
3	1.51291	1.51291	1.512914	-4.30E-06	3	1.05064	1.05064	1.0506407	-6.86E-07
4	6.05316	6.05379	6.05379	1.40E-07	4	3.89488	3.90338	3.9033829	-2.85E-06
5	13.61943	13.61977	13.61977	3.16E-06	5	8.45868	8.46357	8.4635681	1.86E-06
6	24.21083	24.21085	24.21085	4.77E-06	6	14.73119	14.7312	14.731197	3.44E-06
7	37.82680	37.82702	37.82703	-5.05E-06	7	22.70955	22.70627	22.706268	1.91E-06
8	54.46972	54.46831	54.46831	3.72E-06	8	32.39465	32.38878	32.388783	-2.75E-06
9	74.13465	74.13469	74.13469	1.07E-06	9	43.78560	43.77874	43.778741	-5.35E-07
10	96.81329	96.82617	96.82617	-2.99E-06	10	56.87938	56.87614	56.876141	-1.44E-06
11	122.55134	122.5428	122.5428	1.52E-06	11	71.68095	71.68099	71.680985	4.53E-06
12	151.31074	151.2845	151.2844	4.62E-06	12	88.19848	88.19327	88.193273	-2.62E-06
13	183.08382	183.0512	183.0512	-3.70E-06	13	106.52100	106.413	106.413	-2.90E-06
14	217.92139	217.8431	217.8431	-3.44E-06	14	126.39435	126.34018	126.34018	3.70E-06
15	255.80362	255.6601	255.6601	-4.60E-06	15	148.01319	147.97479	147.97479	-2.82E-06
16	296.67349	296.5022	296.5022	2.82E-06	16	171.41096	171.31685	171.31685	-2.47E-06
17	340.55864	340.3694	340.3694	-1.17E-06	17	196.51987	196.36636	196.36636	4.76E-06
18	387.53903	387.2617	387.2617	3.42E-06	18	223.33434	223.1233	223.1233	-1.13E-06
19			437.1791		19			251.58769	
20			490.1216		20			281.75952	
21			546.0892		21			313.6388	
22			605.0819		22			347.22552	
23			667.0997		23			382.51968	
24			732.1426		24			419.52128	
25			800.2106		25			458.23033	
26			871.3037		26			498.64682	
27			945.4219		27			540.77075	
28			1022.565		28			584.60213	
29			1102.734		29			630.14095	
30			1185.927		30			677.38722	

Table II (c). A Comparison between non-relativistic values of ionization potential with other results for series $1s^24p^2P_{1/2}$ and $1s^24d^2D_{1/2}$

5th series ($1s^24p^2P_{1/2}$)					6th series ($1s^24d^2D_{1/2}$)				
Z	$I_{exp}[20]$	$I_{yildiz}[19]$	I_{nr} (eV)	$I_{exp} - I_{nr}$	Z	$I_{exp}[20]$	$I_{yildiz}[19]$	I_{nr} (eV)	$I_{exp} - I_{nr}$
3	0.86995	0.86996	0.869955	4.55E-06	3	0.85088	0.85089	0.850888	1.54E-06
4	3.48627	3.49489	3.494892	-1.90E-06	4	3.40437	3.40427	3.404271	-9.26E-07
5	7.82257	7.82757	7.827573	-3.48E-06	5	7.65991	7.65963	7.659631	-5.19E-07
6	13.86799	13.868	13.868	-1.74E-07	6	13.61696	13.61697	13.61697	2.77E-06
7	21.61960	21.61617	21.61617	-1.99E-06	7	21.27555	21.27628	21.27628	-1.07E-06
8	31.07590	31.07209	31.07209	1.07E-06	8	30.63627	30.63757	30.63757	-2.03E-06
9	42.24083	42.23575	42.23575	-9.97E-07	9	41.70082	41.70084	41.70084	-1.07E-07
10	55.10167	55.10716	55.10716	1.82E-06	10	54.46076	54.46608	54.46609	-5.31E-06
11	69.68630	69.68631	69.68631	-4.93E-07	11	68.96604	68.93331	68.93331	2.37E-06
12	86.02284	85.97321	85.97321	2.08E-06	12	85.26550	85.10251	85.10251	2.92E-06
13	103.98956	103.9679	103.9679	-4.78E-07	13	102.99906	102.9737	102.9737	-3.64E-06
14	123.74763	123.6702	123.6702	1.85E-06	14	122.60092	122.5468	122.5468	2.67E-06
15	145.64399	145.0804	145.0804	-9.53E-07	15	143.86521	143.822	143.822	1.86E-06
16	168.27704	168.1983	168.1982	1.13E-06	16	166.84025	166.7991	166.7991	3.92E-06
17	193.14794	193.0239	193.0239	-1.92E-06	17	191.56114	191.4782	191.4782	-1.13E-06
18	219.73678	219.5572	219.5572	-8.57E-08	18	217.96899	217.8592	217.8592	-3.31E-06
19			247.7984		19			245.9423	
20			277.7472		20			275.7273	
21			309.4038		21			307.2143	
22			342.7682		22			340.4032	
23			377.8403		23			375.2942	

5th series ($1s^24p^2P_{1/2}$)				6th series ($1s^24d^2D_{1/2}$)			
24			414.6201	24			411.8871
25			453.1077	25			450.182
26			493.303	26			490.1789
27			535.2061	27			531.8778
28			578.8169	28			575.2786
29			624.1355	29			620.3814
30			671.1618	30			667.1862

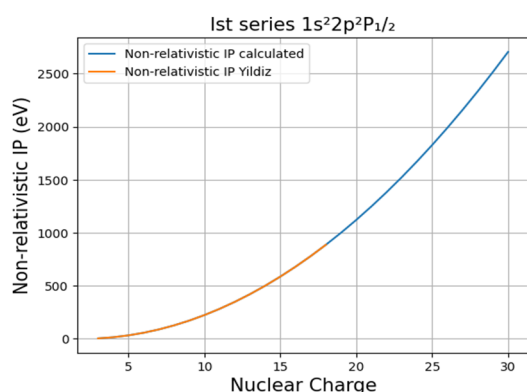


Figure I. Graphs between nuclear charge (Z) and non-relativistic ionization potential for 1st series $1s^22p^1 P_{1/2}$

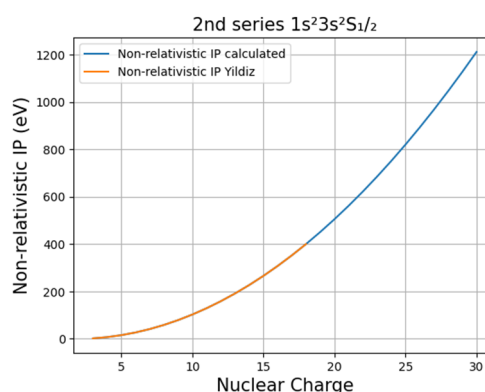


Figure II. Graphs between nuclear charge (Z) and non-relativistic ionization potential for series $1s^23s^2 S_{1/2}$

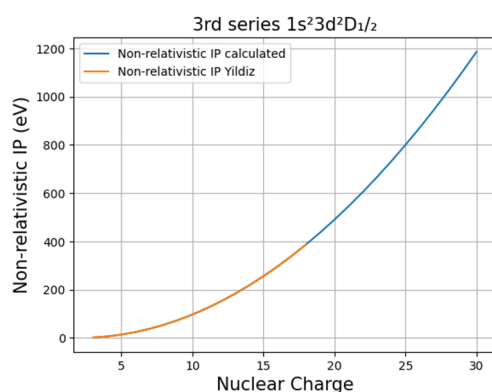


Figure III. graphs between nuclear charge (Z) and non-relativistic ionization potential for series $1s^23d^2 D_{1/2}$

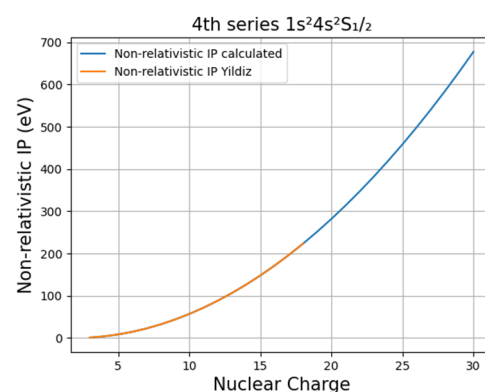


Figure IV. graphs between nuclear charge (Z) and non-relativistic ionization potential for series $1s^24s^2 S_{1/2}$

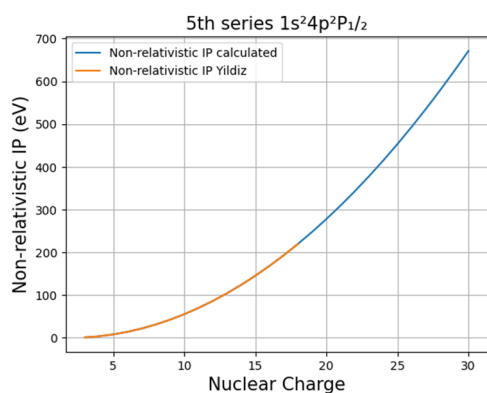


Figure V. graphs between nuclear charge (Z) and non-relativistic ionization potential for series $1s^24p^2 P_{1/2}$

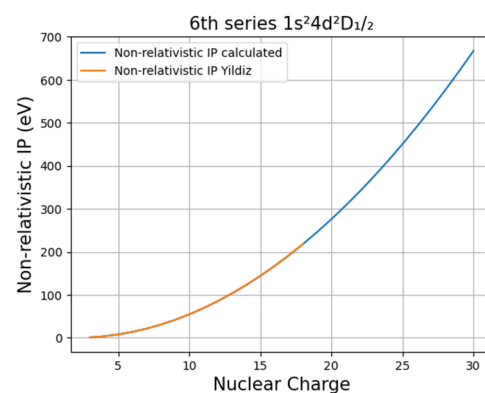


Figure VI. Graphs between nuclear charge (Z) and non-relativistic ionization potential for series $1s^24d^2 D_{1/2}$

CONCLUSION

The Weakest Bound Electron Potential Model Theory the Breit–Pauli approximation is used to calculate the ionization potentials of lithium-like series. The constants in Eq. 7 are determined by using experimental data from the

National Institute of Standards and Technology (NIST) website [23] and reported in Table I. These constants are then used to calculate non-relativistic ionization potentials from $n = 3$ to $n = 30$ for each individual series, as shown in Table II. The experimental values from NIST are close to the calculated values for series. The non-relativistic potential for six series has also been compared with the work of Yildiz [22]. The agreement in the overlap area of the two works is excellent, as can be seen in Figure I-VI. An excellent agreement with previously reported data shows the reliability of calculation. The blue curve an extension of red curve in Fig. I-VI shows the new relativistic ionization potential calculated in this work. This work is an extension of Yildiz's findings.

ORCID

Shafiq Ur Rehman, <https://orcid.org/0009-0001-8598-359X>

REFERENCES

- [1] X. Liu, and J. Zhang, "Study of non-relativistic energy and fine structure splitting using a Rayleigh–Ritz method for a high-angular-momentum state," *Journal of the Korean Physical Society*, **80**, 197–202 (2022). <https://doi.org/10.1007/s40042-021-00349-y>
- [2] A.V. Malyshev, I.S. Anisimova, D.V. Mironova, V.M. Shabaev, and G. Plunien, "QED theory of the specific mass shift in few-electron atoms," *Physical Review A*, **100**(1), 012510 (2019). <https://doi.org/10.1103/PhysRevA.100.012510>
- [3] V.M. Shabaev, D.A. Glazov, A.V. Malyshev, and I.I. Tupitsyn, "Nuclear recoil effect on the g factor of highly charged Li-like ions," *Physical Review A*, **98**(3), 032512 (2018). <https://doi.org/10.1103/PhysRevA.98.032512>
- [4] V.A. Yerokhin, A. Surzhykov, and A. Müller, "Relativistic configuration–interaction calculations of the energy levels of the $1s^2 2l$ and $1s 2l 2l'$ states in lithiumlike ions: Carbon through chlorine," *Phys. Rev. A*, **96**, 042505 (2017). <https://doi.org/10.1103/PhysRevA.96.042505>
- [5] V.A. Yerokhin, E. Berseneva, Z. Harman, I.I. Tupitsyn, and C.H. Keitel, "g factor of light ions for an improved determination of the fine-structure constant," *Physical Review Letters*, **116**(10), 100801 (2016). <https://doi.org/10.1103/PhysRevLett.116.100801>
- [6] M.H. Chen, K.T. Cheng, and W.R. Johnson, "Relativistic configuration–interaction calculations of $n=2$ triplet states of heliumlike ions," *Physical Review A*, **47**(5), 3692 (1993). <https://doi.org/10.1103/PhysRevA.47.3692>
- [7] A. Ynnerman, and C. F. Fischer, "Multiconfigurational–Dirac–Fock calculation of the $2s 21S_0$ – $2s 2p 3P_1$ spin–forbidden transition for the Be–like isoelectronic sequence," *Physical Review A*, **51**(3), 2020 (1995). <https://doi.org/10.1103/PhysRevA.51.2020>
- [8] F.A. Parpia, C.F. Fischer, and I.P. Grant, "GRASP92: A package for large-scale relativistic atomic structure calculations," *Computer physics communications*, **94**(2–3), 249–271 (1996). [https://doi.org/10.1016/0010-4655\(95\)00136-0](https://doi.org/10.1016/0010-4655(95)00136-0)
- [9] J.A. Fernley, A. Hibbert, A.E. Kingston, and M.J. Seaton, "Atomic data for opacity calculations: XXIV. The boron-like sequence," *Journal of Physics B: Atomic, Molecular and Optical Physics*, **32**(23), 5507 (1999). <https://doi.org/10.1088/0953-4075/32/23/307>
- [10] G. Tachiev, and C.F. Fischer, "Breit–Pauli energy levels, lifetimes and transition data: boron-like spectra," *Journal of Physics B: Atomic, Molecular and Optical Physics*, **33**(13), 2419 (2000). <https://doi.org/10.1088/0953-4075/33/13/304>
- [11] K.M. Aggarwal, A. Hibbert, and F.P. Kenan, "Oscillator Strengths for Transitions in O III," *Astrophys. J. Suppl.* **108**, 393 (1997). <https://doi.org/10.1086/312949>
- [12] U.I. Safronova, W.R., Johnson, and A.E. Livingston, "Relativistic many-body calculations of electric-dipole transitions between $n=2$ states in B-like ions," *Physical Review A*, **60**(2), 996 (1999). <https://doi.org/10.1103/PhysRevA.60.996>
- [13] M.J. Vilkas, Y. Ishikawa, and K. Koc, "Second-order multiconfigurational Dirac–Fock calculations on boronlike ions," *International journal of quantum chemistry*, **70**(4–5), 813–823 (1998). [https://doi.org/10.1002/\(SICI\)1097-461X\(1998\)70:4/5%3C813::AID-QUA28%3E3.0.CO;2-0](https://doi.org/10.1002/(SICI)1097-461X(1998)70:4/5%3C813::AID-QUA28%3E3.0.CO;2-0)
- [14] N.W. Zheng, Y.J. Sun, T. Wang, D.X. Ma, Y. Zhang, and W. Su, "Transition probability of lithium atom and lithiumlike ions with weakest bound electron wave functions and coupled equations," *International Journal of Quantum Chemistry*, **76**(1), 51–61 (2000). [https://doi.org/10.1002/\(SICI\)1097-461X\(2000\)76:1%3C51::AID-QUA5%3E3.0.CO;2-M](https://doi.org/10.1002/(SICI)1097-461X(2000)76:1%3C51::AID-QUA5%3E3.0.CO;2-M)
- [15] N.W. Zheng, T. Zhou, T. Wang, R.Y. Yang, Y.J. Sun, F. Wang, and C.G. Chen, "Ground-state atomic ionization energies for $Z=2$ –18 and up to 18 electrons," *Physical Review A*, **65**(5), 052510 (2002). <https://doi.org/10.1103/PhysRevA.65.052510>
- [16] N.W. Zheng, and T. Wang, "Systematical study on the ionization potential of excited states in carbon-like sequence," *Chemical physics letters*, **376**(5–6), 557–565 (2003). [https://doi.org/10.1016/S0009-2614\(03\)01021-2](https://doi.org/10.1016/S0009-2614(03)01021-2)
- [17] N.W. Zheng, and T. Wang, "Ionization potential of excited states of Be-like sequence in the concept of iso-spectrum-level series," *International journal of quantum chemistry*, **93**(5), 344–350 (2003). <https://doi.org/10.1002/qua.10487>
- [18] N.W. Zheng, and T. Wang, "Calculation of excited-state ionization potential for boron-like sequence," *International journal of quantum chemistry*, **98**(6), 495–501 (2004). <https://doi.org/10.1002/qua.20109>
- [19] N.W. Zheng, T. Wang, D.X. Ma, T. Zhou, and J. Fan, "Weakest bound electron potential model theory," *International journal of quantum chemistry*, **98**(3), 281–290 (2004). <https://doi.org/10.1002/qua.20021>
- [20] R. Siddiq, M.N. Hameed, M.H. Zaheer, M.B. Khan, and Z. Uddin, "Rydberg energies and transition probabilities of Li I for np – ms ($m \leq 5$) transitions," *Beni-Suef University Journal of Basic and Applied Sciences*, **11**(1), 42 (2022). <https://doi.org/10.1186/s43088-022-00224-0>
- [21] M. Saeed, and Z. Uddin, "Lifetimes of Fine Levels of Li Atom for $20 < n < 31$ by Extended Ritz Formula," (2023). <https://doi.org/10.48550/arXiv.2308.01087>
- [22] G. Çelik, M. Yildiz, and H.Ş. Kiliç, "Determination of Excited-State Ionization Potentials for Lithium-Like Sequence Using Weakest Bound Electron Potential Model Theory," *Acta Physica Polonica A*, **112**(3), 485–494 (2007). <https://bibliotekanauki.pl/articles/2047731.pdf>
- [23] J.R. Fuhr, W.C. Martin, A. Musgrove, J. Sugar, and W.L. Wiese, "NIST Atomic Spectroscopic Database," (1998). <http://physics.nist.gov/PhysRefData/contents.html>
- [24] A. Veillard, and E. Clementi, "Correlation Energy in Atomic Systems. V. Degeneracy Effects for the Second-Row Atoms," *The Journal of Chemical Physics*, **49**(5), 2415–2421 (1968). <https://doi.org/10.1063/1.1670415>

- [25] J.B. Mann, and W.R. Johnson, "Breit interaction in multielectron atoms," *Physical Review A*, 4(1), 41 (1971).
<https://doi.org/10.1103/PhysRevA.4.41>
- [26] R.D. Cowan, *The theory of atomic structure and spectra*, No. 3, (Univ. of California Press, 1981).

**НЕРЕЛЯТИВІСТСЬКИЙ РОЗРАХУНОК ПОТЕНЦІАЛІВ ІОНІЗАЦІЇ У ЗБУДЖЕНОМУ СТАНІ
 ДЛЯ ЛІТІЙ-ПОДІБНИХ ІОНІВ З ВИКОРИСТАННЯМ ТЕОРІЇ МОДЕЛІ СЛАБШОГО ЗВ'ЯЗАНОГО
 ЕЛЕКТРОННОГО ПОТЕНЦІАЛУ**

Мухаммад Раміз Матін^a, Рухі Зафар^b, Ахмад Алі Раджпут^a, Шафік Ур Рехман^a, Мухаммад Мустакім Захід^a

^a *Кафедра фізики, Університет Карачі, Пакистан*

^b *Кафедра фізики, Університет інженерії та технології NED, Карачі, Пакистан*

У цьому дослідженні добре відома модель потенціалу найслабшого зв'язку електронів (WBEPM) була використана для визначення потенціалу іонізації збудженого стану літєподібних елементів для різних серій ізоспектру, таких як $1s^2 2p^1 P_{1/2}$, $1s^2 3s^2 S_{1/2}$, $1s^2 3d^2 D_{1/2}$, $1s^2 4s^2 S_{1/2}$, $1s^2 4p^2 P_{1/2}$, та $1s^2 4d^2 D_{1/2}$, які мають заряди ядра від $Z = 3$ до $Z = 18$. З іншого боку, для використання релятивістської поправки до іонізації також було застосовано наближення Бріє-Паулі потенціал, використовуючи поліноміальний вираз четвертого порядку в заряді ядра Z . Відхилення в діапазоні 0,1% спостерігалось між розрахунковими та експериментальними значеннями, що є досить примітним. Крім того, були запропоновані нові потенціали іонізації для ізо-рядів із Z в діапазоні від 19 до 30.

Ключові слова: *нерелятивістський потенціал іонізації; потенціали іонізації; апроксимація Брейта-Паулі; модель потенціалу найслабшого зв'язку електронів (WBEPMT); ядерні заряди*

SIMULTANEOUS DOCKING OF ANTIVIRAL DRUGS AND CYANINE DYES WITH PROTEINS USING MULTIPLE LIGAND APPROACH

Olga Zhytniakivska*, **Uliana Tarabara**, **Kateryna Vus**, **Valeriya Trusova**, **Galyna Gorbenko**

*Department of Medical Physics and Biomedical Nanotechnologies, V.N. Karazin Kharkiv National University
4 Svobody Sq., Kharkiv, 61022, Ukraine*

**Corresponding Author: olga.zhytniakivska@karazin.ua*

Received October 7, 2023; revised November 10, 2023; accepted November 17, 2023

The protein-based nanosystems for targeted drug delivery of a wide array of substances, ranging from small drugs and therapeutic proteins to nucleic acids and genes, attract increasing attention due to their biocompatibility and biodegradability, extraordinary binding capacity for different ligands, accessibility from natural sources, effective drug protection and gentle encapsulation conditions. Due to the multitude of binding pockets and functional groups on the protein surface, these nanocarriers seem to be highly efficient multifunctional nanotheranostic systems that could incorporate both a therapeutic drug and a visualizing agent. This integration serves multiple purposes, including the regulation of drug release, monitoring the alterations at the target site in response to treatment, and offering crucial insights into the efficacy of the intervention in its early stages. The development of these advanced nanosystems necessitates a thorough comprehension of the potential interactions within these intricate systems. In the present study we assessed the potential of six trimethine and seven pentamethine cyanine dyes to serve as visualizing agents in the drug-protein-dye systems which include functionally significant proteins (cytochrome *c*, serum albumin, lysozyme and insulin and four antiviral drugs, *viz.* favipiravir, molnupiravir, nirmatrelvir and ritonavir). The ternary systems with the highest dye-protein surface shape complementarity were established for all groups of the examined cyanine dyes. The influence of the cyanine dye structure on the stability of the drug-protein-dye complexes was assessed. The obtained results indicate that the dye-protein affinity is not solely dependent on the length of the polymethine chain. It was found that the most prospective drug delivery systems containing the trimethines and pentamethines as visualizing agents are AK5-6-, AK5-8- and AK3-11-drug-albumin complexes.

Keywords: *Protein-drug-dye complexes, Antiviral agents, Protein nanoparticles, Drug nanocarriers, Cyanine dyes, Multiple molecular docking*

PACS: 87.14.C++c, 87.16.Dg

During the past decades the field of engineering materials for drug delivery applications in cancer therapy [1-3], central nervous system indications [4,5], antiviral therapy [6,7], inflammatory [8,9] and cardiovascular diseases [10,11] has witnessed a growing interest in utilizing the nanostructured drug delivery systems (DDS). The evolution of these second-generation DDS offers a range of advantages that aim to tackle numerous challenges associated with conventional therapies including: i) enhanced stability and solubility of drugs; ii) reduced drug toxicity; iii) uniform dosing; iv) improved drug pharmacokinetics and distribution, to name only a few [12-15]. Among the plethora of biomaterials and synthetic polymers explored as fundamental blocks for creating nanopharmaceuticals tailored for targeted drug delivery of a wide array of substances, ranging from small drugs and therapeutic proteins to nucleic acids and genes, particular attention is devoted to the protein-based nanosystems [13-15]. Their appeal lies in numerous advantageous attributes, such as: i) biocompatibility and biodegradability; ii) extraordinary binding capacity for various drugs; iii) abundance of proteins available from natural sources; iv) drug protection from enzymatic degradation and rapid renal excretion; v) gentle formulation and drug encapsulation requirements; vi) capability of surface covering with ligands specific to target tissues, vii) streamlined synthesis procedures with cost-effective outcomes [13-16]. Moreover, owing to the presence of numerous binding pockets and functional groups within the proteins, protein nanocarriers are especially promising for the development of effective multifunctional nanotheranostic systems merging both the therapeutic and diagnostic properties [17-19]. Theranostic nanomedicines assume the simultaneous integration of a therapeutic drug and visualizing agent for control of drug release, monitoring the changes at the target site in response to the treatment, and providing valuable insights into the effectiveness of the intervention at an early stage [17-18]. The fabrication of these advanced second-generation nanosystems requires a comprehensive understanding of the possible interactions within the complex systems.

In our previous work, we employed the multiple ligand simultaneous docking technique to investigate the interactions among four functionally significant proteins (cytochrome *c*, serum albumin, lysozyme and insulin), four antiviral drugs (favipiravir, molnupiravir, nirmatrelvir and ritonavir) and a series of cyanine dyes represented by four monomethines and two heptamethines. Our primer focus was to identify the most suitable systems for creating the protein nanoparticles carrying both antiviral drugs and cyanine dyes as visualizing agents [20]. The obtained results indicate that the albumin-based nanosystems functionalized by the heptamethine cyanine dyes can serve as effective carriers for targeted delivery of the explored antiviral agents. In continuation of our previous work, in the present study we extended our investigation to other cyanine dyes (six trimethines and seven pentamethines). The main was threefold: i) to delve

into the interactions within the ternary protein-dye-drug complexes using the multiple ligand simultaneous docking (MLSD) technique; ii) to identify the most promising candidates for the development of protein-based theranostic drug delivery nanoplateforms; iii) to determine the structural features of the cyanine dyes responsible for their loading in the multicomponent protein-based drug delivery nanosystems.

MATERIALS AND METHODS

Molecular docking studies

The three-dimensional X-ray crystal structures of the examined proteins in their native monomeric form were obtained from the Protein Data Bank using the PDB IDs 1REX, 3I40, 3ZCF, 6M4R for lysozyme (Lz), insulin (Ins), cytochrome *c* (Ct) and serum albumin (SA), respectively. The structural model for serum albumin was prepared by employing the DockPrep module of UCSF Chimera molecular software [21]. This involved the removal of water molecules and the addition of polar hydrogen atoms and Kollman charges [21]. The structure of the antiviral drugs (favipiravir, molnupiravir, nirmatrelvir and ritonavir) [20] and the investigated cyanine dyes (Figure 1) were constructed using the MarvinSketch (version 18.10.0) and optimized in Avogadro (version 1.1.0) using the Universal Force Field with the steepest descent algorithm [22,23]. Notably, counterions were omitted from the dye structures to retain molecular charges. Initially, the blind docking of the drugs or dyes (control dye-protein systems) with the proteins was carried out using the PatchDock server (<http://bioinfo3d.cs.tau.ac.il/PatchDock/php.php>) which focuses on finding the maximum surface shape complementarity while minimizing the steric clashes [24]. Subsequently, the top-scored docked drug-protein complexes were utilized as a receptor for docking of the second ligand, which represents either a trimethine or pentamethine cyanine dye, using the PatchDock server. To characterize the possible interactions involved in the formation of composite drug-dye-protein systems, the protein-ligand interaction profiler (PLIP, <https://plip-tool.biotech.tudresden.de/plip-web/plip/index>) was employed [25]. The selected docking poses were visualized using the UCSF Chimera software (version 1.14), combining the docking models with the best geometric shape complementarity in the same image to optimize visibility of the binding sites [26].

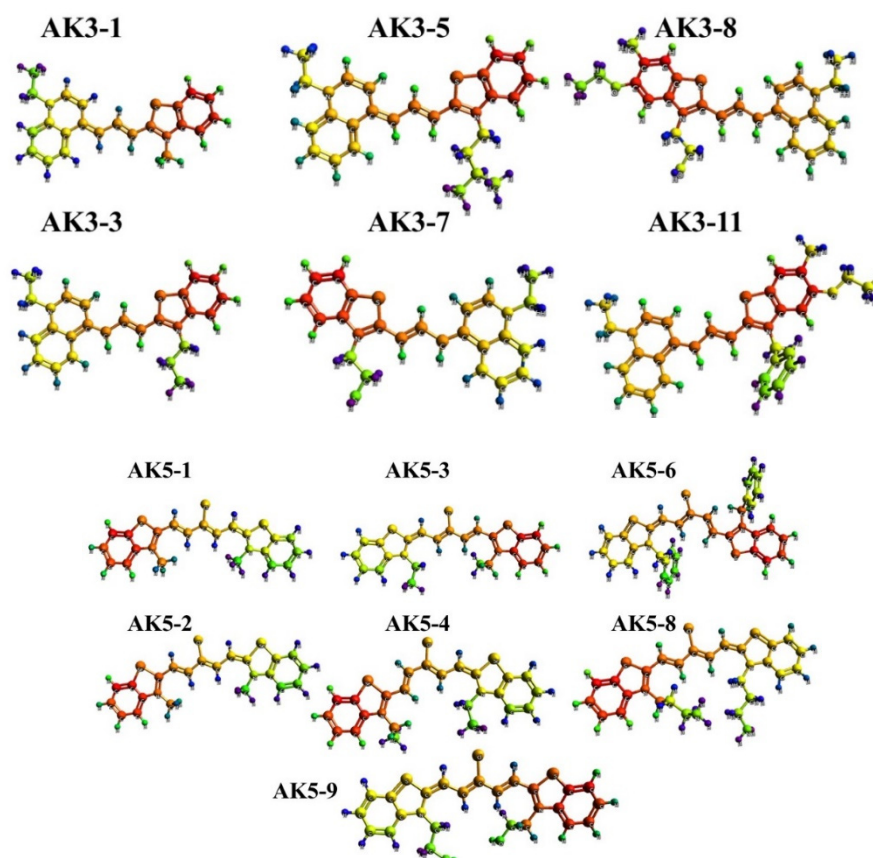


Figure 1. Structural formulas of the examined cyanine dyes

RESULTS AND DISCUSSION

The ternary complexes with the highest scores, comprising proteins, drugs, and dyes are depicted in Fig.2 (the drugs and dyes binding modes were identified for cytochrome *c* (Fig. 2), albumin (Fig. 3), lysozyme (Fig. 4) and insulin (Fig. 5). The examined tri- and pentamethines as well as previously reported mono- and heptamethines [20] are situated in close proximity to each other near the surfaces of cytochrome *c*, lysozyme and insulin. The binding sites for favipiravir,

molnupiravir, nirmatrelvir and ritonavir did not change compared to our previous findings [20]. However, the distinct binding pockets of albumin are observed for the drugs and the cyanine dyes examined here.

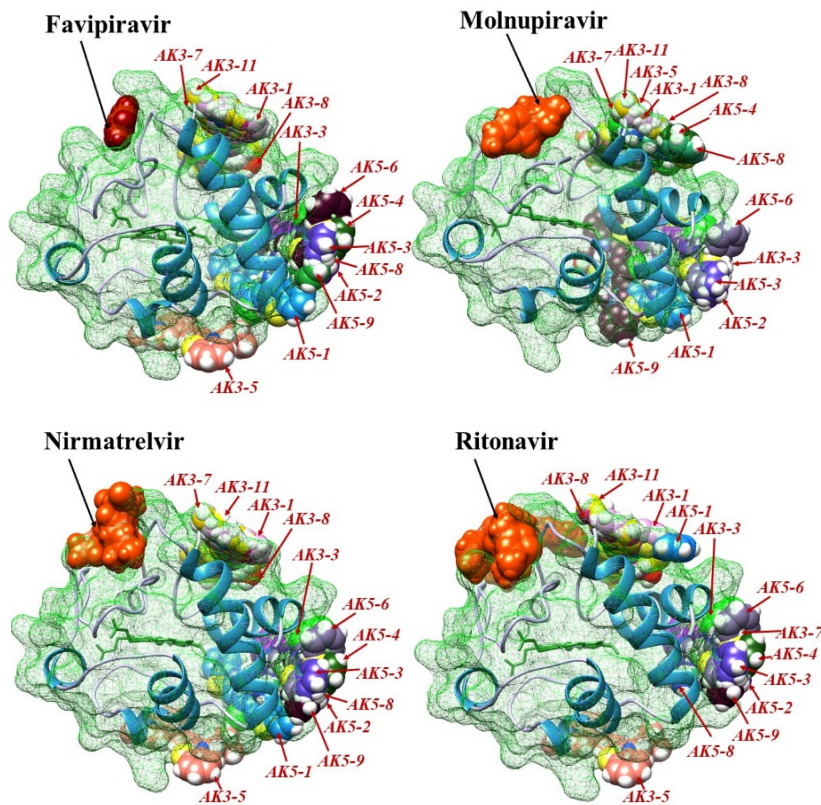


Figure 2. The highest-score docking poses obtained for cytochrome *c* using the MLSD in PatchDock

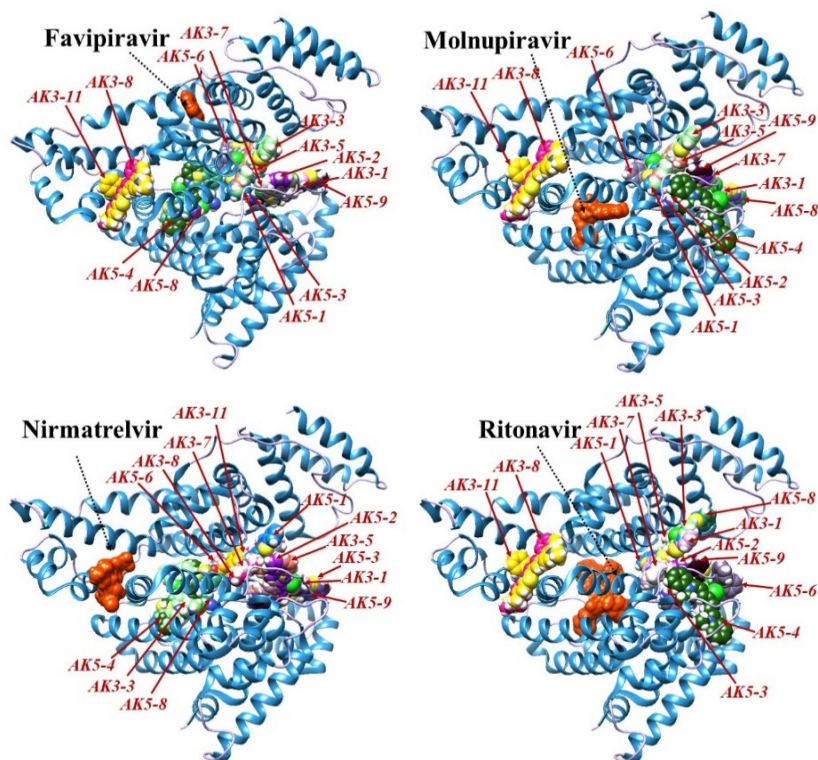


Figure 3. The highest-score docking poses obtained for albumin using the MLSD in PatchDock

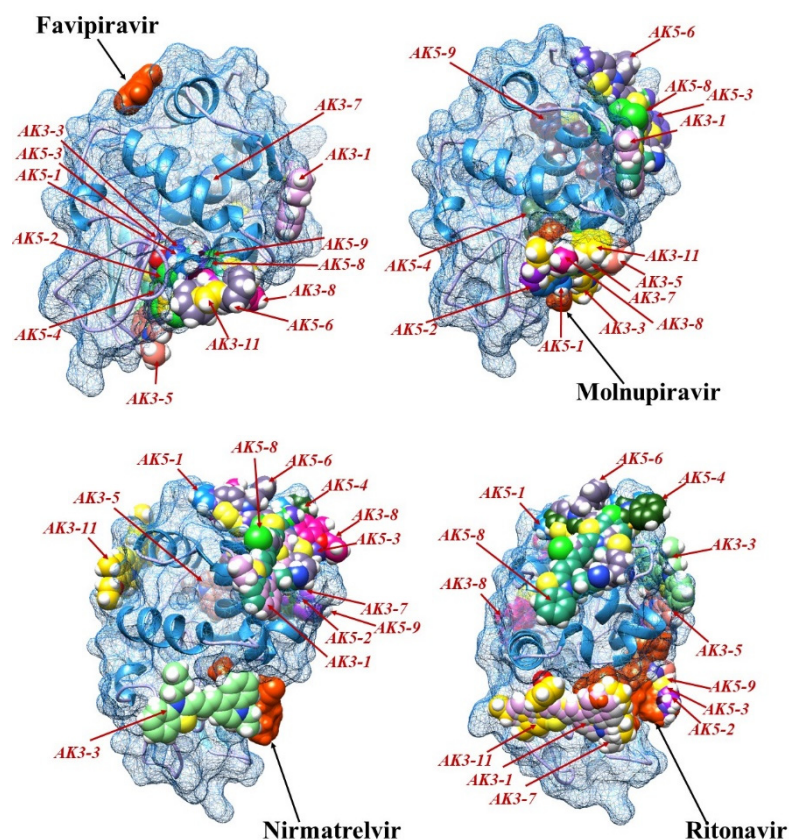


Figure 4. The highest-score docking poses obtained for lysozyme using the MLSD in PatchDock.

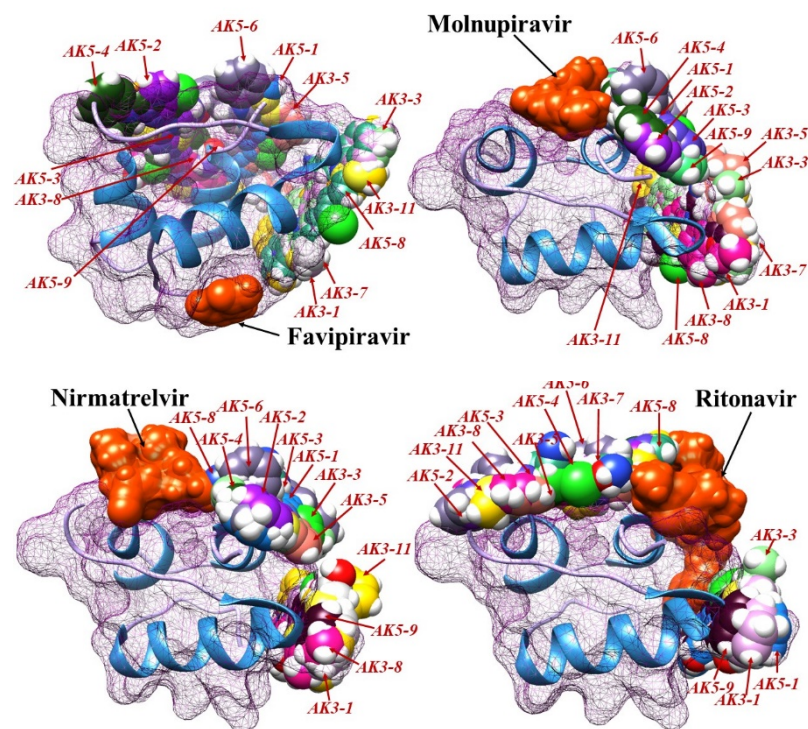


Figure 5. The highest-score docking poses obtained for insulin using the MLSD in PatchDock.

Next, the geometric shape complementarity scores and approximate interface areas for the protein-drug-dye systems were analyzed. In the cytochrome *c*-drug-dye systems the antiviral agents have no impact on the docking positions compared to the protein-dye complexes (Table 1). This observation does not hold true only in the specific cases of AK3-

3, AK3-5, (AK5-3), AK5-4, AK5-8, AK5-for molnupiravir and AK3-1, AK3-7, AK3-8, AK3-11, AK5-1 for ritonavir, where the dye-protein affinity slightly decrease (increase). The interface area slightly decreased (increased) by molnupiravir in the systems with AK3-3, AK3-5, (AK5-3), AK5-4, AK5-8, AK5-9 and increased by ritonavir for ternary complexes with the AK3-7, AK3-8, AK3-11, AK5-1. For the rest examined systems including previously reported [20], the comparison of the docking outcomes was performed in order to detect the most prospective dyes. It was found that the dye-protein affinity follows the order: AK7-5 > AK7-6 > AK5-6 > AK-1-2-20 > AK-1-2-19 > AK3-11 > AK5-8 (F, N, R) > AK5-9 (F, N, R) > AK3-5 (F, N, R) > AK3-8 > AK5-3 (F, N, R), AK3-3 (F, N, R) > AK3-7 (F, M, N) > AK5-2 > AK5-4 (F, N, R) > AK-1-2-17 > AK5-1 > AK3-1 > AK-1-2-18; while the interface area decreases in the order: AK7-6 > AK7-5 > AK5-6 > AK-1-2-20 > AK-1-2-19 > AK5-8 > AK5-9 > AK3-3 > AK3-11 > AK5-3 > AK-1-2-17 > AK3-5 > AK-1-2-18 > AK5-2 > AK5-4 > AK3-8 > AK5-1 > AK3-7 > AK3-1.

Table 1. The geometric shape complementarity score and approximate interface area of the complex derived for the cytochrome *c*-drug-dye systems (F- Favipiravir, M – Molnupiravir, N - Nirmatrelvir, R – Ritonavir).

Cytochrome <i>c</i>										
Dye	Score					Approximate interface area of the complex, Å ²				
	F	M	N	R	-	F	M	N	R	-
-	2220	3648	4292	6062	-	237.40	384.30	576.30	797.80	-
AK3-1	4578	4578	4578	4636	4578	500.30	500.30	500.30	506.60	500.30
AK3-3	4944	4788	4944	4944	4944	616.00	593.80	616.00	616.00	616.00
AK3-5	5062	4962	5062	5062	5062	600.90	583.90	600.90	600.90	600.90
AK3-7	4780	4780	4780	4678	4780	522.80	522.80	522.80	600.80	522.80
AK3-8	5034	5034	5034	5016	5034	561.70	561.70	561.70	572.90	561.70
AK3-11	5372	5372	5372	5440	5372	614.20	614.20	614.20	647.90	614.20
AK5-1	4584	4584	4584	4666	4584	527.10	527.10	527.10	531.90	527.10
AK5-2	4736	4736	4736	4736	4736	579.10	579.10	579.10	579.10	579.10
AK5-3	4944	5200	4944	4944	4944	610.90	627.30	610.90	610.90	610.90
AK5-4	4734	4604	4734	4734	4734	563.30	582.80	563.30	563.30	563.30
AK5-6	5638	5638	5638	5638	5638	766.10	766.10	766.10	766.10	766.10
AK5-8	5266	4970	5266	5266	5266	675.10	632.70	675.10	675.10	675.10
AK5-9	5122	4932	5122	5122	5122	632.00	584.70	632.00	632.00	632.00

The drug influence on the docking parameters in the albumin-cyanine systems was found to be more pronounced (Table 2). The docking score remains the same for the systems AK3-1 + F/M/N, AK3-3 + N, AK3-5 + N, AK3-7 + N, AK3-8 + F/M/R, AK3-11 + F/M/R, AK5-1 + N, AK5-2 + N, AK5-3 + all drug systems, AK5-4 + F/N, AK5-6 + F/M/N, AK5-8 + F/N, AK5-9 + F/N; decreases in the systems AK3-5 + F/M/R, AK3-7 + F/M/R, AK3-8 + N, AK3-11 + N, AK5-1 + F/M, AK5-2 + F/M, AK5-8 + M/R, AK5-9 + M/R; and increases in the systems AK3-1+R, AK3-3 + F/M/R, AK5-1+ R, AK5-2 + R, AK5-4 + M/R, AK5-6+R. The ranking of the explored complexes according to aforementioned parameter appeared to be as follows: AK7-5 (N) > AK7-6 > AK-1-2-20 (F, M, N) > AK-1-2-19 (N) > AK3-11 (F, M, R) > AK5-8 (F, N, R) > AK5-6 (F, M, N) > AK-1-2-18 (F, N) > AK-1-2-17 (F, N) > AK5-9 (F, N) > AK3-8 (F, M, R) > AK3-5 (N) > AK5-4 (F, N) > AK5-3 > AK3-3 (N) > AK5-1 (N) > AK3-7 (N) > AK3-1 (F, M, N) > AK5-2 (N). The highest albumin-cyanine interface area was observed for AK7-5 (N, R), AK-1-2-20 (F, M, N), AK7-6, AK-1-2-19, AK5-6, AK5-8, AK3-11.

Table 2. The geometric shape complementarity score and approximate interface area of the complex derived for the albumin-drug-dye systems (F- Favipiravir, M – Molnupiravir, N - Nirmatrelvir, R – Ritonavir)

Serum albumin										
Dye	Score					Approximate interface area of the complex, Å ²				
	F	M	N	R	-	F	M	N	R	-
-	2900	5054	6212	8412	-	343.60	553.10	719.50	1036.60	-
AK3-1	5280	5280	5280	5332	5280	600.50	600.50	600.50	626.60	600.50
AK3-3	5672	5672	5606	5672	5606	677.80	677.80	672.80	677.80	672.80
AK3-5	5824	5824	6030	5792	6030	739.20	739.20	690.50	746.80	690.50
AK3-7	5306	5306	5372	5320	5372	636.90	636.90	658.80	690.30	658.80
AK3-8	6074	6074	6022	6074	6074	695.60	695.60	730.90	695.60	695.60
AK3-11	6634	6634	6428	6634	6634	753.10	753.10	834.70	753.10	753.10
AK5-1	5338	5338	5406	5560	5406	682.90	682.90	672.80	674.40	672.80
AK5-2	5198	5198	5208	5234	5208	634.70	634.70	639.00	647.20	639.00
AK5-3	5854	5854	5854	5854	5854	683.60	683.60	683.60	683.60	683.60
AK5-4	5868	5870	5868	5870	5868	681.40	747.80	681.40	747.80	681.40
AK5-6	6556	6556	6556	6960	6556	814.60	814.60	814.60	914.90	814.60
AK5-8	6562	5922	6562	5944	6562	775.70	695.90	775.70	690.00	775.70
AK5-9	6188	5948	6188	5948	6188	691.90	700.10	691.90	700.10	691.90

Table 3. The geometric shape complementarity score and approximate interface area of the complex derived for the lysozyme-drug-dye systems (F- Favipiravir, M – Molnupiravir, N - Nirmatrelvir, R – Ritonavir).

Lysozyme										
Dye	Score					Approximate interface area of the complex, A ²				
	F	M	N	R	-	F	M	N	R	-
-	2184	3628	4690	5922	-	245.40	394.70	522.30	702.70	-
AK3-1	4212	4212	4212	4232	4212	481.80	481.80	481.80	530.10	481.80
AK3-3	4520	4646	4514	4538	4520	507.50	540.90	538.10	574.80	507.50
AK3-5	4634	4708	4606	4600	4634	548.40	557.60	493.70	605.30	548.40
AK3-7	4334	4344	4334	4462	4334	537.20	525.50	537.20	547.80	537.20
AK3-8	4872	4866	4718	4706	4872	580.60	570.50	489.30	604.30	580.60
AK3-11	5176	5198	5044	5228	5176	626.40	641.60	604.80	671.30	626.40
AK5-1	4526	4680	4502	4546	4526	510.70	554.40	584.20	569.20	510.70
AK5-2	4534	4656	4382	4428	4534	522.40	547.50	556.40	549.30	522.40
AK5-3	4812	4548	4548	4702	4812	544.30	517.40	517.40	572.10	544.30
AK5-4	4624	4580	4522	4624	4624	531.50	506.00	662.40	545.50	531.50
AK5-6	5550	5304	5304	5218	5550	652.70	614.70	614.70	628.20	652.70
AK5-8	5196	4992	4992	4992	5196	585.10	556.80	556.80	556.80	585.10
AK5-9	5004	4640	4640	4680	5004	547.40	589.50	589.50	569.10	547.40

Table 4. The geometric shape complementarity score and approximate interface area of the complex derived for the insulin-drug-dye systems (F- Favipiravir, M – Molnupiravir, N - Nirmatrelvir, R – Ritonavir).

Insulin										
Dye	Score					Approximate interface area of the complex, A ²				
	F	M	N	R	-	F	M	N	R	-
-	1944	2826	3544	4582	-	244.40	327.80	410.40	619.30	-
AK3-1	4096	4096	4096	3848	4096	460.40	460.40	460.40	436.70	460.40
AK3-3	4202	4202	4366	4112	4202	469.30	469.30	493.60	472.90	469.30
AK3-5	4234	4070	4208	4386	4234	476.80	457.50	480.00	564.40	476.80
AK3-7	4046	4046	4046	4072	4046	447.50	447.50	447.50	505.10	447.50
AK3-8	4560	4456	4456	4568	4560	572.40	547.80	547.80	561.20	572.40
AK3-11	4536	4536	4536	5044	4536	534.00	534.00	534.00	646.50	534.00
AK5-1	4268	4202	4154	3946	4268	477.40	477.30	477.80	458.00	477.40
AK5-2	4276	4010	3984	3980	4276	529.20	474.70	471.40	506.50	529.20
AK5-3	4298	4086	4094	4320	4298	556.80	476.50	480.60	513.90	556.80
AK5-4	4242	4300	4268	4388	4242	552.50	508.30	528.00	527.20	552.50
AK5-6	4560	4844	4792	4584	4560	532.70	564.90	555.00	602.00	532.70
AK5-8	4392	4392	4428	4330	4392	523.60	523.60	528.80	533.00	523.60
AK5-9	4392	4366	4342	4172	4392	551.00	541.80	516.20	509.60	551.00

The docking score remains the same for all lysozyme-favipiravir-dye complexes (Table 3) and for the systems: AK3-1 + M/N, AK3-7 + N, AK5-4 + R; decreases in the systems: AK3-3 + N, AK3-5 + N/R, AK3-8 + M/N/R, AK3-11 + N, AK5-1 + N, AK5-2 + N/R, AK5-3 + M/N/R, AK5-4 + M/N, AK5-6 + M/N/R, AK5-8 + M/N/R, AK5-9 + M/N/R; and increases in the systems: AK3-1 + R, AK3-3 + M/R, AK3-5 + M, AK3-7 + M/R, AK3-11 + M/R, AK5-1 + M/R, AK5-2 + M. The dye-lysozyme affinity was found to follow the order: AK7-5 > AK-1-2-20 > AK7-6 > AK5-6 > AK-1-2-19 > AK-1-2-18 > AK5-8 > AK3-11 > AK5-9 > AK-1-2-17 > AK3-8 > AK5-3 > AK3-5 > AK5-4 > AK5-2 > AK5-1 > AK3-3 > AK3-7 > AK3-1, while the highest protein-cyanine interface area was observed in the case of AK-1-2-20, AK7-5, AK-1-2-19, AK7-6, AK5-6, AK3-11. The favipiravir do not exert influence on the dye-protein affinity and interface area in the cases of insulin and lysozyme (Table 4). The score remains the same for the complexes: AK3-1 + M/N, AK3-3 + M, AK3-7 + M/N, AK3-11 + M/N; decreases in the systems: AK3-1 + R, AK3-3 + R, AK3-5 + M/N, AK3-8 + M/N, AK5-1 + M/N/R, AK5-2 + M/N/R, AK-3 + M/N, AK5-8 + R, AK5-9 + M/N/R; and increases in the systems: AK3-3 + N, AK3-5 + R, AK3-7 + R, AK3-8 + R, AK3-11 + R, AK5-3 + R, AK5-4 + M/N/R, AK5-6 + M/N/R, AK5-8 + N. The dye-insulin affinity decreases in the order: AK-1-2-19 > AK-1-2-20 > AK7-6 > AK7-5 > AK5-6, AK3-8 > AK3-11 > AK5-8, AK5-9 > AK5-3 > AK5-2 > AK5-1 > AK5-4 > AK3-5 > AK3-3, AK-1-2-18 > AK3-1 > AK3-7 > AK-1-2-17, while the interface area follows the order: AK-1-2-19 > AK7-6 > AK-1-2-20 > AK7-5 > AK3-8 > AK5-3 > AK5-4 > AK5-9 > AK3-11 > AK5-6 > AK5-2 > AK5-8 > AK5-1 > AK3-5 > AK-1-2-18 > AK3-3 > AK3-1 > AK3-7 > AK-1-2-17. The crucial contribution of hydrophobic interactions in all examined dye-protein complexes was revealed by the PLIP analysis. The other types of interactions involved hydrogen bonds, salt and water bridges.

CONCLUSIONS

In conclusion, the present study was focused on the use of multiple ligand simultaneous docking technique to investigate the interactions between the four functionally significant proteins (cytochrome c, serum albumin, lysozyme

and insulin), four antiviral drugs (favipiravir, molnupiravir, nirmatrelvir and ritonavir) and the cyanine dyes (six trimethines and seven pentamethines). The comparison with ternary complexes from our previous work (that included four monomethines and two heptamethines) was conducted. The obtained results indicate that the dye-protein affinity seems to be not directly dependent on the polymethine chain length. The strongest complexes with the proteins were formed by the heptamethines (AK7-5, AK7-6), monomethines with CH₃O substitution (AK-1-2-20, AK-1-2-19), pentamethines with CH₂C₆H₆ and C₃H₄N substitution (AK5-6, AK5-8), trimethines with OC₂H₅ and CH₃ substitution (AK3-11, AK3-8). Among the examined proteins, the cyanine dyes showed the highest affinity binding to the albumin molecule, while the lowest values of the docking score were observed for insulin. The other results include: i) the cyanines and drugs occupy the different binding sites, except the lysozyme cavity that seems to be suitable for accommodation of both ligands (in the case of molnupiravir, nirmatrelvir and ritonavir); ii) the obtained complexes are predominantly stabilized by hydrophobic forces.

Overall, the most prospective drug delivery systems with the trimethines and pentamethines as visualizing agents are AK5-6-, AK5-8- and AK3-11-drug-albumin complexes, but, generally, the albumin-based nanosystems functionalized by the heptamethine cyanine dyes seem to be the most effective carriers for targeted delivery of the explored antiviral agents.

Acknowledgements

This work was supported by the Ministry of Education and Science of Ukraine (the project “Development of novel means of medical diagnostics by biomedical nanotechnologies and modern ultrasonic and fluorescence methods”).

ORCID IDs

- Olga Zhytniakivska, <https://orcid.org/0000-0002-2068-5823>; Uliana Tarabara, <https://orcid.org/0000-0002-7677-0779>
Kateryna Vus, <https://orcid.org/0000-0003-4738-4016>; Valeriya Trusova, <https://orcid.org/0000-0002-7087-071X>
Galyna Gorbenko, <https://orcid.org/0000-0002-0954-5053>

REFERENCES

- [1] Md. I. Khan, M.I. Hossain, M.K. Hossain, M.H.K. Rubel, K.M. Hossain, et al., ACS. Appl. Bio Mater. 5, 971 (2022). <https://doi.org/10.1021/acsabm.2c00002>
- [2] J. Wang, Y. Li, and G. Nie, Nat. Rev. Mat. 6, 766 (2021). <https://doi.org/10.1038/s41578-021-00315-x>
- [3] X. Sun, J. Wang, Z. Wang, C. Zhu, J. Xi, L. Fan, J. Han, and R. Guo, J. Colloid Interface Sci. 610, 89 (2022). <https://doi.org/10.1016/j.jcis.2021.11.189>
- [4] E. Nance, S.H. Pun, R. Saigal, and D.L. Sellers, 7, 31 (2022). <https://doi.org/10.1038/s41578-021-00394-w>
- [5] T.P. Crowe, and W.H. Hsu, Pharmaceutics, 14, 629 (2022). <https://doi.org/10.3390/pharmaceutics14030629>
- [6] A.S. Ali, M.G. Alrashedi, O.A.A. Ahmed, I.M. Ibrahim, Polymers, 14, 2616 (2022). <https://doi.org/10.3390/polym14132616>
- [7] N.B. Kiremitler, M.Z. Kemerli, and N. KAyaci, et al., ACS Appl. Nano Mater. 5, 6029 (2022). <https://doi.org/10.1021/acsanm.2c00181>
- [8] C. Medina-Montano, I. R. Berti, R. C. Gambaro, M.J. Limeres, M. Svensson, et al., Pharmaceutics, 14, 1611 (2022). <https://doi.org/10.3390/pharmaceutics14081611>
- [9] M. Ferreira, L.L. Chaves, S.A. Costa Lima, S. Reis, Int. J. Pharm. 492, 65 (2015). <https://doi.org/10.1016/j.ijpharm.2015.07.013>
- [10] Y. Deng, X. Zhang, H. Shen, Q. He, Z. Wu, W. Liao, and M. Yuan, Front. Bioeng. Biotechnol. 7, (2019). <https://doi.org/10.3389/fbioe.2019.00489>
- [11] T. Alam, M.A. Ansari, S. Baboota, and J. Ali, Drug Deliv. Transl. Res. 12, 577 (2022). <https://doi.org/10.1007/s13346-021-00958-x>
- [12] H. Zhang, T. Fan, W. Chen, Y. Li, and B. Wang, Bioactive Materials. 5, 1071 (2020). <https://doi.org/10.1016/j.bioactmat.2020.06.012>
- [13] A.L. Martínez-López, C. Pangua, C. Reboredo, R. Campión, J. Morales-Gracia, and J.M. Irache, Int. J. Pharm. 581, 119289 (2020). <https://doi.org/10.1016/j.ijpharm.2020.119289>
- [14] A.O. Elzoghby, W.M. Samy, and N.A. Elgindy, Journal of Controlled Release, 161, 38 (2012). <https://doi.org/10.1016/j.jconrel.2012.04.036>
- [15] E. Kianfar, J. Nanobiotechnol. 19, 159 (2021). <https://doi.org/10.1186/s12951-021-00896-3>
- [16] C. Wen, J. Zhang, H. Zhang, Y. Duan, Foods. 11, 1701 (2022). <https://doi.org/10.3390/foods11121701>
- [17] S. Lee, T.C. Pham, C. Bae, Y. Choi, Y.K. Kim, and J. Yoon, Coord. Chem. Rev. 412, 213258 (2020). <https://doi.org/10.1016/j.ccr.2020.213258>
- [18] L. Xu, S.-B. Wang, C. Xu, D. Han, X.-H. Ren, X.-Z. Zhang, and S.-X. Cheng, ACS Appl. Mater. Interfaces. 11, 38385 (2019). <https://doi.org/10.1021/acsami.9b11263>
- [19] Y. Wang, H. Iqbal, U. U.-Rehman, L. Zhai, Z. Yuan, A. Razzaq, M. Lv, et al., J. Drug Deliv. Sci. Technol. 79, 104072 (2023). <https://doi.org/10.1016/j.jddst.2022.104072>
- [20] O. Zhytniakivska, U.K. Vus, V. Trusova, and G. Gorbenko, East. European Journal of Physics, 3, 585 (2023). <https://doi.org/10.26565/2312-4334-2023-3-69>
- [21] E. Pettersen, T. Goddard, C. Huang, G. Couch, D. Greenblatt, E. Meng, and T. Ferrin, UCSF Chimera – a visualization system for exploratory research and analysis, J. Comput. Chem. 25, 1605–1612(2004). <https://doi.org/10.1002/jcc.20084>
- [22] P. Csizmadia, in: *Proceedings of ECSOC-3, the third international electronic conference on synthetic organic chemistry*, (1999), pp. 367-369. <https://doi.org/10.3390/ECSOC-3-01775>
- [23] M.D. Hanwell, D.E. Curtis, D.C. Lonie, T. Vandermeersch, E. Zurek, and G.R. Hutchison, J. Cheminform. 4, 17 (2012). <https://doi.org/10.1186/1758-2946-4-17>
- [24] D. Schneidman-Duhovny, Y. Inbar, R. Nussinov, and H.J. Wolfson, Nucl. Acids. Res. 33, W363 (2005). <https://doi.org/10.1093/nar/gki481>

- [25] M.F. Adasme, K.L. Linnemann, S.N. Bolz, F. Kaiser, S. Salentin, V.J. Haupt, and M. Schroeder, Nucl. Acids. Res. **49**, W530 (2021). <https://doi.org/10.1093/nar/gkab294>
- [26] E.F. Pettersen, T.D. Goddard, C.C. Huang, G.S. Couch, D.M. Greenblatt, E.C. Meng, and T.E. Ferrin, J. Comput. Chem. **25**, 1605 (2004). <https://doi.org/10.1002/jcc.20084>

ОДНОЧАСНИЙ ДОКИНГ ПРОТИВІРУСНИХ ПРЕПАРАТІВ ТА ЦІАНИНОВИХ БАРВНИКІВ З БІЛКАМИ З ВИКОРИСТАННЯМ МУЛЬТИЛІГАНДНОГО ПІДХОДУ

Ольга Житняківська, Уляна Тарабара, Катерина Вус, Валерія Трусова, Галина Горбенко

Кафедра медичної фізики та біомедичних нанотехнологій, Харківський національний університет імені В.Н. Каразіна м. Свободи 4, Харків, 61022, Україна

Наносистеми на основі білків для цільової доставки широкого спектру лікарських засобів, починаючи від невеликих ліків і терапевтичних білків до нуклеїнових кислот і генів, привертають все більшу увагу завдяки своїй біосумісності та здатності до біодеградації, надзвичайній здатності до зв'язування різних лігандів, доступності з природних джерел, ефективному захисту ліків і м'яким умовам інкапсуляції тощо. Завдяки численним центрам зв'язування та функціональним групам на поверхні білків, ці наносистеми є високоефективними багатофункціональними нанотераностичними системами, які можуть включати як терапевтичний препарат, так і візуалізуючий агент. Ця інтеграція служить багатьом цілям, включаючи регулювання вивільнення ліків, моніторинг змін у цільовій ділянці у відповідь на лікування та оцінку ефективності втручання на ранніх стадіях. Розробка цих передових наносистем другого покоління вимагає детального розуміння потенційних взаємодій у цих складних системах. У даній роботі ми оцінили потенціал шести триметинових та семи пентаметинових ціанінових барвників як потенційних візуалізуючих агентів в системах білок-лікарський препарат, що включали функціонально важливі білки (цитохром *c*, сироватковий альбумін, лізоцим та інсулін) та чотири противірусні препарати (фавіпіравір, молнупіравір, нірматрелвір і ритонавір). Для всіх груп досліджуваних ціанінових барвників визначені потрібні системи з найвищою комплементарністю форми поверхні барвник-білок, а також типи стабілізуючих взаємодій. Проведено оцінку впливу структури ціанінових барвників на стабільність комплексів лікарський препарат-білок-зонд. Отримані результати вказують на те, що спорідненість барвник-білок не залежить безпосередньо від довжини поліметинового ланцюга. Виявлено, що найбільш перспективними системами доставки ліків, що містять розглянуті триметини та пентаметини як візуалізуючі агенти, це комплекси АК5-6-, АК5-8- та АК3-11-ліки-альбумін.

Ключові слова: *комплекси білок-лікарський препарат-барвник; противірусні агенти; білкові наночастинки; наносистеми ліків; ціанінові барвники; одночасний молекулярний докінг*

NUMERICAL INVESTIGATION OF THERMOPHORESIS AND ACTIVATION ENERGY EFFECTS ON MAXWELL NANO FLUID OVER AN INCLINED MAGNETIC FIELD APPLIED TO A DISK

Dudekula Dastagiri Babu^{a*}, S. Venkateswarlu^a, E. Keshava Reddy^b

^a Department of Mathematics, Rajeev Gandhi Memorial College of Engineering and Technology, Nandyal-518501, Andhra Pradesh, India

^b Department of Mathematics, JNTUA College of Engineering, Ananthapuramu-515002, Andhra Pradesh, India

*Corresponding Author e-mail: dastagiri478@gmail.com

Received October 7, 2023; revised November 15, 2023; accepted November 17, 2023

Numerical model is conducted to investigate the behavior of an incompressible Maxwell nanofluid model flow on a convectively stretched surface, considering the effects of thermophoresis and an inclined magnetic field. The system, originally formulated as a set of partial differential equations, is transformed into a system of ordinary differential equations using similarity transformations. The resulting equations are solved using the Runge-Kutta-Fehlberg method in conjunction with the shooting technique. The obtained physical parameters from the derived system are presented and discussed through graphical representations. The numerical process is assessed by comparing the results with existing literature under various limiting scenarios, demonstrating a high level of proficiency. The key findings of this study indicate that the velocity field decreases as the fluid parameters increase, while the fluid temperature diminishes accordingly. Additionally, the heat transfer rate decreases with increasing fluid and thermophoresis parameters, but it increases with Biot and Prandtl numbers.

Keywords: MHD; Nano fluid; Maxwell fluid; Thermophoresis; Activation energy

PACS: 44.05.+e, 44.40.+a, 47.65.-d, 47.70.Fw

INTRODUCTION

Non-Newtonian fluid flow is fast growing field of interest due to its various applications in different fields of engineering (Rivlin and Ericksen [1]). Examples of these applications include hot rolling paper manufacturing, optical fiber production, plastic polymer processing, cosmetic procedures, and many others. In everyday life, numerous substances such as melts, soaps, apple sauce, soaps, emulsions, shampoos, and blood exhibit the properties of non-Newtonian fluids. Since there is no single constitutive relation that can accurately describe the behavior of such materials, researchers have proposed various models to study the characteristics of non-Newtonian fluids comprehensively. Therefore, different models have been developed in the forms of (i) differential-type, (ii) rate-type, and (iii) integral-type models (Hayat et al. [2]). The rate-type model takes into account the effects of relaxation and retardation times.

Among these models, the Maxwell model belongs to the rate-type category and specifically accounts for the impact of relaxation time, which cannot be captured by differential-type models. The Maxwell fluid model is particularly useful for analyzing polymers with low molecular weight. In a study conducted by Sudarmozhi et al. [3], it was demonstrated that the continuous flow of an MHD Maxwell viscoelastic fluid on a porous plate result in radiation and heat generation. Ibrahim et al. [4] investigated the mixed convection flow of a Maxwell nanofluid with the inclusion of Hall and ion-slip effects, employing the spectral relaxation method. Seshra et al. [5] focused on discussing the convection heat-mass transfer of a generalized Maxwell fluid, taking into account radiation effects, exponential heating, and chemical reactions using fractional Caputo-Fabrizio derivatives. Khan et al. [6] explored the flow of a Maxwell nanofluid over an infinitely tall vertical plate with ramped and isothermal wall temperature and concentration. Shateyi and Hillary [7] conducted a numerical analysis on the unsteady flow of a thermomagnetic reactive Maxwell nanofluid over a stretching or shrinking sheet, considering ohmic dissipation and Brownian motion. In their research, Jawad et al. [8] conducted an analytical study on the mixed convection flow of an MHD Maxwell nanofluid, considering variable thermal conductivity as well as Soret and Dufour effects. Reddy and Reddy [9] performed a comparative analysis of unsteady and steady flows of Buongiorno's Williamson nanoliquid over a wedge, $ShRe_r^{-1/2} = -\phi'(0)$; taking slip effects into account. Jamir and Konwar [10] investigated the effects of radiation absorption, Soret and Dufour effects, as well as slip condition and viscous dissipation on the unsteady MHD mixed convective flow past a vertical permeable plate. In separate studies, various authors [11, 12, 13, 14] explored the behavior of radioactive nanoparticles with exponential heat source and slip effects on an inclined permeable stretching surface. Additionally, authors [15, 16, 17] examined the heat and mass transfer of an MHD nanofluid with chemical reaction on a rotating disk under convective boundary conditions.

Heat transfer plays a crucial role in various industrial and consumer products. However, traditional working liquids like water, ethylene glycol, and oil exhibit low thermal conductivity, posing a significant challenge in improving heat transport within engineering systems. In contrast, metals possess higher thermal conductivities compared to liquids.

To overcome this limitation, the thermal performance of conventional working liquids has been improved by incorporating ultrafine nanoparticles into the base liquids. The goal of adding nanoparticles to liquids is to enhance the thermal properties of regular fluids. In their research, Huang et al. [18] focused on investigating the influence of the Prandtl number on free convection heat transfer from a vertical plate to a non-Newtonian fluid. Rahbari et al. [19] presented both analytical and numerical solutions for the heat transfer and MHD flow of a non-Newtonian Maxwell fluid through a parallel plate channel. Khan et al. [20] conducted an analysis of the flow of a non-Newtonian fluid past a stretching or shrinking permeable surface, considering heat and mass transfer effects. Liu and Liancun [22] examined the unsteady flow and heat transfer characteristics of a Maxwell nanofluid in a finite thin film, taking into account internal heat generation and thermophoresis. Arulmozhi et al. [22] provided an analysis of heat and mass transfer effects, including radioactive and chemical reactive effects, on MHD nanofluid flow over an infinite moving vertical plate. Vijay et al. [23] conducted a numerical investigation on the dynamics of stagnation point flow of a Maxwell nanofluid, considering combined heat and mass transfer effects.

Activation energy refers to the minimum energy required to initiate a chemical reaction. Once the reaction commences, the activation energy of the system becomes zero. The Arrhenius equation is commonly used to describe this relationship and is expressed as $K = B(T/T_\infty)^n \exp(-Ea/\kappa T)$. The activation energy for a specific reaction can be determined by analyzing the rate constant's variation with temperature using the Arrhenius equation. The concept of activation energy finds application in various fields, including geothermal engineering, chemical engineering, oil emulsions, and food processing. In their study, Zhang et al. [24] investigated the influence of activation energy and thermal radiation on bio-convection flow of rate-type nanoparticles around a stretching or shrinking disk. Bhatt et al. [25] examined the impact of activation energy on the movement of gyrotactic microorganisms in a magnetized nanofluid flowing past a porous plate. Gangadhar et al. [26] considered the effects of nonlinear radiation, viscous dissipation, and activation energy on a convective heat transfer in a Maxwell fluid. Dessie [27] explored the effects of chemical reaction, activation energy, and thermal energy on the flow of a magnetohydrodynamics (MHD) Maxwell fluid in a rotating frame. Saini et al. [28] studied the combined effects of activation energy and convective heat transfer on the radiative Williamson nanofluid flow over a radially stretching surface, taking into account Joule heating and viscous dissipation. Vaddemani et al. [29] investigated the effects of Hall current, activation energy, and diffusion thermo on the flow of an MHD Darcy-Forchheimer Casson nanofluid in the presence of Brownian motion and thermophoresis.

Upon reviewing the existing research, it is evident that no prior studies have explored the axi-symmetric flow of Maxwell fluid, combined with nanoparticles, over a radially stretched surface. Therefore, the main objective of this study is to investigate the impact of an aligned magnetic field and activation energy on Maxwell nanofluid. Additionally, the study will consider the passive control of nanoparticles at the surface. By conducting this analysis, a deeper understanding of the combined effects and potential control mechanisms can be obtained.

MATHEMATICAL FORMULATION

The flow being considered is a steady axi-symmetric two-dimensional (r, z) flow of a Maxwell liquid with nanoparticles induced by a sheet that is stretched radially. The flow occurs in the region where z is greater than or equal to 0, with a sheet velocity $u = u_w = ar$ in the radial direction and w in the z -direction. The parameter 'a' is a positive number. An aligned magnetic field with strength of B_0 is applied along the z -direction at an acute angle γ , as depicted in Figure 1. The effects of activation energy and chemical reaction are accounted for in mass transfer, while the convective temperature is denoted by T_f and the heat transport coefficient is h_f . Additionally, a zero-mass flux condition is enforced at the surface. Under these assumptions, the governing equations for the flow of Maxwell nanofluid are as follows:

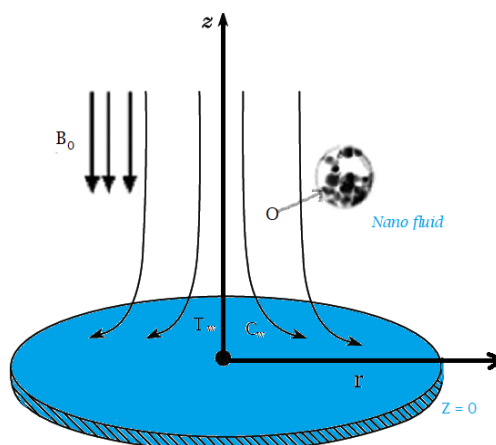


Figure 1. Schematic diagram of the problem

$$\frac{\partial u}{\partial r} + \frac{\partial w}{\partial z} + \frac{u}{r} = 0 \tag{1}$$

$$u \frac{\partial u}{\partial r} + w \frac{\partial u}{\partial z} = \nu \frac{\partial^2 u}{\partial z^2} - k_0 \left(u^2 \frac{\partial^2 u}{\partial r^2} + 2uw \frac{\partial^2 u}{\partial r \partial z} + w^2 \frac{\partial^2 u}{\partial z^2} \right) - \frac{\sigma B_0(r)}{\rho_f} u \sin^2 \gamma \tag{2}$$

$$u \frac{\partial T}{\partial r} + w \frac{\partial T}{\partial z} = \frac{k}{\rho c_p} \frac{\partial^2 T}{\partial z^2} + \tau D_B \frac{\partial T}{\partial z} \frac{\partial C}{\partial z} + \tau \frac{D_T}{T_\infty} \left[\frac{\partial T}{\partial z} \right]^2 \tag{3}$$

$$u \frac{\partial C}{\partial r} + w \frac{\partial C}{\partial z} = D_B \frac{\partial^2 C}{\partial z^2} + \frac{D_T}{T_\infty} \frac{\partial^2 T}{\partial z^2} - k_r^2 \{C - C_\infty\} \left(\frac{T}{T_\infty} \right)^n e^{\wedge} \left(\frac{-E_a}{kT} \right) \tag{4}$$

With boundary conditions

$$\left. \begin{aligned} u = u_w + L \frac{\partial u}{\partial z}; w = 0; D_B \frac{\partial C}{\partial z} + \left(\frac{D_B}{T_\infty} \right) \frac{\partial T}{\partial z} = 0; (-k) \frac{\partial T}{\partial z} = h_f (T_f - T) \text{ at } z = 0 \\ u = 0; T = T_\infty; C = C_\infty \text{ as } z \rightarrow \infty \end{aligned} \right\} \tag{5}$$

In the given context, (u, w) represents the velocity components in the radial (r) and axial (z) directions, respectively. σ signifies the electrical conductivity, α denotes the thermal diffusivity, k_0 represents the relaxation time of the fluid, ν signifies the kinematic viscosity, ρ denotes the density of the base fluid, D_T signifies the thermophoresis diffusion coefficient, D_B refers to the Brownian diffusion coefficient, and $\tau = \frac{(\rho c)_p}{(\rho c)_f}$ represents the ratio of nanoparticle heat capacity to the base fluid heat capacity.

To facilitate the analysis, we introduce the following similarity transformations:

$$\theta = \frac{T - T_\infty}{T_f - T_\infty}; \eta = \sqrt{\frac{a}{\nu}} z; \phi = \frac{C - C_\infty}{C_f - C_\infty}; u = a r f'(\eta); w = -2\sqrt{a\nu} f(\eta); \tag{6}$$

Through the utilization of Equation (6), the fulfillment of the equation of continuity requirement is achieved automatically. Furthermore, Equations (2)–(5) undergo a transformation into a system of ordinary differential equations (ODEs), accompanied by the imposition of suitable boundary conditions.

$$\frac{d^3 f}{d\eta^3} - \left(\frac{df}{d\eta} \right)^2 + 2f \left(\frac{d^2 f}{d\eta^2} \right) + \beta \left(4f \left(\frac{df}{d\eta} \right) \left(\frac{d^2 f}{d\eta^2} \right) - 4f^2 \frac{d^3 f}{d\eta^3} \right) - M \left(\frac{df}{d\eta} \right) \sin^2 \gamma = 0 \tag{7}$$

$$\frac{d^2 \theta}{d\eta^2} + 2Prf \frac{d\theta}{d\eta} + PrNb \frac{d\theta}{d\eta} \frac{d\phi}{d\eta} + PrNt \left(\frac{d\theta}{d\eta} \right)^2 = 0 \tag{8}$$

$$\frac{d^2 \phi}{d\eta^2} + 2Scf \frac{d\phi}{d\eta} + \left(\frac{Nt}{Nb} \right) \frac{d^2 \theta}{d\eta^2} - Sc\sigma (1 + \delta\theta)^n e^{\wedge} \left(\frac{-E}{1 + \delta\theta} \right) \phi = 0 \tag{9}$$

The corresponding boundary conditions are

$$\left. \begin{aligned} f(0) = 0; f'(0) = 1 + sf''; \theta(0) = 1 + \frac{\theta'(0)}{Bi}; Nt\theta' + Nb\phi' = 0 \text{ at } \eta = 0 \\ f' \rightarrow 0; \theta \rightarrow 0; \phi \rightarrow 0 \text{ as } \eta \rightarrow \infty \end{aligned} \right\} \tag{10}$$

In Equations (6)–(9), the key parameters are defined as follows:

$$M = \frac{\sigma B_0^2}{\rho_a}, \quad \beta = ak_0, \quad Pr = \frac{\nu}{\alpha}, \quad Sc = \frac{\nu}{D_B}, \quad Nt = \frac{\tau D_T}{\nu} \left(\frac{T_f - T_\infty}{T_\infty} \right), \quad Nb = \frac{\tau D_T}{\nu} (C_\infty), \quad Bi = \sqrt{\frac{\nu}{a}} \left(\frac{h_f}{k} \right), \quad \sigma = \frac{k_r^2}{\alpha},$$

$$\delta = \frac{(T_f - T_\infty)}{T_\infty}.$$

To quantify the skin friction coefficient, local Nusselt number, and Sherwood number, providing valuable insights into the flow characteristics, heat transfer, and mass transfer properties of the system, we can follow

$$C_f Re_r^{1/2} = (1 + \beta) f''(0); \quad Nu Re_r^{-1/2} = -\theta'(0);$$

Here $Re_r = \frac{U_w(r)r}{\nu}$ is the local Reynolds number.

METHODOLOGY

The initial step in the shooting scheme (Ali et al. [30]) involves obtaining numerical solutions by fixing the value of η_∞ . The shooting method aims to transform boundary conditions (BCs) into initial conditions (ICs) in order to obtain numerical solutions for the desired system. A detailed procedure outlining the entire process can be found in Table 1, while Fig. 2 provides a visual representation of the method.

Table 1. Mathematical steps for shooting technique

$f' = g_1, f'' = g_2, f''' = g_3, \theta = g_4, \theta' = g_5, \phi = g_6, \phi' = g_7$
$g_1' = g_2, g_2' = g_3, g_4' = g_5, g_6' = g_7$
g_3'
g_5'
g_7'

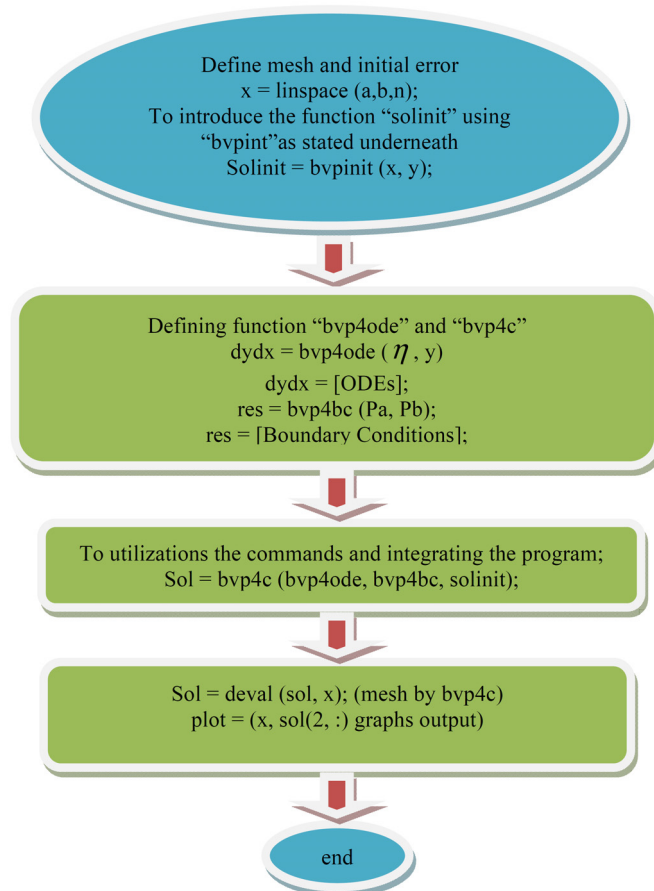


Figure 2. Solution chart via Matlab Procedure

For getting a clear view of the corporal problem, numerical calculations have been continued by the method explained in the preceding section for variety values of dissimilar parameters. For illustrations of the outcomes, numerical data are plotted in figures 3-19. To validate the present solution, comparison has been made with Xu and Eric [31] published data from the literature to $-f''(0)$ for various values of M when $\beta = 0$ in Table 2, and they are found to be in a favorable agreement.

Figures 3–5 depict the impact of parameter M on velocity, temperature, and concentration field. In Figure 3, as M enlarges, a noticeable decrease in velocity can be observed. This behavior is attributed to the rise in Lorentz force, a resistive force that opposes fluid flow. Consequently, the fluid velocity decreases, and the momentum layer becomes thinner. Figure 4 reveals that rising M leads to higher liquid temperatures, as the resistive force grows stronger. The effect of M on the concentration profile is shown in Figure 5, where it is evident that increasing M results in an incremental change in the profile.

Figures 6–8 illustrate the influence of the elasticity parameter β on velocity, temperature, and concentration field. These graphs reveal that an increase in β leads to a decrease in velocity and the associated momentum layer, while the opposite trend is observed for temperature and concentration distribution.

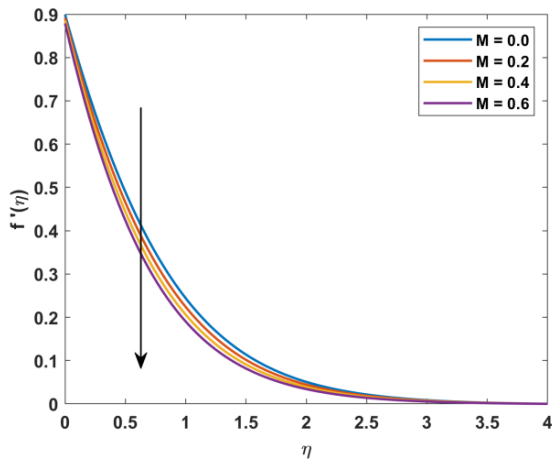


Figure 3. Impact $f'(\eta)$ on M

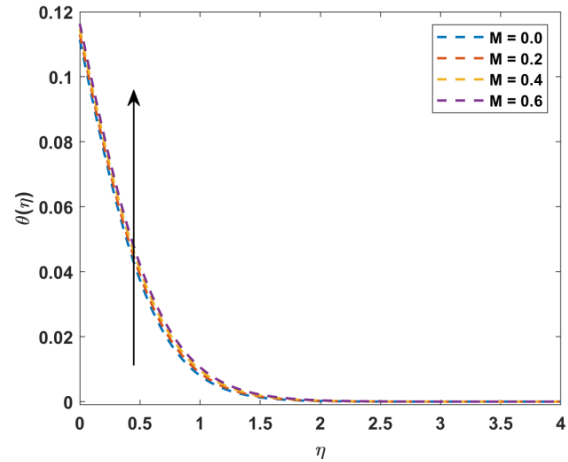


Figure 4. Impact $\theta(\eta)$ on M

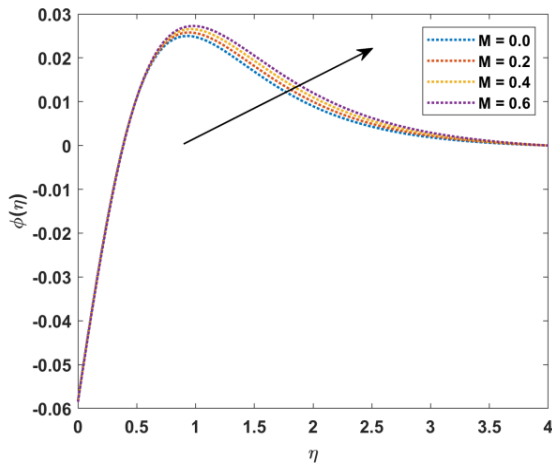


Figure 5. Impact $\phi(\eta)$ on M

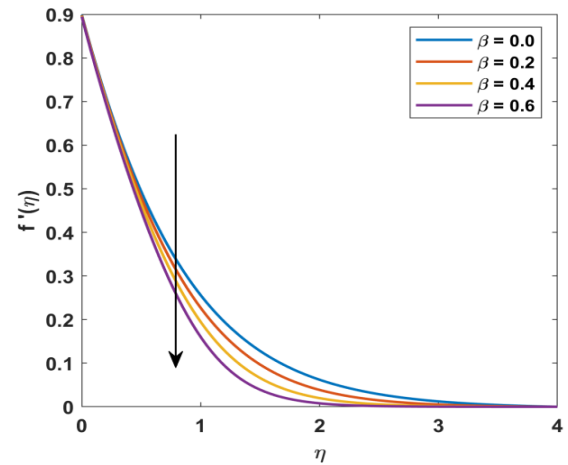


Figure 6. Impact $f'(\eta)$ on Beta

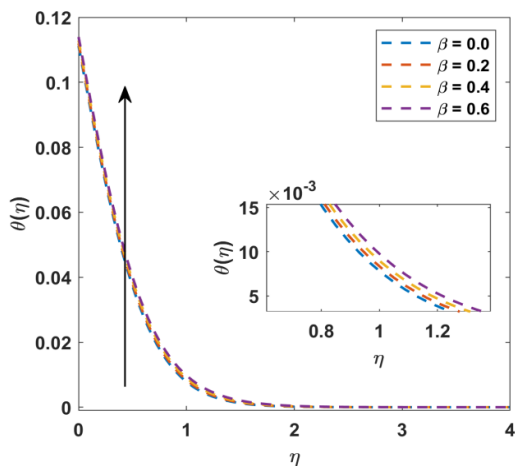


Figure 7. Impact $\theta(\eta)$ on Beta

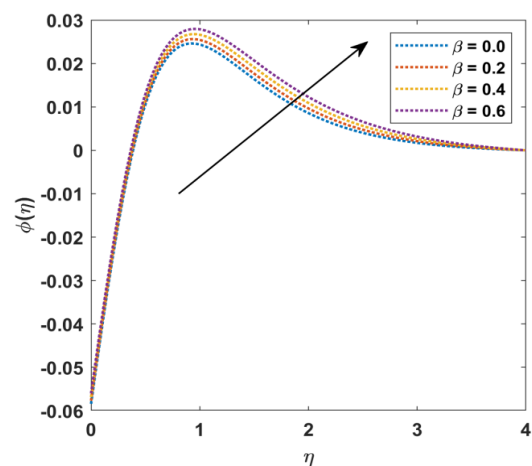


Figure 8. Impact $\phi(\eta)$ on Beta

The elasticity parameter β is related to the relaxation time, which represents the time required for the liquid to reach equilibrium after the application of stress. Smaller values of β result in liquid-like behavior, while larger values enhance liquid viscosity, causing a decline in velocity which is noticed in Figure 6. Moreover, for higher β values, the material exhibits solid-like characteristics. In Figure 7, it is evident that an increase in β leads to higher temperatures and a thicker corresponding layer over time. This behavior can be attributed to the influence of relaxation time, which becomes larger as β increases. Figure 8 clearly demonstrates that the concentration field increases as the magnetic number β rises.

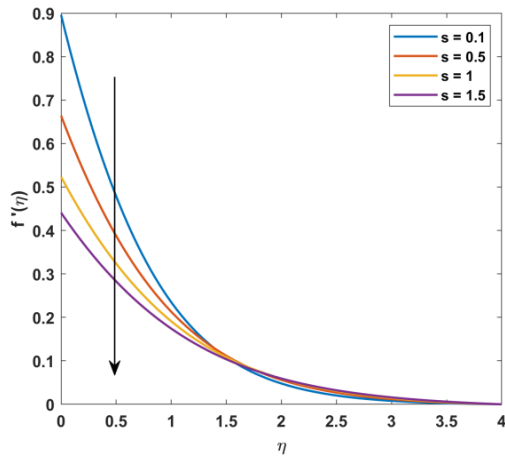


Figure 9. Impact $f'(\eta)$ on S

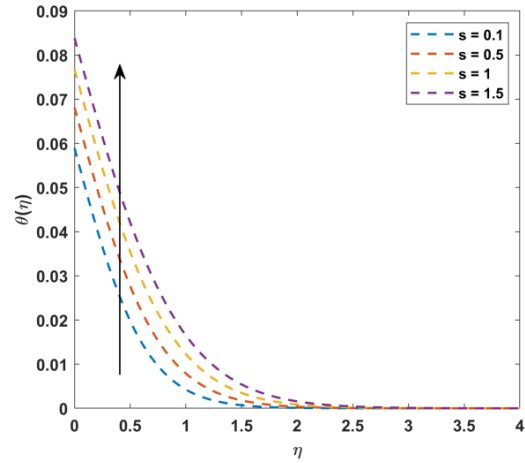


Figure 10. Impact $\theta(\eta)$ on S

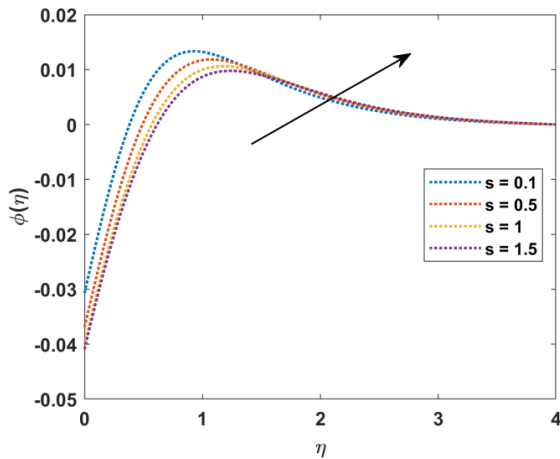


Figure 11. Impact $\phi(\eta)$ on S

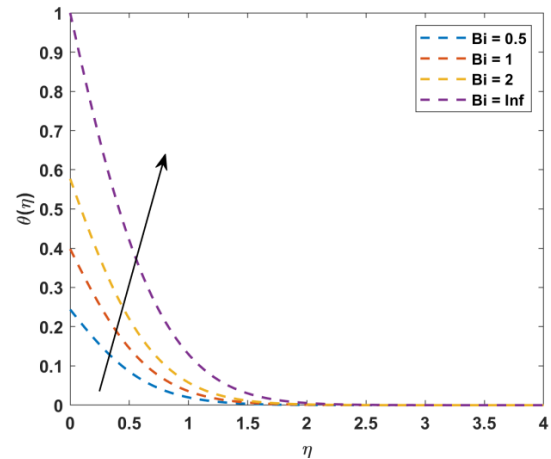


Figure 12. Impact $\theta(\eta)$ on Bi

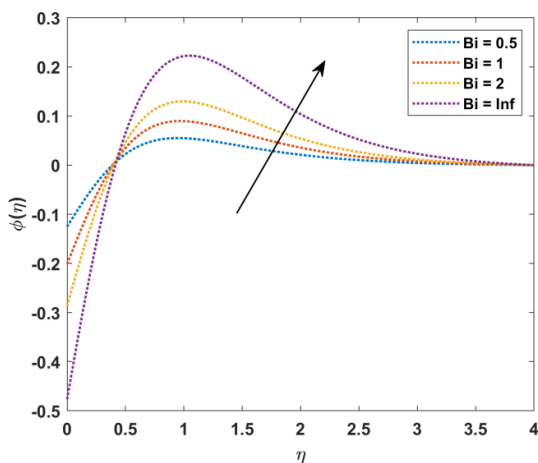


Figure 13. Impact $\phi(\eta)$ on Bi

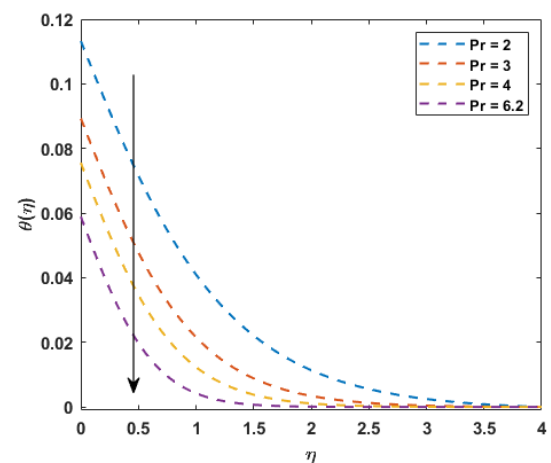


Figure 14. Impact $\theta(\eta)$ on Pr

Figures 9-11 demonstrate the influence of the velocity slip parameter (s) on the distributions of velocity, temperature, and concentration. An observed trend is a decline in the velocity profile as the s values increase. This is

because higher s values result in stretching effects partially penetrating the fluid, causing a decrease in velocity, and it is depicted in figure (9). Moreover, from figure (10), and figure (11), an increase in s values is observed to enhance both temperature and concentration profiles. When $s = 0$, the fluid adheres to the boundary and slides with no resistance $s \rightarrow \infty$. However, as s values increase, the movement of fluid particles decreases, leading to an increase in both temperature and concentration.

Figure 12 and 13 depicts the impact of the Biot number (Bi) on temperature (θ) and concentration (ϕ) profiles. It is evident from the figure that an increase in Bi leads to an enlargement of $\theta(\eta)$ as well as $\phi(\eta)$. Furthermore, it can be observed that an enhancement in the Biot number results in an increase in the heat transfer coefficient, which in turn contributes to an increment in $\theta(\eta)$.

Figures 14 and 15 are presented to analyze the influence of the Prandtl number (Pr) on $\theta(\eta)$, and $\phi(\eta)$, representing temperature and thermal layer thickness, respectively. In physical terms, Pr is inversely proportional to thermal conductivity. As a result, an increase in Pr leads to a weaker thermal diffusion. Consequently, both the temperature $\theta(\eta)$ and concentration $\phi(\eta)$ profiles decrease.

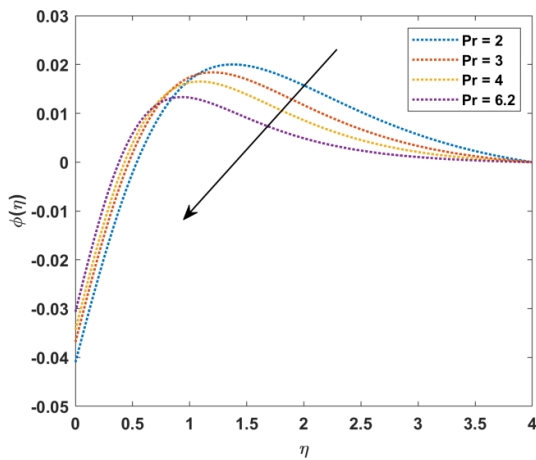


Figure 15. Impact $\phi(\eta)$ on Pr

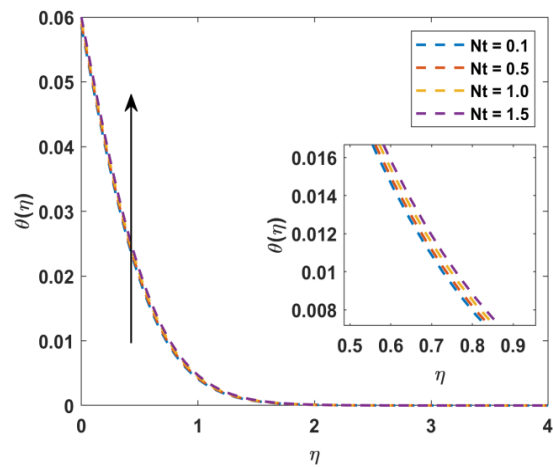


Figure 16. Impact $\theta(\eta)$ on Nt

Figures 16 and 17 illustrate the impact of thermophoresis (Nt) on nanofluid temperature and concentration fields. Both distributions show a similar trend, with an increase in Nt . However, in Figure 18, the opposite trend is observed for the augmentation of Nb the concentration distribution. Physically, as Nt increases, more nanoparticles are transported from the hotter surface to the colder region. This results in an increase in the temperature and concentration of the nanofluid. On the other hand, due to the random nature of Brownian motion, the concentration exhibits a decreasing tendency against Nb .

Figure 19 is plotted to observe the variation of $\phi(\eta)$ with respect to the activation energy (E). It can be observed that both $\phi(\eta)$ and its layer thickness increase as E values increase. Additionally, it was noticed that higher activation energy and less temperature decay result in a decrease in the reaction rate, leading to a decline in the chemical reaction mechanisms. As a result, the concentration of the Maxwell nanofluid increases.

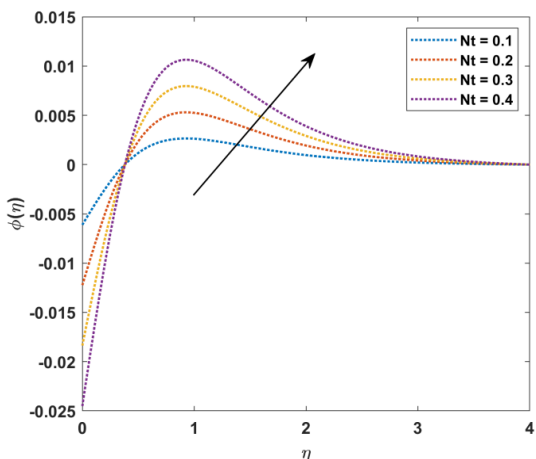


Figure 17. Impact $\phi(\eta)$ on Nt

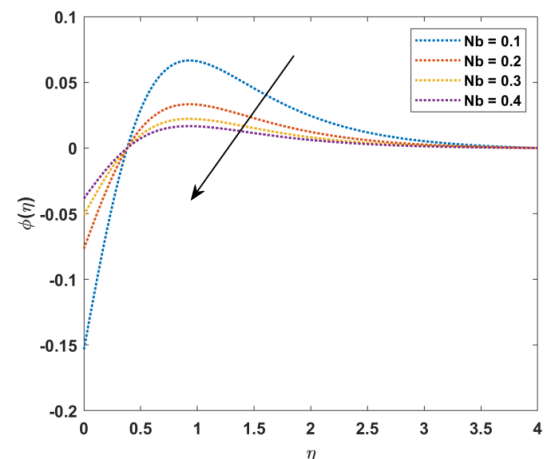


Figure 18. Impact $\theta(\eta)$ on Nb

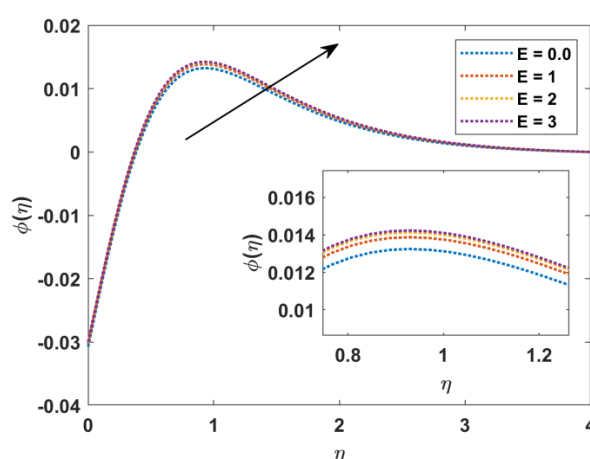


Figure 19. Impact on E

Table 2. Comparison of $-f''(0)$ for various values of M when $\beta = 0$.

M	Xu and Eric [31]	Present Results
1	1.41421	1.414032
5	2.4494	2.449456
10	3.3166	3.316624
50	7.1414	7.141424
100	10.0498	10.049896
500	22.38302	22.383032

CONCLUSION

The Maxwell's nanofluid model of incompressible, hydromagnetic flow is reduced using the Runge-Kutta-Fehlberg method with the shooting technique. This reduction is accomplished through the use of similarity variables. Additionally, the effects of inclined magnetic strength and thermophoresis are taken into account. The numerical analysis yields the following findings regarding the physical parameters:

- The momentum boundary layer decreases as the parameter β increases.
- An increase in the parameter M results in a decrease in the flow field $f(\eta)$, while an increase in the parameter γ elevates it.
- The parameters Sc and σ contribute to the reduction of the concentration curves, while an increase in the parameter M enhances the concentration field.
- The thermal field $\theta(\eta)$ and its associated boundary layer decrease with proper increments in the parameters Pr and γ . However, the opposite effect is observed when the parameters Bi and Nt are enhanced.
- The Sherwood number accelerates as the parameter β increases.
- The Nusselt number increases with the parameters Bi and Pr .

ORCID

©D. Dastagiri Babu, <https://orcid.org/0000-0001-8114-3860>; ©S. Venkateswarlu, <https://orcid.org/0009-0004-8224-374X>

©E. Keshava Reddy, <https://orcid.org/0000-0003-3880-0989>

REFERENCES

- [1] R.S. Rivlin, and J.L. Ericksen, "Stress-deformation relations for isotropic materials," *J. Rational Mech. Anal.* **4**, 323–425 (1955). <https://doi.org/10.1512/iumj.1955.4.54011>
- [2] T. Hayat, M. Mustafa, S. A. Shehzadand, and S. Obaidat, "Meltingheat transfer in the stagnation-point flow of an upper-convected Maxwell (UCM) fluid past a stretching sheet," *Int. J. Numer. Meth. Fl.*, **68**, 233–243 (2012). <https://doi.org/10.1002/flid.2503>
- [3] K. Sudarmozhi, D. Iranian, and Ilyas Khan, "A steady flow of MHD Maxwell viscoelastic fluid on a flat porous plate with the outcome of radiation and heat generation," *Frontiers in Physics*, **11**, (2023). <https://doi.org/10.3389/fphy.2023.1126662>
- [4] W. Ibrahim and T. Anbessa, "Mixed convection flow of a Maxwell nanofluid with Hall and ion-slip impacts employing the spectral relaxation method," *Heat Transfer*, **49**(5), 3094–3118 (2020). <https://doi.org/10.1002/htj.21764>
- [5] Sehra, H. Sadia, N. Gul, A. Zeb, and Z. A. Khan, "Convection heat–mass transfer of generalized Maxwell fluid with radiation effect, exponential heating, and chemical reaction using fractional Caputo–Fabrizio derivatives," *Open Physics*, **20**(1), 1250–1266 (2022). <https://doi.org/10.1515/phys-2022-0215>
- [6] N. Khan, F. Ali, M. Arif, Z. Ahmad, A. Aamina, and I. Khan, "Maxwell nanofluid flow over an infinite vertical plate with ramped and isothermal wall temperature and concentration," *Mathematical Problems in Engineering*, **2021**, 1–19 (2021). <https://doi.org/10.1155/2021/3536773>

- [7] S. Shateyi, and H. Muzara, "A numerical analysis on the unsteady flow of a thermomagnetic reactive Maxwell nanofluid over a stretching/shrinking sheet with ohmic dissipation and Brownian motion," *Fluids*, **7**(8), 252 (2022). <https://doi.org/10.3390/fluids7080252>
- [8] M. Jawad, A. Saeed, A. Khan, I. Ali, H. Alrabaiah, T. Gul, E. Bonyah, and M. Zubair, "Analytical study of MHD mixed convection flow for Maxwell nanofluid with variable thermal conductivity and Soret and Dufour effects," *AIP Advances*, **11**(3), (2021). <https://doi.org/10.1063/5.0029105>
- [9] R. Chandra Sekhar Reddy, and P. Sudarsana Reddy, "A comparative analysis of unsteady and steady Buongiorno's Williamson nanoliquid flow over a wedge with slip effects," *Chinese Journal of Chemical Engineering*, **28**(7), 1767-1777 (2020). <https://doi.org/10.1016/j.cjche.2020.04.016>
- [10] T. Jamir, and H. Konwar, "Effects of Radiation Absorption, Soret and Dufour on Unsteady MHD Mixed Convective Flow past a Vertical Permeable Plate with Slip Condition and Viscous Dissipation," *Journal of Heat and Mass Transfer Research*, **9**(2), 155-168 (2022). <https://doi.org/10.22075/jhmtr.2023.28693.1399>
- [11] T. Abbas, K. Al-Khaled, A.H. Raza, M. Ayadi, W. Chammam, and S.U. Khan, "Inclined Magnetized Flow of Radioactive Nanoparticles with Exponential Heat Source and Slip Effects: Keller Box Simulations," *Journal of Nanofluids*, **12**(2), 571-579 (2023). <https://doi.org/10.1166/jon.2023.1935>
- [12] S. Shah, S. M. Atif, and A. Kamran, "Radiation and slip effects on MHD Maxwell nanofluid flow over an inclined surface with chemical reaction," *Heat Transfer*, **50**(4), 4062-4085 (2021). <https://doi.org/10.1002/htj.22064>
- [13] A.B. Patil, V.S. Patil, P.P. Humane, N.S. Patil, and G.R. Rajput, "Thermally and chemically reacted MHD Maxwell nanofluid flow past an inclined permeable stretching surface," *Proceedings of the Institution of Mechanical Engineers, Part E: Journal of Process Mechanical Engineering*, **236**(3), 838-848 (2022). <https://doi.org/10.1177/09544089211050715>
- [14] B.K. Taid, and N. Ahmed, "MHD free convection flow across an inclined porous plate in the presence of heat source, Soret effect, and chemical reaction affected by viscous dissipation Ohmic heating," *Biointerface Research in Applied Chemistry*, **12**(5), 6280-6296 (2022). <https://doi.org/10.33263/BRIAC125.6280-6296>
- [15] S.M. Upadhyaya, R.L.V. Renuka Devi, C.S.K. Raju, and H.M. Ali, "Magneto hydrodynamic nonlinear thermal convection nanofluid flow over a radiated porous rotating disk with internal heating," *Journal of Thermal Analysis and Calorimetry*, **143**, 1973-1984 (2021). <https://doi.org/10.1007/s10973-020-09669-w>
- [16] M.S. Arif, Y. Nawaz, M. Bibi, and Z. Ali, "Mass Transfer of MHD Nanofluid in Presence of Chemical Reaction on A Permeable Rotating Disk with Convective Boundaries, Using Buongiorno's Model," *CMES-Computer Modeling in Engineering & Sciences*, **116**(1), (2018). <https://doi.org/10.31614/cmescs.2018.03834>
- [17] I. Ali, T. Gul, and A. Khan, "Unsteady Hydromagnetic Flow over an Inclined Rotating Disk through Neural Networking Approach. Mathematics," **11**(8), 1893 (2023). <https://doi.org/10.3390/math11081893>
- [18] M. Huang, J. Huang, Y. Chou, and C.O. Chen, "Effects of Prandtl number on free convection heat transfer from a vertical plate to a non-Newtonian fluid. *Journal of Heat Transfer*," *Transactions of the ASME Series C*, **111**(1), (1989). <https://doi.org/10.1115/1.3250645>
- [19] A. Rahbari, M. Abbasi, I. Rahimipetroudi, B. Sundén, D. DomiriGanji, and M. Gholami, "Heat transfer and MHD flow of non-Newtonian Maxwell fluid through a parallel plate channel: analytical and numerical solution," *Mechanical Sciences*, **9**(1), 61-70 (2018). <https://doi.org/10.5194/ms-9-61-2018>
- [20] S. Khan, M.M. Selim, A. Khan, A. Ullah, T. Abdeljawad, Ikramullah, M. Ayaz, and W. K. Mashwani, "On the analysis of the non-Newtonian fluid flow past a stretching/shrinking permeable surface with heat and mass transfer," *Coatings*, **11**(5), 566 (2021). <https://doi.org/10.3390/coatings11050566>
- [21] T. Liu, L. Lin, and L. Zheng, "Unsteady flow and heat transfer of Maxwell nanofluid in a finite thin film with internal heat generation and thermophoresis," *Thermal Science*, **22**(6 Part B), 2803-2813 (2018). <https://doi.org/10.2298/TSCI170129097L>
- [22] S. Arulmozhi, K. Sukkiramathi, S. S. Santra, R. Edwan, U. Fernandez-Gamiz, and S. Noeiaghdam, "Heat and mass transfer analysis of radiative and chemical reactive effects on MHD nanofluid over an infinite moving vertical plate," *Results in Engineering* **14**, 100394 (2022). <https://doi.org/10.1016/j.rineng.2022.100394>
- [23] N. Vijay, and K. Sharma, "Dynamics of stagnation point flow of Maxwell nanofluid with combined heat and mass transfer effects: A numerical investigation," *International Communications in Heat and Mass Transfer* **141**, 106545 (2023). <https://doi.org/10.1016/j.icheatmasstransfer.2022.106545>
- [24] T. Zhang, S. U. Khan, M. Imanan, I. Tlili, H. Waqas, N. Ali, "Activation energy and thermal radiation aspects in bioconvection flow of rate-type nanoparticles configured by a stretching/shrinking disk," *Journal of Energy Resources Technology*, **142**(11), 112102 (2020). <https://doi.org/10.1115/1.4047249>
- [25] M.M. Bhatti, A. Shahid, T. Abbas, S.Z. Alamri, and R. Ellahi, "Study of activation energy on the movement of gyrotactic microorganism in a magnetized nanofluids past a porous plate," *Processes*, **8**(3), 328, (2020). <https://doi.org/10.3390/pr8030328>
- [26] K. Gangadhar, D. Vijayakumar, and K. Thangavelu, "Nonlinear radiation on Maxwell fluid in a convective heat transfer with viscous dissipation and activation energy," *Heat Transfer*, **50**(7), 7363-7379 (2021). <https://doi.org/10.1002/htj.22233>
- [27] H. Dessie, "Effects of Chemical Reaction, Activation Energy and Thermal Energy on Magnetohydrodynamics Maxwell Fluid Flow in Rotating Frame," *Journal of Nanofluids*, **10**(1), 67-74 (2021). <https://doi.org/10.1166/jon.2021.1767>
- [28] S. K. Saini, R. Agrawal, and P. Kaswan, "Activation energy and convective heat transfer effects on the radiative Williamson nanofluid flow over a radially stretching surface containing Joule heating and viscous dissipation," *Numerical Heat Transfer, Part A: Applications*, 1-24 (2023). <https://doi.org/10.1080/10407782.2023.2226815>
- [29] V. Ramachandra Reddy, G. Sreedhar, and K. Raghunath, "Effects of Hall Current, Activation Energy and Diffusion Thermo of MHD Darcy-Forchheimer Casson Nanofluid Flow in the Presence of Brownian Motion and Thermophoresis," *Journal of Advanced Research in Fluid Mechanics and Thermal Sciences*, **105**(2), 129-145, (2023). <https://doi.org/10.37934/arfmts.105.2.129145>
- [30] M. Ali, M. Shahzad, F. Sultan, W.A. Khan, and S.Z.H. Shah, "Characteristic of heat transfer in flow of Cross nanofluid during melting process," *Applied Nanoscience*, **10**, 5201-5210, (2020). <https://doi.org/10.1007/s13204-020-01532-6>
- [31] L. Xu, and E.W.M. Lee, "Variational iteration method for the magnetohydrodynamic flow over a nonlinear stretching sheet," *Abstract and Applied Analysis, Hindawi*, **2013**, 1085-3375 (2013). <https://doi.org/10.1155/2013/573782>

ЧИСЕЛЬНЕ ДОСЛІДЖЕННЯ ЕФЕКТІВ ТЕРМОФОРЕЗУ ТА ЕНЕРГІЇ АКТИВАЦІЇ НАНОРІДИНИ МАКСВЕЛЛА НАД НАХИЛЕНИМ МАГНІТНИМ ПОЛЕМ, ПРИКЛАДЕНИМ ДО ДИСКА**Д. Дастагірі Бабу^а, С. Венкатесварлу^а, Е. Кешава Редді^б**^а *Кафедра математики, меморіальний коледж інженерії та технології Раджива Ганді,
Нандьял-518501, Андхра-Прадеш, Індія*^б *Факультет математики, інженерний коледж JNTUA,
Анантхапураму-515002, Андхра-Прадеш, Індія*

Розроблена числова модель для дослідження поведінки течії моделі нестисливої нанорідини Максвелла на конвективно розтягнутій поверхні з урахуванням ефектів термофорезу та похилого магнітного поля. Система, спочатку сформульована як набір рівнянь у частинних похідних, перетворюється на систему звичайних диференціальних рівнянь за допомогою перетворень подібності. Отримані рівняння розв'язуються за допомогою методу Рунге-Кутта-Фельберга в поєднанні з технікою стрільби. Отримані фізичні параметри похідної системи представлені та обговорені за допомогою графічних зображень. Чисельний процес оцінюється шляхом порівняння результатів з існуючою літературою за різними сценаріями обмеження, що демонструє високий рівень кваліфікації. Основні висновки цього дослідження вказують на те, що поле швидкості зменшується зі збільшенням параметрів рідини, тоді як температура рідини відповідно зменшується. Крім того, швидкість тепловіддачі зменшується зі збільшенням параметрів рідини та термофорезу, але зростає із збільшенням чисел Біо та Прандтля.

Ключові слова: МГД; нанорідина; рідина Максвелла; термофорез; енергія активації

AXIAL STRUCTURE OF GAS DISCHARGE SUSTAINED BY THE EIGEN DIPOLAR WAVE OF THE METAL WAVEGUIDE WITH VARYING RADIUS FILLED BY MAGNETIZED NONUNIFORM PLASMA

 Volodymyr Olefir^{a,b*},  Oleksandr Sporov^a,  Mykola Azarenkov^{a,b}

^a V.N. Karazin Kharkiv National University, 4, Svobody Sq., Kharkiv, 61022, Ukraine

^b National Science Center “Kharkiv Institute of Physics and Technology”, 1, Akademychna St., Kharkiv, 61108, Ukraine

*Corresponding Author e-mail: vpolefir@gmail.com

Received September 30, 2023; revised November 10, 2023; accepted November 22, 2023

The article presents the results of the theoretical study of the plasma density axial distribution in a stationary gas discharge sustained by the eigen dipolar wave that propagates in a long cylindrical plasma-metal structure. The discharge structure consists of a column of magnetized non-uniform plasma placed in the metal waveguide of variable radius. The study of the gas discharge is carried out within the framework of the electrodynamic model, in which the main attention is paid to the electrodynamic part of the model. To describe the processes that take place in plasma, the model equations are used. The influence of the metal waveguide inhomogeneity along the structure and the plasma density radial non-uniformity on the phase characteristics of the dipolar wave, its spatial attenuation, the field components radial distribution, the axial distribution of the plasma density sustained by this mode are determined. It is also analysed the condition for the discharge stability and find the regions, where dipolar mode can sustain the stable discharge. The obtained results can be useful for various technological applications.

Keywords: Gas discharge; Plasma-metal waveguide; Dipolar eigen wave; Phase and attenuation properties; Zakrzewski criterion

PACS: 52.35-g, 52.50.Dg

1. INTRODUCTION

Till now microwave gas discharge in stationary regime that is sustained by the eigen electromagnetic wave of the discharge structure is used as the effective plasma sources in different technological applications [1, 2, 3]. One of the important property of such discharges that take place in cylindrical structures and sustained by the waves with azimuthal wave numbers $m = 0, \pm 1, \pm 2$ is good uniformity of plasma density axial distribution [1, 2, 4]. Theoretical modeling of plasma density axial distribution of the eigen wave sustained discharges and the study of the stability conditions of such discharges, was carried out within the framework of the electrodynamic approach [2], which shows a good agreement with the experimental data [1]. One of the characteristic feature of this approach is the detailed study of the electrodynamic characteristics of the eigenwaves of the discharge structure, such as the dispersion (phase) properties, the spatial attenuation coefficient, and the wave field spatial structure. According to this approach plasma is described with rather simple model equations. Such model approach is simple but allow us to take into account the elementary processes occurring in plasma in proper manner, that relates, among other things, with the wave energy transfer to plasma in the diffusion and recombination gas discharge regimes [2, 5]. The number of articles were devoted to the study of the plasma density axial distribution in the stationary microwave discharges that take place in cylindrical plasma-metal structures with the fixed radius of metal enclosure [1, 6]. Besides it was shown that variable radius of the metal wall of plasma – metal cylindrical discharge structure can be used as one of the mechanism to control the plasma density value and its axial distribution in such discharges [7]. The work [8] was devoted to the study of plasma density axial distribution in the discharges, that are sustained by the eigen waves of such discharge structure taking into account the approximation of plasma density radial uniformity. The involving of a plasma density radial density nonuniformity to the model leads to more accurate description of the plasma density axial distribution in the discharge. Let emphasize that long gas discharges can be sustained not only by symmetric ($m = 0$), but also by the dipolar ($m = \pm 1$), eigen wave what significantly affect as the plasma density axial profile, as the stability region of such discharge. The experiments have shown that the use of eigen dipole ($m = \pm 1$) waves give the possibility to obtain somewhat smaller plasma density values, but axial uniformity of plasma density profile is much better as compared with the discharges sustained by the symmetric wave [1, 2].

Previously, the study of the plasma density radial distribution for the discharges sustained by the symmetric ($m = 0$) mode was carried out in the work [9] with taking into account the radial inhomogeneity of the plasma density and changes in the radius of the metal waveguide along the discharge. The influence of the variable radius

of the waveguide metal enclosure and the kind of plasma density radial profile on the dispersion properties, the attenuation coefficient and radial field structure of the eigen dipole ($m = \pm 1$) wave that sustains the discharge was studied in [10]. The aim of this work is to study the influence of the variable radius of the waveguide metal enclosure and the kind of plasma density radial profile on axial structure of the discharge sustained by the eigen dipole ($m = \pm 1$) waves of the discharge structure.

2. TASK SETTINGS

Let us study the plasma density axial distribution in a long cylindrical discharge structure that consists of non-uniform magnetized plasma column with radius R_p that surrounds by metal enclosure of radius $R_m > R_p$. The thin dielectric tube that separates plasma region from metal enclosure is not presented in this model. It is supposed that it's influence on wave phase and attenuation properties is not very strong [11]. Plasma region is separated from the waveguide metal wall by the vacuum (air) region with thickness $(R_m - R_p)$. The metal enclosure is supposed to be slightly varying in the axial direction. The studied discharge is sustained by the eigen dipolar ($m = \pm 1$) wave of this discharge structure that propagates along the discharge. External steady magnetic field \vec{B}_0 is directed along the axis of waveguide structure.

Plasma is described according to the hydrodynamic approach as cold and weakly absorbing media. The wave while propagating along the discharge damps due to the collisions in plasma. These collisions are characterized by the effective electron collision rate ν . The collision rate is supposed to be small as compared with wave frequency ω . It is also supposed that plasma density is non-uniform not only is axial, but also in radial directions. In the gas discharge model the plasma density radial distribution $n(r)$ models by the Bessel-like profile of the form $n(r) = n(0)J_0(\mu r)$, where $n(0)$ is plasma density at the axis of the plasma column ($r = 0$), J_0 is the Bessel function of the first kind and μ is the plasma density non-uniformity parameter. It's value can vary from $\mu = 0$ for the case of radial uniform plasma up to the $\mu = 2.405$ for the case of strong radially non-uniform plasma that corresponds to the discharge in the ambipolar diffusion regime. Such choice of plasma density radial profile give the possibility to model different gas discharge regimes [1, 9]. A detailed description of the procedure for deriving the electrodynamic equations is given in the previous work [1, 9]. Here we present the results that are important for the current study.

The dipolar wave (azimuth wave number $m = \pm 1$) propagates along the axis of the structure in the direction of the external magnetic field \vec{B}_0 . It was supposed that wave damps slightly while propagates along the discharge and sustains plasma column. So, as wave field, as plasma density also slightly varies in along the discharge on the distances of wavelength order. Thus, the solutions of the Maxwell equations system that governs the wave propagation along the discharge structure can be found according to the WKB approach [12]:

$$E, H_{r,\varphi,z}(r, \varphi, z) = E, H(r, z) \exp \left(-i\omega t + im\varphi + \int_{z_0}^z k_3(z') dz' \right), \quad (1)$$

here r, φ, z are coordinates in cylindrical coordinate system, k_3 is the axial wavenumber, E and H are the amplitudes of the electric and the magnetic wave field components, respectively. Let us suppose that changing any quantity A value, that varies in the axial direction, along the discharge at the distances of the wavelength order is small compared to the magnitude of this quantity ($(A^{-1}(\partial A/\partial z) \ll k_3)$, where symbol A denotes E, H, k_3 , or n). Thus, in all further equations all terms of order $O(k_3^{-1}(\partial \ln(A)/\partial z))$ are neglected [12].

Taking in to the account the expression (1) the equations for radial wave components in plasma region ($r < R_p$) can be obtained from the system of Maxwell equations [11] and can be written as:

$$\begin{cases} H_r^p(r) &= -\frac{m}{\kappa r} E_z^p(r) - \frac{k_3}{k} E_\varphi^p(r), \\ E_r^p(r) &= \frac{k_3 H_\varphi^p(r)}{k \varepsilon_1(r)} - \frac{m H_z^p(r)}{k r \varepsilon_1(r)} - \frac{i \varepsilon_2(r) E_\varphi^p(r)}{\varepsilon_1(r)}. \end{cases} \quad (2)$$

In the approximation of slight axial varying of the plasma density the system of ordinary differential equations for tangential wave field components in plasma region ($r < R_p$) can be written as:

$$\begin{cases} \frac{dE_z^p(r)}{dr} &= \frac{k_3 \varepsilon_2(r)}{\varepsilon_1(r)} E_\varphi^p(r) + i \frac{k_3^2 - k^2 \varepsilon_1(r)}{k \varepsilon_1(r)} H_\varphi^p(r) - i \frac{m k_3}{k r \varepsilon_1(r)} H_z^p(r), \\ \frac{dE_\varphi^p(r)}{dr} &= \left(\frac{m \varepsilon_2(r)}{r \varepsilon_1(r)} - \frac{1}{r} \right) H_\varphi^p(r) + ik \left(1 - \frac{m^2}{k^2 r^2 \varepsilon_1(r)} \right) H_\varphi(r) + i \frac{m k_3}{k r \varepsilon_1(r)} H_\varphi^p(r), \\ \frac{dH_z^p(r)}{dr} &= \frac{k_3 \varepsilon_2(r)}{\varepsilon_1(r)} H_\varphi(r) - i \frac{p(r)}{k r \varepsilon_1(r)} E_\varphi^p(r) + i \frac{m k_3}{k r} E_z^p(r) - \frac{m \varepsilon_2(r)}{r \varepsilon_1(r)} H_z^p(r), \\ \frac{dH_\varphi^p(r)}{dr} &= -\frac{1}{r} H_\varphi^p(r) - i \frac{m k_3}{k r} E_\varphi^p(r) + i \frac{m k_3}{k r} E_\varphi^p(r) + ik \left(\frac{m^2}{k^2 r^2} - \varepsilon_3(r) \right) E_z^p(r), \end{cases} \quad (3)$$

where $p(r) = \varepsilon_1(r)(k_3^2 - k^2\varepsilon_1(r)) + k^2\varepsilon_2^2(r)$, $\varepsilon_{1,2,3}$ are the components of the dielectric tensor cold collisional plasma [11].

It is possible to obtain analytic solutions for the wave field components in the vacuum region ($R_p < r < R_m$):

$$\begin{cases} E_z(r) = A_1 I_m(\kappa r) + A_2 K_m(\kappa r), \\ E_\varphi(r) = \frac{mk_3 A_1 I_m(\kappa r)}{\kappa^2 r} + \frac{mk_3 A_2 K_m(\kappa r)}{\kappa^2 r} + \frac{ik A_3 I'_m(\kappa r)}{\kappa} + \frac{imk A_4 K'_m}{\kappa^2 r}, \\ E_r(r) = -\frac{ik_3 A_1 I'_m(\kappa r)}{\kappa} - \frac{imk_3 A_2 K'_m(\kappa r)}{\kappa r} + \frac{mk A_3 I_m(\kappa r)}{\kappa^2 r} + \frac{mk A_4 K_m(\kappa r)}{\kappa^2 r}, \\ H_z(r) = A_3 I_m(\kappa r) + A_4 K_m(\kappa r), \\ H_\varphi(r) = -\frac{ik A_1 I'_m(\kappa r)}{\kappa} - \frac{imk A_2 K'_m(\kappa r)}{\kappa} + \frac{mk_3 A_3 I_m(\kappa r)}{\kappa^2 r} + \frac{mk_3 A_4 K_m(\kappa r)}{\kappa^2 r}, \\ H_r(r) = -\frac{mk A_1 I_m(\kappa r)}{\kappa^2 r} - \frac{mk A_2 K_m(\kappa r)}{\kappa^2 r} - \frac{ik_3 A_3 I'_m(\kappa r)}{\kappa} + \frac{imk_3 A_4 K'_m(\kappa r)}{\kappa}. \end{cases} \tag{4}$$

The expressions for A_{1-4} can be obtained from the boundary conditions at the plasma-vacuum interface (3), that consists of the continuity of tangential electric and magnetic wave field components when $r = R_p$:

$$\begin{cases} A_1 = \kappa R_p K'_m(\kappa R_p) E_z^P(R_p) - i \frac{mk_3 K_m(\kappa R_p)}{k} H_z^P(R_p) + i \frac{\kappa^2 R_p K_m(\kappa R_p)}{k} H_\varphi^P(R_p), \\ A_2 = \kappa R_p I'_m(\kappa R_p) E_z^P(R_p) - i \frac{mk_3 I_m(\kappa R_p)}{k} H_z^P(R_p) - i \frac{\kappa^2 R_p I_m(\kappa R_p)}{k} H_\varphi^P(R_p), \\ A_3 = -\kappa R_p K'_m(\kappa R_p) H_z^P(R_p) + i \frac{mk_3 K_m(\kappa R_p)}{k} E_z^P(R_p) - i \frac{\kappa^2 R_p K_m(\kappa R_p)}{k} E_\varphi^P(R_p), \\ A_4 = \kappa R_p I'_m(\kappa R_p) H_z^P(R_p) - i \frac{mk_3 I_m(\kappa R_p)}{k} H_z^P(R_p) - i \frac{\kappa^2 R_p I_m(\kappa R_p)}{k} E_\varphi^P(R_p), \end{cases} \tag{5}$$

here the quantities $E_z^P(R_p)$, $E_\varphi^P(R_p)$, $H_z^P(R_p)$, $E_\varphi^P(R_p)$ are the appropriate electric and magnetic wave field components in plasma at plasma - vacuum interface $r = R_p$. These components are obtained by the numeric solution of the system of ordinary differential equations (3).

The vanishing of the tangential electric wave field components at the waveguide metal wall ($E_z(R_m) = 0$, $E_\varphi(R_m) = 0$) gives the following system that can be treated as local dispersion equation:

$$\begin{cases} A_1 I_m(\kappa R_m) + A_2 K_m(\kappa R_m) = 0, \\ A_3 I'_m(\kappa R_m) + A_4 K'_m(\kappa R_m) = 0. \end{cases} \tag{6}$$

The solution of the ordinary dispersion equation gives the relationship between the frequency ω of the eigenwave of the structure and its axial wave number k_3 . When the analogue of the dispersion equation (so called phase equation) (6) is studied for the discharge modelling it is necessary to mention that the wave frequency ω is fixed and its value is set externally by the wave generator. This equation connects the local plasma density value $n(z)$ and the axial wave number k_3 . The eigen wave propagates along the structure and sustains the discharge, the plasma density changes in axial direction, the wave frequency remains unchanged, while the complex value of the axial wave number also changes along the discharge. The real part of the normalized wave number $x = \text{Re}(k_3)R_p$ determines the wavelength, and its imaginary part $\alpha(n) = \text{Im}(k_3)R_p$ determines the spatial attenuation coefficient of the wave in the direction of its propagation. The dependence $\alpha(n)$ can be used to determine the density axial gradient dn/dz for the discharges in the diffusion controlled regime from the relation [2, 5, 6].

According to article [2, 5, 6, 4], the dependence $\alpha(n)$ can be used to determine the axial gradient of plasma density dn/dz in discharges in the diffusion mode, using the following ratio:

$$\frac{dn}{dz} = -\frac{2n\alpha}{1 - \frac{n}{\alpha} \frac{d\alpha}{dn}}. \tag{7}$$

When studying the axial distribution of plasma density, it is important to control the conditions of gas discharge stability for the diffusion control regime. Such criterion was presented in one of the previous works [6]:

$$\frac{n}{\alpha} \frac{d\alpha}{dn} < 1. \tag{8}$$

It is necessary to check this Zakrzewski stability criterion because there are possible the situations when the eigen wave has energy to sustain the discharge, but stability criterion is not fulfilled and the end of the discharge is determined by the determined by the ending of the stability region [6, 2].

3. BASIC RESULTS

The main aim of this work is to study the influence of the plasma density radial non-uniformity and the slight axial variation of the waveguide metal wall radius on the plasma density axial distribution in the discharge sustained by the eigen dipolar wave of the discharge structure. In the early work [6] it was noted that the dispersion properties and spatial attenuation of the eigenwaves of the discharge structure strongly determine both the axial distribution of the plasma density and the conditions for the stability of the discharge. So, the first step in the research is the study the phase properties and the spatial attenuation of the eigen wave considered [1, 2, 5, 8, 6, 9, 10]. The results of this step will help us to go to the next two steps: to determine the region of the stability according to the Zakrzewski stability criterion (8) and to choose appropriate parameters for axial plasma density profile calculation (7).

The dispersion equation (6) was solved with the help of numerical methods by introducing the following dimensionless parameters: normalized wave frequency $\tilde{\omega} = \omega/\omega_p$ and the complex normalized axial wavevector $k_3 R_p$, the real part of which $x = \text{Re}(k_3)R_p$ determines wavelength, and the imaginary part $\alpha = \text{Im}(k_3)R_p$ determines the normalized wave attenuation coefficient. The influence of the external magnetic field value on the attenuation coefficient α and the normalized wave frequency $\tilde{\omega}$ is taken into account by introducing the dimensionless parameter $\Omega = \omega_{Ce}/\omega$ (ω_{Ce} is the electron cyclotron frequency). The geometrical parameters of discharge structure is introduced into the model throw dimensionless plasma column radius $\sigma = R_p\omega/c$ and the dimensionless radius of the waveguide metal enclosure $\eta = R_m/R_p$. Such normalized parameters are very convenient for gas discharge modeling, where wave frequency ω is fixed but plasma density n varies along the discharge length. Thus let us determine such values of the parameters of the discharge structure for further gas discharge axial structure investigation that give good axial uniformity and large area of stability.

The Figure 1 presents the influence of the normalized effective collision plasma electron frequency ν/ω on the phase characteristics $\tilde{\omega}$ (Figure 1a) and spatial attenuation α (Figure 1b) of the $m = +1$ mode for the case of radially uniform plasma. The parameters of the discharge structure were chosen to be equal: normalized plasma radius $\sigma = 0.8$, normalized external magnetic field $\Omega = 0.2$. At a fixed frequency of the generator ω , an increase in the frequency of collisions of electrons ν in the range from 0.001 up to 0.1 practically does not affect the normalized frequency of the wave $\tilde{\omega} = \omega/\omega_p$. A further increase of ν/ω from 0.1 to 0.4 leads to a slight decrease in $\tilde{\omega}$ in the range of axial wavenumbers $x \leq 0.6$. The increasing of the normalize collisions frequency leads to a significant increase in the spatial attenuation of the $m = +1$ mode in the entire range of axial numbers both in the region of sufficiently small x and, especially, in the region of $x \geq 3.0$ (Figure 1b). As a result, for each studied value of ν/ω the dependence $\alpha(x)$ possesses some minimum value for some value of x .

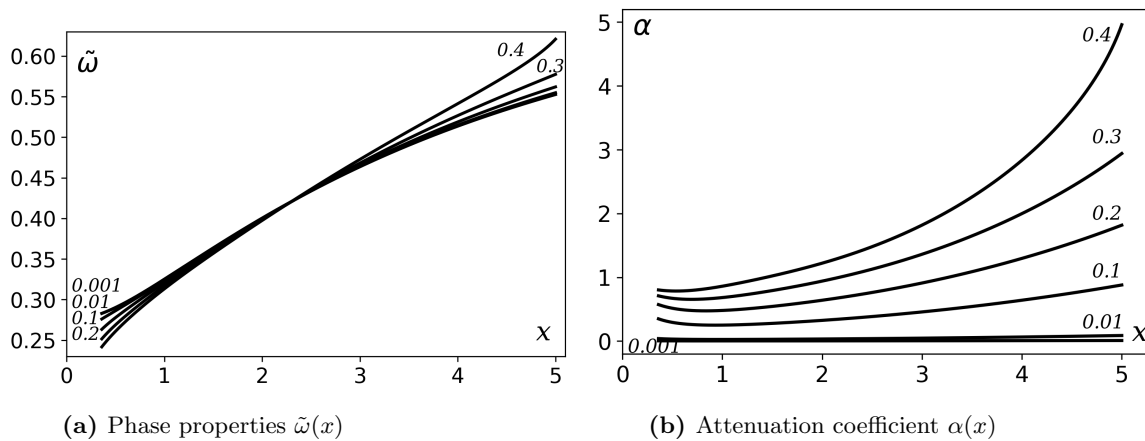


Figure 1. The dependence of the dimensionless phase and attenuation properties of the $m = +1$ mode via the dimensionless wavenumber x for different parameter ν/ω values. The numbers near the curves are the parameter ν/ω values. Other parameters are equal: $\Omega = 0.2$, $\sigma = 0.3$, $\eta = 1.1$, $\mu = 0.0$

The influence of the normalized collision frequency ν/ω on the phase properties $\tilde{\omega}$ (Figure 2a) and spatial attenuation α (Figure 2b) of the eigen dipolar $m = -1$ mode of the discharge structure under the same parameter set as for the Figure 1 is presented in the Figure 2. Let us note that the dimensionless collision frequency ν has a much smaller influence on the phase properties of the $m = -1$ eigen mode (Figure 2a) than on the $m = +1$ eigen mode (1a). At the same time, an increase in the dimensionless collision frequency ν/ω in the specified range (from 0.01 up to 0.1) leads to a significant increase in the spatial attenuation of the $m = -1$ mode in the entire range of x axial numbers (Figure 2b).

The influence of the normalized radius of the waveguide metal wall η on the phase properties $\tilde{\omega}$ and spatial attenuation coefficient α for the discharge structure with constant radius of metal enclosure for the $m = +1$ eigen

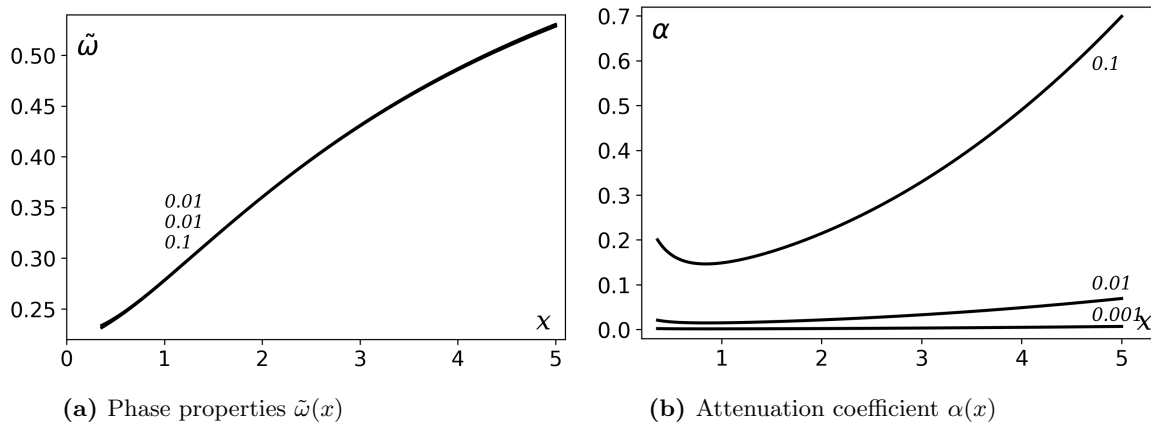


Figure 2. The dependence of the dimensionless phase and attenuation properties of the $m = -1$ mode via the dimensionless wavenumber x for different parameter ν/ω values. Problem parameters and curve numbering are the same as for the Figure 1

mode is presented in the Figure 3. The parameters of the calculations were chosen to be equal $\Omega = 0.2$, $\sigma = 0.3$, $\nu = 0.001$, $\mu = 0.0$. The modelling shows that the increase of the vacuum gap size between the plasma column and the waveguide metal due to parameter η variation in the following interval of values $\eta \geq 1.1$ and $\eta \leq 1.8$ leads to the increase of the normalized wave frequency $\tilde{\omega}$ in the entire range of axial wavenumbers x , especially in the region when $x \leq 2$. A further increase of the parameter η up to $\eta \geq 1.3$ values leads to a weakening of the parameter η influence on the phase characteristics of the dipole mode $m = +1$. The Figure 3b presents the influence of the normalized radius of the waveguide metal wall η on the spatial attenuation coefficient α for the $m = +1$ mode. The increase of the parameter η leads to the increase of the coefficient α , especially in the wavenumber region $x \geq 3$ for the following range of parameter $\eta \geq 1.4$. It is necessary to mention the presence of the small region where the attenuation coefficient α growth when wavenumber x decrease in the region of small axial wavenumber values $x < 0.7$.

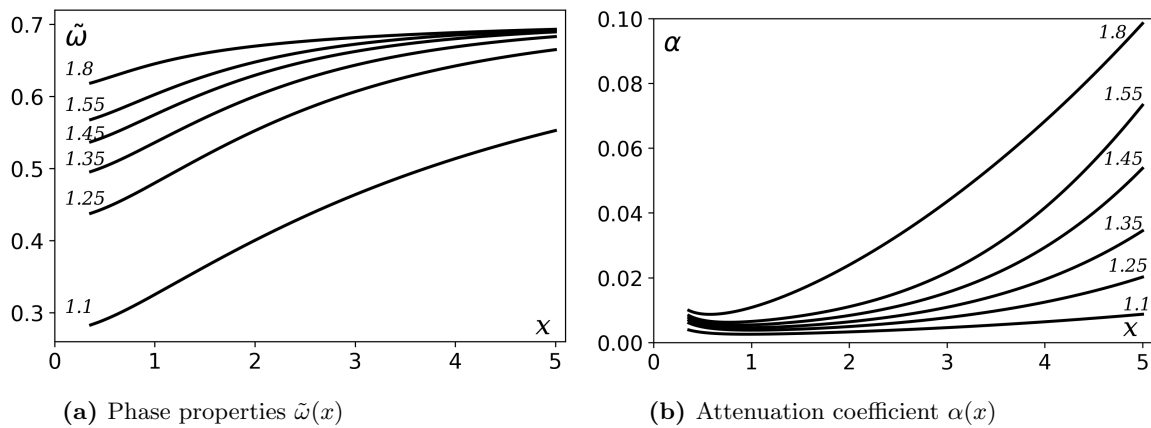


Figure 3. The dependence of the dimensionless phase and attenuation properties of the $m = +1$ mode via the dimensionless wavenumber x for different parameter η values. The numbers near the curves are the parameter η values. Other parameters are equal: $\Omega = 0.2$, $\sigma = 0.3$, $\nu = 0.001$, $\mu = 0.0$

The Figure 4 shows the influence of the value of the normalized radius η of the waveguide metal wall on the phase characteristics (Figure 4a) and spatial attenuation (Figure 4b) of the eigen dipolar mode $m = -1$ for the waveguide with the constant radius of metal enclosure for the same parameters suite as for the Figure 3. The parameter η that characterises the radius of the waveguide metal wall has the same influence of the on the phase characteristics $\tilde{\omega}$ and attenuation coefficient α for the $m = -1$ mode as for the $m = +1$ mode. It should be noted that with the same parameters of the waveguide structure, the normalized wave frequency $\tilde{\omega}$ of the $m = -1$ mode is somewhat lower than the normalized frequency of the $m = +1$ mode for the same axial wavenumber x value (see Figure 4a and Figure 3a). At the same time the spatial attenuation coefficient α of the $m = -1$ mode is approximately in 2 – 3 times smaller than attenuation coefficient of the $m = +1$ mode (see

Figure 4b and Figure 3b). Let us mention that similar to the case of dipolar $m = +1$ mode the region where the attenuation coefficient α growth with the axial wavenumber x decrease also exists for the dipolar $m = -1$ mode in the region of small axial wavenumber values $x < 0.7$ (Figure 4b).

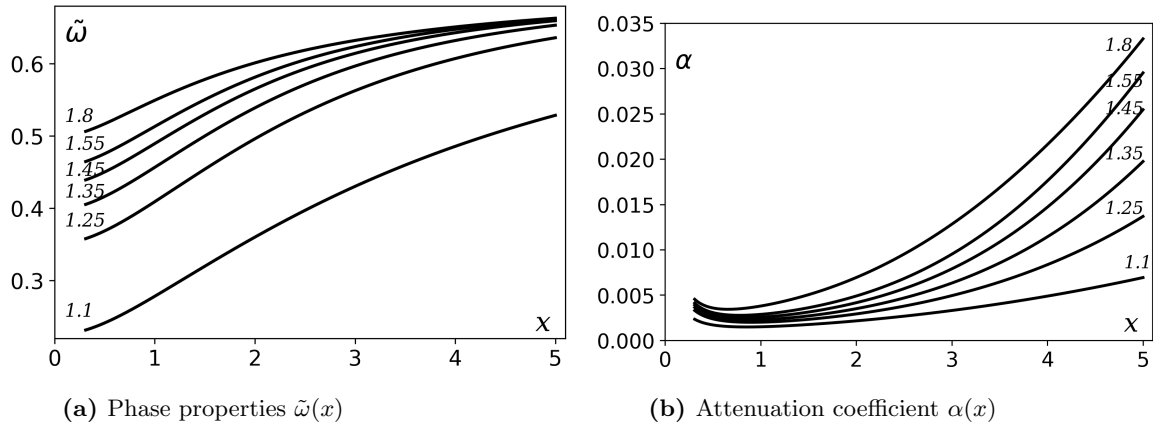


Figure 4. The dependence of the dimensionless phase and attenuation properties of the $m = -1$ mode via the dimensionless wavenumber x for different parameter η values. Problem parameters and curve numbering are the same as for the Figure 3

For our further research, it is very important to determine the influence of the plasma column radius R_p on the phase characteristics and spatial attenuation of the eigen dipolar waves of the waveguide structure. The influence of the normalized parameter σ , that characterises the dimensionless plasma column radius, on the eigen wave characteristics is shown in the Figure 5 and Figure 6 for the dipolar modes $m = +1$ and $m = -1$, respectively. It was obtained, that parameter σ has the same general influence on the phase characteristics $\tilde{\omega}(x)$ and spatial attenuation $\alpha(x)$ of the $m = +1$ and $m = -1$ waves, respectively. At the same time, the normalized frequency values $\tilde{\omega}$ of eigen dipolar modes $m = \pm 1$ for a given value of the axial wavenumber are quite close (see, Figure 5a and Figure 6a), but the $\tilde{\omega}$ value of the $m = -1$ mode is somewhat lower than that of the $m = +1$ mode. The spatial attenuation coefficient α of eigen modes $m = +1$ and $m = -1$ also possesses similar behavior (see, Figure 5b and Figure 6b), but eigen mode with $m = -1$ is attenuates somewhat weaker than the mode with $m = +1$, especially in the region of small axial wavenumbers $x \geq 3$. It is also necessary to mention the the existence of the region where attenuation coefficient α decreases with the axial wavenumber x increase ($x < 1.0$) for small parameter σ values ($\sigma \leq 0.6$). For the plasma columns with rather large radius ($\sigma > 1$) such region is not present.

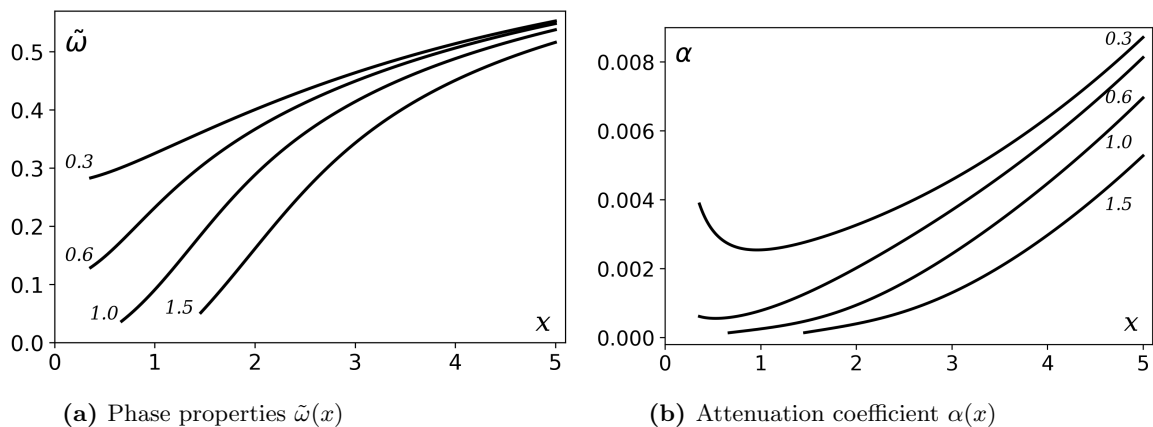


Figure 5. The dependence of the dimensionless phase and attenuation properties of the $m = +1$ mode via the dimensionless wavenumber x for different parameter σ values. The numbers near the curves are the parameter σ values. Other parameters are equal: $\Omega = 0.2$, $\eta = 1.1$, $\nu = 0.001$, $\mu = 0.0$

After the detailed study of the phase and attenuation properties of the eigen dipolar waves of the discharge structure (see results presented above in the Figures 1-6 and also in [10]) it is necessary to choose suitable parameters for further research and to move to the next study step. It is obvious that to obtain rather long

discharge sustained by the eigen dipole waves with a high degree of plasma density axial homogeneity it is convenient to choose such parameters of the system, that give moderate values of the spatial attenuation coefficient α together with rather big value of dimensionless plasma density $N = \omega_p^2/\omega^2 = 1/\tilde{\omega}^2$. The analysis of the previously obtained results shows that small parameter η values ($\eta = 1.1$, see Figures 3, 4) leads to the quite small spatial attenuation coefficient value, but at the same time, in the future, it is quite possible to obtain the problems associated with gas discharge modeling in the waveguide with metal enclosure with decreasing radius along the discharge. The increase in the plasma column normalized radius σ leads to the decrease of the spatial attenuation coefficient α (see Figures 5, 6), but at the same time the value of the minimum permissible axial wave number x increases. In [10] it was shown that the decreasing of the external magnetic field value (the decrease of the parameter Ω value) leads to the decrease of the normalized frequency $\tilde{\omega}$ of the $m = +1$ wave and to the increase of its spatial attenuation coefficient α . In [10] it was also shown that the decreasing of the external magnetic field value leads to the increase of dimensionless frequency $\tilde{\omega}$ in the region of small values of the axial wave number x and to the decrease of $\tilde{\omega}$ in the region of sufficiently large x values for the dipolar wave $m = -1$. In contrast to the $m = +1$ dipolar wave, the attenuation coefficient α of the $m = -1$ dipolar mode in the region of small x values increases but decreases in the region of sufficiently large axial wavenumbers x with the decrease of the external magnetic field value Ω . As for the value of the parameter ν , the smaller is the normalized effective collision frequency of ν/ω , the smaller is the attenuation coefficient α (see Figure 1, 2).

Thus, taking into account the above considerations, the following normalized parameters of the waveguide structure were chosen for further gas discharge axial structure modeling: $\eta = 1.3$, $\sigma = 0.8$, $\Omega = 0.2$, $\nu = 0.001$.

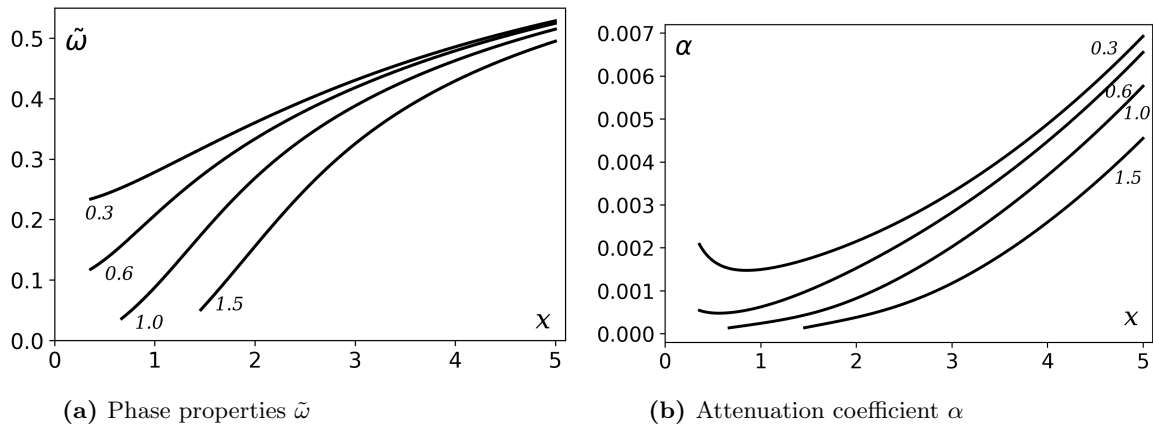


Figure 6. The dependence of the dimensionless phase and attenuation properties of the $m = -1$ mode via the dimensionless wavenumber x for different parameter σ values. Problem parameters and curve numbering are the same as for the Figure 5

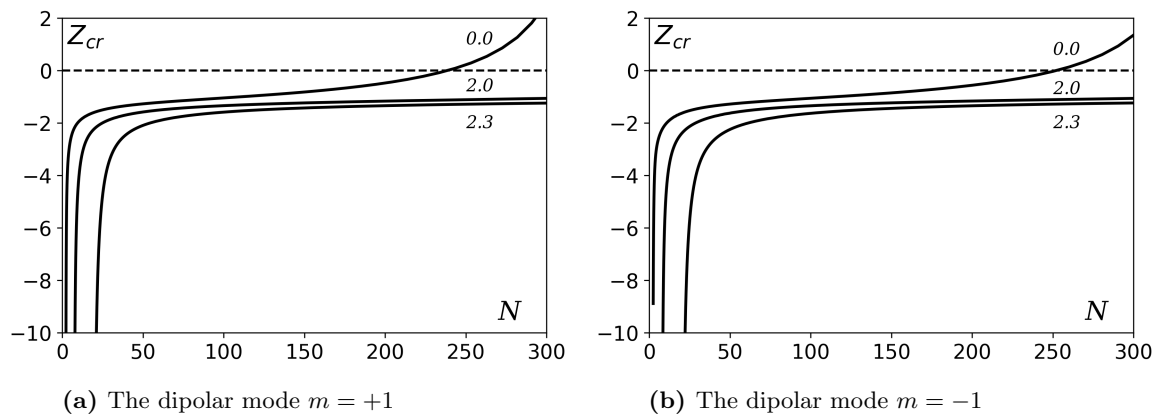


Figure 7. The Zakrzewski stability criterion (8). The numbers near the curves are the non-uniformity parameter μ values. Other parameters are equal: $\omega = 0.2$, $\sigma = 0.8$, $\eta = 1.3$, $\nu/\omega = 0.001$

The next step of the study is the determination of the $\tilde{\omega}$ region where the discharge can be sustained according to the Zakrzewski stability criterion (8). Some results of such study are presented in Figure 7. The

Figure 7a and Figure 7b shows the influence of plasma density radial non-uniformity (parameter μ varies in the range $\mu \in [0.0; 2.3]$) on the stability criterion (8) for dipolar mode with $m = +1$ and $m = -1$, respectively. Other parameters of calculations are equal to $\omega = 0.2$, $\sigma = 0.8$, $\eta = 1.3$, $\nu/\omega = 0.001$. The criterion in the Figure 7 is presented in the following equivalent to (8) form: $Z_{cr} = (n/\alpha) \cdot (d\alpha/dn) - 1 < 0$, so negative value of Z_{cr} corresponds to the regime of the stable gas discharge sustaining. When the parameter μ increases from zero (radially homogeneous plasma) up to $\mu = 2.3$ (the radial distribution of the plasma density is close to the ambipolar diffusion regime profile), the maximum possible plasma density value $N = \omega_p^2/\omega^2$ in the discharge that can be sustained by the dipolar mode $m = \pm 1$ becomes bigger and the corresponding density range becomes larger (see Figure 7a, 7b).

The final step of our study is the finding the plasma density axial distribution in the discharge sustained by the dipolar $m = \pm 1$ waves by solving ordinary differential equation (7). The Zakrzewski stability criterion (8) was also under the control. The dimensionless plasma density $N = \omega_p^2/\omega^2$ (ω_p is the electron plasma frequency) axial distributions in the discharge sustained by the eigen dipolar $m = \pm 1$ mode for different plasma density radial profiles (non-uniformity parameter $\mu = 0.0, \mu = 2.0, \mu = 2.1, \mu = 2.2, \mu = 2.3$) is presented in Figure 8. The normalized normalized axial coordinate is equal to $\xi = (\nu z)/(\omega R_p)$. At this modeling the radius of the waveguide metal enclosure is considered to be constant along the discharge. Other parameters are equal to $\Omega = 0.2, \sigma = 0.8, \eta = 1.3, \nu = 0.001$.

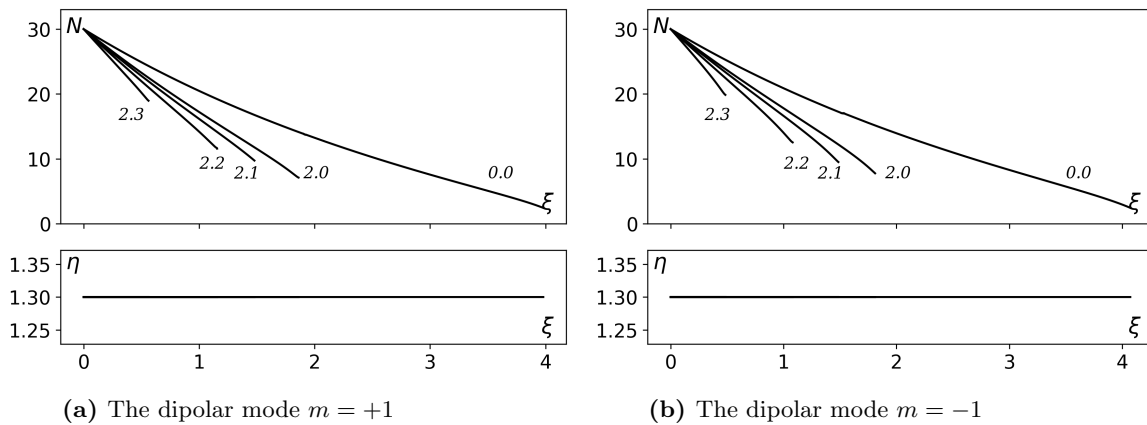


Figure 8. Plasma density axial distribution in dipolar mode sustained gas discharge. The numbers near the curves are the non-uniformity parameter μ values. Other parameters are equal: $\Omega = 0.2, \sigma = 0.8, \eta = 1.3, \nu = 0.001$

The Figures 8a, 8b present the normalized plasma density axial distribution $N = \omega_p^2/\omega^2$ along the discharge (normalized coordinate ξ) for a radially homogeneous plasma $\mu = 0$ and for such values of non-uniformity parameter μ at which the effect of radial non-uniformity becomes significant. The discharges, sustained by the $m = \pm 1$ waves in the considered discharge structure possess the similar axial gradients and the discharge lengths.

The Figure 9 presents the plasma density axial distribution in the discharge sustained by the eigen dipolar mode in the case of radially uniform plasma for the metal waveguide with constant, increasing and decreasing radius in the direction of wave propagation. The other parameters are the same as in the Figure 8. The normalized plasma density value at the beginning of the discharge was chosen to be equal to $N = 30$. When the discharge is sustained in the metal waveguide with increasing radius one can obtain the discharge length approximately twice as long as for the discharge in a waveguide of constant radius. Besides one can obtain significantly smaller axial gradients of density non-uniformity, especially at the end of the discharge. When the discharge takes place in metal metal waveguide with the decreasing radius along the discharge the discharge length decreases approximately in half, as compared with the discharge in the waveguide of constant radius. At this case the axial gradients of density non-uniformity increases, especially at the end of the discharge. It is necessary to note the similarity of the axial profiles of the discharges sustained by the dipolar mode $m = \pm 1$.

The Figure 10 shows the plasma density axial structure in the discharge sustained by the dipolar mode in the case when the non-uniformity parameter is equal to $\mu = 2.0$. The normalized plasma density value at the beginning of the discharge was also chosen equal to $N = 30$. The increase of waveguide metal radius along the discharge gives the possibility to obtain a longer discharge than in a waveguide of constant radius. In addition let us note that the plasma density decreases along the discharge almost linearly. In a waveguide with the decreasing radius along the discharge one can obtain a shorter discharge with a large axial density gradient at the end of the discharge. The model with such non-uniformity parameter possesses the similarity of the plasma

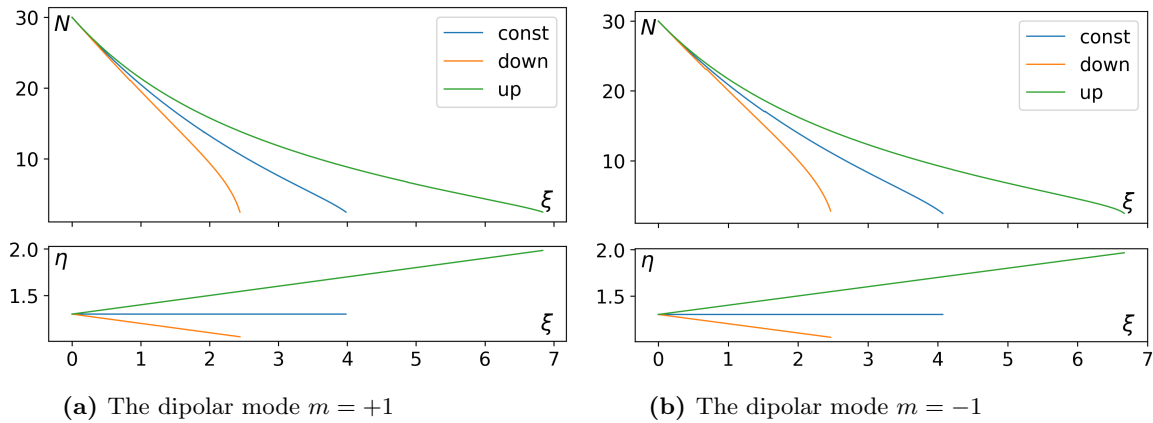


Figure 9. Plasma density axial distribution in dipolar mode sustained gas discharge for $\mu = 0.0$, $\Omega = 0.2$, $\sigma = 0.8$, $\eta = 1.3$, $\nu = 0.001$

density axial profiles for the discharges sustained by the dipolar mode $m = \pm 1$.

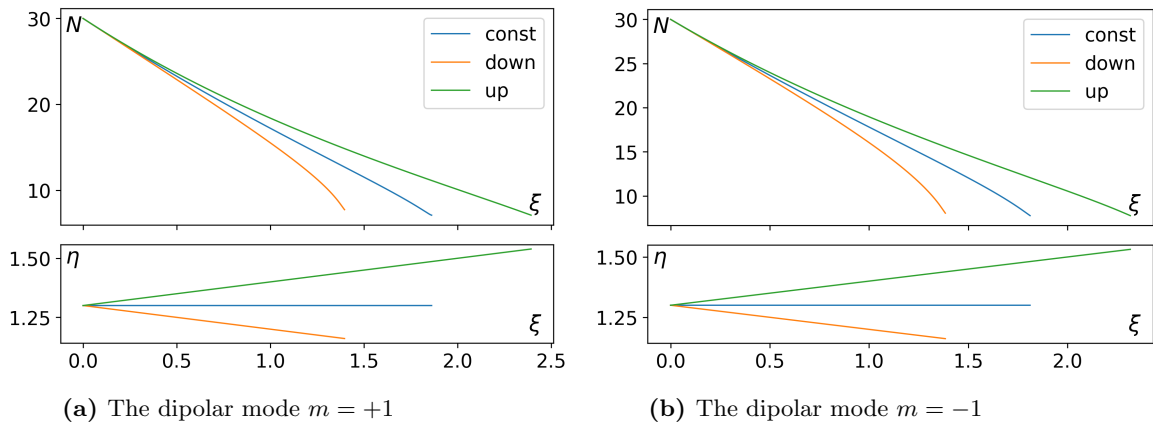


Figure 10. Plasma density axial distribution in dipolar mode sustained gas discharge for $\mu = 2.0$, $\Omega = 0.2$, $\sigma = 0.8$, $\eta = 1.3$, $\nu = 0.001$

At the larger values of the non-uniformity parameter μ ($\mu = 2.1$), such similarity of the plasma density axial profiles in the discharges sustained by the dipolar mode $m = \pm 1$ starts to disappear (see Figure 11). In the discharges sustained by the $m = +1$ mode, the influence of the variable radius of the metal waveguide is essential almost at the beginning of the discharge (Figure 11a). At the same time, in the discharges sustained by the $m = -1$ mode, the plasma density decreases along the discharge practically according to a linear law (Figure 11b). Besides the discharges length and the plasma density axial gradients for metal waveguides with variable radius somewhat differ from such quantities for the discharges in waveguide structure with constant radius $\eta = 1.3$. It is also should be noted that the length of discharge sustained by the mode $m = -1$ is slightly smaller as compared to the length of the discharge in the mode $m = +1$.

When the non-uniformity parameter increases up to $\mu = 2.2$, the axial profile of plasma density in the discharges sustained by the $m = \pm 1$ dipolar modes (Figure 12) become again similar, but since the discharges on the $m = +1$ mode are longer than the discharges on the mode $m = -1$, then the corresponding plasma density axial gradient for the discharge on the mode $m = +1$ is somewhat smaller.

The further growth of the non-uniformity parameter μ up to $\mu = 2.1$ leads to the further discharge decrease and to the increase of plasma density axial gradient.

4. CONCLUSIONS

This article presents the results of the theoretical modelling of the axial structure of gas discharge sustained by the eigen dipolar ($m = \pm 1$) wave of the discharge structure that consists of cylindrical magnetized slightly collisional plasma column that surrounds by the vacuum region and enclosed by the metal wall of constant or

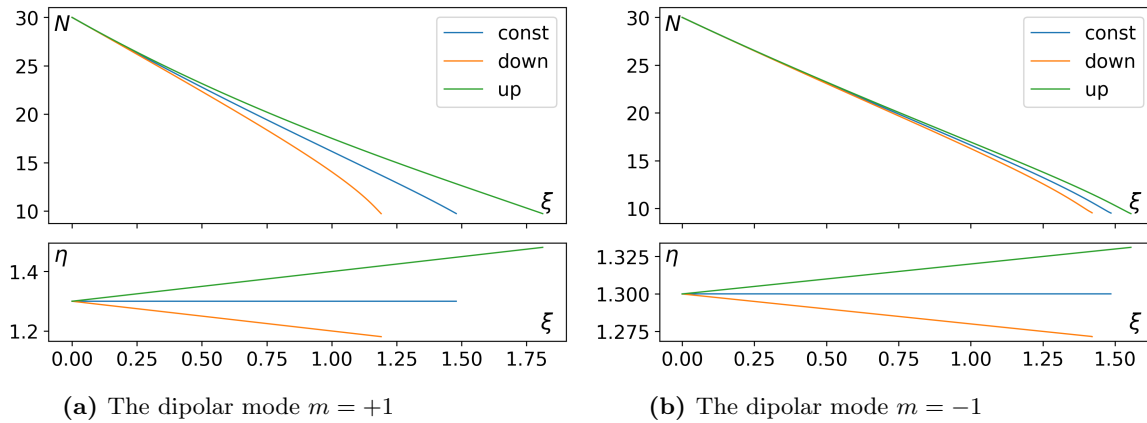


Figure 11. Axial structure of gas discharge for $\mu = 2.1, \Omega = 0.2, \sigma = 0.8, \eta = 1.3, \nu = 0.001$

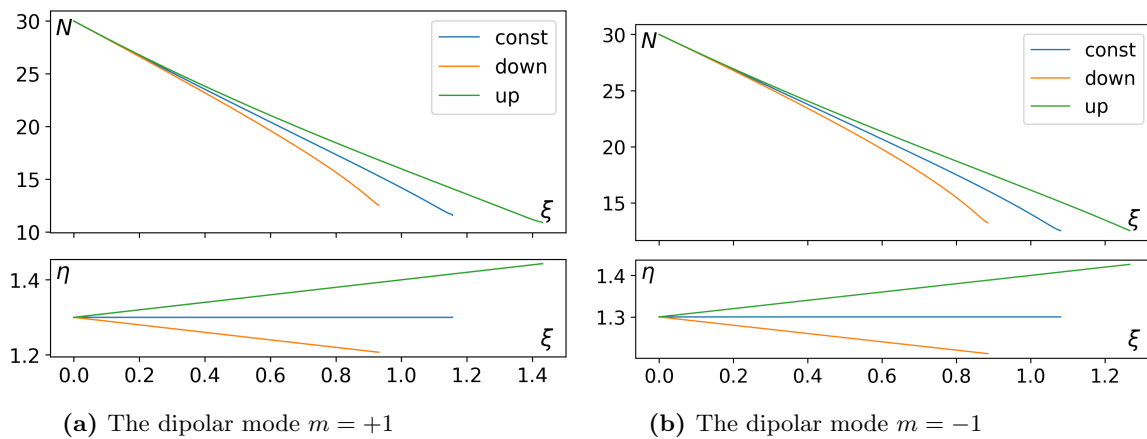


Figure 12. Plasma density axial distribution in dipolar mode sustained gas discharge for $\mu = 2.2, \Omega = 0.2, \sigma = 0.8, \eta = 1.3, \nu = 0.001$

slightly varying along the discharge radius. The modelling was carried out in the framework of electrodynamics approach taking into account slightly axial and strongly radial non-uniformity of plasma density.

For the discharge structure with a constant radius of metal enclosure it was shown that the increase of the plasma density radial non-uniformity leads to the significant decrease of the discharge length and to the increase of the plasma density axial gradients. It was also obtained that plasma density radial non-uniformity has the essential influence on plasma density axial distribution starting from the non-uniformity parameter value $\mu \geq 2.0$. This influence is getting stronger when $\mu \rightarrow 2.3$. It was also obtained that gas discharges sustained in the waveguides with expanding along the discharge metal enclosure possesses a longer length with significantly smaller axial density gradients at the end of the discharge as compared to a constant-radius discharge structure. The use of a waveguide with narrowing along the discharge metal enclosure leads to the decrease of the discharge length and to the increase of the plasma density axial gradient, especially at the end of the discharge. The study of the simultaneous influence of the plasma density radial non-uniformity and the waveguide metal enclosure axial inhomogeneity on the plasma density axial structure in the discharge have showed that in the discharge structures with an expanding metal waveguide the length of the discharge sustained by the $m = +1$ mode is slightly bigger than for the discharge sustained by the $m = -1$ mode. It was obtained that plasma density decreases in the direction of wave propagation approximately according to a linear law when non-uniformity parameter value $\mu \geq 2.0$. The carried out simulation have shown that when the non-uniformity parameter μ increases from $\mu = 0.0$ (radially uniform plasma) up to $\mu = 2.3$ (the plasma density radial distribution that is close to the profile of the ambipolar diffusion regime), the plasma density value increases and also increases the corresponding density range of stable discharge that can be sustained by the $m = \pm 1$ dipolar modes. The obtained results can be useful for various different applications.

Acknowledgments

This work was supported by the Ministry of Education and Science of Ukraine, under the grant 0121U109922.

ORCID

 Volodymyr Olefir, <https://orcid.org/0000-0002-8022-2556>;  Oleksandr Sporov, <https://orcid.org/0000-0002-4610-9656>;  Mykola Azarenkov, <https://orcid.org/0000-0002-4019-4933>

REFERENCES

- [1] I. Zhelyazkov, and V. Atanassov, Physics Reports, **255**(2-3), 79 (1995). [https://doi.org/10.1016/0370-1573\(94\)00092-H](https://doi.org/10.1016/0370-1573(94)00092-H).
- [2] H. Schlüter, and A. Shivarova, Physics Reports, **443**(4-6), №4-6, 121 (2007). <https://doi.org/10.1016/j.physrep.2006.12.006>.
- [3] E. Benova, P. Marinova, R. Tafradjiiska-Hadjiolova, Z. Sabit, D. Bakalov, N. Valchev, L. Traikov, et al., Appl. Sci. **12**, 969 (2022). <https://doi.org/10.3390/app12030969>
- [4] M. S. Kovacevic, L. Kuzmanovic, M.M. Milosevic, and A. Djordjevich, Physics of Plasmas, **28**(2), (2021). <https://doi.org/10.1063/5.0035035>
- [5] C.M. Ferreira, J. of Phys. D: Appl. Phys. **16**(9), 1673 (1983). <https://doi.org/10.1088/0022-3727/16/9/013>.
- [6] M. Moisan, and Z. Zakrzewski, J. of Phys. D: Appl. Phys. **24**(7), 1025 (1991). <https://doi.org/10.1088/0022-3727/24/7/001>.
- [7] J. Wolinska-Szatkowska, J. of Phys. D: Appl. Phys. **20**, 977 (1987). <https://doi.org/10.1088/0022-3727/20/7/024>.
- [8] N.A. Azarenkov, V.P. Olefir, and A.E. Sporov, Problems of Atomic Science and Technology. Series «Plasma Physics», 25(6), 113 (2018). https://vant.kipt.kharkov.ua/ARTICLE/VANT_2018_6/article_2018_6_113.pdf.
- [9] N.A. Azarenkov, V.P. Olefir, and A.E. Sporov, Problems of Atomic Science and Technology. Series “Plasma Physics”, 130(6), 69 (2020). <http://dx.doi.org/10.46813/2020-130-069>
- [10] N.A. Azarenkov, V.P. Olefir, and A.E. Sporov, Problems of Atomic Science and Technology. Series “Plasma Physics”, 143(1) 1, 98 (2023). <http://dx.doi.org/10.46813/2023-143-098>
- [11] D. Gary Swanson, *Plasma Waves*, 2nd Edition, (IOP Publishing Ltd, Bristol and Philadelphia, 2003).
- [12] G.G. Lister, and T.R. Robinson, J. of Phys. D: Appl. Phys. **24**(11), 1993 (1991). <https://doi.org/10.1088/0022-3727/24/11/013>.

АКСІАЛЬНА СТРУКТУРА ГАЗОВОГО РОЗРЯДУ, ЩО ПІДТРИМУЄТЬСЯ ВЛАСНОЮ ДИПОЛЬНОЮ ХВИЛЕЮ МЕТАЛЕВОГО ХВИЛЕВОДУ ЗМІННОГО РАДІУСУ, ЗАПОВНЕНОГО МАГНІТОАКТИВНОЮ НЕОДНОРІДНОЮ ПЛАЗМОЮ Володимир Олефір^{a,b}, Олександр Споров^a, Микола Азаренков^{a,b}

^a Харківський національний університет ім. В.Н. Каразіна, майдан Свободи, 4, 61022, Харків, Україна

^b Національний Науковий Центр “Харківський Фізико-Технічний Інститут”,
вул. Академічна, 1, 61108, Харків, Україна

В статті наведено результати теоретичного дослідження аксіального розподілу густини плазми в стаціонарному газовому розряді, який підтримується власною дипольною хвилею, що поширюється в довгій циліндричній плазмово-металевій структурі. Структура складається зі стовпа магнітоактивної неоднорідної плазми, що знаходиться всередині металевого хвилеводу змінного радіусу. Дослідження газового розряду проводиться в рамках електродинамічної моделі, в якій основна увага приділяється електродинамічній частині. Для опису процесів, що відбуваються в плазмі, використовуються модельні рівняння. Визначено вплив неоднорідності металевого хвилеводу вздовж структури та радіальної неоднорідності густини плазми на фазові характеристики дипольної хвилі, її просторове загасання, радіальний розподіл компонент поля, аксіальний розподіл густини плазми, що підтримується цією модою, проведено аналіз умов стаціонарності протікання розряду. Отримані результати можуть бути корисними для різних технологічних застосувань.

Ключові слова: газовий розряд; плазмово - металевий хвилевід; дипольна власна хвиля; фазові властивості та просторове загасання; критерій Закревського

CATHODIC VACUUM ARC MULTILAYER COATINGS (TiZrSiY)N/NbN: STRUCTURE AND PROPERTIES DEPENDING ON THE DEPOSITION INTERVAL OF ALTERNATE LAYERS

 Vyacheslav M. Beresnev^a,  Serhii V. Lytovchenko^{a*},  Mykola O. Azarenkov^{a,b},  Olga V. Maksakova^{a,c},
 Denis V. Horokh^a,  Bohdan O. Mazilin^a,  Diana Kaynts^d,  Irina V. Doshchechkina^e,  Oleg V. Gluhov^f

^a V.N. Karazin Kharkiv National University, 4, Svobody Sq., 61022 Kharkiv, Ukraine

^b National Science Center «Kharkov Institute of Physics and Technology», 1, Akademicheskaya St., 61108 Kharkiv, Ukraine

^c Institute of Materials Science, Slovak University of Technology in Bratislava, 25, Jána Bottu Str., 917 24 Trnava, Slovakia

^d Uzhhorod National University, 3, Narodna Sq., 88000 Uzhhorod, Ukraine

^e Kharkiv National Automobile and Highway University, 25, Ya. Mudryi St., 61200 Kharkiv, Ukraine

^f Kharkiv National University of Radio Electronics, Nauki Ave. 14, 61166, Kharkiv, Ukraine

*Corresponding Author e-mail: s.lytovchenko@karazin.ua

Received October 9, revised November 20, accepted November 23, 2023

Two series of multilayer coatings with different numbers of bilayers (268 and 536, respectively) were synthesised using the cathodic vacuum-arc deposition (CVAD) with the simultaneous sputtering of two different cathodes. The first cathode was made of the multicomponent TiZrSiY material, and the second one was made of technical niobium. The coatings were condensed in a nitrogen atmosphere at a constant negative bias potential applied to the substrate. The resulting coatings have a distinct periodic structure composed of individual layers of (TiZrSiY)N and NbN with the thicknesses determined by the deposition interval (10 or 20 s, respectively). The total thicknesses of the coatings determined by the number of bilayers were 11 and 9 microns, respectively. The formation of polycrystalline TiN and NbN phases with grain size comparable to the size of the layers has been identified for both series of coatings. The layers exhibit a columnar structure growth with a predominant orientation (111). The hardness of the experimental coatings depends on the thickness of the layers and reaches 39.7 GPa for the coating with the smallest layer thickness. The friction coefficient of the obtained coatings varies from 0.512 to 0.498 and also depends on the thickness of the layers. A relatively large value of the friction coefficient is due to high roughness and the presence of a droplet fraction on the surface as well as in the volume of the coatings.

Keywords: Cathodic vacuum-arc deposition; Multilayer coatings; Layer number; Texture; Microhardness; Tribological properties; Friction parameters

PACS: 61.46.-w; 62.20.Qp; 62-25.-g; 81.15.Cd

INTRODUCTION

Modern high-tech production requires new materials with unique properties. In many cases, to provide the required surface properties, functional coatings formed using modern technologies are used. The application of such coatings can significantly increase equipment reliability, reduce maintenance costs, extend service life, restore working surfaces and parts, and protect against high loads and aggressive environments.

Multilayer functional coatings are one of the most effective types of protective coatings. Its characteristic feature is the difference in the physical, mechanical, and chemical properties of the constituent layers. Ion plasma deposition technologies have significant advantages in terms of creating multilayer coating systems for tribological applications.

The architecture and construction of multilayer coatings, taking into account their functions and structure, constituent materials of individual layers, their sequence, and thickness, makes it possible to control the properties of the surface (for example, hardness and elastic modulus), and therefore its functionality. Several scientific works have proposed a mechanism for increasing the hardness of multilayer coatings, based on the transition of the alternating layer thicknesses to the nanometre scale, in which the formation of dislocations is suppressed, and the difference in the elastic moduli of neighbouring layers prevent the dislocations motion [1-3].

Binary nitrides, such as TiN and ZrN coatings, have been widely used to improve the surface properties of substrate materials. They are highly resistant to hardness, wear, and corrosion, making them useful for many industrial applications. TiZrN coatings not only have a relatively higher resistance to corrosion, high adhesion, and low COF, but also excellent hardness and wear resistance. One of the ways to further improve the coating system based on the TiZrN system is to increase the number of alloying elements. Si, Y, V, Cr, and other elements can be used for this purpose. Thus, the addition of Si leads to the formation of a nanocrystalline structure and strengthening of the coating. This is consistent with the Hall-Petch relation, from which it follows that reducing the grain size to a certain critical value leads to an increase in the hardness and strength of the nitride compound [4]. At silicon concentrations of 6-8 at.%, the TiZrN coating has a nanocomposite structure characterised by the formation of an amorphous tissue Si₃N₄ [5-8]. Coatings with

Cite as: V.M. Beresnev, S.V. Lytovchenko, M.O. Azarenkov, O.V. Maksakova, D.V. Horokh, B.O. Mazilin, D. Kaynts, I.V. Doshchechkina, O.V. Gluhov, East Eur. J. Phys. 4, 347 (2023), <https://doi.org/10.26565/2312-4334-2023-4-45>

© V.M. Beresnev, S.V. Lytovchenko, M.O. Azarenkov, O.V. Maksakova, D.V. Horokh, B.O. Mazilin, D. Kaynts, I.V. Doshchechkina, O.V. Gluhov, 2023; [CC BY 4.0 license](https://creativecommons.org/licenses/by/4.0/)

high concentrations of Si are characterized by the formation of SiO_2 layers in the near-surface region, which serve as an additional barrier to the diffusion of oxygen atoms [9].

The addition of yttrium to the coating composition helps to increase oxidation due to the possible formation of the YO_2 phase at grain boundaries, as well as eliminate the formation of columnar crystals [10,11]. The simultaneous addition of Si and Y to the coating can further improve its oxidation stability, corrosion resistance, and also reduce the level of internal stresses [12].

Further improvement in the properties of multicomponent coatings based on monophase nitride systems containing Ti, Zr, Cr, Si, Y, Al or other elements can be achieved under certain formation conditions under which the increase in the hardness increases but the Young modulus decreases. Young's modulus is an important characteristic of a material, largely determining its hardness. While increased hardness is desirable for high-performance coatings for tribological applications, Young's modulus of such coatings must be low enough to improve strain resistance and thermal stability.

The formulated conditions can be met when creating a multilayer coating, where one layer is a multicomponent nitride system, for example (TiZrSiY) , and the second layer is a mononitride, for example, NbN. The plastic properties of the suggested mononitride are ensured by a decrease in Young's modulus and, in some cases, an increase in heat resistance during the formation of a surface oxide film NbO_x [13].

This article reports on the application of cathodic vacuum-arc deposition [14] for the synthesis of multilayer nitride coatings based on niobium and a multi-element system (TiZrSiY) with nanoscale layers, as well as a study of the influence of the structural phase state of obtained coatings on their physical and mechanical properties.

EXPERIMENTAL DETAILS

Experimental coatings were grown by cathodic arc in a non-commercial deposition system (see Figure 1). The elemental composition of the first target was (in at. %): 72.5 Ti + 20 Zr + 5.0 Si + 2.5 Y. The second target was made of niobium with a purity of 98.2 at. Coating deposition was carried out in a nitrogen environment at a nitrogen pressure (P_N) of 0.53 Pa and a negative bias applied to the substrate (U_b) of 200 V. The substrates were made of AISI 321 steel with dimensions of $15 \times 15 \times 2,0 \text{ mm}^3$.

Two series of samples with coatings based on a two-layer system $(\text{TiZrSiY})\text{N}/\text{NbN}$ were produced. The total thickness of the coating of the first series was about 11 μm , and that of the second series was about 9 μm . The sample of the first series contained 536 layers, and the second series contained 268 layers.

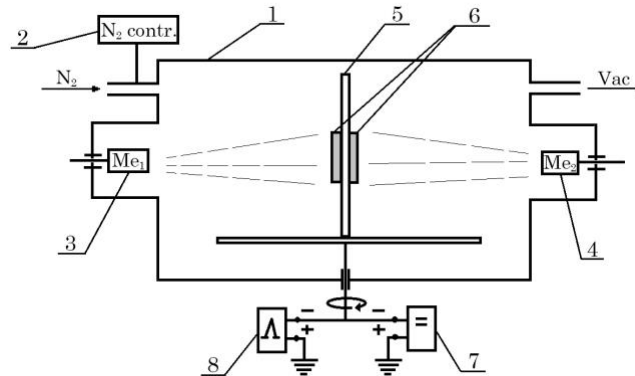


Figure 1. Scheme of the deposition unit used for the synthesis of multilayer coatings: 1 – vacuum chamber; 2 – automatic nitrogen pressure control system; 3 – TiZrSiY multi-element target evaporator (Me_1); 4 – Nb target evaporator (Me_2); 5 – substrate holder; 6 – substrates; 7, 8 – DC and pulse voltage sources.

The cross-sectional microstructure of the coatings at different magnifications, as well as morphology of the surface after wear tests were studied using scanning electron microscopy in a Quanta 600 FEG and FEI Nova NanoSEM 450 microscopes. The phase state of the coatings was characterised using X-ray diffraction in a DRON-3M diffractometer in $\text{Cu-K}\alpha$ radiation. Identification of the phases and calculation of main crystal structural parameters was done using Malvern Panalytical's XRD software.

The microhardness of the coatings was measured using an automated ultramicrohardness tester, called «Shiumadzu», using the Vickers indenter. The applied load was 245 mN and the holding time was 10 s. The accuracy of the measurement result according to the device's passport indicators is $\pm 1,5 \%$.

Tribological tests of the coatings were carried out in air using the 'ball-disk' scheme. The "Tribometer" device from CSM Instruments was used as a friction machine. For tribological tests, coatings were deposited on the surface of polished cylindrical samples (42 mm in diameter, 5 mm in height) made of 45 steel (surface roughness $R_a = 0,088$ microns). A ball with a diameter of 6.0 mm made of sintered certified aluminium oxide Al_2O_3 was used as a counterbody. The applied load was 6,0 H, the sliding speed was 10 sm/s. The tests comply with international standards ASTM G99-959, DIN50324 and ISO 20808.

RESULTS AND DISCUSSION

Figure 2 shows cross-sectional SEM images of multilayer coatings (TiZrSiY)N/NbN at two magnifications. Both coatings show distinct alternating of (TiZrSiY)N and NbN layers with thicknesses of $(35 \div 39)$ and $(17 \div 22)$ nm (seria 1) and $(36 \div 45)$ and $(31 \div 39)$ nm, respectively. It should be noted that the thickness of the (TiZrSiY)N layers exceeds the thickness of the NbN layers. An explanation for this fact may be, on the one hand, a higher rate of evaporation of metals from a multielement cathode. On the other hand, the smaller thickness of NbN can also be associated with the lower formation energy of the NbN compound (213 kJ/mol) compared to TiN (337 kJ/mol).

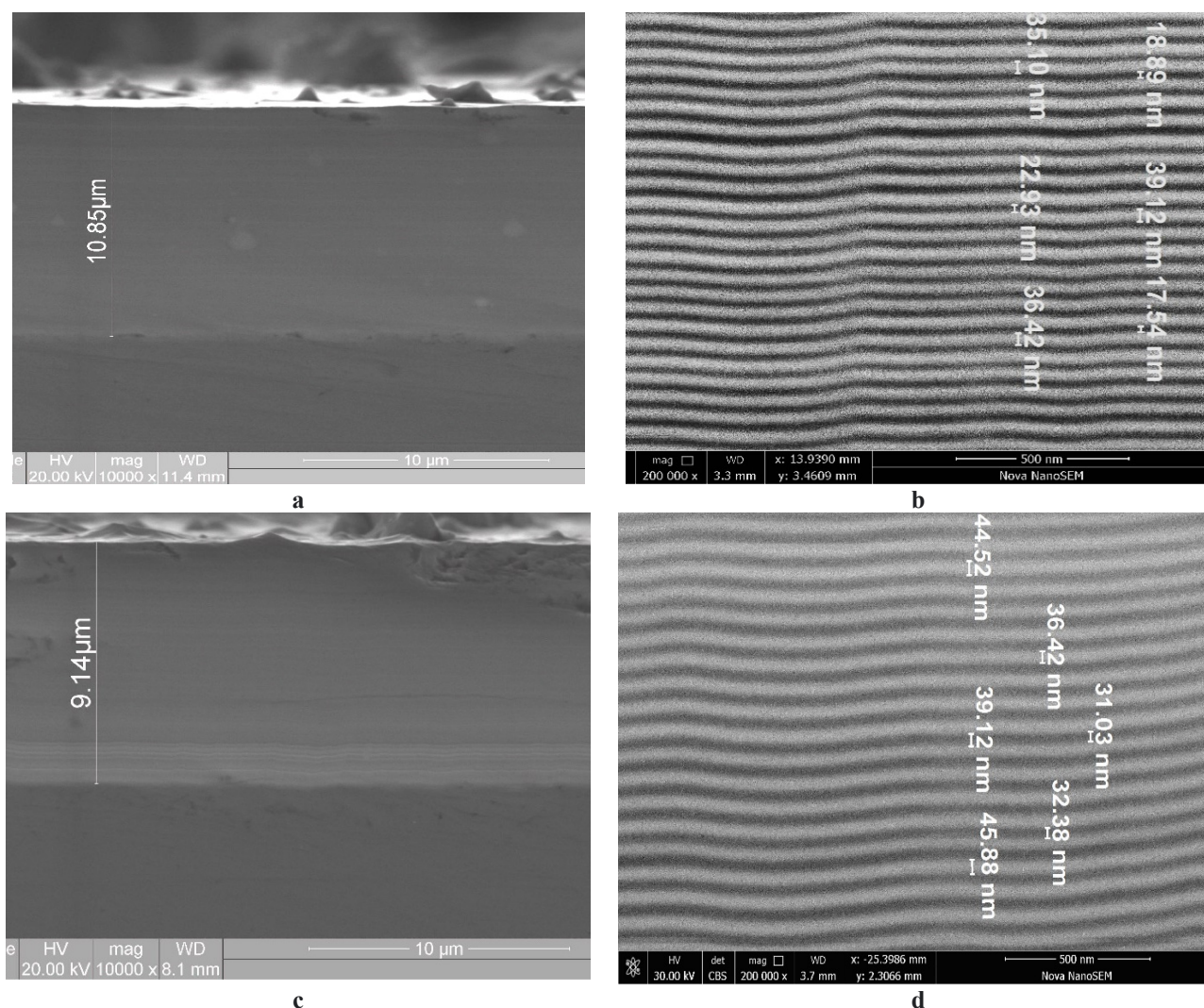


Figure 2. SEM cross section micrographs of multilayer (TiZrSiY)N/NbN coatings at low (left) and high magnifications (right): seria 1 (a, b) and seria 2 (c, d)

There is some unevenness in the thickness of the layers in depth. The alternation of layers of different thicknesses is apparently due to the dynamics of the technological parameters during the coating deposition process. The characteristic waviness of the forming layers is caused in part by the presence of the droplet fraction, as well as by the influence of electromagnetic fields in the deposition area. The formation of the wavy structure of the layers is also influenced by the initial morphology of the substrate surface.

To improve the adhesive bond between the substrate and the coating, before the coating, additional cleaning of the substrate surface from adsorbed substances and oxide films was carried out using a stream of accelerated ions. Speaking about oxide films, it should be emphasised that after preliminary cleaning (mechanical treatment, ultrasonic treatment, degreasing), a layer of oxides up to 2.5 nm thick may be formed on the surface, and after heating in a vacuum to the deposition temperature of the coating, the thickness of the oxide film can increase almost in half. To remove these contaminants from the surface of the substrate, it is necessary to apply a negative bias voltage of about 10^3 V. This parameter may ensure the cleaning at the atomic level. Surface cleaning with TiZrSiY and Nb ions occurred under a high vacuum under the pressure of 0.001 Pa and with a negative potential on the substrate of 1300 V, which led to heating of the substrate and its partial sputtering. As a result, a certain amount of cathode material still settles on the surface of the substrate and diffuses to a small depth, thus forming a transition layer between the coating and the substrate, the thickness of which is 29.5 nm (see Figure 3).

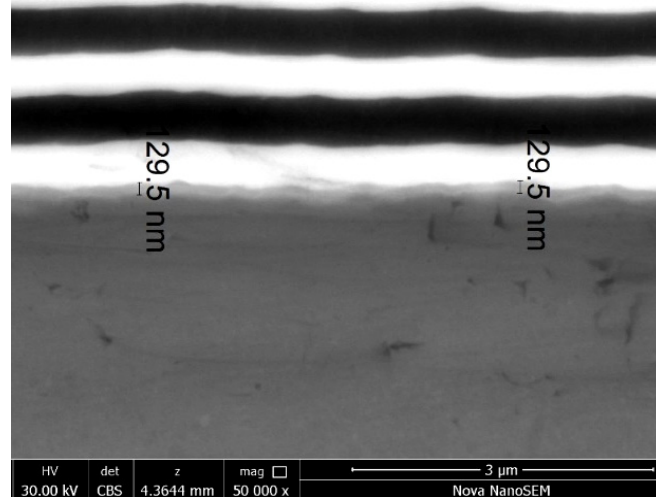


Figure 3. High-magnification SEM image of the transition zone between the substrate and multilayer (TiZrSiY)N/NbN coating seria 2.

The results of the X-ray diffraction analysis of multilayer (TiZrSiY)N/NbN coatings are shown in Figure 4. As one can see, the formation of complex phase structure is identified for all experimental coatings. The fcc-TiN phase with (111) and (222) planes was revealed for (TiZrSiY)N layers and mixture of hcp-NbN-ε phase (PDF-2 6-719), as well as a small amount of NbN-δ' (PDF-2 20-802) was identifies for NbN layers. The NbN-δ' phase (space group P6₃/mmc) having the anti-NiAs-type structure appears as a metastable structure during the phase transformation NbN-δ → NbN-ε.

In the coatings of the first seria, the lattice parameter of TiN is 0.4301 nm. The grain size of TiN is 17.9 nm and the level of microdeformation is 2.27×10^{-3} . The line intensity distribution corresponds to texture (200) with the texture coefficient $T_{c(200)} = 3.97$. The lattice parameters of NbN-ε are 0.2959 nm and 0.1140 nm. The grain size of NbN is 10.2 nm and the microdeformation level of microdeformation is 5.97×10^{-3} . Line intensity distribution of the line corresponds to the texture (004). The lattice parameters of NbN-δ' are 0.2988 nm and 0.5573 nm. Line intensity distribution corresponds to texture (002).

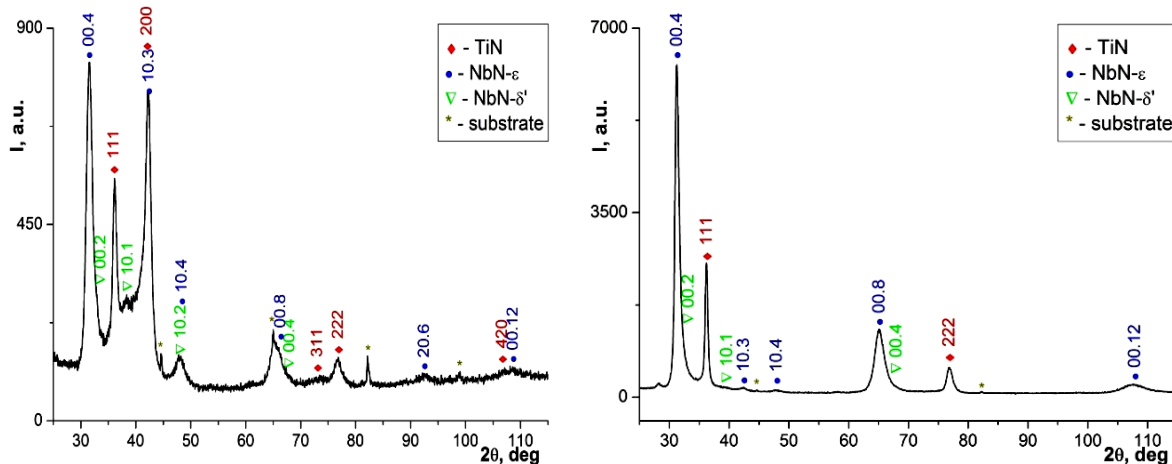


Figure 4. Diffraction patterns of multilayer (TiZrSiY)N/NbN coatings: seria 1 (left) and seria 2 (right)

In the coatings of the second seria, the lattice parameter of TiN is 0,4295 nm. The grain size of TiN is 20.4 nm and the level of microdeformation is 3.74×10^{-3} . The line intensity distribution corresponds to texture (111) with the texture coefficient $T_{c(111)} = 6.00$. The lattice parameters of NbN-ε are 0.2959 nm and 0.1145 nm. The grain size of NbN is 26.4 nm and the level of microdeformation is 6.70×10^{-3} . Line intensity distribution of the line corresponds to texture (004). The lattice parameters of NbN-δ' are 0.2967 nm and 0.5642 nm. Line intensity distribution corresponds to texture (002).

During the crystallisation of niobium nitride, several phases can form [17], and in most cases, NbN films have a mixed phase composition [18, 19]. Because of the complex composition and structure of the experimental coatings, the diffraction patterns contain diffraction peaks from different phases with some overlapping of the peaks.

It is known that Nb atoms dissolve in the TiN lattice to form a substitutional solid solution (TiNb)N. According to the Hume-Rothery rule, isomorphism of elements at temperatures far from the melting point appears when the difference in atomic sizes is less than 15% (the atomic radii for titanium is 0.147 nm and for niobium is 0.146 nm).

Therefore, for the experimental coatings, the predominant formation of a substitutional solid solution (TiNb)N is possible at the interfaces of (TiZrSiY)N and NbN layers. For the coatings of the first seria, obtained at a 10 s interval for the growth of each layer, the joined diffraction peak of (103)NbN- ϵ and (200)TiN is found at $2\theta = 42.7^\circ$ (see Fig. 4a). We suppose that this peak is related to the formation of a (TiNb)N solid solution (hcp crystal structure) at the interfaces of the (TiZrSiY)N and NbN layers or even the formation of interlayer transition zones between layers.

It has been revealed that the interval for the growth of each layer to 20 s (coatings of the second seria), the line intensity distribution from all peaks increases and broadening of diffraction peaks decreases (see Fig. 4b). The joined diffraction peak of (103)NbN- ϵ and (200)TiN as well as other diffraction peaks from NbN- ϵ and NbN- δ' disappear. The line intensity of (004) NbN- ϵ increases dramatically. Nitride NbN- ϵ has a homogeneity region at nitrogen concentrations in the range of 48.0 to 50.6 at.% [17], and nitride NbN- δ' exist at nitrogen concentrations in the range of 28.6 to 34.4 at.%. Based on these data, it can be assumed that an increase in the deposition time and, accordingly, the thickness of the layer leads to a change in the nitrogen concentration in the NbN bilayers and, as a consequence, to an increase in the volume fraction of the nitrogen-rich NbN- ϵ phase. In addition, the deposition time also influences the lattice parameters of the nitride phase. When the interval for the growth of each layer is 10 s (coatings of the first seria), the lattice parameter of TiN is 0.4301 nm, but when the interval for the growth of each layer is 10 s (coatings of the second seria), the lattice parameter of TiN decreases to 0.4295 nm. One can suppose that the changes in the lattice parameter point to the change in the the nitrogen content in TiZrSiYN layers. Several studies report this dependence, i.e. the decrease of the lattice parameter with a decrease in the nitrogen content. In summary, for multilayer coatings it is possible to influence the phase-structural state of the growth layers by varying the interval [20].

The change in modulation period affects the state of the interfaces of multilayer coatings, which play a decisive role in their properties [21]. Reducing the thickness of the layers while maintaining the total thickness of the coating increases the number of interfaces between layers, which act as a barrier to the migration of dislocations and the propagation of microcracks [22, 23]. The main mechanical properties of the multilayer (TiZrSiY)N/NbN coating as well as thickness ratio between the constituent layers are summarized in Table 1. The ratios H/E^* and H^3/E^{2*} are used to represent resistance against elastic strain to failure and resistance to plastic deformation, respectively.

Table 1. Mechanical properties of multilayer (TiZrSiY)N/NbN coatings

Number of seria and thickness ratio between layers, nm	Hardness H, GPa	Young modulus E^* , GPa	H/E^*	H^3/E^{2*}
seria 1: 18/36	39.7	438	0.09	0.32
seria 2: 31/45	37.1	421	0.088	0.28

The data from the table indicate that coating with a smaller layer thickness has better mechanical parameters, which is associated with the size effect and with the formation of incoherent (with different types of crystalline lattice) interphase boundary in the layers.

To study the adhesive strength of the multilayer (TiZrSiY)N/NbN coatings, we performed a sclerometric study of the best coating of the first seria using the Revetest scratch tester. The coating has been subjected to deformation (scratching) in the elastic and elastic-plastic regions to the limiting state, followed by destruction during horizontal movement of the indenter, previously embedded to a certain depth. The critical loads L_c , leading to the destructural changes during the test, have been determined as follows: (1) L_{c1} corresponds to the onset of penetration of the indenter into the coating; (2) L_{c2} corresponds to the appearance of the first cracks; (3) L_{c3} corresponds to the appearance of clusters of cracks; (4) L_{c4} characterizes the peeling of some regions of the coating, and (5) L_{c5} characterizes the chipping of the coating or its plastic abrasion. According to the obtained data, the wear of the coating occurs quite evenly without the formation of avalanche chips, which can be determined by the insignificant level of acoustic emission signals with increasing load on the indenter (see Figures 5 and 6).

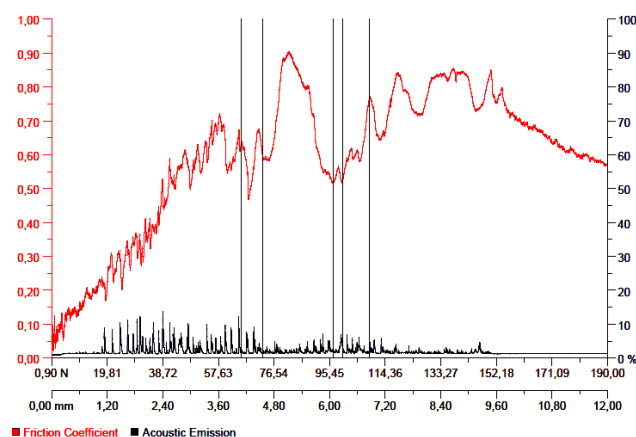


Figure 5. Results of scratch test of multilayer (TiZrSiY)N/NbN coating seria 1

The cohesive failure of the coating starts at 72.81 N, the adhesive failure is noted at 99.78 N and the full interfacial failure is registered at 109.07 N.

The results of tribological tests at room temperature during dry friction of multilayer (TiZrSiY)N/NbN coatings are given in Table 2. As can see, the friction coefficient of the coatings varies from 0.512 to 0.498. These relatively high values can be explained by the high roughness and the presence of a droplet fraction on the surface and in the volume of the coatings, the formation of which is due to the deposition technique.

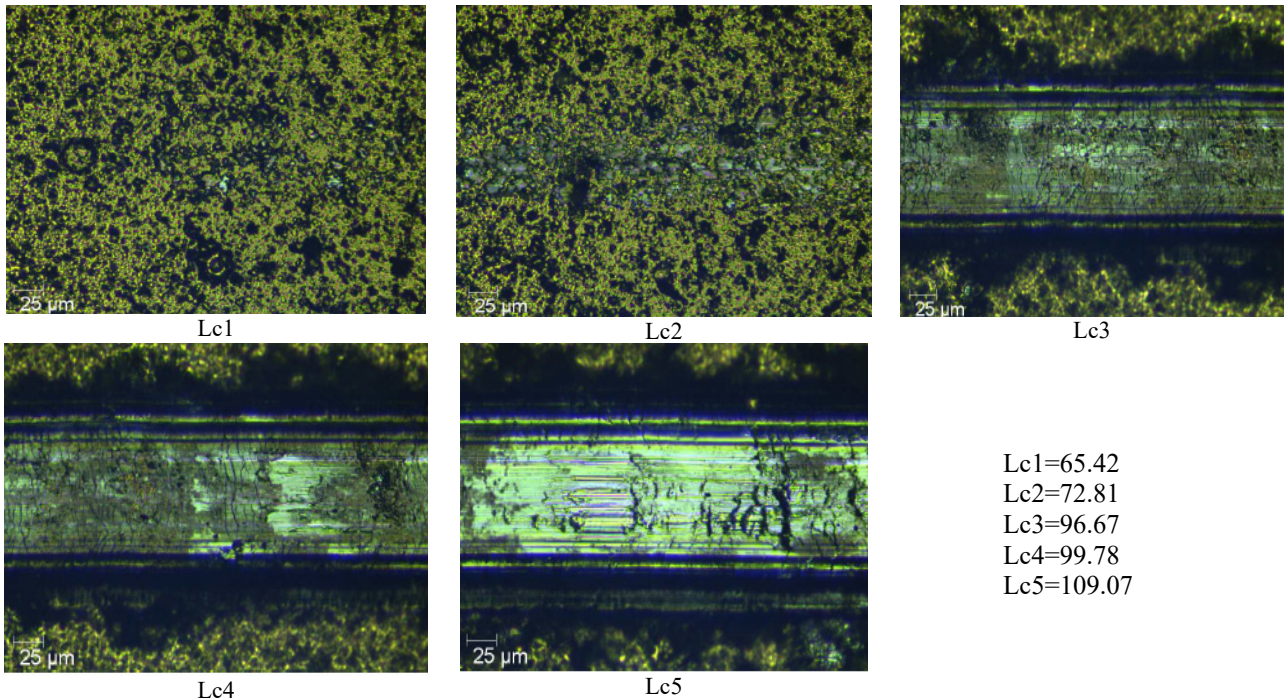


Figure 6. Images of the scratch on the surface of multilayer (TiZrSiY)N/NbN seria 1 at different loads

Table 2. Tribological parameters of multilayer (TiZrSiY)N/NbN coatings

Number of seria and thickness ratio between layers, nm	Friction coefficient		Wear factor, $\text{mm}^3 \times \text{N}^{-1} \times \text{m}^{-1}$	
	initial	tested	counterbody ($\times 10^{-6}$)	coatings ($\times 10^{-5}$)
seria 1: 18/36	0.318	0.498	2.2	1.4
seria 2: 31/45	0.341	0.512	2.0	1.5

When the wear tracks, some conclusions can be drawn about the wear mechanism. It is known that the main wear mechanisms of coatings are (1) adhesive wear with buildup of the coating material to the counterbody, (2) abrasive wear with the formation of grooves on the coatings surface by a more rigid counterbody, (3) tedious wear with removal of particles of the coating’s material, and (4) plastic deformation of the coatings material.

The SEM image of the worn surface and the corresponding profile of multilayer (TiZrSiY)N/NbN coating seria 1 is shown in Figure 7.

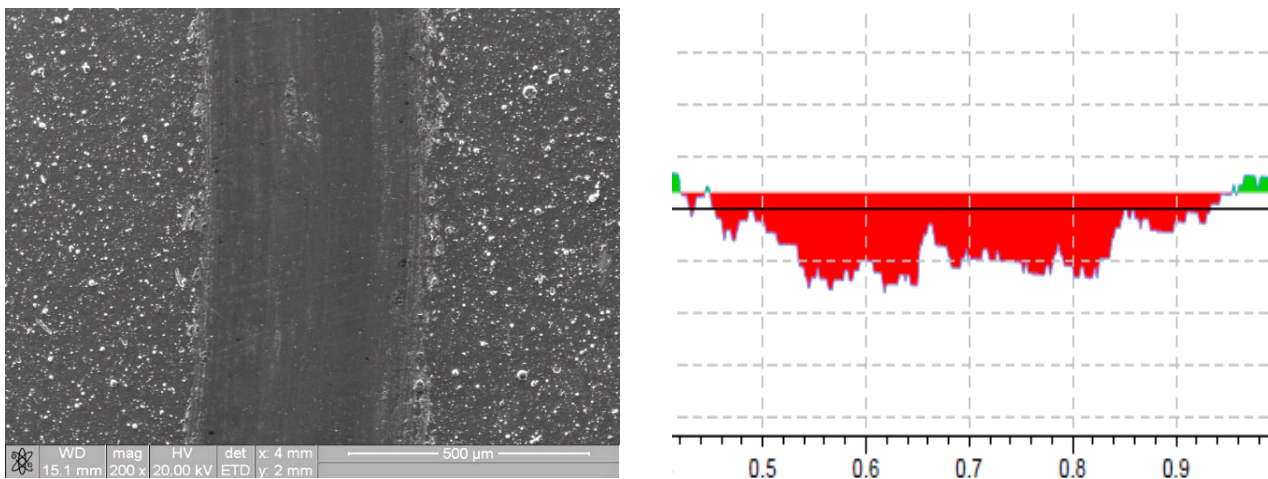


Figure 7. SEM image of the wear track and corresponding depth profile of multilayer (TiZrSiY)N/NbN coating seria 1

The nature of the wear track indicates the abrasive wear mechanism of the experimental coating. The bottom of the groove has a rather ridged structure, which is obviously associated with the presence of droplet defects in the volume of the coating.

Experimental studies indicate that under certain friction conditions, not only material transfer occurs, but also the interaction of the environment with sliding surfaces activated by friction energy. Under non-equilibrium friction conditions in air, it is possible to form a polyoxide tribofilm on the worn surface, which will contain oxidation products and the interaction of the phase components of the coating and the counterbody. It indicates that tribochemical oxidation occurred in the atmosphere.

The intensity of wear strongly depends on the hardness of the coating and the strength of the adhesive bond between the layers. It should be noted that for multilayer composite nanostructured coatings, the grain and interlayer boundaries are zones of intense energy dissipation. Cracks deviate from the direction of initial propagation and are partially or completely inhibited, which is actually a strengthening of the coating material. Furthermore, grain boundaries, which contribute to grain formation and material texture, can effectively strengthen the coating. Therefore, coatings with a nanoscale structure and multilayer architecture are characterised by longer service life, especially under conditions of cyclic thermomechanical stresses [24].

CONCLUSIONS

It is shown that in cathodic vacuum-arc multilayer (TiZrSiY)N/NbN coatings, a change in the thickness of individual layers and the bilayer period leads to a change in the lattice parameter of the nitride phases. The lattice parameter of TiN decreases with 0.4301 nm (the interval for the growth of each layer is 10 s) to 0.4295 nm (the interval for the growth of each layer is 20 s).

Experimental coatings have the complex structural state of the fcc-TiN phase and the mixture of hcp-NbN- ϵ and NbN- δ' phases. The increase in deposition time and, accordingly, thickness of the layers leads to a change in nitrogen concentration and, as a consequence, to an increase in the volume fraction of nitrogen-rich NbN- ϵ phase in NbN layers. The decrease in the deposition time results in the diffusion of NbN atoms into (TiZrSiY)N layers and the formation of a solid solution (TiNb)N phase (hcp crystal structure).

The mechanical and tribological data indicate the advantages of the coating with thinner layers (the interval for the growth of each layer is 10 s) and its high resistance to the initiation and propagation of cracks. This coating has a hardness of 39.7 GPa, Young's modulus of 438 GPa, and an adhesion strength of 99.78 N. The complete interfacial failure of the coating occurs at a critical load of 109.07 N.

Under dry conditions, both multilayer (TiZrSiY)N/NbN coatings have high wear resistance. The friction coefficients vary from 0.512 to 0.498. The wear mechanism of the experimental coating is mainly abrasive. Tribochemical oxidation in the atmosphere environment is revealed.

Acknowledgment

This work was supported by the National Research Foundation of Ukraine in the framework of the project No 2020.02/0234

ORCID

- Vyacheslav M. Beresnev, <https://orcid.org/0000-0002-4623-3243>; • Serhiy V. Lytovchenko, <https://orcid.org/0000-0002-3292-5468>
- Mykola O. Azarenkov, <https://orcid.org/0000-0002-4019-4933>; • Olga V. Maksakova, <https://orcid.org/0000-0002-0646-6704>
- Denis V. Horokh, <https://orcid.org/0000-0002-6222-4574>; • Bohdan O. Mazilin, <https://orcid.org/0000-0003-1576-0590>
- Diana Kaynts, <https://orcid.org/0000-0002-7242-027X>; • Irina V. Doshchechkina, <https://orcid.org/0000-0002-6278-7780>
- Oleg V. Gluhov, <https://orcid.org/0000-0003-2453-5504>

REFERENCES

- [1] A. Cavaleiro and J.T. de Hosson, editors *Nanostructured Coatings*, (Springer-Verlag, USA, 2006). <https://link.springer.com/content/pdf/bfm:978-0-387-48756-4/1?pdf=chapter%20toc>
- [2] A.D. Pogrebnyak, O.M. Ivasishin, and V.M. Beresnev. *Uspehi Fiziki Metallov*, **17**(1), 1 (2016). <https://doi.org/10.15407/ufm.17.01.001>
- [3] M. Stueber, H. Holleck, H. Leiste, et al., *J. Alloys Compd.* **483**, 321 (2009) <https://doi.org/10.1016/j.jallcom.2008.08.133>
- [4] N. Hansen. *Scr. Mater.* **51**, 801 (2004). <https://doi.org/10.1016/j.scriptamat.2004.06.002>
- [5] S.Z. Li, Y. Shi, and H. Peng, *Plasma Chem. and Plasma Proc.* **12**, 287 (1992). <https://doi.org/10.1007/BF01447027>
- [6] V.V. Vasil'ev, A.A. Luchaninov, E.N. Reshetnyak, V.E. Strel'nitskij, G.N. Tolmatcheva, and M.V. Reshetnyak, *PAST*, **2009**(2), 173 (2009). https://vant.kipt.kharkov.ua/ARTICLE/VANT_2009_2/article_2009_2_173.pdf
- [7] O.D. Pohrebniak, O.V. Bondar, O.V. Sobol, and V.M. Beresnev, *Soft Nanoscience Letters*, **3**, 46 (2013). <http://dx.doi.org/10.4236/snsl.2013.33009>
- [8] Q. Wan, N. Liu, B. Yang, H. Liu, and Y. Chen, *Journal of Wuhan University of Technology-Mater. Sci. Ed.* **34**, 774 (2019). <https://doi.org/10.1007/s11595-019-2116-9>
- [9] J. Musil, and H. Polakova. *Surf. Coat. Technol.* **127**, 99 (2000). [https://doi.org/10.1016/S0257-8972\(00\)00560-0](https://doi.org/10.1016/S0257-8972(00)00560-0)
- [10] D.C. Tsai, Y.L. Huang, S.R. Lin, et al. *Appl. Surf. Sci.* **257**, 1361 (2010) <http://dx.doi.org/10.1016/j.apsusc.2010.08.078>
- [11] B.D. Beake, L. Bergdoll, L. Isern, et al., *Int. J. Refract. Met. Hard Mater.* **95**, 105441 (2021). <https://doi.org/10.1016/j.ijrmhm.2020.105441>
- [12] M. Li, R. Wang, Y. Fan, and L. Wang, *Materials Research Innovations*, **19**(8), S8–190 (2015). <https://doi.org/10.1179/1432891715Z.0000000001653>

- [13] J. Yi, J. Xiong, Z. Guo, et al., *Ceram. Int.* **48**, 6208 (2022). <http://dx.doi.org/10.1016/j.ceramint.2021.11.161>
- [14] I. Aksionov, A. Andreev, V. Belous, et al., *Вакуумная дуга: источники плазмы, осаждение покрытий, поверхностное модифицирование [Vacuum arc: plasma sources, coating deposition, surface modification]* (Naukova dumka, Kyiv, 2012). (in Russian).
- [15] A. Bolgar, and V. Linvinenko, *Термодинамические свойства нитридов [Thermodynamic properties of nitrides]* (Naukova dumka, Kyiv, 1980). (in Russian).
- [16] M. Azarenkov, O. Sobol', A. Pogrebniak, and V. Beresnev, *Инженерия вакуумно-плазменных покрытий [Engineering of vacuum plasma coatings]*, (KhNU, Kharkiv, 2011). (in Russian).
- [17] H. Holleck, *Binäre und ternäre Carbide- und Nitridsysteme der Übergangsmetalle. Materialkundlich-Technische Reihe*, Nr. 6 (Hrsg. G. Petzow). (Gebrüder Borntraeger, Berlin - Stuttgart, 1984).
- [18] G.Y. Oya, and Y. Onodera. *J. Appl. Phys.* **45**, 1389 (1974). <https://doi.org/10.1063/1.1663418>
- [19] G.Y. Oya, and Y. Onodera. *J. Appl. Phys.* **47**, 2833 (1976). <https://doi.org/10.1063/1.323080>
- [20] V.M. Beresnev, S.V. Lytovchenko, D.V. Horokh, B.O. Mazilin, et. al., *Journal of nano- and electronic physics.* **11**(5), 05037 (2019). https://jnep.sumdu.edu.ua/download/numbers/2019/5/articles/jnep_11_5_05037.pdf
- [21] M. Hock, E. Schaffer, W. Doll, and G. Kleer, *Surface and Coatings Techn.* **163-164**, 689 (2003). [https://doi.org/10.1016/S0257-8972\(02\)00658-8](https://doi.org/10.1016/S0257-8972(02)00658-8)
- [22] V. Ivashchenko, S. Veprek, A. Pogrebniak, and B. Postolnyi, *Science and Technology of Advanced Materials.* **15**(2), 025007 (2014). <https://doi.org/10.1088/1468-6996/15/2/025007>
- [23] A.D. Pogrebniak, V.I. Ivashchenko, P.L. Skrynskyu, et al., *Composites Part B: Engineering*, **142**, 85 (2018). <https://doi.org/10.1016/j.compositesb.2018.01.004>
- [24] V.M. Beresnev, O.V. Sobol, S.S. Grankin, U.S. Nemchenko, et al., *Inorg. Mater. Appl. Res.* **7**, 388 (2016) <https://doi.org/10.1134/S2075113316030047>

ВАКУУМНО-ДУГОВІ БАГАТОШАРОВІ ПОКРИТТЯ (TiZrSiY)N/NbN: БУДОВА ТА ВЛАСТИВОСТІ ЗАЛЕЖНО ВІД ТРИВАЛОСТІ ОСАДЖЕННЯ ШАРІВ, ЩО ЧЕРГУЮТЬСЯ

Вячеслав М. Береснев^a, Сергій В. Литовченко^a, Микола О. Азаренков^{a,b}, Ольга В. Максакова^{a,c},
Денис В. Горох^a, Богдан О. Мазілін^a, Діана Кайниц^d, Ірина В. Дощечкіна^e, Олег В. Глухов^f

^a Харківський національний університет імені В.Н. Каразіна, майдан Свободи 4, 61022, м. Харків, Україна

^b Національний науковий центр «Харківський фізико-технічний інститут», вул. Академічна, 1, 61108, м. Харків, Україна

^c Інститут матеріалознавства, Словацький технічний університет у Братиславі,
вул. Яна Ботту, 25, 917-24, м. Трнава, Словаччина

^d Ужгородський національний університет, вул. Народна, 3, 88000, м. Ужгород, Україна

^e Харківський національний автомобільно-дорожній університет, вул. Ярослава Мудрого, 25, 61002, м. Харків, Україна

^f Харківський національний університет радіоелектроніки, проспект Науки, 14, 61166, м. Харків, Україна

Вакуумно-дуговим способом при одночасному розпиленні двох катодів різного складу сформовані багатошарові покриття, що містять різну кількість подвійних шарів (бішарів, відповідно 268 і 536). Один катод був виготовлений з багатокомпонентного матеріалу TiZrSiY, а другий – з технічного ніобію. Осадження покриття проводили в азотній атмосфері за негативного потенціалу зміщення на підкладці. Отримане покриття (TiZrSiY)N/NbN має періодичну шарувату структуру з товщинами окремих шарів, що визначаються тривалістю осадження (10 або 20 с). Загальна товщина покриття визначається кількістю сформованих бішарів. Зафіксовані у покритті фази TiN і NbN є полікристалічними, розміри зерен можна порівняти з розмірами шарів. У шарах спостерігається стовпчаста структура з переважною орієнтацією (111). Твердість сформованих покриттів залежить від товщини шарів і сягає 39.7 ГПа у покритті з найменшою з отриманих товщиною шарів. На всіх зразках з покриттям залежно від товщини шарів коефіцієнт тертя змінюється від 0,512 до 0,498. Досить велика величина коефіцієнта тертя обумовлена високою шорсткістю та наявністю краплинної фракції на поверхні та в покритті.

Ключові слова: вакуумно-дугове розпилення; багатошарові покриття; кількість шарів; текстура; мікротвердість; трибологічні властивості; фрикційні характеристики

COUNTING EFFICIENCY OF REGISTRATION OF CONTRIBUTIONS OF FAST NEUTRON REACTION PRODUCTS BY DETECTORS BASED ON OXIDE SCINTILLATORS

ZnWO₄, Bi₄Ge₃O₁₂, CdWO₄ and Gd₂SiO₅

✉ Gennadiy Onyshchenko^{a,b,*}, ✉ Borys Grynyov^b, ✉ Ivan Yakymenko^a, ✉ Sergei Naydenov^c,
✉ Pylyp Kuznietsov^a, ✉ Oleksandr Shchus^a

^a V.N. Karazin Kharkiv National University, 4 Svobody Sq., Kharkiv, 61022, Ukraine

^b Institute for Scintillation Materials, STC "Institute for Single Crystals", National Academy of Sciences of Ukraine,
60 Nauky Ave., 61001 Kharkiv, Ukraine

^c Institute for Single Crystals, STC "Institute for Single Crystals", National Academy of Sciences of Ukraine,
60 Nauky Ave., 61001 Kharkiv, Ukraine

*Corresponding Author e-mail: gennadiy.m.onyshchenko@karazin.ua

Received September 27, 2023; revised November 14, 2023; accepted November 25, 2023

The results of the study of the contributions of the interaction reactions of fast neutron sources of ²³⁹Pu-Be and ²⁵²Cf to the counting efficiency of registration by oxide scintillators CdWO₄, ZnWO₄, Bi₄Ge₃O₁₂ and Gd₂SiO₅, presented. The amount of gamma quanta per input neutron emitted from final nuclei excited in the reactions of inelastic scattering (n, n' γ)_{in}, resonant scattering (n, n)_{res} and capture (n, γ)_{res} and radiation capture (n, γ)_{cap} was measured. PMT R1307 operating in single-electron mode was used as a photodetector, the background rate was $\sim 5 \cdot 10^3 \text{ s}^{-1}$. The measured efficiency ε for scintillators $\varnothing 40 \times 40 \text{ mm}$ was 752 for ZWO, 532 for CWO, 37 for GSO, and 23 for BGO in "counts/neutron" units, measurement error rate $\sim 3\text{-}5\%$. The formation of the detector response is influenced by the parameters of the scintillator nuclei, such as the values of the interaction cross sections in the resonance region, the density of nuclear levels of the final nuclei, the lifetime of excited nuclear states, the upper limit of the resonance region of the cross section, as well as the scintillation time and geometric parameters of the scintillators. A phenomenological model of the response of an oxide scintillator to fast neutrons is proposed.

Keywords: Oxide scintillator, ZWO, BGO, CWO, GSO, Fast neutrons, ²³⁹Pu-Be, Resonance capture, Counting efficiency, Density of nuclear levels, Single photoelectron mode

PACS 29; 29.40.Mc; 29.40.-n

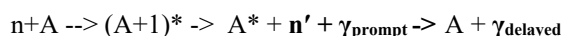
Creation of compact, highly-sensitive detectors of fast neutrons emitted by sources of the Pu-Be, ²⁵²Cf type is an actual task. Small-sized neutron and gamma-neutron radiation monitoring systems, designed to combat unauthorized transportation of fissile and radioactive materials, are especially needed in such detectors.

Registration of fast neutrons is possible with organic scintillators of the stilbene type however, detectors based on them require rather complex electronics, as a rule, they are grown in limited sizes. Detectors based on scintillation plastic have an insignificant efficiency of recording fast neutrons, $\varepsilon \sim 0.1$, while the necessary sensitivity is achieved due to the increase in the geometric dimensions and mass of the detector. The shortage of ³He and the high cost of manufacturing ³He counters stimulate the development of detectors based on new principles of recording fast neutrons.

The development of new fast neutron detectors requires information on the contributions to the detector response of the products of various mechanisms of interaction of neutrons with scintillator nuclei, since the energy of a fast neutron upon interaction with the substance of the detector changes approximately 10^8 times, from $\sim 11 \text{ MeV}$ to 0.025 eV . In addition, the magnitude of the detector's neutron response, in addition to the nuclear subsystem, is influenced by the atomic subsystem of the scintillator, namely the scintillation time, which must be considered when analyzing the contributions of mechanisms and developing new types of neutron detectors.

Fast neutrons from radioactive sources with energy $E \leq 10 \text{ MeV}$ experience such types of interaction with scintillator nuclei as elastic and inelastic scattering, resonance scattering, resonance capture, radiation capture. Therefore, three conditional energy intervals are distinguished:

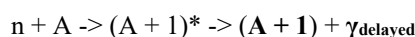
$\Delta E_{\text{in}} \sim 10 \text{ MeV} - 0.5 \text{ MeV}$, (n, n' γ)_{in}:



$\Delta E_{\text{res}} \sim 0.5 \text{ MeV} - 0.1 \text{ keV}$, (n, n')_{res} and (n, γ)_{res}:



$\Delta E_{\text{cap}} \sim 0.1 \text{ keV} - 0.025 \text{ eV}$, (n, γ)_{cap}:



In [1], it was shown that heavy elements can be used for calorimetry of fast neutrons, while the experimental efficiency of registration at the lowest registration threshold was $\varepsilon \sim 0.4-0.5$ instead of the expected $\varepsilon \sim 0.1$. Such a significant increase in the efficiency of the registration of high-energy neutrons was explained by the cascading action of the generation of secondary neutrons on heavy lead nuclei in the reaction of inelastic scattering. It was shown that the mechanism of inelastic scattering can be used to create highly efficient neutron calorimeters and neutron detectors of a new generation. In our work, heavy oxide scintillators such as ZWO (ZnWO₄), BGO (Bi₄Ge₃O₁₂), CWO (CdWO₄), GSO (Gd₂SiO₅) were studied [2-3, 26].

In these works, the inelastic scattering reaction $(n, n'\gamma)_{in}$ is the starting point that generates primary instantaneous and delayed gamma quanta from end-product nuclei and initiates the process of formation of secondary neutrons and multiple gamma quanta arising from the decay of excited states of final nuclei and increasing the statistics of events, generated by the primary fast neutron [4-7, 25, 27-28].

At the first stages of research [8], the contribution of high-energy gamma quanta ($E \sim 0.5-3$ MeV) from the inelastic scattering reaction $(n, n'\gamma)$ arising during the discharge of excited solid-state scintillator nuclei was carried out by small-sized oxide scintillators, $V \sim 1$ cm³. At the same time, the efficiency of the registration of fast neutrons, measured by a spectrometric path with an integration time of $\tau = 30$ us and a registration threshold of ~ 20 keV, was $\varepsilon \sim 0.4 - 0.5$ counts/neutron. Such a choice of the detector signal generation time was due to the need to suppress secondary cascade gamma quanta, and the small size of the detectors did not allow neutrons to reach the resonant energy range. Thus, for the reaction of inelastic scattering, the oxide scintillators looked practically equivalent.

In the future, in order to increase the counting efficiency of fast neutron registration, in our works [2, 3, 26] it was proposed to register multiple (cascade) gamma quanta generated between the highly excited transitions of final nuclei in the reactions of the interaction of neutrons with nuclei. For this purpose, it was proposed to register, in addition to the products of the inelastic scattering reaction, also the products of the resonance scattering and capture reactions.

The basis for such an approach is that the nuclei that make up some oxide scintillators (for example, Cd, W, Gd, Zn) have significant neutron interaction cross sections in the resonance region ($\sim 350 - 400$ barn), while cross sections in the inelastic region are only $\sim 2-3$ barn.

In addition, in the reaction of inelastic scattering and resonance capture of secondary neutrons, both instantaneous gamma quanta from excited states of final nuclei $(A+1)^*$ with lifetimes of $\sim 10^{-14} - 10^{-12}$ s are emitted, as well as delayed ones due to the lifetime consisting of final nuclei of several nanoseconds or more: – nucleus A^* from the reaction $A(n, n'\gamma)_{in}A^*$ and $(A+1)^*$ from the capture reaction $A(n, \gamma)_{res}(A+1)^*$.

The intermediate (compound) nucleus $(A+1)^*$ receives the average excitation energy $E \sim S_n + E_{n, kin}$ and, after the escape of the secondary neutron, which reduces the energy of the compound nucleus by the value of the neutron separation energy S_n , turns into the final nucleus A^* with an excitation energy equal to energy of the incident neutron $E_{n, kin}$. At the same time, mainly gamma quanta with an energy of about 1-3 MeV are emitted, which are confidently registered by the electronic path even with moderate speed and sensitivity. Another secondary cascade gamma quanta is also produced, initiated by secondary neutrons from the reaction of inelastic scattering upon capture in the resonant region. That is why the cross section of the resonance zone becomes important.

It should be noted that in the reaction of inelastic scattering $(n, n'\gamma)_{in}$, the neutron ejected from the nucleus has a significantly lower energy (on average $\sim 1-3$ MeV) compared to the initial energy ($\sim 4-10$ MeV), i.e. there is an effective slowing down of fast neutrons, which increases the probability of the subsequent capture of the escaped secondary neutron in the $(n, \gamma)_{res}$ reaction and the formation of a new compound nucleus.

In the case of capture of secondary slowed neutrons in the resonance region, it becomes possible to register additional instantaneous and delayed gamma quanta of small energies arising during the discharge of excited states of final nuclei $(A+1)^*$, if the density of levels of excited nuclei is such that the distance between the levels exceeds excitation threshold of scintillator molecules.

Our estimate of the densities of the levels included in the considered scintillators, carried out in this work on the basis of the thermodynamic model of reactions [9, 10, 11], is consistent with estimates of the multiplicity of gamma quanta in resonance capture reactions and the data of works [12-13, 24], the results of the evaluation indicate the existence of low-energy gamma quanta emitted between the transitions of highly excited states of final nuclei, capable of effectively exciting the molecules of the oxide scintillator. The energy range of incident neutrons, for which the contributions of researched mechanisms of nuclear reactions involving neutrons can be realized, is also estimated.

To implement the possibility of registering low-energy gamma quanta from transitions between highly excited short-lived states of nuclei when their energy is close to the excitation threshold of scintillator molecules, for example, for ZWO, it was necessary to use a photodetector operating in the single-electron counting mode and to develop a high-speed, low-noise amplifier path operating in the current-voltage converter mode, which has a resolution time of $\sim 1-2$ ns (bandwidth $\Delta f \sim 300$ MHz), a high amplification factor (~ 3000), low noise and a low registration threshold. The average excitation energy of the scintillator molecule was estimated based on the light output of the scintillator. For example, for ZWO, the light output is $\sim 10,000$ photons/MeV, so the excitation threshold of the ZWO molecule is $E_{thr} \sim 0.1$ keV. To ensure the necessary time separation of signals from the interaction of primary and secondary neutrons, scintillation detectors with a sufficiently extended geometry were used, the thickness of the scintillator is $\sim 40-50$ mm.

Thus, the registration of cascades of gamma quanta of various energies in the range from a few MeV to hundreds of eV, genetically related to the input neutron emitted by excited nuclei, in the presence of a high-speed measuring path with a low registration threshold and a low noise level, made it possible to significantly increase the statistics of useful events, occurring per one input neutron.

Literary data also confirm the generation of a significant number of secondary cascade gamma quanta from inelastic scattering reactions [14], from radiation and resonance capture reactions [12, 15-16]. But, at the same time, it should be borne in mind that the data on the multiplicity of secondary gamma quanta, if not specified, were accumulated by the spectrometric technique during a long-time interval, and were processed in a delayed time mode.

In addition to theoretical estimates of the multiplicity of gamma quanta, this work developed a technique and provided measurements of the efficiency of recording fast neutrons, confirming the increase in the measured efficiency of the detector due to the use of secondary products of the resonance scattering reaction and capture.

The scintillator response model proposed in this paper also indicates the very significant role of the time of scintillation of the excited states of the atomic subsystem of the scintillator. The results of the estimation of the travel lengths of fast neutrons considering elastic and inelastic scattering point to a noticeable role of light oxygen nuclei, which are part of scintillators, for the process of slowing down neutrons.

1. EXPERIMENT

In Table 1 shows some characteristics of the investigated scintillators.

Table 1. Main characteristics of the investigated oxide scintillators

Scintillator	ZnWO ₄	CdWO ₄	Bi ₄ Ge ₃ O ₁₂	Gd ₂ SiO ₅
nucleus (Natural abundance) (cross section, barn)	part of nuclei in a molecule			
Zn ($\sigma_{\text{cap}}=1.079$; $\sigma_{\text{res}}=2.495$; $\sigma_{\text{in}}=0.491$; $\sigma_{\text{el}}=1.697$; $\sigma_{\text{el res}}=97.22$)	1/6			
W ($\sigma_{\text{cap}}=18.11$; $\sigma_{\text{res}}=355.1$; $\sigma_{\text{in}}=0.485$; $\sigma_{\text{el}}=2.978$; $\sigma_{\text{el res}}=1118.5$)	1/6	1/6		
Cd ($\sigma_{\text{cap}}=2463$; $\sigma_{\text{res}}=71.935$; $\sigma_{\text{in}}=0.366$; $\sigma_{\text{el}}=2.650$; $\sigma_{\text{el res}}=85.13$)		1/6		
Gd ($\sigma_{\text{cap}}=48700$; $\sigma_{\text{res}}=398.3$; $\sigma_{\text{in}}=1.487$; $\sigma_{\text{el}}=1.937$; $\sigma_{\text{el res}}=170.61$)				2/8
Bi-209 ($\sigma_{\text{cap}}=0.0338$; $\sigma_{\text{res}}=0.1919$; $\sigma_{\text{in}}=0.392$; $\sigma_{\text{el}}=2.81$; $\sigma_{\text{el res}}=144.48$)			4/19	
Ge ($\sigma_{\text{cap}}=2.229$; $\sigma_{\text{res}}=5.935$; $\sigma_{\text{in}}=0.612$; $\sigma_{\text{el}}=1.686$; $\sigma_{\text{el res}}=120.08$)			3/19	
Si ($\sigma_{\text{cap}}=0.160$; $\sigma_{\text{res}}=0.0834$; $\sigma_{\text{in}}=0.524$; $\sigma_{\text{el}}=0.734$; $\sigma_{\text{el res}}=25.38$)				
O ($\sigma_{\text{cap}}=0.00016$; $\sigma_{\text{res}}=0.00016$; $\sigma_{\text{in}}=0.309$; $\sigma_{\text{el}}=0.957$; $\sigma_{\text{el res}}=46.13$)	4/6	4/6	12/19	5/8
Energy resolution, % (661.66 keV)	8.5	7	9	7.2
Density, g/cm ³	7.87	7.9	7.13	6.71
Effective atomic number	61	66	74	59
Light decay time, us	20	18	0.30	0.06/0.6
Light yield, pc/MeV	10000	20000	(8-10)*10 ³	(8-12.5)*10 ³
Gamma penetration depth, 1/e, cm (E _γ =0.662 MeV) 1/e, cm	1.44	1.45	1.40	1.49
Omission, (E _γ =0.662 MeV), a.u. (d = 4 cm)	0.062	0.064	0.058	0.069
The free path length of a neutron Σ, cm ⁻¹ Σ=Nσ, (E _n = 4 MeV)	0.389	0.373	0.390	0.394
Neutron penetration depth (1/e), 1/Σ, cm	2.571	2.682	2.563	2.540
Omission neutrons, a.u. (d = 4 cm)	0.211	0.225	0.210	0.207
Counting efficiency of registration of the fast neutrons, counts/neutron, ε, (n,n'γ) _{in} + (n,γ) _{res} ,	574	443	19.3	22.2
Counting efficiency of registration of the fast neutrons, counts/neutron, ε, (n,n'γ) _{in} + (n,γ) _{res} + (n,γ) _{cap}	752	532	23	37
Size, mm	Ø 52x42	Ø 45x42	Ø 40x40	18x18x42

The structural scheme for measuring the efficiency of fast neutron registration in spherical geometry is presented in Fig. 1a, b [19]. In the neutron ²³⁹Pu-Be source, accompanying gamma radiation from the reactions is present:

- ${}^4\text{He} + {}^9\text{Be} \rightarrow {}^{13}\text{C}^* \rightarrow {}^{12}\text{C}^* + \text{n} \rightarrow {}^{12}\text{C} + \gamma$, (${}^{12}\text{C}^*$, $E_\gamma = 4.43 \text{ MeV}$);
- ${}^4\text{He} + {}^9\text{Be} \rightarrow {}^{13}\text{C}^* \rightarrow {}^{13}\text{C} + \gamma$, (${}^{13}\text{C}^*$, $E_\gamma = 3.68 \text{ MeV}$).

The advantage of spherical geometry is the elimination of the need to introduce corrections for neutron scattering in the lead sphere, which is used to attenuate the accompanying gamma radiation from the source. The measurements used (α, n) a ²³⁹Pu-Be source and a ²⁵²Cf spontaneous fission neutron source with a flow of fast neutrons $\sim 10^5 \text{ neutron} \cdot \text{s}^{-1}$.

The source was placed inside a lead ball with a diameter of 100 mm with a channel to the center of the ball with a diameter of 20 mm. Photomultiplier R1307 Hamamatsu is used. The detector-source distance is 1000 mm. To weaken the external gamma background, a lead screen $d = 5$ mm is used.

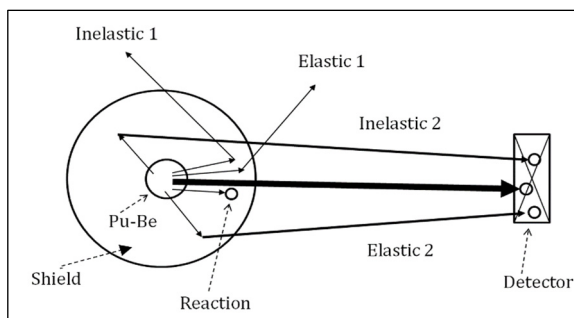


Figure 1a. Structural diagram of measurement of the counting efficiency of registration of fast neutrons in spherical geometry: 1 - photomultiplier R1307; 2 - scintillator under investigation; 3 - lead screen $d = 5$ mm for weakening the gamma background; 4 - lead layer $\varnothing 100$ mm with a cylindrical channel $\varnothing 20 \times 50$ mm; 5 - $^{239}\text{Pu-Be}$ neutron source; distance detector - source - 1000 mm

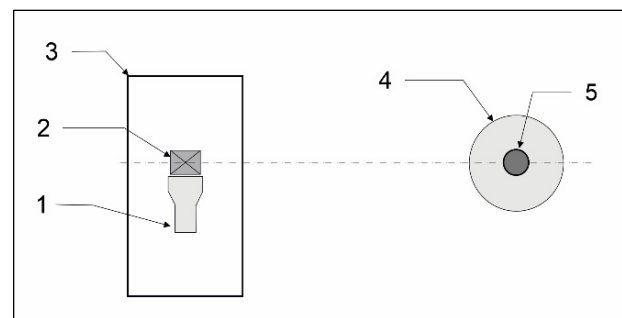


Figure 1b. The processes of scattering (\rightarrow) and absorption (\circ) of fast neutrons in spherical geometry

The response to neutrons in the scintillators under study is formed by cascade gamma quanta emitted in the reactions of inelastic scattering $(n, n'\gamma)_{in}$, resonant scattering $(n, n)_{res}$ and capture $(n, \gamma)_{res}$, radiation capture $(n, \gamma)_{cap}$, as well as due to cascade gamma quanta that appear during the capture of secondary slowed neutrons. The value of the "count efficiency of neutron registration" (CENR) by oxide scintillators CWO, ZWO, BGO, GSO was measured in units of "counts/neutron", i.e. in units of the ratio of the detector count rate to the number of particles falling on the entire detector in 1s (the flow on the entire detector), i.e. CENR is the average number of pulses from the detector that fall on one input particle.

The source of neutrons is located in a lead sphere, which effectively scatters neutrons, both in elastic and inelastic scattering, while absorbing them very weakly, so that the number of neutrons emitted into space does not change and can be considered. The capture cross section of fast neutrons in Pb is ~ 1.11 mb.

Scattering in the direction of the detector, i.e. into the front hemisphere is completely compensated by backscattering into the detector from other points of the sphere, i.e. posterior hemisphere. Thanks to the spherical symmetry of the scatterer, the number of neutrons passing through each square centimeter of the spherical surface will also remain unchanged. Consequently, the lead spherical scatterer practically does not affect the number of scattered neutrons arriving at the detector, with the exception of neutrons absorbed in the lead layer due to the (n, γ) reaction. Thus, the scattering layer does not change the neutron count rate in the detector, performs the function of weakening gamma quanta, which leads to a decrease in the harmful influence of secondary gamma quanta from the Pu-Be source on the accuracy of measurements, reduces errors due to the "accumulation factor" of gamma quanta, scattered from the walls of the room. The contribution of scattered fast neutrons from the walls of the laboratory room was $\sim 3\%$. Due to the increase in the effective size of the neutron source, it is necessary to carry out measurements at somewhat larger distances (~ 1 m) compared to the "narrow" geometry. Deviation from the law of inverse squares for a distance of 1.2 m does not exceed 3%.

The correction for the absorption coefficient of fast neutrons in the shielding sphere was measured by a $^6\text{LiI}(\text{Eu})$ detector for a source-detector distance of 2 m and amounted to $\sim 2.5\%$. Scintillator size $^6\text{LiI}(\text{Eu})$: $\varnothing 15 \times 10$ mm, ^6Li enrichment 96%. The thermal peak $(\alpha + t)$ for $^6\text{LiI}(\text{Eu})$ had a gamma equivalent of 3.98 MeV, fast neutrons were registered in the energy range of 3.98 MeV \div 14 MeV.

The additional contribution from gamma quanta with energy $E_\gamma = 4.43$ MeV for the ZWO scintillator (correction for registration efficiency of gamma) amounted to $\sim 7\%$, while the following was assumed: the γ/n ratio for the $^{239}\text{Pu-Be}$ source is 1, the transmission of gamma quanta with energy of 4.43 MeV by a lead sphere with a thickness of 50 mm $\sim 9\%$, absorption of such gamma quanta in ZWO with an effective thickness of 46 mm $\sim 76\%$.

The correction for the absorption coefficient of fast neutrons in the protective sphere was also measured using a ^{252}Cf source. A distinctive feature of the ^{252}Cf source is the absence of high-energy accompanying gamma radiation and a "softer" form of the spectrum, which can affect the efficiency of the excitation of the gamma quanta generation mechanisms. The difference in the measurement results for the ZWO scintillator was 11.8%, which can be explained by the presence of accompanying gamma quanta with an energy of $E = 4.43$ MeV (7%) and a harder form of the spectrum of the Pu-Be source, which leads to an increase in the output of secondary gamma quanta (4.8 %). The background attenuation coefficient in the energy range of 10–150 keV by a 5-mm-thick lead shield around the scintillator was ~ 3 .

In order to reduce the influence of fluctuations of the cosmic neutron background, the measurement of the registration efficiency was carried out by five exposures - "100 s - background measurement, then 100 s - signal measurement". The statistical error for each exposure was $\sim 1\%$.

On Fig. 2 shows the structural diagram of the measuring path, consisting of three channels - single-electron (counting channel) ($\tau \sim 1$ ns), fast spectrometric ($\tau \sim 50$ ns, Amptek DPP PX-5), slow spectrometric (linear spectrometric amplifier, $\tau \sim 1$ us). The photodetector is a Hamamatsu R1307 PMT, the rise time of the signal is ~ 7 -8 ns. The single-electronic account mode is used to lower the registration threshold, increase sensitivity, and reduce the registration resolution time.

To amplify signals from PMT, a current-voltage converter was developed, Fig. 3, amplifying signals with a rise time of $\tau_{ris} \sim 0.5$ ns. The first stage is made according to the "current - voltage converter" scheme on OP type 4817, the input bias current is 2 nanoamps, the total voltage gain of the second - seventh stages is $k_{amp} \sim 740$, which made it possible to register low-energy ($E \sim 0.1$ keV) gamma quanta. As the output driver, the 7th stage on the opamp type 7171 was used.

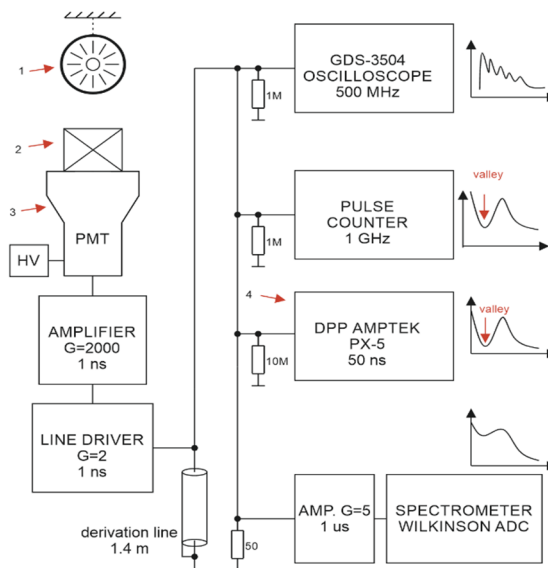


Figure 2. Structural diagram of the electronic path for measuring the counting efficiency of registration of fast neutrons by scintillators. 1 – neutron source, 2 – scintillator, 3 – PMT R1307, 4 – digital pulse processor

In order to reduce the dead time of the tract and quickly restore the baseline of the tract, shortening (differentiation) of signals using a cable delay line was used.

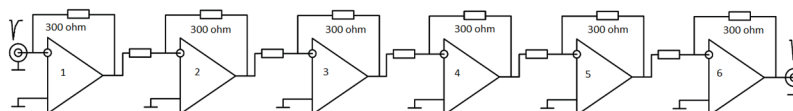


Figure 3. Structural diagram of a broadband pulse preamplifier on OP type ADA4817. The input resistors in the OP are 100 Ohm. The rise time of the first cascade is $\tau_{ris} \sim 0.5$ ns

The total dark noise of the PMT base line and the electronic preamplifier noise is 50 mV at a voltage of 1250 V on the PMT. The dark loading of the measuring path in the single-electron mode for this PMF sample and a $\varnothing 45 \times 40$ mm scintillator is $\sim 5 \times 10^3$ c⁻¹. A DPP Amptek digital processor, signal processing time of 50 ns, and a pulse counter with a bandwidth of $\Delta f \sim 1$ GHz were used as a recorder.

On Fig. 4 shows the response of the ZWO scintillator to neutrons from the ²³⁹Pu-Be source in the single-photoelectron (upper figure) and spectrometric ($\tau_{rise} \sim 1$ μ s, lower figure) modes. The speed of the electronic path $\tau_{rise} \sim 1$ ns.

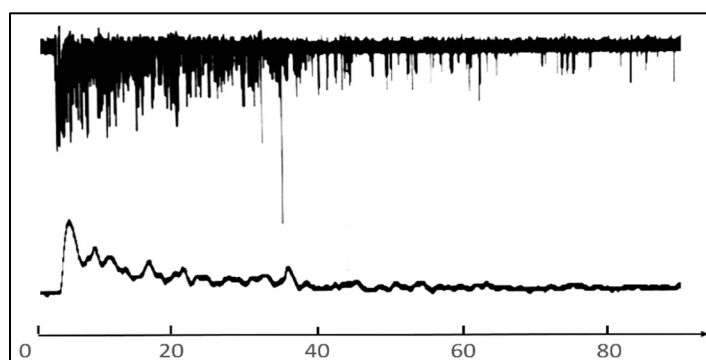


Figure 4. The response of the ZWO scintillator to fast neutrons from the ²³⁹Pu-Be source in the single-photoelectron ($\tau_{rise} \sim 1$ ns, upper figure) and spectrometric ($\tau_{rise} \sim 1$ μ s, lower figure) modes. Here X is time, μ s

On Fig. 5 shows the waveform at the output of the broadband channel during the registration of neutrons from the ^{239}Pu -Be source by the ZWO scintillator. The duration of the leading edge of the signals $\tau \sim 8$ ns is determined by the PMT parameters.

The hardware spectrum measured by DDP Amptek during irradiation of the ZWO scintillator with neutrons from the ^{239}Pu -Be source is shown in Fig. 6. Signal processing time is 50 ns.

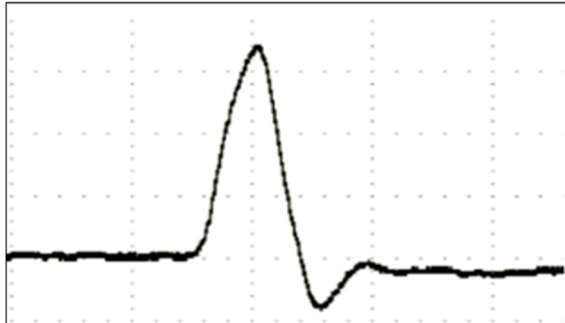


Figure 5. Response to neutrons from the ZWO scintillator at the output of the broadband channel. The dropout at the trailing edge of the signal is due to the shortening delay line, $2\tau = 20$ ns. Scale along the X axis is 25 ns/div

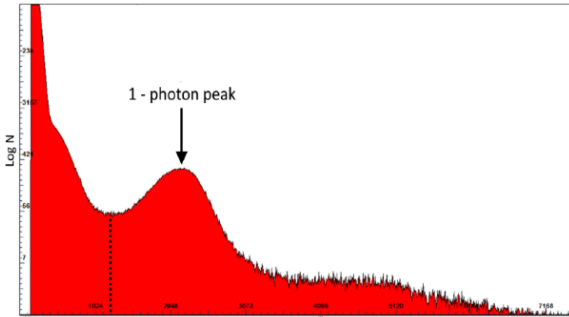


Figure 6. Hardware spectrum of the ZWO scintillator on PMT R1307, HV = 1250 V. Y axis – Log(Counts), X axis – channels

2. METHODOLOGY FOR THE STUDY OF CONTRIBUTIONS OF PRODUCTS OF REACTIONS WITH NEUTRONS TO THE SCINTILLATOR RESPONSE

The processes of generation of cascade gamma quanta and secondary neutrons in the reactions of elastic and inelastic scattering, resonant elastic scattering and capture of fast neutrons on the nuclei of the ZWO scintillator are schematically presented as follows:

- **elastic processes** – $(n, n')_{el}$: $n + (A) \rightarrow n' + (A)$;
 $\sigma(n, n) = 0.957b$ (O-16, $E=14\text{MeV}$)
- **inelastic processes** – $(n, n'\gamma)_{in}$: $n + (A) \rightarrow (A+1)^* \rightarrow n' + (A)_{final}^*$
 $\sigma(n, n'\gamma)_{in} = 0.491 b$ (Zn);
 $\sigma(n, n'\gamma)_{in} = 0.485 b$ (W)
 $\downarrow \gamma_{prompt} \quad \downarrow \gamma_{delay}$
- **resonance elastic scattering** – $(n, n')_{res}$: $n + (A) \rightarrow n' + (A)$
 $\sigma(n', n'')_{res} = 113 b$ (Zn);
 $\sigma(n', n'')_{res} = 136 b$ (W)
 $\downarrow n' \rightarrow \dots$
- **resonance capture** – $(n', \gamma)_{res}$: $n' + (A) \rightarrow (A+1)_{final}^* \rightarrow (A+1)$
 $\sigma(n, \gamma)_{res} = 2.495 b$ (Zn);
 $\sigma(n, \gamma)_{res} = 355.1 b$ (W)
 $E_n \sim 8 \text{ keV} - 600 \text{ keV}$
 $\downarrow \gamma_{del}$
- **resonance capture** – $(n', \gamma)_{cap}$: $n' + (A) \rightarrow (A+1)^* \rightarrow (A+1)$
 $\sigma(n, \gamma)_{cap} = 1.079 b$ (Zn)
 $\sigma(n, \gamma)_{cap} = 18.11 b$ (W)
 $\downarrow \gamma_{del}$

In the reactions of inelastic scattering $(n, n'\gamma)_{in}$ on heavy nuclei of scintillators, such as Bi, W, Gd, Cd, neutrons can lose energy up to 2-3 MeV on average, slowing down considerably. Along with inelastic scattering, neutrons are effectively slowed down in the elastic scattering reaction on light nuclei that are part of oxide scintillators, such as ^{16}O .

Secondary neutrons can re-enter the resonance capture reaction $(n, \gamma)_{res}$. At the same time, the role of such nuclei as ^{64}Zn , in which $E_{res} \sim 0.6 \text{ MeV}$, can be very significant. When neutrons interact with nuclei, both excited compound nuclei $(A+1)^*$ and final excited nuclei A^* appear. In $(n, n'\gamma)_{in}$ reactions from $(A+1)^*$, as a rule, 2-4 instantaneous gamma quanta with different energies fly out on average, but all of them will be registered in real time as one response due to the small the lifetime of compound nuclei.

An insignificant amount of gamma quanta with different energies from the final nuclei A^* from the $(n, n'\gamma)_{in}$ reaction can be recorded separately in real time due to the low excitation energy, because some A^* nuclei can be in an excited state for a few nanoseconds or more.

In the capture reactions $(n, \gamma)_{res}$ from the final nuclei $(A+1)^*$, due to the significantly higher excitation energy than in the $(n, n'\gamma)_{in}$ reaction, from several tens to several hundreds of instantaneous gamma quanta fly out with different energy, but their registration on a real time scale will depend on the life time of excited states.

In works [12, 24] the values of the multiplicity of gamma quanta arising in the radiation capture of neutrons on nuclei are given, i.e. from excited nuclei $(A+1)^*$. The value of the multiplicity of N_γ during the capture of thermal neutrons by nuclei of average atomic weight (these are Si, Zn, Ge isotopes) fluctuates within the limits of $N_\gamma = 17-175$ counts/neutron. For nuclei of high atomic weight (isotope W), the value of multiplicity varies within $N_\gamma = 75-225$ counts/neutron.

In the inelastic scattering of neutrons on the nuclei, there is also a certain multiplicity of gamma quanta emitted by final excited nuclei A^* . This is confirmed by the data of works [14, 20]. The value of the multiplicity of N_γ in the interaction of neutrons with nuclei of average atomic weight is in the range of 4-14 counts/neutron. For heavy nuclei, the value of multiplicity N_γ is in the range of 70-130 counts/neutron.

The smaller value of the multiplicity in inelastic scattering compared to the resonance capture reaction can be explained by the fact that the final nuclei A^* in inelastic scattering have a significantly lower excitation energy than the final nuclei of radiation capture due to neutron escape, which sharply reduces the excitation energy by the amount of nuclear binding energy.

It should be noted that separate hardware registration of cascaded gamma quanta in real time is possible only if the lifetimes of excited states, the intervals between cascade events, and the transport delay of secondary neutrons when moving into the scintillator material until the moment of capture are units of nanoseconds or more.

The use of a high-speed measuring path capable of processing signals with a rise time of ~ 0.5 nanoseconds, for example, a PMT path in the single photoelectron counting mode, contributed to a significant decrease in the energy threshold of registration to the energy of gamma quanta, which constitutes the excitation threshold of oxide scintillator molecules, about $E_{thr} \sim 0.02 - 0.1$ keV.

Lowering the threshold of registration made it possible to increase the contribution to the detector response of low-energy gamma quanta from high-lying transitions of excited final nuclei $(A+1)^*$, especially from the reaction of resonance capture on heavy nuclei, for example W, Gd.

This paper presents the experimental results of measurements of contributions of multiple gamma quanta generated both in inelastic scattering and in resonance and radiation capture of neutrons by oxide scintillators. In addition, it was experimentally confirmed in our work [3] that the growth of useful statistics of events due to cascade gamma quanta, which are caused by incident neutrons, ultimately leads to an increase in the sensitivity of the neutron detector.

Secondary neutrons from the inelastic scattering reaction $(n, n'\gamma)$ have significantly lower energy and after additional deceleration on light nuclei can be captured more effectively in the resonance region of Zn ($E_{res_max}(Zn) \sim 600$ keV) and W ($\sigma_{el_res} = 355.1$ b), which will contribute to an increase in the multiplicity of secondary neutrons and an increase in the statistics of events.

2.1 ESTIMATION OF THE MULTIPLICITY OF GAMMA QUANTA FROM THE INELASTIC SCATTERING REACTION

In reactions with neutrons, four types of spectra are experimentally observed: – a monoline with an energy equal to the binding energy of a neutron, if an excited light nucleus emits a gamma quantum, it is in the ground state; – cascades of gamma quanta with discrete, energy-separated levels for light nuclei (Si) (Fig. 7a); – cascades of gamma quanta overlapping in the low-energy region, but still separated in the high-energy region (medium nuclei, Zn) (Fig. 7b). As the atomic weight increases in the region of 1.5-3.5 MeV, a wide hump appears, which is formed by gamma quanta from overlapping highly excited compound nuclei (heavy nuclei, W) (Fig. 7c) [16].

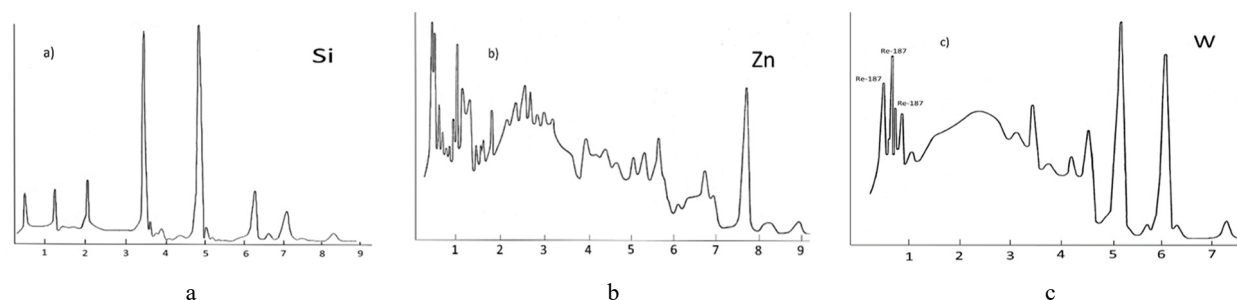


Figure 7. Types of spectra observed during the interaction of fast neutrons from the reaction $(n, n'\gamma)_{in}$ with nuclei of different atomic weights:

a) – light Si nucleus; b) – the nucleus of the average atomic weight of Zn, the hump in the region of 1.5-3.5 MeV begins to form; c) – heavy nucleus W, a hump is formed in the region of 1.5-3.5 MeV. The Y axis is the number of counts, the X axis is the energy, MeV [16]

The region of the spectrum in the interval 1.5-3.5 MeV is formed in the reaction of inelastic scattering by gamma transitions of excited states of the final nucleus. In this interval, the levels in the middle nuclei of Zn are resolved by energy. It can be seen in Fig. 7 c that in the interval of 1.5-3.5 MeV in the heavy nucleus W, the levels are not resolved in terms of energy, therefore, the energy of gamma-quantum transitions between these levels may not be large enough for reliable registration. This fact can be explained by the high density of excited levels in heavy final nuclei, because the responses of the levels located in the high-density zone merge into one instantaneous response of gamma quanta.

Both excited compound nuclei $(A+1)^*$ and final excited nuclei of scintillators A^* participate in the formation of cascade gamma quanta. In addition, secondary neutrons from the reactions of inelastic scattering $(n, n'\gamma)_{in}$ and resonant scattering $(n, n)_{res}$ can experience capture again, thus allowing to separate in time the cascade events initiated by the primary neutron and increase the useful statistics of gamma quanta generated primary neutron.

In Table 2 presents the neutron cross sections of reactions of resonance capture $(n, \gamma)_{res}$, elastic resonance scattering $(n, n)_{res}$, inelastic scattering $(n, n'\gamma)_{in}$, radiation capture $(n, \gamma)_{cap}$ for a natural mixture of nuclear isotopes entering in the compound of the studied oxide scintillators $ZnWO_4$, $Bi_4Ge_3O_{12}$, $CdWO_4$, Gd_2SiO_5 . [21-22].

Table 2. Cross sections of neutron reactions $(n, n'\gamma)_{in}$, $(n, \gamma)_{res}$, $(n, n)_{el}$, $(n, \gamma)_{cap}$ for a natural mixture of nuclear isotopes included in scintillators $ZnWO_4$, $Bi_4Ge_3O_{12}$, $CdWO_4$, Gd_2SiO_5

	0.0253 eV, (b) $(n, \gamma)_{cap}$	0.5 eV-10 MeV, (b) $(n, n)_{res}$	0.5 eV-10 MeV, (b) $(n, \gamma)_{res}$	14 MeV, (b) $(n, n'\gamma)_{in}$	14 MeV, (b) $(n, n)_{el}$	Threshold, keV $(n, n'\gamma)_{in}$	E_{res_max} keV
(A)	(A+1)	(A)	(A+1)	(A)	(A)		
$^{48}Cd\text{-nat}$	2463.26	85.13	71.935	0.366	2.650	247.6	8
$^{74}W\text{-nat}$	18.11	1118.48	355.1	0.48505	2.798	46.7	6
$^{30}Zn\text{-nat}$	1.079	97.224	2.4955	0.49025	1.697	94.7	600
$^{83}Bi\text{-nat}$	0.0342	144.48	0.19196	0.3923	2.810	900.7	200
$^{32}Ge\text{-nat}$	2.229	120.08	5.9348	0.61168	1.686	0.595	15
$^{64}Gd\text{-nat}$	48699	170.61	398.3	1.4872	1.937	54.88	8
$^{14}Si\text{-nat}$	0.1604	25.378	0.0834	0.52419	0.734	1.779	1800
$^8O\text{-16}$	1.6e-4	46.13	1.6e-4	0.3095	0.957	0.71	

In our opinion, the most significant parameters of the indicated nuclei, which are used in the analysis of deposits of neutron interaction products, are the resonance capture cross section, the density of nuclear levels of the final nuclei, and the elastic scattering cross section in the resonance region $(n, n)_{res}$.

It should be noted that since the Gd and W nuclei have similar parameters of the resonance capture zone (sections and the upper limit of the resonance zone), then, from the point of view of the nuclear subsystem, the GSO and ZWO scintillators should have approximately the same CENR, but this is not observed in reality. Apparently, an equally important role in the formation of the scintillator response is played by the atomic subsystem of the scintillator, i.e., time of scintillation. Indeed, the ratio of the efficiencies of the scintillators $ZWO - \varepsilon = 574 \text{ cnt/neutron}$ and $GSO - \varepsilon = 22.2 \text{ imp/neutron}$ correlates with the ratio of the durations of the scintillation times: $ZWO - \tau = 20 \text{ us}$ and $GSO - \tau = 0.6 \text{ us}$.

The work [13] (Fig. 8) shows the densities of the levels of final nuclei depending on the mass number of nuclei. Ellipses highlight regions of ^{64}Zn and ^{182}W nuclei. The upper dashed line is the density of levels corresponding to the transition energy equal to $E \sim 0.001 \text{ keV}$ – this is the lower threshold of the single-electron registration mode, the lower dashed line is the average excitation energy of the ZWO molecule, $E \sim 0.1 \text{ keV}$. It is possible to conclude that practically all gamma quanta from reactions of inelastic scattering and resonance capture on Zn and W nuclei can be registered in the single-electron mode and will contribute to increasing the counting efficiency of registration.

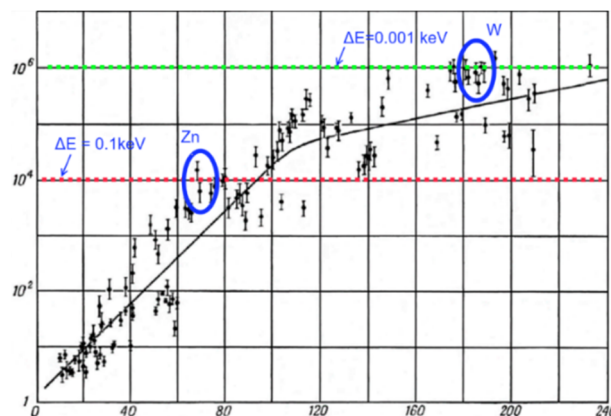


Figure 8. Density of levels of final -state nuclei ρ depending on the mass number of nuclei. Here Y is the density of levels, MeV^{-1} ; here X is the mass number of nuclei. Ellipses highlight regions of ^{64}Zn and ^{182}W nuclei. The upper dotted line is the lower threshold of registration $E_{th} \sim 0.001 \text{ keV}$ in the single-electron mode, the lower dotted line is the average excitation energy of the ZWO molecule, $E \sim 0.1 \text{ keV}$ [13]

In this paper, based on the thermodynamic model of nuclear reactions, some parameters of the levels of the final nuclei included in the studied scintillators [9-11] are estimated. The density of the nuclear levels ρ of the excited states of the final nuclei from inelastic scattering reactions $(n, n'\gamma)_{in}$ and resonant capture $(n, \gamma)_{res}$ on the nuclei are estimated. The working interval of energies of incident neutrons, in which gamma quanta are generated, registered by the photodetector, the energy of the secondary neutron is estimated. (Table 3). The possibility of a statistical description of nuclei is associated with a large number of system states in the energy interval of averaging, excited in compound nuclei and final nuclei during neutron capture.

The basis of the model of the reaction $a + A \rightarrow C^* \rightarrow b + B$, passing through a compound nucleus, is the description of the distribution of ejected particles by energy (spectrum): $W(E) \sim E b \sigma_C(E) \rho_B(E_{Bb} - E)$, where

E is the energy of the ejected particles, $\sigma_c(E)$ is the formation cross section of the compound nucleus, $\rho_B(E_{Bb} - E)$ is the density of levels of the final nucleus, $E_B = E_{Bb} - E$ is the excitation energy of the final nucleus, E_{Bb} is the energy of particle b , E_{Bb}^{max} is the maximum energy b corresponding to the formation of the final nucleus B in the ground state, E_a is the energy of the incident particle.

Table 3. Comparative evaluation of the parameters of light and heavy final nuclei excited by fast neutrons in the reactions of inelastic scattering and resonance capture

Reaction A(a, b)B	$^{64}\text{Zn}(n, \gamma)_{\text{res}}^{65}\text{Zn}$		$^{64}\text{Zn}(n, n'\gamma)_{\text{in}}$		
The energy of the incident neutron E_a , MeV	0,01	0,600	1.3	5	12.5
Neutron attachment energy	7.981		7.981		
1 level energy E_1	-	-	0.992		
Excitation energy compound nuclei, MэB	7.99	8.58	8.29	12	19.5
Excitation energy end nuclei state, макс., E_B , MeV	-	-	0.31	4.0	11.5
E_{Bb}^* max, max energy b , (n')	-	-	0.31	4.0	11.5
End nuclei temperature, Θ , MeV	1.348	1.397	0.27	0.96	1.63
Level density ρ , MeV^{-1}	2201	2937	106	259	10200
Levels distance, $D=1/\rho$, keV	0.45	0.34	9.4	3.9	0.1
$E_{\text{kin. out.}}(n')$, 2Θ , MeV	-	-	0.53	1.92	3.26
Reaction A(a, b)B	$^{182}\text{W}(n, \gamma)_{\text{res}}^{183}\text{W}$		$^{182}\text{W}(n, n'\gamma)_{\text{in}}$		
The energy of the incident neutron E_a , MeV	0,001	0,01	1.01	2.0	2.58
Neutron attachment energy	6.191		6.191		
1 level energy E_1	-	-	0.1001		
Excitation energy compound nuclei, MэB	6.19	6.20	7.1	8.09	8.67
Excitation energy end nuclei state, макс., E_B , MeV	-	-	0.91	1.90	2.48
E_{Bb}^* max, max energy b , (n')	-	-	0.91	1.90	2.48
End nuclei temperature, Θ , MeV	0.711	0.711	0.27	0.39	0.45
Level density ρ , MeV^{-1}	9.6e+05	9.7e+05	944	4200	9710
Levels distance, $D=1/\rho$, keV	0.001	0.001	1.06	0.24	0.1
$E_{\text{kin. out.}}(n')$, 2Θ , MeV	-	-	0.55	0.79	0.90

Considering the nucleus as a degenerate Fermi gas, the Weiskopf formula can be used for $\rho(E_B) = (C/E_B^2) \exp(2\sqrt{aE_B})$, where E_B is the excitation energy of the final nucleus, a constant $C \sim 1$, the constant a was determined by the density of single-particle compounds on the Fermat surface according to the formula $a = (\frac{\pi^2}{2}) (\frac{A}{E_F})$, $E_F \sim 37 \text{ MeV}$. The temperature of the final nuclei B was estimated for a given excitation energy according to $\theta = \sqrt{E_B/a}$. The temperature of the compound nuclei C was estimated as $\theta = \sqrt{E_{Bb}^{max}/a} = \sqrt{E_a/a}$.

The probability of recording gamma quanta from inelastic scattering reactions on W nuclei is significantly lower due to the high density of W levels. Despite the high gamma multiplicity N_γ for W , from the results of the estimates given in Tab. 3 shows that the working interval of W nuclei ($\Delta E=1-2.6 \text{ MeV}$) is significantly smaller than that of Zn ($\Delta E= 1.3-12.5 \text{ MeV}$). Only gamma quanta from the discharge of some long-lived states can contribute to multiplicity, and the registration of short-lived low-energy gamma quanta from highly excited states requires a highly sensitive single-electron path.

From Tab. 3 shows that low-energy cascade gamma quanta with energy from $E \sim 0.1 \text{ keV}$ and higher are generated in transitions of highly excited states of final nuclei (neutron energy range $E \sim 1.3 - 12.5 \text{ MeV}$ for Zn and $\sim 1.0 - 2.6 \text{ MeV}$ for W). At the same time, the final nuclei of average weight Zn^* in the inelastic scattering reaction have the density of nuclear levels from $1.06 \cdot 10^2 \text{ MeV}^{-1}$ to $\sim 1.0 \cdot 10^4 \text{ MeV}^{-1}$, which corresponds to the transition energy from 9.4 keV to 0.1 keV . Gamma quanta in this energy range can excite ZWO molecules and be recorded in the single-electron mode.

In the final heavy nucleus - W^* in the reaction of inelastic scattering, the density of nuclear levels ranges from 944 to $\sim 9.7 \cdot 10^3 \text{ MeV}^{-1}$ in the energy interval of incident neutrons $1-2.6 \text{ MeV}$, which corresponds to the distance between levels from 1 keV to 0.1 keV . Gamma quanta in this energy range can also excite ZWO molecules and be recorded in the single-electron mode.

Consequently, model calculations indicate that in inelastic scattering reactions, the multiplicity of cascaded gamma quanta of final nuclei of medium weight will be greater than that of final heavy nuclei due to a wider operating range of neutron energies.

At the same time, the energy of the cascade gamma quanta of final medium-weight nuclei will be greater than for heavy nuclei due to the lower density of levels in excited medium-weight nuclei, i.e. the reaction of inelastic scattering from the point of view of neutron detection is more productive for nuclei of medium weight, if the threshold of registration of electronics is big.

The operating range of neutron energies for Zn nuclei is $\Delta E \sim 11$ MeV (from $E \sim 1.3$ to 12.5 MeV), and it is limited from below by the excitation energy, and from above by the density of nuclear levels of the order of 10^4 MeV⁻¹. The operating range of neutron energies for W nuclei is much narrower, $\Delta E \sim 1.6$ MeV (from $E \sim 1$ to 2.6 MeV) due to the lower value of the nucleon separation energy in W (6.191 MeV) than in Zn (7.981 MeV).

2.2. ISOLATION OF THE CONTRIBUTION OF INELASTIC SCATTERING

In inelastic scattering through a compound nucleus $n + A \rightarrow (A+1)^* \rightarrow A^* + n' + \gamma_{\text{prt}} \rightarrow A + \gamma_{\text{del}}$, two types of emitted gamma quanta are distinguished. First, these are instantaneous gamma quanta of the discharge of the compound nucleus $(A+1)^*$, since they are emitted during the short lifetime of the compound nucleus ($\sim 10^{-14}$ s). As a rule, the number of them is small, from 1 to 4 counts/neutron. [20]. Their separate registration is practically impossible, all the energy of nuclear decay is concentrated in one pulse of the scintillator. Secondly, these are delayed gamma quanta discharges of excited long-lived states of a final nuclei, for which separate registration is possible, and which form cascades of gamma quanta.

The work [14] presents data on the multiplicity of cascade gamma quanta in inelastic reactions with fast neutrons. For example, the gamma multiplicity of final nuclei $^{64,66,68}\text{Zn}$ is $N_\gamma = 18, 8, 7$ counts/neutron, respectively. The gamma multiplicity of nuclei $^{182,184,186}\text{W}$ is $N_\gamma = 126, 71, 86$ counts/neutron, respectively. The gamma multiplicity of nuclei $^{156,158,160,155,157}\text{Gd}$ is $N_\gamma = 15, 17, 14, 11, 7$ counts/neutron respectively. The gamma multiplicity of $^{110, 112, 114}\text{Cd}$ nuclei is $N_\gamma = 62, 62, 71$ counts/neutron, respectively.

Gamma quanta of the discharge of compound nuclei are quite simply isolated, for example, by using small-sized scintillators, or by filtering the signal stream, i.e. by an integrated filter with a time constant from units to tens of microseconds. Integration provides an efficient combination of cascaded gamma quanta into a single signal and eliminates signal delays during the deceleration of secondary neutrons in $d \sim 4-5$ cm samples. As a rule, the gamma multiplicity remains low and the efficiency does not exceed the value of 0.5–0.6 counts/neutron for small-sized ($d \sim 1$ cm) of scintillators and is close to 1 counts/neutron for scintillators with a size of $d \sim 4-5$ cm. When using a highly sensitive broadband preamplifier and integrating the signal with a spectrometric amplifier ($\tau \sim 1$ ns + 1 μ s), the counting efficiency of registration remains practically at the same level - 3 - 4 counts/neutron for sizes $d \sim 4$ cm.

Thus, the filtration mode with the appropriate selection of the formation time value effectively suppresses cascade gamma quanta of low energies from highly excited transitions in the final nuclei, i.e. estimate the contribution of the inelastic scattering mechanism to the counting efficiency of registration. For example, the efficiency for small-sized ZWO scintillators with a size of $10 \times 10 \times 10$ mm in the spectrometric (i.e., without the use of a broadband preamplifier) mode of $\tau = 1$ μ s is ~ 0.73 counts/neutron, and increases to only 2.3 counts/neutron for a large-sized ZWO with a size of $\varnothing 52 \times 42$ mm with the use of a broadband preamplifier (mode $\tau = 1$ ns + 1 μ s, amplification factor ~ 3000). Similarly, in BGO and GSO scintillators in the filtration mode $\tau = 1$ ns + 1 μ s, the mechanism of inelastic scattering $(n, n'\gamma)_{\text{in}}$ is also distinguished, while the recording efficiency $\varepsilon_n \sim 1$ counts/neutron for BGO and $\varepsilon_n \sim 1.9$ counts/neutron for GSO.

Due to the fact that the inelastic scattering reaction produces secondary neutrons with significantly reduced energy, they are more likely to enter the resonance capture reaction on the nuclei. Also, due to the transport delay in time of the secondary neutron until the possible subsequent capture, the use of a high-speed counting path allows to increase the number of registered cascade gamma quanta from the capture reaction.

2.3. ESTIMATION OF THE MULTIPLICITY OF GAMMA QUANTA FROM THE RESONANCE CAPTURE REACTION

The contribution of gamma quanta from the reactions of inelastic scattering $(n, n'\gamma)_{\text{in}}$ and resonance capture $(n, \gamma)_{\text{res}}$ to the spectrum of gamma radiation on heavy and medium nuclei was studied in [16]. On Fig. 9 a, b show the averaged spectra of gamma radiation from the reactions of inelastic scattering $(n, n'\gamma)_{\text{in}}$ at the excitation energy $E_n = 7.5$ MeV and resonance capture $(n, \gamma)_{\text{res}}$ at the neutron energy $E_n = 0.1$ MeV on the heavy nucleus W and the medium nucleus weights of Cu.

It can be seen that the N_γ -multiplicity from the inelastic scattering reaction $(n, n'\gamma)_{\text{in}}$ on nuclei of medium and heavy weight exceeds the N_γ -multiplicity from the resonance capture reactions $(n, \gamma)_{\text{res}}$.

The fact that the increase in energy release after the capture of a resonant neutron with an energy of $E = 0.1$ MeV for the medium Cu nucleus was noticeably higher than for the heavy W nucleus can be explained by the higher density of the final W nucleus, which means the emission of lower-energy gamma quanta from excited levels of final nuclei W, for the registration of which the sensitivity of the electronic path was not high enough, therefore, with the same registration threshold, significantly less of them will be registered from W than from Cu.

This is confirmed by our estimates according to the evaporation model, which give the value of the density of the levels of the final nuclei in the capture reaction for $W - \rho = 9.6 \cdot 10^5$ MeV⁻¹, and for $Zn - \rho = 2.2-2.9 \cdot 10^3$ MeV⁻¹. In addition, model estimates performed for the inelastic scattering reaction give a value of the density of levels for Zn nuclei that is lower than for W nuclei, and in a wider energy interval (Zn, $\Delta E = 1.3 \div 12.5$ MeV; W, $\Delta E = 1 \div 2.6$ MeV) (see Table 3).

It should be noted that the multiplicity of N_γ , as a rule, is measured in a spectrometry mode, i.e. in a delayed mode, so it may not agree with the value of the estimated registration efficiency, which is measured in real time.

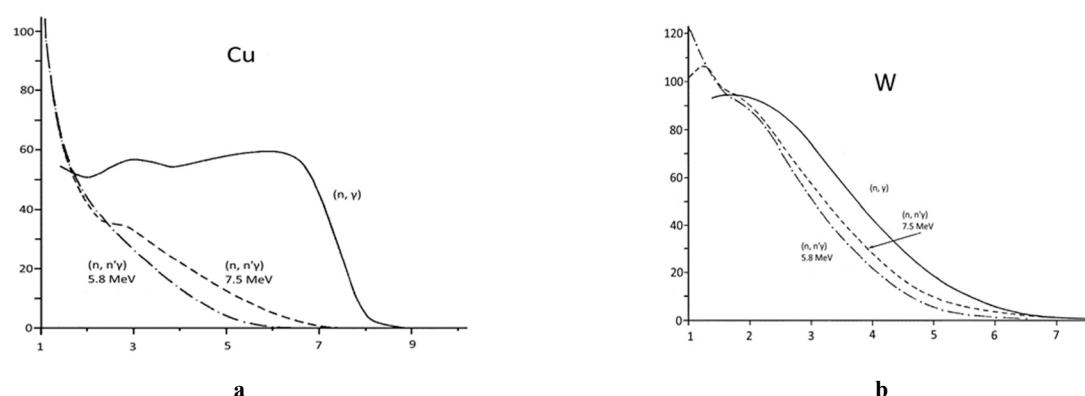


Figure 9. Averaged spectra of gamma radiation from reactions $(n,\gamma)_{res}$ and $(n,n'\gamma)_{in}$. a) – heavy nucleus W, solid line – $(n,\gamma)_{res}$, dashed and dash-dotted – $(n,n'\gamma)_{in}$; b) – nucleus of average atomic weight Cu, solid line – $(n,\gamma)_{res}$, dashed and dash-dotted – $(n,n'\gamma)_{in}$; The spectra were measured using a NaI crystal. The spectra (n,γ) were measured at neutron energy $E = 0.1$ MeV. Here Y is the number of accounts ($E*\rho(E)$), i.e. conditionally, $N\gamma$ is multiplicity), and X is MeV [16].

In our experiments on measuring the efficiency of recording fast neutrons by scintillators containing nuclei of medium and high atomic weight, the contribution of resonance capture ($\varepsilon = 574$ counts/neutron) exceeds the contribution of inelastic scattering (3 counts/neutron) to the experimental efficiency of registration by more than 2 orders.

This fact can be explained by the combined effect of the following factors: – high sensitivity and speed of the electronic circuit operating in single-electron registration mode; – the generation of sufficiently slowed secondary neutrons from the reactions of inelastic scattering and resonant scattering; – additional slowing down of neutrons on light oxygen nuclei; – by the large resonance capture cross-section of heavy W nuclei ($\sigma_{res} = 361.6$ b) and the emission of low-energy, short-lived cascade gamma quanta in the transitions of highly excited states of the final nucleus; – contributions of long-lived states of the final nucleus $(A+1)^*$, for example, W-183, $E=453$ keV, $\tau=18$ ns, W-185, $E=244$ keV, $\tau=19.3$ ns; – the contribution of a significant amount consists of a lifetime of $\sim 1-2$ ns; – a considerable time of luminescence of the scintillator ZWO (20 us).

It should be noted that the low efficiency of registration in BGO can be explained by the absence of resonances in the heavy Bi nucleus - $\sigma_{res}=0.192$ b and the insignificant value of the scintillation time - $\tau_{scint} = 300$ ns, and in GSO it can be explained by the small value of the scintillator scintillation time - $\tau_{scint} = 600$ ns compared to $\tau_{scint}= 20$ us for ZWO. Resonance capture on nuclei of medium weight (Z_n , $\sigma_{res} = 2.49$ b) cannot be productive due to the low cross section in resonance zone.

Also, a significant increase in the counting efficiency of registration for ZWO – with $\varepsilon = 574$ counts/neutron to $\varepsilon = 752$ counts/neutron with additional slowing down of neutrons flying out of the scintillator confirms the fact that the main mechanism for increasing the registration efficiency is capture of neutrons, primarily resonant, then, as the neutrons slow down – radiation capture.

In addition to the fact that the density of nuclear levels plays an important role in the formation of the response of the scintillator to neutrons, one should also consider the fact that sufficiently long-lived states can be excited in final nuclei in the resonance capture reaction on W nuclei, for example, W-183, $E=453$ keV, $\tau=18$ ns, W-185, $E=244$ keV, $\tau=19.3$ ns. Also, long-lived states can be excited in the final nuclei of inelastic scattering W, for example, $E=2230$ keV, $\tau=1.4$ us, $E=1286$ keV, $\tau=8.3$ us.

In medium-weight Zn isotopes, long-lived states can be excited in the final nuclei of resonance capture, for example, Zn-65, $E = 53.9$ keV, $\tau = 1.6$ us; Zn-67, $E = 93$ keV, $\tau=9.2$ us.

Therefore, it can be noted that the results obtained in our experiments to determine the efficiency of registration of oxide scintillators using a high-speed electron path do not contradict the results of work [16] on increasing the contribution to the energy release of scintillators due to the neutron capture reaction.

2.4. ISOLATION OF THE RESONANCE CAPTURE CONTRIBUTION

In resonant capture through the compound nucleus $n+A \rightarrow (A+1)^* \rightarrow (A+1)+\gamma_{del}$, as in the case of inelastic scattering, the appearance of delayed gamma quanta of the discharge of excited long-lived states of the final nucleus $(A+1)$, for which separate registration is possible and which form cascades of gamma quanta, can be observed.

In work [12, 24] values of the multiplicity of gamma quanta arising in the radiation capture of neutrons on nuclei, i.e. from excited state nuclei $(A+1)^*$. The value of the multiplicity of N_γ during the capture of thermal neutrons by nuclei of average atomic weight (these are Si, Zn, Ge isotopes) fluctuates within the limits of $N_\gamma = 17-175$ counts/neutron. For nuclei of high atomic weight (isotope W), the multiplicity varies within the range of $N_\gamma = 75-225$ counts/neutron. It is necessary to keep in mind that data on the multiplicity of secondary gamma quanta, unless otherwise specified, are accumulated by the spectrometric technique during a long-time interval, and are processed in a delayed time mode. In this case, the registration threshold is usually $\sim 1-10$ keV units and higher. This leads to the fact that there is always a significant discrepancy in the value of the efficiency ε (CENR) and the multiplicity N_γ .

The estimation of the level densities in the resonance capture reaction by the studied scintillators based on the thermodynamic model of reactions (see Tab. 3) gives a very high value of the level density for heavy nuclei – approximately 10^6 MeV^{-1} . Therefore, the value of the observed counting efficiency of registration can be explained by the total contribution as long-lived states of the final nucleus (A+1), for example, W-183, $E=453 \text{ keV}$, $\tau=18 \text{ ns}$, W 185, $E=244 \text{ keV}$, $\tau=19.3 \text{ ns}$, as well as a significant number of low-energy gamma quanta from transitions with a lifetime of $\sim 1\text{-}2 \text{ ns}$. In this case, the use of a high-sensitivity, high-speed, low-noise measurement path operating in the single-electron mode ($\tau=1 \text{ ns}$) makes it possible to effectively register gamma quanta of short-lived compounds, which leads to an increase in the efficiency (CENR) of neutron registration. It should be noted that when switching to the spectrometric mode, when suppressing short-lived gamma quanta, the efficiency decreases by more than two orders of magnitude - from $\varepsilon=574 \text{ counts/neutron}$ to $\varepsilon=3 \text{ counts/neutron}$ for ZWO.

Also, the increase in the contribution of resonance reactions contributes to the increase in the number of slowed down secondary neutrons from the reactions of inelastic scattering and resonance scattering, the presence of oxygen nuclei, which participate in the effective slowing down of neutrons.

Thus, for effective registration of the products of the resonance capture reaction - cascade gamma quanta - it is necessary to use a specialized broadband electronic path operating in the single-electron mode. In addition, scintillators should contain nuclei with a high cross-section of resonant capture.

2.5. CONTRIBUTIONS TO THE EFFICIENCY OF RECORDING GAMMA QUANTA OF SCINTILLATOR NUCLEI OF DIFFERENT ATOMIC WEIGHTS

Based on the experimental results of measuring the efficiency of recording fast neutrons of ^{239}Pu -Be and ^{252}Cf sources by GSO ($\varepsilon=22.2 \text{ counts/neutron}$) and ZWO ($\varepsilon=574 \text{ counts/neutron}$) scintillators and estimates of the densities of the levels of final nuclei according to the thermodynamic model for of Zn and W nuclei in the energy range of incident neutrons $1 - 2.6 \text{ MeV}$ (W) and $1.3 - 12.5 \text{ MeV}$ (Zn), it can be concluded that nuclei of average atomic weight (for example, Zn) provide a significant decrease in the energy of secondary neutrons from the inelastic scattering reaction, and at the same time, they can generate gamma quanta from transitions of final nuclei with energy from $\sim 0.1 \text{ keV}$ to $\sim 9.4 \text{ keV}$. Resonance capture on medium nuclei (Zn) can also contribute to gamma multiplicity both in the presence of long-lived stable final nuclei and generate cascade gamma quanta from transitions of final nuclei with energy from $\sim 0.34 \text{ keV}$ to $\sim 0.45 \text{ keV}$. But in this case, one should take into account the insignificant value of the cross section for the inelastic scattering and resonant capture of nuclei of middle weight.

A more important role in increasing the efficiency of registration is played by heavy nuclei with a high cross-section of resonance capture - W, Gd nuclei. Unlike BGO (efficiency $\varepsilon=19.3 \text{ counts/neutron}$), which includes heavy nuclei (Bi, $\sigma=0.1919 \text{ b}$, short scintillation time – $\tau=300 \text{ ns}$), which do not have resonances, the ZWO scintillator (efficiency $\varepsilon=574 \text{ counts/neutron}$) has a significant a higher multiplicity of secondary gamma quanta, which can be explained by a combination of resonant capture (W, $\sigma_{\text{res}}=361.6 \text{ b}$) and a long scintillation time ($20 \mu\text{s}$).

Heavy nuclei (W), according to estimates of the level density (Table 3), contribute to the efficiency of neutron registration (CENR) in the inelastic scattering reaction in a narrow range of energies ($E \sim 1\text{-}2.6 \text{ MeV}$) ($D \sim 1.06\text{-}0.1 \text{ keV}$).

The contribution to the gamma multiplicity of the resonance capture reaction on heavy W nuclei is provided by both long-lived states of final nuclei, for example, $\tau=18 \text{ ns}$, $\tau=19.3 \text{ ns}$, and a significant amount of low-energy gamma quanta from transitions with a lifetime of $\sim 1\text{-}2 \text{ ns}$, which is confirmed by the high density of levels ($\sim 9.6 \cdot 10^5$).

The use of a high-speed, highly sensitive measuring path operating in the single-electron mode ($\tau \sim 1\text{-}2 \text{ ns}$) can ensure the registration of short-lived cascade gamma quanta up to energy $\sim 0.1 \text{ keV}$ and below, emitted by final heavy nuclei from the reactions of inelastic neutron scattering and resonance capture secondary neutrons.

2.6. DELAYED GAMMA QUANTA FROM FINAL NUCLEI INCLUDED IN THE ZWO SCINTILLATOR

In Tab. 4 presents data on the lifetimes of Zn and W isotopes excited in the reactions of inelastic scattering and resonance capture, which are part of the ZWO scintillator, which were used in the analysis of the results of measurements of the efficiency of fast neutron registration [23].

It can be noted that despite the high multiplicity of N_γ , which is significantly greater than unity for heavy nuclei and sufficiently large for nuclei of average atomic weight, the number of long-lived levels in the isotopes of the heavy nucleus W is 18, of which 7 are excited in the capture reaction, 11 in the reaction of inelastic scattering. The number of long-lived levels in isotopes of the middle nuclei of Zn is much smaller - 5, of which 3 are excited in the capture reaction, 2 - in the inelastic scattering reaction. The remaining states of the isotopes of both nuclei undergo discharge for times less than 1 ns. We note that it is due to the registration of gamma quanta of the discharge of short-lived compounds with lifetimes $\tau \sim 1 \text{ ns}$ and less that the contribution of resonance capture increases, since long-lived compounds (18.4 ns, 8.3 μs , 19.3 ns, Table 4) in the final nuclei of the capture will not enough to form the necessary multiplicity ($\varepsilon \sim 574 \text{ counts/neutron}$ for ZWO).

Thus, on the basis of estimates based on the thermodynamic model and the analysis of the experimental data obtained in this work, it is possible to conclude about the possibility of increasing the efficiency of recording fast neutrons by oxide scintillators containing nuclei of high atomic weight and having a large cross section of resonant capture, due to the registration of multiple gamma quanta of final nuclear from resonance capture reactions, if it is possible to register delayed

gamma quanta due to the transport delay of secondary neutrons in the crystal provided by the necessary dimensions of the scintillator crystal, especially in the presence of a high-speed, highly sensitive recording path operating in the single-electron mode and allowing to register gamma quanta of delayed nuclear states with a resolution no worse than 0.5-1.0 ns.

For the GSO scintillator, which has practically the same cross-section value in the resonance region as that of the ZWO ($\sigma(\text{Gd}) = 398.3 \text{ b}$, $\sigma(\text{W}) = 355.1 \text{ b}$), but a significantly smaller value of the efficiency of fast neutron registration – $\varepsilon(\text{GSO}) = 22.2 \text{ counts/neutron}$ compared to $\varepsilon(\text{ZWO}) = 574 \text{ counts/neutron}$, this can be explained by the short time of GSO scintillations ($\tau \sim 600 \text{ ns}$, long-lived component of scintillation). It should be noted that the scintillation time plays an important role in the formation of the registration efficiency value, and in some cases is the determining value. This is indicated, for example, by a comparison of the neutron registration efficiencies of BGO and GSO scintillators, which have practically comparable values of the registration efficiency, although the values of the resonance cross sections in BGO and GSO differ by hundreds of times.

Table 4. Lifetimes, multiplicity of excited states in reactions of inelastic scattering and resonance capture of Zn and W isotopes included in the ZWO scintillator

$(n, n'\gamma)_{\text{in}}$	$(n, \gamma)_{\text{res}}$	Abundance, %	Gamma-ray energy, keV	N_{γ} [12]
Zn-64		48.6	< 1ns	
	Zn-65		0.0539 [1.6 μs]	78
Zn-66		27.9	< 1ns	
	Zn-67		0.093 [9.3 μs], 185 [1ns]	17
Zn-67		4.1	0.093 [9.3 μs], 185 [1ns]	
	Zn-68		< 1ns	175
Zn-68		18.7	< 1ns	
	Zn-69		< 1ns	33
Zn-70		0.62	< 1ns	
	Zn-71		< 1ns	79
W-182		26.5	100.0 [1.27ns], 1289 [1.04 ns], 1374 [2.2 ns], 1488 [1.7 ns], 1553 [1,3 ns], 2230 [1.4 μs]	
	W-183		453 [18.4 ns]	131
W-183		14.3	453 [18.4 ns]	
	W-184		111.2 [1.3 ns], 904 [1.1 ns], 1286 [8.3 μs], 1502 [2.3ns]	211
W-184		30.6	111.2 [1.3 ns], 904 [1.1 ns], 1286 [8.3 μs], 1502 [2.3ns]	
	W-185		244 [19.3 ns]	75
W-186		28.4	122 [1.1 ns]	
	W-187		< 1ns	225

3. MEASUREMENT RESULTS

Selected contributions of responses from reactions with fast neutrons $(n, n'\gamma)_{\text{in}}$, total contribution of reactions $(n, n'\gamma)_{\text{in}} + (n, \gamma)_{\text{res}} + (n, n)_{\text{res}}$, and total contribution of reactions $(n, n'\gamma)_{\text{in}} + (n, \gamma)_{\text{res}} + (n, n)_{\text{res}} + (n, \gamma)_{\text{cap}}$ in the counting efficiency of registration ε_n of neutron, counts/neutron, by oxide single-crystal scintillators ZWO, CWO, BGO, GSO of fast neutrons from the ^{239}Pu Be source are presented in Fig. 10 and in Table 5.

The results of the response of these scintillators to gamma quanta from the ^{137}Cs source are also presented. The measurement modes are as follows: $\tau_f = 1 \text{ ns}$ - single-electron mode, $\tau_f = 1 \text{ mks}$ - spectrometric mode. To increase the contribution of radiation capture of neutrons flying out of the scintillator, a moderator with a thickness of $d=1 \text{ cm}$ was used, surrounding the scintillator from the outside and a tape Cd-converter.

In Table 5 shows the contribution of products of reactions with fast neutrons of the ^{239}Pu -Be source to the counting efficiency of registration ε of neutron by single-crystal oxide scintillators ZWO, CWO, GSO, BGO.

In Tab. 5 a), the contributions of the inelastic scattering reaction $(n, n'\gamma)_{\text{in}}$ are presented, the measurement mode is spectrometric, $\tau=1 \text{ ns} + 1 \text{ us}$.

Tab. 5 b) contains the total contribution of the reactions of the inelastic and resonance mechanisms $(n, n'\gamma)_{\text{in}}$, $(n, \gamma)_{\text{res}}$, $\tau = 1 \text{ ns}$, the measurement mode is single-electron. It is possible to note a significant increase in the efficiency of ZWO and CWO due to the contribution of the resonance capture reaction of neutrons by W tungsten nuclei.

The total contribution of reactions of inelastic scattering, resonance and radiation capture $(n, n'\gamma)_{\text{in}}$, $(n, \gamma)_{\text{res}}$, $(n, \gamma)_{\text{cap}}$ is presented in Tab. 5 c), the measurement mode is single-electron, $\tau = 1 \text{ ns}$. A further increase in the efficiency of ZWO and CWO can be explained by the use of a neutron moderator with a thickness of 1 cm, which has an entrance window, covered with a scintillator and surrounded by a cadmium converter tape. The low value of the efficiency of the GSO and BGO scintillators can be explained by the short scintillation time of the scintillators – $\tau = 600 \text{ ns}$ (slow component) and $\tau = 300 \text{ ns}$, respectively.

Tab. 5 d). To evaluate the efficiency of gamma quanta registration by the atomic subsystem of the scintillator, the results of measurements with a Cs-137 source in the $\tau = 1 \text{ ns}$, single-electron mode are presented. It can be seen that the effectiveness of ZWO for fast neutrons is approximately 2.4 times higher than for gamma quanta.

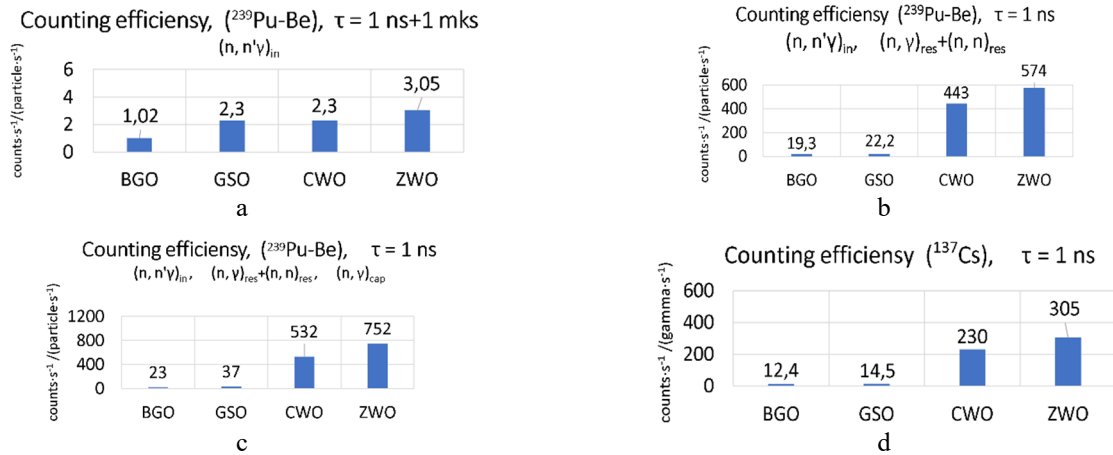


Figure 10. Contributions of reaction products with fast neutrons of the $^{239}\text{PuBe}$ source to the counting efficiency of registration ε_n , counts/neutron, oxide scintillators ZWO, CWO, GSO, BGO. Response of scintillators to gamma quanta of the ^{137}Cs source
 a) – contribution of inelastic scattering, $(n, n'\gamma)_{in}$, measurement mode – $\tau_f = 1 \text{ ns} + 1 \text{ us}$;
 b) – is the total contribution of inelastic scattering, resonance capture and scattering reactions $(n, n'\gamma)_{in} + (n, \gamma)_{res} + (n, n)_{res}$, $\tau_f = 1 \text{ ns}$;
 c) – is the total contribution of inelastic scattering, resonance and radiation trapping $(n, n'\gamma)_{in} + (n, \gamma)_{res} + (n, n)_{res} + (n, \gamma)_{cap}$, $\tau_f = 1 \text{ ns}$ – single photoelectron mode;
 d) – is the contribution of the scintillator atomic subsystem, $\tau_f = 1 \text{ ns}$

Table 5. Values of contributions of products of reactions with fast neutrons of the $^{239}\text{Pu-Be}$ source to the counting efficiency of registration ε_n of neutron by oxide scintillators ZWO, CWO, GSO, BGO

Deposits of products in reactions	BiGeO ($\tau_{sc} = 300 \text{ ns}$)			GdSiO ($\tau_{sc \text{ slow}} = 0.6 \text{ us}$)			CdWO ($\tau_{sc} = 18 \text{ us}$)			ZnWO ($\tau_{sc} = 20 \text{ us}$)		
	Bi	Ge	O	Gd	Si	O	Cd	W	O	Zn	W	O
$\sigma(n, n'\gamma)_{in}$	0.392	0.612	0.309	1.487	0.524	0.309	0.366	0.485	0.309	0.491	0.485	0.309
$\sigma(n, n)_{res}$	144.48	120.08	46.13	170.61	25.38	46.13	85.13	1118.48	46.13	97.22	1118.48	46.13
$\sigma(n, \gamma)_{res}$	0.1919	5.935	0.00016	398.3	0.0834	0.00016	71.94	355.1	0.00016	2.495	355.1	0.00016
$\sigma(n, \gamma)_{cap}$	0.0342	2.229	0.00017	48699.8	0.1604	0.00017	2463.3	18.111	0.00017	1.079	18.111	0.00017
a) $\varepsilon(n, n'\gamma)_{in}$, counts/neutron, $\tau = 1 \text{ ns} + 1 \text{ us}$. $V \sim 1 \times 1 \times 1 \text{ cm}$	1.02			2.3			2.3			3.05		
b) $\varepsilon((n, n'\gamma)_{in} + (n, n)_{res} + (n, \gamma)_{res})$, counts/neutron, $\tau = 1 \text{ ns}$. $V \sim \varnothing 4 \times 4 \text{ cm}$	19.3			22.2			443			574		
c) $\varepsilon(n, n'\gamma)_{in} + (n, \gamma)_{res} + (n, n)_{res} + (n, \gamma)_{cap}$, counts/neutron, $\tau = 1 \text{ ns}$. $V \sim \varnothing 4 \times 4 \text{ cm}$	23			37			532			752		
d) ε_γ , counts/gamma, Cs-137, $\tau = 1 \text{ ns}$, $V \sim \varnothing 4 \times 4 \text{ cm}$	12.4			14.5			230			305		

3.1. A MODEL OF THE RESPONSE OF A SCINTILLATION DETECTOR TO FAST NEUTRONS

Based on the results of measurements of the counting efficiency of registration of fast neutron, the authors of the paper proposed a phenomenological model of the response of a fast neutron detector based on an oxide scintillator. The following values are used as parameters of the model: cross section of resonance capture, cross section of inelastic scattering, time of scintillation. In this case, the response of the detector can be presented in the form: $R \sim [\sigma_{in} + \sigma_{res}] \cdot \tau_{scint}$, where σ_{in} is the inelastic scattering cross section, σ_{res} is the resonant capture cross section, and τ_{scint} is the scintillation time. It should be noted that for BGO, due to the high sensitivity of the measuring path, correction for afterglow was required.

On Fig. 11 compares the model estimation of the counting efficiency of registration of fast neutrons by oxide scintillators with the experimental results obtained in this work. Calculated values of ZWO efficiency are compared to experimental values. The measurement errors are 5%. The value of the agreement criterion was $\chi^2 = 1.2$.

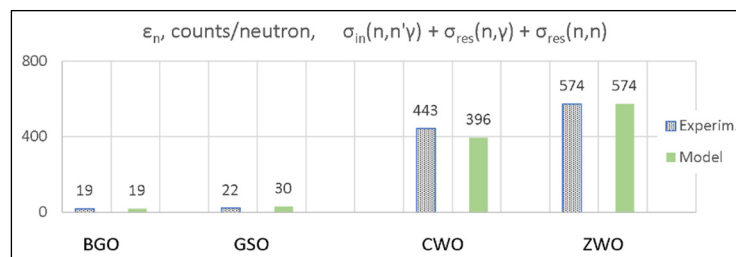


Figure 11. Comparison of the model estimation of the calculated efficiency ε of the registration of fast neutrons (solid columns) by oxide scintillators ZWO, CWO, BGO, GSO and the results of measurements (hatched columns, our experiment)

4. CONCLUSIONS

1. Experimental data on the counting efficiency of registration ε_n of fast neutron of Pu-Be sources with oxide scintillators CWO, ZWO, BGO, and GSO were obtained, which are consistent with the experimental data of other authors on the multiplicity of gamma quanta N_γ from inelastic scattering reactions ($N_\gamma \sim 2-5$ counts/neutron) and resonance capture ($N_\gamma \sim 50-500$ counts/neutron).

2. Measured contributions of reaction products of the interaction of fast neutrons from a $^{239}\text{PuBe}$ source with the substance of oxide scintillators to the counting efficiency of registration of fast neutron registration ε_n (counts/neutron). At the same time, the technique of efficiency measurements was used using a low-noise, high-sensitivity broadband pre-amplifier as part of a single-electron counter.

3. The following were used to select reaction deposits:

- the results of measuring the counting efficiency in the filtration mode $\tau \sim 1 \text{ ns} + 1 \text{ us}$, which allows to distinguish the contribution to the efficiency of the reaction products of inelastic scattering $(n, n'\gamma)_{in}$;

- the results of measuring the counting efficiency of registration in the single-electron mode $\tau \sim 1 \text{ ns}$, which allows to distinguish the contribution to the efficiency of the resonance capture reaction products $(n, \gamma)_{res}$ on heavy nuclei due to the registration of a significant number of low-energy gamma quanta from transitions between highly excited short-lived ($\tau \sim 1 \text{ ns}$) states of final nuclei.

- results of comparing the counting efficiency of registration of ZWO ($\varepsilon \sim 574$ counts/neutron, $\sigma_{res}(W) \sim 355 \text{ b}$) and GSO ($\varepsilon \sim 22$ counts/neutron, $\sigma_{res}(Gd) \sim 404 \text{ b}$). It is proved that, despite the close and very large values of the resonance capture cross sections for heavy W and Gd nuclei, the counting efficiency also depends on the scintillation time.

- the results of comparing the counting efficiency of BGO ($\varepsilon \sim 19$ counts/neutr., $\sigma_{res}(\text{Bi}) \sim 0.192 \text{ b}$) and GSO ($\varepsilon \sim 22$ counts/neutr., $\sigma_{res}(\text{Gd}) \sim 404 \text{ b}$). The low value of the efficiency for BGO can be explained by the small value of the capture cross section of the heavy Bi nucleus and the short time of scintillator exposure.

3. Registration of low-energy gamma quanta with energies up to $E_\gamma \geq 0.1 \text{ keV}$ required the development and application of a high-speed, highly sensitive path operating in the single-electron mode. This made it possible to separately register genetically related cascade events that occur in the detector, occurring per one input neutron, including secondary neutrons from the resonance scattering reaction, which are subsequently captured in the resonance energy region and increase the useful statistics of events.

4. The results of the measurements of the registration efficiency are consistent with the estimates of the thermodynamic model for medium (Zn) and heavy (W) nuclei for the densities of the ρ levels of final and compound nuclei. The high value of the ZWO efficiency can be explained by the significant value of the cross section of the resonant capture of W nuclei, the possibility of recording in the single-electron mode with maximum efficiency not only some gamma quanta consisting of a final nucleus with lifetimes in the interval from $\tau > 10 \text{ ns}$, but also shorter-lived cascades, $\tau \sim 1 \text{ ns}$ of low-energy gamma-quanta of W nuclei emitted in highly excited transitions.

5. A phenomenological model of the response of oxide scintillators to fast neutrons is proposed, using the parameters of the inelastic scattering cross section, the resonance capture cross section, and scintillator exposure times τ . The model can be used for the development of new efficient fast neutron scintillators.

6. On the basis of the proposed method of increasing the counting efficiency of registration of fast neutron by the scintillator due to the use of cascade gamma quanta from the resonance capture reaction by heavy W-type nuclei and the developed measurement technique using the single-electron registration mode, a highly efficient fast neutron detector based on the ZWO oxide scintillator was created [3].

In the future, the proposed method will make it possible to create neutron and gamma-quantum detectors that are more compact than the existing ^3He counters for monitoring neutron and gamma-neutron fields of low intensity, for use in search gamma-neutron dosimeters and surveillance systems.

Acknowledgements

The authors express their gratitude to Dr. M. Malovytsia for participating in the discussion of the results of this work.

ORCID

©Gennadiy Onyshchenko, <https://orcid.org/0000-0001-6945-8413>; ©Borys Grynyov, <https://orcid.org/0000-0003-1700-0173>
 ©Ivan Yakymenko, <https://orcid.org/0000-0002-0194-8376>; ©Sergiy Naydenov, <https://orcid.org/0000-0002-5585-763X>
 ©Pylyp Kuznietsov, <https://orcid.org/0000-0001-8477-1395>; ©Oleksandr Shchus, <https://orcid.org/0000-0001-6063-197X>

REFERENCES

- [1] M. Anelli, G. Battistoni, S. Bertolucci, C. Bini, P. Branchini, C. Curceanu, G. De Zorzi, et al., Nuclear Instruments and Methods in Physics Research A, **581**, 368 (2007). <https://doi.org/10.1016/j.nima.2007.08.005>
- [2] G. Onyshchenko, V. Ryzhikov, I. Yakymenko, V. Khodusov, S. Naydenov, A. Opolonin, and S. Makhota, East European Journal of Physics, (3), 54 (2019). <https://doi.org/10.26565/2312-4334-2019-3-07>
- [3] G.M. Onyshchenko, V.D. Ryzhikov, I.I. Yakymenko, and O.P. Shchus', East European Journal of Physics, (4), 91-94 (2019). <https://doi.org/10.26565/2312-4334-2019-4-10>
- [4] B. Grynyov, V. Ryzhikov, L. Nagornaya, G. Onishchenko and L. Piven', Patent of USA. US 8.058.624 B2 (15 November 2011).
- [5] G.M. Onyshchenko, A method of recording fast neutrons and a combined detector for its implementation, Pat. 117862 Ukraine № a 2016 11057; publ. 10.10.2018, bull. № 19.

- [6] I.I. Yakymenko, and G.M. Onyshchenko, Neutron detector: Pat. 127053 Ukraine. № u 2018 02276; publ. 10.07.2018, bull. No. 13.
- [7] B.V. Grinev, V.D. Ryzhikov, L.L. Nagornaia, G.M. Onyshchenko, and L.A. Piven, Pat. of Ukraine, N96428. The method of registration of fast neutrons. 10.11.2011.
- [8] L.L. Nagornaya, V.D. Ryzhikov, B.V. Grinyov, L.A. Piven', G.M. Onyshchenko, and E.K. Lysetska, *Abstracts IEEE Nuclear Science Symposium*, (Dresden, Germany, 2008).
- [9] O.I. Axiczep, and Yu.A. Berezhnoy, *Теорія ядерних реакцій [Theory of nuclear reactions]*, (Kharkiv, 2011). (in Ukrainian)
- [10] A.G. Sitenko, *Theory of Nuclear Reactions*, (World Scientific, 1990).
- [11] J.M. Blatt, and V.F. Weisskopf, *Theoretical Nuclear Physics*, (2010).
- [12] H.D. Choi, R.B. Firestone, R.M. Lindstrom, G.L. Molnar, S.F. Mughabghab, R. Paviotti-Corcuera, et al., *Database of prompt gamma rays from slow neutron capture for elemental analysis*, (International Atomic Energy Agency, Vienna, 2007).
- [13] G. Breit, *Theory of resonance reactions and allied topics*, (Springer-Verlag, 1959).
- [14] A.M. Demidov, L.I. Govor, Yu.K. Cherepantsev, M.R. Ahmed, S. Al-Najjar, M.A. AlAmili, N. Al-Assafi, and N. Rammo, *Atlas of Gamma-Ray Spectra from the Inelastic Scattering of Reactor Fast Neutrons*, (Nuclear Research Institute, Baghdad, Iraq, 2017). <https://nucleardata.berkeley.edu/atlas/download.html>
- [15] Z. Alfassi, and C. Chung, *Prompt Gamma Neutron Activation Analysis*, (CRC Press, Boca Raton, FL, 1995).
- [16] I. Bergqvist, B. Lundberg, I. Nilsson, and N. Starfelt, *Nuclear physics*, **80**, 198 (1966). [https://doi.org/10.1016/0029-5582\(66\)90836-4](https://doi.org/10.1016/0029-5582(66)90836-4)
- [17] L. Bardelli, M. Bini, P.G. Bizzezi, L. Carraresi, F.A. Danevich, T.F. Fazzini, B.V. Grinyov, et al., *Nuclear Instruments and Methods in Physics Research Section A, Accelerators Spectrometers Detectors and Associated Equipment*, **569**, 743 (2006). <https://doi.org/10.1016/j.nima.2006.09.094>
- [18] J.B. Marion, and J.L. Fowler, *Fast neutron physics*, Part I, Techniques, (1961).
- [19] J.B. Marion, and J.L. Fowler, *Fast neutron physics*, Part II: Experiments and Theory, (1961).
- [20] H. Goldstein, *Fundamental Aspects of Reactor Shielding*, (Addison-Wesley, 1959).
- [21] Tables of Nuclear Data. Japanese Evaluated Nuclear Data Library (JENDL). <https://www.ndc.jaea.go.jp/NuC/index.html>
- [22] JANIS Book of neutron-induced cross-sections. Java-based Nuclear Information Software (JANIS). https://www.oecd-nea.org/jcms/pl_44624/janis-books
- [23] Brookhaven national laboratory. Databases. <https://www.nndc.bnl.gov/ensdf/>
- [24] T. von Egidy, and D. Bucurescu, *Physical Review C*, **72**, 044311 (2005). <https://doi.org/10.1103/PhysRevC.72.044311>
- [25] M. Grodzicka-Kobyłka, T. Szczesniak, L. Swiderski, K. Brylew, M. Moszyński, J.J. Valiente-Dobón, P. Schotanus, et al., *Nuclear Instruments and Methods in Physics Research, Section A: Accelerators, Spectrometers, Detectors and Associated Equipment*, **1019**, 165858 (2021). <https://doi.org/10.1016/j.nima.2021.165858>
- [26] V. Ryzhikov, G. Onyshchenko, I. Yakymenko, S. Naydenov, A. Opolonin, S. Makhota, *East European Journal of Physics*, (2), 11 (2019). <https://doi.org/10.26565/2312-4334-2019-2-02>
- [27] M. Grodzicka-Kobyłka, M. Moszyński, and T. Szczesniak, *Nuclear Instruments and Methods in Physics Research, Section A: Accelerators, Spectrometers, Detectors and Associated Equipment*, **926**, 129 (2019). <https://doi.org/10.1016/j.nima.2018.10.065>
- [28] S. Mianowski, D.M. Borowicz, K. Brylew, A. Dziedzic, M. Grodzicka-Kobyłka, A. Korgul, M. Krakowiak, et al., *Journal of Instrumentation*, **15**(3), P03002 (2020), <https://doi.org/10.1088/1748-0221/15/03/P03002>

ЛІЧИЛЬНА ЕФЕКТИВНІСТЬ РЕЄСТРАЦІЇ ВКЛАДІВ ПРОДУКТІВ РЕАКЦІЙ ШВИДКИХ НЕЙТРОНІВ СЦИНТИЛЯЦІЙНИМИ ОКСИДНИМИ ДЕТЕКТОРАМИ $ZnWO_4$, $Bi_4Ge_3O_{12}$, $CdWO_4$ та Gd_2SiO_5

Геннадій М. Онищенко^{a,b}, Борис В. Гриньов^b, Іван І. Якименко^a, Сергій В. Найденів^c,
Пилип Є. Кузнєцов^a, Олександр П. Щусь^a

^a Харківський Національний Університет імені В.Н. Каразіна, пл. Свободи, 4, Харків, 61022, Україна

^b Інститут Сцинтиляційних Матеріалів, НТЦ "Інститут Монокристалів", НАН України, пр. Науки, 60, 61001, Харків, Україна

^c Інститут Монокристалів, НТЦ "Інститут Монокристалів", НАН України, пр. Науки, 60, 61001, Харків, Україна

Представлені результати дослідження величини вкладів реакцій взаємодії швидких нейтронів джерел $^{239}\text{Pu-Be}$ та ^{252}Cf в лічильну ефективність реєстрації оксидними сцинтиляторами $CdWO_4$, $ZnWO_4$, $Bi_4Ge_3O_{12}$ і Gd_2SiO_5 . Виміряно кількість гамма-квантів, що припадає на один вхідний нейтрон, випущених з кінцевих ядер, збуджених у реакції непружного розсіювання ($n, n'\gamma$)_{in}, резонансного розсіювання (n, n)_{res} і захоплення (n, γ)_{res} і радіаційного захоплення (n, γ)_{cap}. У якості фотоприймача використовується РМТ R1307, що працює в одноелектронному режимі, фонове завантаження складо $n \sim 5 \cdot 10^3 \text{ c}^{-1}$. Виміряна лічильна ефективність ϵ для сцинтиляторів $\phi 40 \times 40 \text{ мм}$ складо для ZWO – 752, для CWO – 532, для GSO – 37 і для BGO – 23 в одиницях «імпульс/нейтрон», похибка вимірювань $\sim 3\text{-}5\%$. На формування відгуку детектора впливають такі параметри ядерного сцинтилятора, як величина взаємодії в резонансній області, щільність ядерних рівнів кінцевого ядра, час життя збуджених ядерних станів, верхня межа резонансної області перерізу, а також час висвічування та геометричні параметри сцинтилятора. Запропонована феноменологічна модель відгуку оксидного сцинтилятора до швидких нейтронів.

Ключові слова: оксидний сцинтилятор; ZWO; BGO; CWO; GSO; швидкі нейтрони; $^{239}\text{Pu-Be}$; резонансний захват; лічильна ефективність; густина ядерних рівнів; одноелектронний режим

ASSESSMENT OF INDOOR RADON GAS CONCENTRATION IN NATIONAL OPEN UNIVERSITY OF NIGERIA: A CASE STUDY OF CALABAR STUDY CENTRE

Kolawole M. Lawal,  Etido P. Inyang*, Efiang A. Ibang,  Funmilayo Ayedun

Department of Physics, National Open University of Nigeria, Jabi, Abuja

*Corresponding Author email: etidophysics@gmail.com, einyang@noun.edu.ng

Received October 5, revised November 7, accepted November 23, 2023

The current work deals with indoor radon (^{222}Rn) concentrations measurements in the Calabar Study Centre of the National Open University of Nigeria using a Corentium Arthings digital radon detector meter for seven days representing a short-term average measurement of indoor radon gas concentration level. The geographical coordinates were recorded using a hand-held geographical positioning system for the sample point. Measurement was taken for seven days and the following data were obtained $83 \pm 2.19 \text{ Bq/m}^3$, $80 \pm 3.69 \text{ Bq/m}^3$, $86 \pm 5.57 \text{ Bq/m}^3$, $84 \pm 1.59 \text{ Bq/m}^3$, $82 \pm 3.59 \text{ Bq/m}^3$, $81 \pm 4.89 \text{ Bq/m}^3$ and $85 \pm 5.59 \text{ Bq/m}^3$. The average radon (^{222}Rn) concentration level was found to be $83 \pm 3.87 \text{ Bq/m}^3$ with a geometric mean of $82 \pm 3.54 \text{ Bq/m}^3$. It was observed that the radon concentration was below the reference level of 100 Bq/m^3 recommended by the World Health Organization (WHO). Although the current exposure of members of the public to natural radiation is not critical, the situation could change abruptly when other activities commenced. The excess life time cancer risk calculated for 70 years, 60 years, 50 years, 40 years and 30 years were 1.72×10^{-3} , 1.65×10^{-3} , 1.44×10^{-3} , 1.39×10^{-3} and 0.69×10^{-3} respectively. The calculated values of the excess life time cancer risk are all higher than the set limit of 0.029×10^{-3} by International Commission on Radiological Protection. However, there are no observed cases of lung cancer epidemic in this Centre. Therefore, it is advised to use fans and effective ventilation techniques to reduce radon levels. Identifying the regions of the country where people are most at risk from radon exposure should be the main goal of any national radon policy.

Keywords: *Indoor radon; Radon concentration; Digital Radon Gas detector; Calabar Study Centre*

PACS: 92.60.Mt

1. INTRODUCTION

The human environment is continually exposed to ionizing radiation such as radon resulting from natural radionuclides found within the earth's crust and cosmic rays originating from outside the earth's atmosphere [1]. Starting with uranium or thorium, radon is found in decay chains and its daughter are present everywhere [2]. When compared to other naturally occurring radiation sources, it exposes people to the most radiation. This is the rationale behind the numerous radon studies conducted by academic institutions [3]. The radon in groundwater, the atmosphere, and buildings are only a few examples of the broad areas they research [4]. The radon atoms that were stopped in water or air spread through the substance's pore space, eventually becoming the cause of radiation exposure. The main natural source of ionizing radiation and the main factor in the amount of ionizing radiation that the global population is exposed to is radon gas. Numerous in-depth scientific studies on the health impacts of radon, identified radon and the decay products it produces as the second risk factor for the development of lung cancer, right behind smoking [5, 6]. Even in the case of typical residential concentrations, recent studies have shown evidence of a link between lung cancer and radon levels inside buildings [7]. Several authorities [6, 8] have established suitable action thresholds to reduce radon exposure, over which households that exceeded such limits would need to take radon mitigation measures. The World Health Organization (WHO) advised against radon levels in indoor air above $100 \text{ Bq}\cdot\text{m}^{-3}$ or $300 \text{ Bq}\cdot\text{m}^{-3}$ in special circumstances [9]. The concentration of radon in indoor air has been measured in many countries and in a large number of buildings as a consequence of the implementation of radon policies and regulation requirements. This has been done in order to identify all radon-prone regions and to apply the proper corrective measures. Alpha track detectors exposed for at least three months within buildings have been used in the majority of national measurement campaigns [10, 11]. The indoor radon concentration in the Cholula along the Pyramid tunnels was described by Lima Flores et al., [12]. It contributes to the understanding of the radon dynamic inside of the Pyramid tunnels and to evaluate the radiological health risk to visitors, archaeologists, anthropologists and persons who spend extended periods inside the Pyramid. Additionally, Nikolopoulou and Louizi [13] provide estimates of exposure doses as well as passive and active radon concentrations in drinking water and indoor air in Cyprus and Greece. The levels of passive indoor radon in Cyprus ranged from (14 ± 3) and $(74 \pm 6) \text{ Bq}\cdot\text{m}^{-3}$. Attica's active indoor radon concentrations varied from (5.6 ± 1.8) and $(161 \pm 12) \text{ Bq}\cdot\text{m}^{-3}$, while those in Crete ranged from (1.7 ± 0.4) and $(141 \pm 12) \text{ Bq}\cdot\text{m}^{-3}$. In Greece, radon levels in drinking water ranged from (0.8 ± 0.2) and $(24 \pm 6) \text{ Bq}\cdot\text{m}^{-3}$, while those in Cyprus ranged from (0.3 ± 0.3) and $(20 \pm 2) \text{ Bq}\cdot\text{m}^{-3}$. They came to the conclusion that radon is the primary source of exposure and dose in the populations of both Greece and Cyprus. Furthermore, indoor radon was investigated by Janik et al. [14] to be a serious threat to people's health and one of the main factors in lung cancer. They gave a summary of radon-related surveying and research projects carried out in recent years in western, southern, and eastern Asia. They discovered that as the human

development index (HDI) rises, there are more indoor radon measurements per million people. Prior to the start of mining in the Adamawa region of Cameroon in 2022, Sadou et al. [15] investigated indoor radon (^{222}Rn) concentrations and ambient dose-equivalent rate measurements. The ^{222}Rn concentrations ranged between $175 \pm 16 \text{ Bq}\cdot\text{m}^{-3}$ and 43 ± 12 – $270 \pm 40 \text{ Bq}\cdot\text{m}^{-3}$, with a geometric mean of $101 \pm 21 \text{ Bq}\cdot\text{m}^{-3}$. Most of the average values in terms of concentration and radiation dose were found to be above the corresponding world averages given by the United Nations Scientific Commission on the Effects of Atomic Radiation (UNSCEAR). Furthermore, using RADUET detectors and TnP monitors, Nkoulou et al. [16] measured indoor radon (Rn), thoron (Tn), and thoron progeny (TnP) simultaneously in the gold mining areas of Betare Oya. The WHO reference level of $100 \text{ Bq}\cdot\text{m}^{-3}$ is exceeded in 76% of Rn and Tn homes, while only 3% of homes exceed the $300 \text{ Bq}\cdot\text{m}^{-3}$ threshold set by the International Commission on Radiological Protection (ICRP). Radon has been acknowledged as a significant contributor to lung cancer and has been classified as a human lung carcinogen. According to surveys, radon is the main source of radiation for the general population. The biological effects of radon and its offspring's alpha emissions are greater than those of beta and gamma radiation. Experiments on rodents exposed to radon results in similar risk, and confirm a linear relationship between risk and dose [17]. This research therefore seeks to investigate whether or not the accumulation of radon gas within the Calabar Study Centre of the National Open University of Nigeria (NOUN) are within WHO acceptable limits. Hence, this study will be a guide to checkmate the challenges that may occur in the future due to the overexposure of this gas and to advise the Government and the NOUN management on the implications of overexposure to the radon gas.

2. MATERIALS AND METHOD

The Airthings Corentium Digital Radon Detector, created in Oslo, Norway, is the radon detector utilized in this project. The unit of measurement for radon-222 is picocuries per liter, or pCi/L. For daily, weekly, monthly, and annual monitoring of radon concentration levels, the Airthings Corentium digital detector can be used for a minimum of 24 hours. The radon meter operates under the premise that radon diffuses into a chamber for detection. The atoms release energetic alpha particles as they decompose. A silicon photodiode detects the energetic alpha particles. When the alpha particle strikes the photodiode, it produces a small signal current. The signal current is changed into a large voltage signal by using a low power amplifier stage. An analogue to digital converter measures and samples the voltage signal's maximum amplitude. The energy of the alpha particle that struck the photodiode determines the signal's amplitude. A micro-controller serves as the monitor's central processing unit and logs the time and energy of each particle it detects.

The mean radon concentration for daily, weekly, monthly, and yearly time periods is determined using this data. The Arthings digital radon detector was used to measure the indoor radon concentration in-situ at the Calabar Study Center in Cross River State, Nigeria. The GPS was used to determine the geographic coordinates of the sample point. Calabar study Centre is one of the many Study Centres run by the National Open University of Nigeria. The Arthings Corentium digital radon detector was installed in the room at a distance of 0.25 m from the walls, 1.5 m from the window, and 0.5 m from the door [18]. These positions were fixed throughout the work and were maintained since radon levels depend remarkable on the sampling position. The detector was kept for a period of 24 hours before reading was taken and this was repeated for seven days. The windows and doors were kept closed throughout the period of the measurement to ensure that the indoor air is not distorted to achieve accuracy within the period of 24 hours.

2.1. EXCESS LIFE TIME CANCER RISK FROM RADON CONCENTRATION

The possible carcinogenic effects, as determined by a calculation based on the probability of cancer-induced incidence in a population known as the excess lifetime cancer risks (ELCR). The sample location ELCR is the World Standard probability of developing cancer over a given lifetime due to radiation or toxic chemical exposure. According to Ref. [2] the ELCR is given as

$$\text{ELCR} = A_E \times D_L \times R_F \quad (1)$$

where A_E = Annul effective dose rate, D_L = Average duration of life (70 years), R_F = Risk Factor (0.05). By using a tissue and radiation weighting factor, the Annual Effective Dose Rate (AEDR) from Radon Concentration was computed [8, 10]. The inhalation dose equation takes the form:

$$\text{AEDR}(\text{mS v/y}) = D_{Rn} \times W_R \times W_T \quad (2)$$

where D_{Rn} = indoor radon concentration, W_R = radiation weighting factor for alpha particles, and W_T = tissue weighting factor for the lung [18].

2.2 STUDY AREA

The study area is located in Calabar, the capital of Cross River state, Nigeria. Administratively the city is divided into Calabar `municipal and Calabar South Local Government Areas. It has an area of 406 km^2 and had a population of 371,022 at the 2006 census. The city is adjacent to the great Kwa Rivers and creeks of the Cross River (from inland delta) [19]. The study area is located between longitude $\text{N}4^\circ50'$ to $\text{N}5^\circ00'$ and latitude $\text{E}8^\circ15'$ to $\text{E}8^\circ30'$ as indicated in Figure 1 [20]. The location is Calabar study Centre, it was chosen for the study being a less populated Study Centre in NOUN.

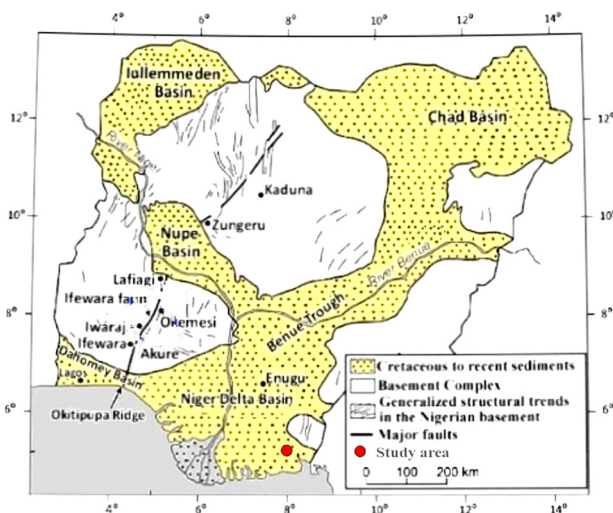


Figure 1. Geological map of Nigeria showing the study area (after NGSA, 2004)

3. RESULTS AND DISCUSSION

The readings were obtained from NOUN Calabar study Centre in Cross River State, Nigeria. The geology of Cross River State lies partly in the Oban Massif and the Calabar flank geological formations. These geological formations are characterized by unique structural imprints. Geological map of Cross River State shows two types of rock formation, the sedimentary and base complex rock. The Obudu Plateau flank and the Oban Massif in Akamkpa shows the basement complex rocks, while the central and the southern parts of the state shows the sedimentary rocks [21]. Before the detector is set for measurement counts or monitoring, on pressing the reset button, it calibrates itself to ensure that the results so obtained would be same ease where under the same physical, environment, geological and meteorological conditions. The reading was for seven days which accounted for short-term average measurement. Figure 2 shows a chart distribution of indoor radon concentration level for seven days.

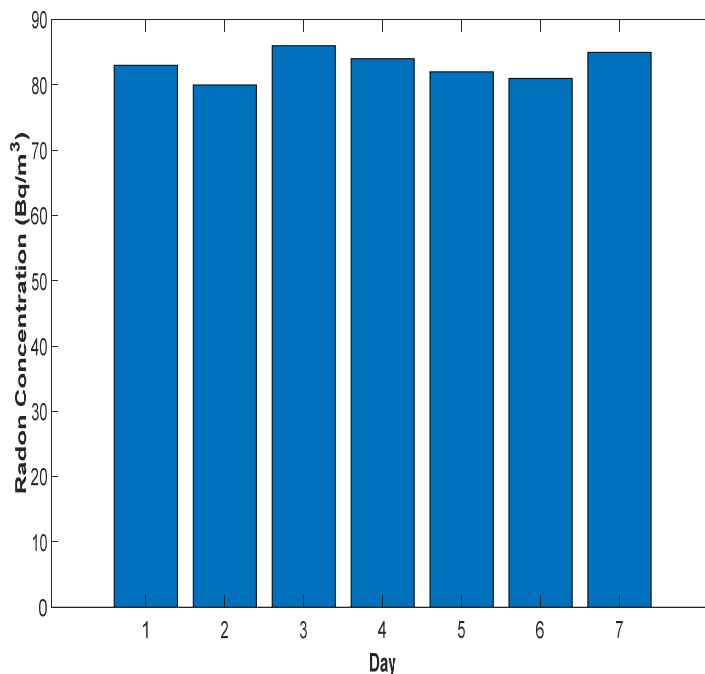


Figure 2. A chart showing Radon distribution in Bq/m³ for 7 days

The average indoor radon concentration level was found to be 83 ± 3.87 Bq/m³ with a geometric mean of 82 ± 3.54 Bq/m³. This shows that the rate of diffusion or exhalation of radon is higher in the study area because of probably humidity, high temperature and exhalation and it was also found that radon concentrations was not above the reference level of 100 Bq/m³ recommended by the WHO. The distribution of radium in soil grains are described as the key factor that affects radon emanation. Original models of radon emanation assumed that radium distribution was

homogenous throughout the grain and that these grains were also spherical. The excess lifetime cancer risk calculated for 70 years, 60 years, 50 years, 40 years, and 30 years are shown in Table 1. The calculated values of the excess life time cancer risk calculated are all higher than the set limit of 0.029×10^{-3} by International Commission on Radiological Protection (ICRP). However, there are no observed cases of lung cancer epidemic in this Centre.

Table 1. Computed values of excess lifetime cancer risk for ages of 70, 60, 50, 40 and 30 years of NOUN Calabar Study Centre

S/N	ELCR $\times 10^{-3}$ 70 years	ELCR $\times 10^{-3}$ 60 years	ELCR $\times 10^{-3}$ 50 years	ELCR $\times 10^{-3}$ 40 years	ELCR $\times 10^{-3}$ 30 years
1	1.72	1.65	1.44	1.39	0.69

4. CONCLUSION

In this work, ^{222}Rn was measured in the Calabar study Centre of the NOUN using Airthings Corentium Digital Radon Detector. The average radon ^{222}Rn concentration was found to be $83 \pm 3.87 \text{ Bq/m}^3$ with a geometric mean of $82 \pm 3.54 \text{ Bq/m}^3$. It is abundantly clear that the exposure level is not dangerous. The situation could change in the near future. However, the excess life time cancer risk for the study Centre was higher than the world average. The current findings will also help with the ongoing project in Nigeria to establish national reference levels for indoor radon. Therefore, it is advised to use fans and effective ventilation techniques to reduce radon levels. Identifying the regions of the country where people are most at risk from radon exposure should be the main goal of any national radon policy.

Acknowledgement

The authors would like to thank the National Open University of Nigeria for the award of the Senate Research Grant.

Funding.

The research was carried out under the National Open University of Nigeria Senate Research Grant: NOUN/DRA/LARTL/GN0025/VOL II

Authors Contributions. Prof. K.M. Lawal and Dr. E. P. Inyang were responsible for the study's conception and design, data collection, analysis, and interpretation; Dr. E. A. Ibanga plotted the chart and Dr. Funmilayo Ayedun was in charge of the review. The final manuscript was read and approved by all authors.

Competing interests.

The authors affirm that they do not have any competing interests.

ORCID

Etido P. Inyang, <https://orcid.org/0000-0002-5031-3297>; Funmilayo Ayedun, <https://orcid.org/0000-0001-5421-9305>

REFERENCES

- [1] E.P. Inyang, E.P. Inyang and M.B. Latif, "A Correlation: TL response of synthetic fused quartz with ^{60}Co gamma (high dose) source and $^{90}\text{Sr}/^{90}\text{Y}$ Beta (low dose) source," *Bulletin of Pure and applied Sciences - Physics*, **38**(1), 06-12 (2019). <https://acspublisher.com/journals/index.php/bpasphy/article/view/9342>
- [2] S.A. Sokari, "Estimation of Radiation Risks Associated with Radon within Residential Buildings in Okrika, Rivers State, Nigeria", *Asian Journal of Physical and Chemical Sciences*, **6**, 12 (2018). <https://doi.org/10.9734/AJOPACS/2018/43400>
- [3] W.S. Kent, and S.E. William, "Geochemical and Ray Characterization of Pennsylvanian Black Shales: Implications for Elevated Home Radon Levels in Vanderburgh County, Indiana", *Journal of Environmental Radioactivity*, **148**, 154-162 (2015). <https://doi.org/10.1016/j.jenvrad.2015.06.023>
- [4] F. Bochicchio, "The radon issue: Considerations on regulatory approaches and exposure evaluations on the basis of recent epidemiological results," *Applied Radiation and Isotopes*, **66**, 1561-1566 (2008). <https://doi.org/10.1016/j.apradiso.2007.11.019>
- [5] WHO, *WHO Handbook on indoor radon: "A public health perspective"*, (World Health Organization, Geneva, 2009).
- [6] UNSCEAR "Effects and risks of ionizing radiations. New York: United Nations Scientific Committee on the Effects of Atomic Radiation" (2000).
- [7] M.R. Usikalu, C.A. Onumejor, J.A. Achuka, A. Akinpelu, M. Omeje, and T.A. Adagunodo, "Monitoring of radon concentration for different building types in Covenant University, Nigeria," *Cogent Engineering*, **7**, 1759396 (2020). <https://doi.org/10.1080/23311916.2020.1759396>
- [8] ICRP "Lung Cancer Risk from Radon and Progeny, statement on Radon" International Commission on radiological Protection Publication 115. *Annal ICRP* 40 (2010).
- [9] WHO, "Handbook on Indoor Radon", (World Health Organisation, 2009).
- [10] ICRP, Recommendations of the International Commission on Radiological Protection, ICRP Publication 60. *Ann. ICRP* 21 3 (1991). <https://www.icrp.org/publication.asp?id=ICRP%20Publication%2060>
- [11] S. Antignani, V. Carelli, C. Cordedda, F. Zonno, M. Ampollini, C. Carpentieri, G. Venoso, and F. Bochicchio, "An affordable proxy of representative national survey on radon concentration in dwellings: design, organisation and preliminary evaluation of representativeness," *Radiat. Meas.* **50**, 136-140 (2013). <https://doi.org/10.1016/j.radmeas.2012.06.015>
- [12] A. Lima Flores, R. Palomino-Merino, E. Espinosa, V.M. Castaño, E. Merlo Juárez, M. Cruz Sanchez, and G. Espinosa, "The Indoor Radon Concentration within the Tunnels of the Cholula Pyramid Through a Nuclear Tracks Methodology," *Journal of Nuclear Physics, Material Sciences, Radiation and Applications*, **4**(1), 77-78 (2016). <https://doi.org/10.15415/jnp.2016.41008>
- [13] D. Nikolopoulou, and A. Louizib, "Study of indoor radon and radon in drinking water in Greece and Cyprus: Implications to exposure and dose," *Radiation Measurements*, **43**, 1305-1314 (2008). <https://doi.org/10.1016/j.radmeas.2008.03.043>
- [14] M. Janik, P. Bossew, M.M. Hasan, and G. Cinelli, "Indoor Radon Research in the Asia-Pacific Region," *Atmosphere*, **14**, 948 (2023). <https://doi.org/10.3390/atmos14060948>

- [15] Saïdou, O. B. Modibo, N. Nkoulou, J. Emmanuel, O. German, K. N. Michaux, and H.Y. Abba. "Indoor Radon Measurements Using Radon Track Detectors and Electret Ionization Chambers in the Bauxite-Bearing Areas of Southern Adamawa, Cameroon," *Int. J. Environ. Res. Public Health*, **17**, 6776 (2020). <https://doi.org/10.3390/ijerph17186776>
- [16] J. Emmanuel, N. Nkoulou, L.N. Engola, Saïdou, M. Hosoda, D. Bongue, T. Suzuki, et al., "Simultaneous indoor radon, thoron and thoron progeny measurements in Betare-Oya gold mining areas, eastern Cameroon," *Radiation Protection Dosimetry*, **185**, 391-401 (2019). <https://doi.org/10.1093/rpd/ncz026>
- [17] C. Gabriel, and A. Peyman, "The dielectric properties of biological tissues; Variation With Age," in: *Conn's Handbook of Models for Human Aging Second Edition*, (2018). pp. 939-952. <https://doi.org/10.1016/B978-0-12-811353-0.00069-5>
- [18] .A. Ndubisi, B.-K.M. Apaem, S.F. Barikpe, and I. Tamunobereton-Ari, "Analysis of Indoor Radon Level and its Health Risks Parameters in Three Selected Towns in Port Harcourt, Rivers State, Nigeria," *J. Nig. Soc. Phys. Sci.* **3**, 181–188 (2021). <https://doi.org/10.46481/jnsps.2021.203>
- [19] E.P. Inyang, E.P. Inyang, and E.S. William, "Assessment of the exposure to radiofrequency radiation from Wi-Fi routers in Calabar metropolis Nigeria," *Nigerian Journal of Scientific Research*, **16**(2), 490-494 (2017).
- [20] Nigerian Geological Survey Agency (2004). Acquisition of Aeromagnetic and Radiometric data by Fugro airborne.
- [21] N. Egesi, and V.U. Ukaegbu, "Petrologic and structural characteristics of the basement units of Bansara Area, Southeastern Nigeria," *Pac. J. Sci. Technol*, **11**(1), 510-525 (2010). <https://doi.org/10.11648/j.earth.20130204.11>

ОЦІНКА КОНЦЕНТРАЦІЇ РАДОНУ В ПРИМІЩЕННЯХ НАЦІОНАЛЬНОМУ ВІДКРИТОГО УНІВЕРСИТЕТУ НІГЕРІЇ: ПРИКЛАД ДОСЛІДНИЦЬКОГО ЦЕНТРУ КАЛАБАРА

Колаволе М. Лавал, Етідо П. Ін'янґ, Ефіонґ А. Ібанґа, Фунмілайо Аїедун

Факультет фізики, Національний відкритий університет Нігерії, Джабі, Абуджа

Поточна робота стосується вимірювань концентрації радону (^{222}Rn) у приміщеннях у Калабарського дослідницького центру Національного відкритого університету Нігерії за допомогою цифрового радонметра Sorentium Arthings протягом семи днів, що представляє короткочасне середнє вимірювання рівня концентрації газу радону в приміщенні. Географічні координати були записані за допомогою портативної системи географічного позиціонування точки вибірки. Вимірювання проводилися протягом семи днів і були отримані наступні дані: $83 \pm 2,19$ Бк/м³, $80 \pm 3,69$ Бк/м³, $86 \pm 5,57$ Бк/м³, $84 \pm 1,59$ Бк/м³, $82 \pm 3,59$ Бк/м³, $81 \pm 4,89$ Бк/м³ та $85 \pm 5,59$ Бк/м³. Середній рівень концентрації радону (^{222}Rn) склав $83 \pm 3,87$ Бк/м³ із середнім геометричним значенням $82 \pm 3,54$ Бк/м³. Було виявлено, що концентрація радону була нижчою за контрольний рівень 100 Бк/м³, рекомендований Всесвітньою організацією охорони здоров'я (ВООЗ). Хоча нинішнє опромінення населення природним випромінюванням не є критичним, ситуація може різко змінитися, коли розпочнуться інші види діяльності. Надлишковий ризик розвитку раку протягом життя, розрахований для 70 років, 60 років, 50 років, 40 років і 30 років, становив $1,72 \times 10^{-3}$, $1,65 \times 10^{-3}$, $1,44 \times 10^{-3}$, $1,39 \times 10^{-3}$ та $0,69 \times 10^{-3}$ відповідно. Усі розрахункові значення ризику розвитку раку протягом тривалого життя перевищують межу $0,029 \times 10^{-3}$, встановлену Міжнародною комісією з радіологічного захисту. Однак випадків епідемії раку легень у Центрі не спостерігається. Тому для зниження рівня радону рекомендується використовувати вентилятори та ефективні методи вентиляції. Головною метою будь-якої національної радонової політики має бути визначення регіонів країни, де люди найбільше піддаються ризику впливу радону.

Ключові слова: радон у приміщеннях; концентрація радону; цифровий детектор газу радону; центр досліджень Калабара

FLRW UNIVERSE IN $f(\mathcal{R}, \mathcal{L}_m)$ GRAVITY WITH EQUATION OF STATE PARAMETER

✉ **Bhupendra Kumar Shukla**^a, ✉ **R.K. Tiwari**^b, ✉ **D. Sofuoğlu**^c, ✉ **A. Beesham**^{d,e,f*}

^aDepartment of Mathematics, Govt. College Bandri Sagar 470442 (M.P.) India

^bDepartment of Mathematics, Govt. Model Science College Rewa 486 001 (M.P.) India

^cDepartment of Physics, Istanbul University Vezneciler 34134, Fatih, Istanbul, Turkey

^dDepartment of Mathematical Sciences, University of Zululand, P Bag X1001, Kwa-Dlangezwa 3886, South Africa

^eFaculty of Natural Sciences, Mangosuthu University of Technology, P O Box 12363, Jacobs, South Africa

^fNational Institute for Theoretical and Computational Sciences, South Africa

*Corresponding Author e-mail: abeesham@yahoo.com

Received October 16, 2023; revised November 19, 2023; accepted November 22, 2023

Available observational data regarding current cosmological characteristics suggest that the universe is, to a large extent, both isotropic and homogeneous on a large scale. In this study, our objective is to analyze the Friedmann-Lemaître-Robertson-Walker (FLRW) space time using an perfect fluid distribution. We specifically investigate the framework of $f(\mathcal{R}, \mathcal{L}_m)$ gravity within certain constraints. To accomplish this, we concentrate on a specific nonlinear $f(\mathcal{R}, \mathcal{L}_m)$ model, represented by $f(\mathcal{R}, \mathcal{L}_m) = \frac{\mathcal{R}}{2} + \mathcal{L}_m^\alpha$. The field equations are solved using the equation of state parameter of the form of the Chevallier-Polarski-Linder (CPL) parameterization. The deceleration parameter study finds an accelerating universe at late times. The transition redshift is found to be $z_{tr} = 0.89 \pm 0.25$. Also we discuss the physical and geometrical properties of the model.

Keywords: $f(\mathcal{R}, \mathcal{L}_m)$ gravity; Dark energy; Acceleration of universe; Equation of state parameter

PACS: 98.80.-k

1. INTRODUCTION

Recent astronomical observations have compellingly substantiated the ongoing expansion of the universe. The concept of cosmic acceleration garners support from diverse sources, encompassing high-redshift supernovae, the cosmic microwave background radiation (CMBR), data derived from the Wilkinson Microwave Anisotropy Probe (WMAP), baryonic acoustic oscillations (BAOs), and the intricate large-scale structure (LSS) [1, 2, 3, 4, 5, 6, 7, 8, 9] of the cosmos. These observations have disclosed the presence of an enigmatic entity known as Dark Energy (DE), which permeates the universe and accounts for approximately 70% of its aggregate energy content. Dark Energy possesses an intriguing trait: it exerts a potent negative pressure, setting it apart from conventional manifestations of matter and energy. This enigmatic quality enhances both the complexity and allure of our pursuit to comprehend the fundamental mechanisms governing the universe. Dark Energy assumes a pivotal role in propelling the accelerated expansion of the universe and is quantified by its equation of state (EoS) parameter, symbolized as $\omega = \frac{p}{\rho}$, where p denotes pressure, and ρ signifies energy density. A multitude of investigations have demonstrated that when the EoS parameter approaches $\omega = -1$ [10, 11], the universe undergoes accelerated expansion. Under specific conditions, Dark Energy can manifest phantom-like behavior, indicated by $\omega < -1$. In such scenarios, a universe governed by phantom Dark Energy is predicted to confront an impending singularity referred to as cosmic doomsday or the big rip, a cataclysmic event where the very fabric of the universe is torn asunder [12, 13, 14]. To illuminate and elucidate the intrinsic nature of Dark Energy and its association with late-time acceleration, scientists have immersed themselves in the exploration of modified theories of gravity. These alternative theories provide an intriguing avenue distinct from conventional approaches, holding the potential to unveil the enigmatic aspects surrounding cosmic acceleration and quintessence [15].

A recent development in the field of gravitational theories comes from Harko et al. [16], who have introduced a novel generalization known as the $f(\mathcal{R}, \mathcal{L}_m)$ theory of gravity. In this theory, ' \mathcal{R} ' represents the scalar curvature, and ' \mathcal{L}_m ' corresponds to the matter Lagrangian density. This extension presents a fresh perspective on understanding gravitational dynamics by simultaneously incorporating the geometric property of curvature and the energy distribution described by the matter Lagrangian density. This intriguing interconnection between matter and geometry results in an additional force that acts perpendicular to the four-velocity vector, leading to the non-geodesic motion of massive particles. Expanding on this concept, researchers have extended

their investigations to explore arbitrary couplings in both matter and geometry [17]. They have conducted comprehensive inquiries into the cosmological and astrophysical implications arising from these non-minimal matter-geometry couplings [18, 19, 20, 21, 22]. It is worth noting that $f(\mathcal{R}, \mathcal{L}_m)$ gravity models explicitly violate the equivalence principle, which has been rigorously constrained by tests within the solar system [23, 24].

Recently, Wang and Liao conducted a study examining energy conditions within the framework of $f(\mathcal{R}, \mathcal{L}_m)$ gravity [25]. Additionally, Goncalves and Moraes analyzed cosmological aspects by considering the non-minimal matter-geometry coupling in $f(\mathcal{R}, \mathcal{L}_m)$ gravity [26]. Solanki et al. made a significant contribution to the background of $f(\mathcal{R}, \mathcal{L}_m)$ by investigating cosmic acceleration within an anisotropic space-time with bulk viscosity [27]. Furthermore, Jaybhaye et al. carried out an insightful study focusing on constraining the equation of state for viscous Dark Energy in the context of $f(\mathcal{R}, \mathcal{L}_m)$ gravity [28]. Their research provides valuable insights into our understanding of the nature of Dark Energy within this specific gravitational framework, thereby contributing to our broader comprehension of cosmic acceleration and its underlying mechanisms. These studies shed light on the intriguing consequences of the interaction between matter and geometry in the context of $f(\mathcal{R}, \mathcal{L}_m)$ gravity. Presently, there is a growing body of literature exploring the fascinating cosmological implications of the $f(\mathcal{R}, \mathcal{L}_m)$ gravity theory [29, 30, 31, 32, 33, 34, 35, 36, 37]. Numerous studies have emerged, delving into various aspects and implications of this theory [38, 39, 40, 41].

In this work, we select the function $f(\mathcal{R}, \mathcal{L}_m)$ to be given by:

$$f(\mathcal{R}, \mathcal{L}_m) = \frac{R}{2} + \mathcal{L}_m^\alpha \quad (1)$$

where R denotes the Ricci scalar and \mathcal{L}_m denotes the matter Lagrangian. If $\alpha = 0$, then, as pointed out by Harko and Lobo [16], we recover the Hilbert-Einstein Lagrangian and the field equations of general relativity. Now the most general function for $f(\mathcal{R}, \mathcal{L}_m)$ gravity is given by Harko and Lobo [43]:

$$f(\mathcal{R}, \mathcal{L}_m) = \frac{1}{2}f_1(R) + G(\mathcal{L}_m)f_2(R) \quad (2)$$

where $f_1(R)$ and $f_2(R)$ are arbitrary, but analytical, functions of the Ricci scalar R and $G(\mathcal{L}_m)$ is an arbitrary, but analytical, function of the matter Lagrangian density \mathcal{L}_m . Since we are interested in a simple deviation from general relativity, we choose the function $f(\mathcal{R}, \mathcal{L}_m)$ to be given by (1). In addition, choosing the function $f_1(R)$ to be arbitrary essentially yields $f(R)$ gravity, and this has been extensively studied in the literature [43]. So we concentrate on the function $G(\mathcal{L}_m)$, and again, for simplicity, we choose $f_2(R) = 1$ and $G(\mathcal{L}_m) = \mathcal{L}_m^\alpha$. These choices are sufficient to enable the equations to be tractable, as well as to indicate broadly the differences from general relativity.

Most studies involving Dark Energy in modified theories have to make some assumption on one of the parameters such as the scale factor, Hubble parameter, deceleration parameter or equation of state (EoS). In this work, we assume a form for the EoS. Our work is arranged as follows. In section II, we give a brief review of $f(\mathcal{R}, \mathcal{L}_m)$ gravity. Our model is discussed in section III. Observational constraints are imposed on the model in section IV. Section V entails the cosmographic parameters. We discuss the physical parameters in section VI. Section VII provides a discussion on the energy conditions. Finally, we conclude in section VIII.

2. REVIEW OF $f(\mathcal{R}, \mathcal{L}_m)$ GRAVITY

The gravitational action for $f(R, \mathcal{L}_m)$ is given by

$$S = \int f(R, \mathcal{L}_m) \sqrt{-g} dx^4. \quad (3)$$

Here R denotes the Ricci scalar and \mathcal{L}_m denotes the matter Lagrangian. The Ricci scalar R is obtained by contracting the Ricci tensor $R_{\mu\nu}$ as

$$R = g^{\mu\nu} R_{\mu\nu}, \quad (4)$$

where the Ricci tensor $R_{\mu\nu}$ can also be written in the following form:

$$R_{\mu\nu} = \partial_\lambda \Gamma_{\mu\nu}^\lambda - \partial_\mu \Gamma_{\lambda\nu}^\lambda + \Gamma_{\mu\nu}^\lambda \Gamma_{\sigma\lambda}^\sigma - \Gamma_{\nu\sigma}^\lambda \Gamma_{\mu\lambda}^\sigma, \quad (5)$$

with $\Gamma_{\alpha\beta}^\lambda$ representing the components of Levi-Civita connection.

Now the given field equations are obtained by variation with respect to the metric tensor $g_{\mu\nu}$:

$$f_R R_{\mu\nu} + (g_{\mu\nu} \square - \nabla_\mu \nabla_\nu) f_R - \frac{1}{2} (f - f_{\mathcal{L}_m} \mathcal{L}_m) g_{\mu\nu} = \frac{1}{2} f_{\mathcal{L}_m} T_{\mu\nu}, \quad (6)$$

Here $f_R = \frac{\partial f}{\partial R}$, $f_{\mathcal{L}_m} = \frac{\partial f}{\partial \mathcal{L}_m}$ and $T_{\mu\nu}$, the stress-energy tensor for the cosmic fluid, is given by:

$$T_{\mu\nu} = \frac{-2}{\sqrt{-g}} \frac{\delta(\sqrt{-g}\mathcal{L}_m)}{\delta g^{\mu\nu}}. \tag{7}$$

Now, we can obtain the following relation by using the covariant derivative in equation (6)

$$\nabla^\mu T_{\mu\nu} = 2\nabla^\mu \ln(f_{\mathcal{L}_m}) \frac{\partial \mathcal{L}_m}{\partial g^{\mu\nu}}. \tag{8}$$

The homogeneous and spatially isotropic FLRW metric is given by:

$$ds^2 = -dt^2 + a^2(t)(dx^2 + dy^2 + dz^2), \tag{9}$$

where $a(t)$ is the cosmic scale factor. Now, the Ricci scalar for the metric (9) is obtained as:

$$R = 6(\dot{H} + 2H^2), \tag{10}$$

where H is the Hubble parameter given by:

$$H = \frac{\dot{a}}{a}. \tag{11}$$

For a perfect fluid

$$T_{\mu\nu} = (\rho + p)u_\mu u_\nu + pg_{\mu\nu}. \tag{12}$$

where ρ is the energy density and p the pressure, the corresponding field equations are given by:

$$3H^2 f_R + \frac{1}{2}(f - f_R R - f_{\mathcal{L}_m} \mathcal{L}_m) + 3H \dot{f}_R = \frac{1}{2} f_{\mathcal{L}_m} \rho, \tag{13}$$

$$\dot{H} f_R + 3H^2 f_R - \ddot{f}_R - 3H \dot{f}_R + \frac{1}{2}(f_{\mathcal{L}_m} \mathcal{L}_m - f) = \frac{1}{2} f_{\mathcal{L}_m} p. \tag{14}$$

3. $f(\mathcal{R}, \mathcal{L}_m)$ GRAVITY MODEL

Since $f(\mathcal{R}, \mathcal{L}_m)$ is an arbitrary function of R and L_m , we choose $f(\mathcal{R}, \mathcal{L}_m)$ as:

$$f(\mathcal{R}, \mathcal{L}_m) = \frac{R}{2} + \mathcal{L}_m^\alpha, \tag{15}$$

where n is free parameter. Following this, for that particular functional type of $\mathcal{L}_m = \rho$ [42], the universe is given by the Friedmann equations (13) and (14):

$$3H^2 = (2\alpha - 1)\rho^\alpha, \tag{16}$$

$$2\dot{H} + 3H^2 = [(\alpha - 1)\rho - \alpha p]\rho^{\alpha-1}. \tag{17}$$

In cosmology, the effective equation of state parameter, often denoted as ω_{eff} is a quantity used to describe the behavior of the dark energy component of the universe. Dark energy is a mysterious form of energy that is thought to be responsible for the observed accelerated expansion of the universe. The equation of state parameter for dark energy, ω , relates the pressure (p) and energy density (ρ) of dark energy through the equation:

$$\omega = \frac{p}{\rho} \tag{18}$$

Now using equations (16) and (17) we get:

$$\omega = -1 + \frac{(2 - 4\alpha)\dot{H}}{3\alpha H^2} \tag{19}$$

3.1. Observational Evidence and Precision Cosmology (Late 20th Century - Present)

Over the years, various cosmological observations, such as the study of Type Ia supernovae, the cosmic microwave background, and large-scale structure, have been used to constrain the value of ω . Current observations suggest that the equation of state parameter for dark energy is close to $\omega = -1$, consistent with a cosmological constant (Λ). However, the possibility of a time-varying equation of state parameter (dynamic dark energy models) has also been explored to explain the observed cosmic acceleration. In summary, the historical discussion of the equation of state parameter in cosmology evolved from its early introduction by Einstein to maintain a static universe, to its modern interpretation as a way to describe the properties of dark energy, which plays a crucial role in the accelerated expansion of the universe.

Observational evidence and precision cosmology have helped refine our understanding of ω and its implications for the nature of dark energy. In the exploration of Dark Energy (DE), researchers have introduced various parameterizations of the Equation of State (EoS) parameter to capture its dynamic characteristics. One commonly employed parameterization is the Chevallier-Polarski-Linder (CPL) parameterization:

$$\omega(z) = n + \frac{mz}{(1+z)}, \quad (20)$$

which is derived from a straightforward Taylor expansion of the EoS with respect to the scale factor [43, 44]. While the CPL parameterization is a dependable choice for characterizing the behavior of the Universe during early ($z \rightarrow \infty$) and present ($z = 0$) epochs, it exhibits singular behavior at future times. Precisely, it encounters issues at a redshift of $z = -1$. Nevertheless, it is worth noting that the CPL parameterization performs effectively at high redshifts and serves as a suitable approximation for slow-roll DE scalar field models. From equations (17) and (18), we obtain:

$$H = \left[(1+z)^{1+m+n} \exp\left(\frac{m}{1+z}\right) \right]^{\frac{3\alpha}{(4\alpha-2)}} \quad (21)$$

4. OBSERVATIONAL CONSTRAINTS

Observational constraints on cosmological models are crucial for understanding the nature and evolution of our universe. One of the fundamental observations used for this purpose is the Hubble parameter ($H(z)$) data, which provides valuable information about the expansion rate of the universe as a function of redshift (z). In this discussion, we will delve into the use of Hubble Data as an observational constraint in cosmology.

Hubble Parameter ($H(z)$): The Hubble parameter is a measure of the rate at which the universe is expanding at a given cosmic time. It is a fundamental parameter in cosmology and is related to the Hubble constant (H_0), which represents the current expansion rate of the universe. In a homogeneous and isotropic universe, the Hubble parameter can be expressed as:

$$H(z) = H_0 \cdot E(z), \quad (22)$$

where $E(z)$ is known as the dimensionless Hubble parameter and is defined as:

$$E(z) = \sqrt{\Omega_m(1+z)^3 + \Omega_\Lambda}, \quad (23)$$

Here, Ω_m , and Ω_Λ represent the densities of matter, radiation, and dark energy, respectively.

Using Hubble Data for Observational Constraints:

Data Collection: Observational constraints on $H(z)$ typically involve collecting data from various astronomical observations. These observations can include measurements of the Hubble parameter at different redshifts, often obtained through techniques like supernova observations, baryon acoustic oscillations (BAO), or cosmic microwave background (CMB) experiments.

Model-Dependent and Model-Independent Approaches:

Model-Dependent: In this approach, cosmologists assume a particular cosmological model, which may include parameters like Ω_m , Ω_Λ , and others. The model's predicted $H(z)$ is then compared to the observed data. Adjusting the model parameters helps find the best-fit values that match the observations.

Model-Independent: Alternatively, cosmologists can analyze the data in a model-independent way. In this case, they use parametric or non-parametric methods to reconstruct $H(z)$ without making strong assumptions about the underlying cosmological model. This approach is valuable for testing the concordance model (Λ CDM) and identifying deviations from it.

Chi-Square Test: To quantify the agreement between the theoretical predictions and observed $H(z)$ measurements, cosmologists often employ a statistical tool known as the chi-square (χ^2) test. The χ^2 test calculates a statistic that quantifies the goodness of fit between the model and the data. Smaller values of χ^2 indicate a better match between the model and observations.

$$\chi^2 = \sum_i \frac{(H_{\text{obs},i} - H_{\text{th},i})^2}{\sigma_i^2}, \tag{24}$$

$H_{\text{obs},i}$: Observed Hubble parameter at redshift z_i . $H_{\text{th},i}$: Theoretical prediction for the Hubble parameter at redshift z_i based on the model. σ_i : Uncertainty (error) associated with the observed $H(z)$ at redshift z_i .
Parameter Estimation: In the model-dependent approach, the χ^2 test helps constrain the values of cosmological parameters, such as the matter density (Ω_m) or dark energy density (Ω_Λ). The goal is to find parameter values that minimize χ^2 , indicating the best agreement between the model and the data.

Model Testing: Observational constraints on $H(z)$ are used to test the validity of different cosmological models, including extensions to the standard Λ CDM model. Deviations between the observed data and model predictions can provide insights into the nature of dark energy, the expansion history of the universe, and potential departures from the standard model.

Cosmic Chronometers: The measurement of $H(z)$ is often referred to as "cosmic chronometry." This approach allows cosmologists to track the cosmic expansion history and assess the behavior of dark energy over cosmic time.

In summary, observational constraints using the Hubble Data in cosmology involves collecting measurements of the Hubble parameter at various redshifts and comparing them to theoretical predictions. These constraints help determine the properties of the universe, the nature of dark energy, and the validity of cosmological models, ultimately advancing our understanding of the cosmos. The chi-square test is a powerful tool for quantifying the agreement between observations and models, allowing cosmologists to extract valuable information about the evolution of the universe.

The priors that we used for the calculation of the model parameters α , m and n are obtained as follows. From equations (16) and (17), we see that $\alpha = 1$ corresponds to general relativity, so we choose (0, 2) as the prior for α . From the equation (20) for $w(z)$, we see that as $z \rightarrow 0$, $\omega(0) = n$. Since $\omega(0) = -1$ for the Λ CDM model, and we do not want a large departure from the Λ CDM model, we take $(-2, 0)$ as the prior for n . For m , we observe that for large z , i.e., at early times, the universe is decelerating, or $\omega(z) \equiv p/\rho > 0$. Now, from equation (20), for $z \rightarrow \infty$, $\omega = n + m$. From the fact that $\omega(z) > 0$ at early times and bounds on the prior for n , we choose (2, 4), as the prior for m .

We now summarise our results for our parameters H_0 , α , m and n using the above-mentioned tests:

MCMC Results				
Dataset	Parameter	$f(R, L_m)$ Model	Parameter	Λ CDM Model
CC	H_0	69 ± 0.012	H_0	67.4
	α	$1.58^{+0.29}_{-0.35}$	Ω_m	0.325231
	m	$4.03^{+0.29}_{-0.59}$	Ω_Λ	0.857423
	n	$-1.71^{+0.11}_{-0.11}$		

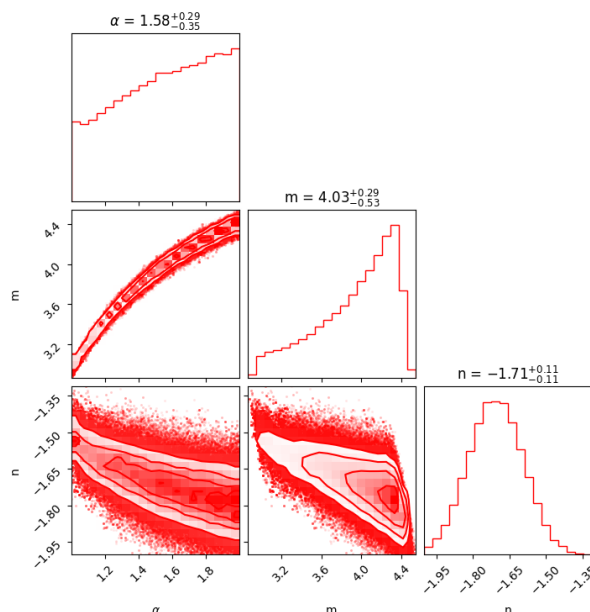


Figure 1. This graph shows the MCMC confidence contours at the 1σ and 2σ levels obtained from the 31 CC datasets.

In Fig. 1, we have plotted the likelihood contours for model parameters H_0, α, m and n at the 1σ and 2σ levels obtained from the 31 Cosmic Chronometers (CC) dataset. The CC dataset comprises the 31 data points, obtained from the differential age method, spanning the redshift range $0.07 < z < 2.42$. The best-fit values for the model parameters obtained are $H_0 = 69 \pm 0.012$, $\alpha = 1.58^{+0.29}_{-0.35}$, $m = 4.03^{+0.29}_{-0.59}$, and $n = -1.71^{+0.11}_{-0.11}$.

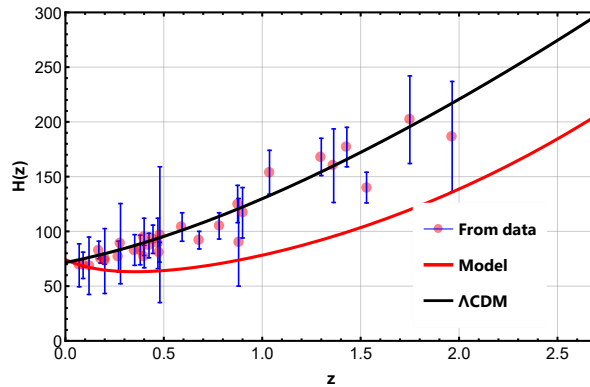


Figure 2. This figure shows our $H(z)$ curve compared to that of the Λ CDM model.

In Fig. 2, we have plotted the curves of $H(z)$ for both the Λ CDM and our models. To plot the curve for our model, we made use of the $H(z)$ equation given by (21), and values of the model parameters $\alpha = 1.58, m = 4.03$ and $n = -1.71$ from our Table.

5. COSMOGRAPHIC PARAMETERS

Cosmographic parameters constitute a collection of cosmological quantities employed to depict the historical expansion of the universe. These parameters are typically derived through a series expansion of scale factor of the universe as a function of cosmic time. This cosmographic approach offers a model-independent means of investigating the expansion of the universe, free from reliance on particular models related to dark energy or dark matter. Among the commonly utilized cosmographic parameters are the Hubble parameter (H), the deceleration parameter (q), the jerk parameter (j), and higher-order parameters. These parameters provide valuable insights into the behavior of the universe at different cosmic epochs and play a role in assessing various cosmological models.

5.1. Deceleration Parameter (q):

The deceleration parameter, denoted as q , stands as a pivotal cosmographic parameter characterizing whether the expansion of the universe is slowing down or accelerating. It is defined as the negative of the ratio between cosmic acceleration and cosmic expansion rate, expressed as:

$$q = -\frac{\ddot{a}}{aH^2}, \tag{25}$$

Here, a represents the scale factor of the universe, H denotes the Hubble parameter, and \ddot{a} signifies the second derivative of the scale factor with respect to cosmic time.

We obtain the deceleration parameter in terms of redshift as:

$$q(z) = -1 + \frac{3\alpha \left((1+m+n) - \frac{n}{1+z} \right)}{(4\alpha - 2) \left[(1+z)^{(1+m+n)} \text{Exp} \left(\frac{n}{1+z} \right) \right]^{\frac{4-\alpha}{4\alpha-2}}}. \tag{26}$$

The deceleration parameter yields essential insights into cosmic dynamics: When $q > 0$, it signifies deceleration, indicating that matter and gravity predominantly influence cosmic expansion. Conversely, when $q < 0$, it suggests acceleration, a hallmark feature of dark energy. In cases involving a cosmological constant (Λ) or forms of dark energy characterized by negative pressure, q is expected to be less than zero.

We now show how we calculate the value of the transition redshift $z_{tr} = 0.89 \pm 0.25$ as in the abstract. The transition redshift is the redshift at which the universe transits from deceleration to acceleration, and is given by $q = 0$. In the table at the end of section 4, we have illustrated the best-fit values of the parameters α, m and n from the chi-squared test using observational values of the Hubble parameter. We substitute these values into equation (26) and put $z = 0$. This give us the value of the transition redshift as $z_{tr} = 0.89 \pm 0.25$. By using the values $\alpha = 1.58, m = 4.03$ and $n = -1.71$ from our table in equation (26), we have illustrated $q(z)$ in Fig. 3.

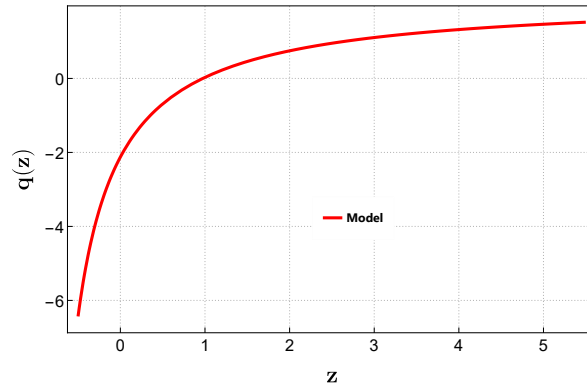


Figure 3. This figure illustrates the deceleration parameter $q(z)$.

It should be pointed out that values of the parameters different from our calculated ones of $\alpha = 1.58$, $m = 4.03$ and $n = -1.71$ can lead to undesirable consequences, such as no transition from deceleration to acceleration and values of the transition redshift that are inconsistent with observations. Similarly, a “bad” choice of the function $f(\mathcal{R}, \mathcal{L}_m)$ can also lead to these problems.

5.2. Statefinder Parameters:

The statefinder parameters encompass a collection of dimensionless cosmological parameters introduced to explore the expansion dynamics of the universe in a model-independent manner. They are derived from derivatives of the scale factor concerning cosmic time and are valuable for distinguishing between different cosmological models and detecting deviations from the conventional Λ CDM model.

Two of the significant statefinder parameters are r and s defined as:

$$r = \frac{\ddot{a}}{aH^3}, \tag{27}$$

$$s = \frac{r - 1}{3(q - 1/2)}, \tag{28}$$

These parameters depend on the scale factor (a), Hubble parameter (H), the third derivative of the scale factor with respect to cosmic time (\ddot{a}), and the deceleration parameter (q).

We now wish to write the statefinder parameters (r, s) from equations (27) and (28) in terms of $H(z)$, its derivatives and $q(z)$:

$$r(1+z) = 1 - 2\frac{H'}{H}(1+z) + \left[\frac{H''}{H} + \left(\frac{H'}{H}\right)^2 \right] (1+z)^2 \tag{29}$$

$$s(1+z) = \frac{r(1+z) + 1}{3[q(1+z) - 1/2]} \tag{30}$$

where the primes denote derivatives with respect to $(1+z)$. To write r and s in terms of z , we use equations (21), and its derivatives, and (26), thereby obtaining equations (29) and (30). These are plotted in Fig. 4 and Fig. 5.

Statefinder parameters are particularly useful in discerning various dark energy models. In the context of the Λ CDM model, both r and s assume fixed values ($r = 1$ and $s = 0$). Deviations from these values can indicate the presence of alternative dark energy models or theories of modified gravity.

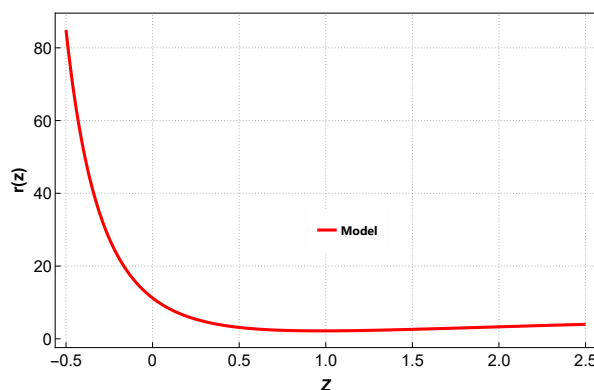


Figure 4. This figure shows the parameter $r(z)$.

Fig. 4 shows the curve $r(z)$. This is obtained from equations (29), (21), (26) and the parameter values $\alpha = 1.58, m = 4.03$ and $n = -1.71$ from our table.

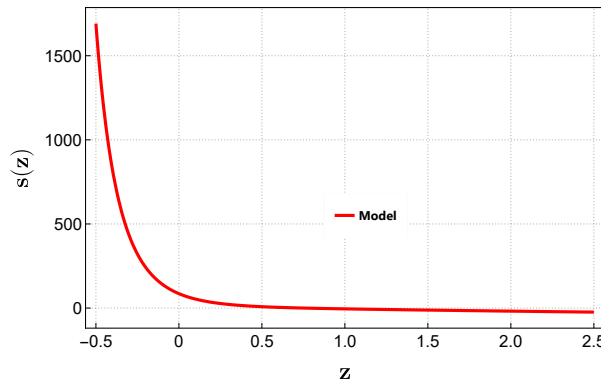


Figure 5. This figure shows the parameter $s(z)$.

Fig. 5 shows the curve $s(z)$. This is obtained from equations (30), (29) and (26), and the parameter values $\alpha = 1.58, m = 4.03$ and $n = -1.71$ from our table.

In summary, cosmographic parameters, including the deceleration parameter (q) and statefinder parameters (r and s), provide valuable insights into the dynamics of cosmic expansion. They enable cosmologists to investigate the effects of dark energy and modified gravity theories without committing to specific models, contributing significantly to our comprehension of the evolution of the cosmos.

6. PHYSICAL PARAMETERS

In cosmology, the behavior of the energy density and pressure plays a crucial role in determining the evolution and dynamics of the universe. These two quantities are described by the energy-momentum tensor and are governed by the equations of state for different components of the cosmic content, such as matter, radiation, and dark energy. Here, we will briefly discuss the behavior of the energy density and pressure in our model:

$$\rho = \left[\frac{3 \left[(1+z)^{1+m+n} \exp\left(\frac{m}{1+z}\right) \right]^{\frac{6\alpha}{(4\alpha-2)}}}{(2\alpha-1)} \right]^{\frac{1}{\alpha}}, \tag{31}$$

$$p = - \frac{\frac{3\alpha}{(2\alpha-1)} \left[(1+z)^{1+m+n} \exp\left(\frac{m}{1+z}\right) \right]^{\frac{6\alpha}{(4\alpha-2)}}}{\alpha \left[\frac{3 \left[(1+z)^{1+m+n} \exp\left(\frac{m}{1+z}\right) \right]^{\frac{6\alpha}{(4\alpha-2)}}}{(2\alpha-1)} \right]^{\frac{\alpha-1}{\alpha}}} + \frac{\left[(1+z)^{1+m+n} \exp\left(\frac{m}{1+z}\right) \right]^{\frac{6\alpha}{(4\alpha-2)}} \left[\frac{3\alpha \left((1+m+n) - \frac{n}{1+z} \right)}{(4\alpha-2) \left[(1+z)^{(1+m+n)} \exp\left(\frac{n}{1+z}\right) \right]^{\frac{4-\alpha}{4\alpha-2}}} \right]}{\alpha \left[\frac{3 \left[(1+z)^{1+m+n} \exp\left(\frac{m}{1+z}\right) \right]^{\frac{6\alpha}{(4\alpha-2)}}}{(2\alpha-1)} \right]^{\frac{\alpha-1}{\alpha}}}. \tag{32}$$

6.1. Matter-Dominated Universe:

Energy Density (ρ): In a matter-dominated universe, such as the present cosmic era, the energy density associated with matter (both dark matter and baryonic matter) dominates. In general relativity, the energy density of matter scales with the volume of the universe, decreasing as the universe expands. Specifically, for non-relativistic matter (where particles move much slower than the speed of light), the energy density scales as $\rho \propto a^{-3}$, where a is the scale factor of the universe.

Pressure (p): In the case of non-relativistic matter, the pressure is negligible ($p \approx 0$). Ordinary matter particles do not exert significant pressure on the universe’s expansion. Therefore, matter contributes to cosmic deceleration due to its gravitational attraction.

6.2. Radiation-Dominated Universe:

Energy Density (ρ): In the early universe, during radiation domination (e.g., during the era of the cosmic microwave background radiation), radiation (including photons and relativistic particles) dominates the energy density. Radiation energy density scales differently from matter and decreases faster with cosmic expansion: In general relativity, $\rho \propto a^{-4}$. This rapid decrease is due to the redshifting of photon energies as the universe expands.

Pressure (p): Radiation exerts significant pressure (In general relativity, $p = \frac{1}{3}\rho$). The high pressure associated with radiation contributes to the early rapid expansion of the universe. It leads to the deceleration of cosmic expansion, but at a slower rate compared to the matter-dominated era.

6.3. Dark Energy-Dominated Universe:

Energy Density (ρ): In the current era, observations suggest that dark energy dominates the energy density of the universe. Unlike matter and radiation, dark energy does not dilute with cosmic expansion (its energy density remains nearly constant).

Pressure (p): Dark energy is characterized by negative pressure ($p < 0$), and it behaves like a cosmological constant (Λ) in the Λ CDM model. This negative pressure drives cosmic acceleration, causing the universe to expand at an accelerating rate. The pressure of dark energy counteracts the gravitational attraction of matter and radiation, leading to the observed cosmic acceleration.

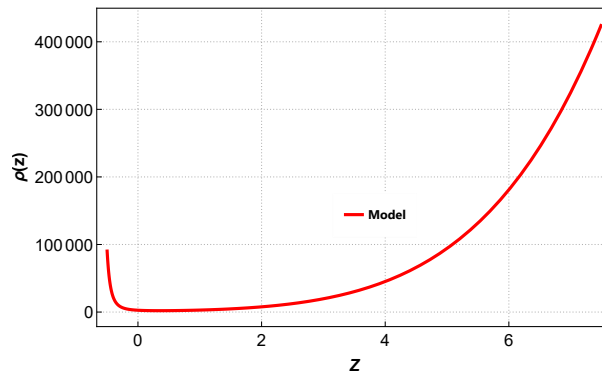


Figure 6. This figure illustrates the energy density $\rho(z)$.

In Fig. 6 we have plotted the energy density $\rho(z)$ from equation (31), using the parameter values $\alpha = 1.58, m = 4.03$ and $n = -1.71$ from our table. We notice that the energy density is non-negative.

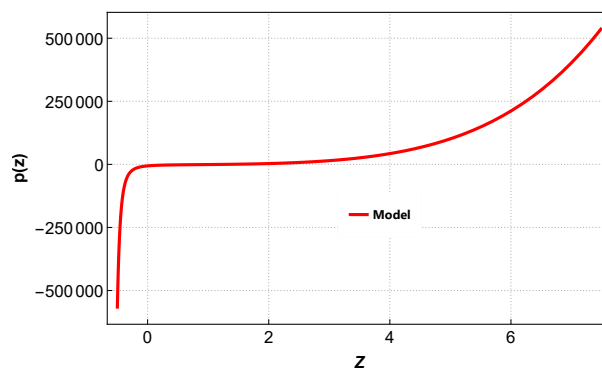


Figure 7. This figure illustrates the pressure $p(z)$.

In Fig. 7 we have plotted the pressure $p(z)$ from equation (32), using the parameter values $\alpha = 1.58, m = 4.03$ and $n = -1.71$ from our table. The Fig shows that the pressure is initially positive (deceleration), but at a redshift of $z_{tr} = 0.89 \pm 0.25$, it changes sign from positive to negative, signifying a transition from deceleration to acceleration.

6.4. Equation of State:

The relationship between energy density and pressure is often described by an equation of state parameter ($\omega \equiv p/\rho$). For matter, $w \approx 0$, for radiation, $w = \frac{1}{3}$, and for dark energy in the Λ CDM model, $w = -1$. Different components with varying values of w have distinct effects on cosmic expansion and evolution.

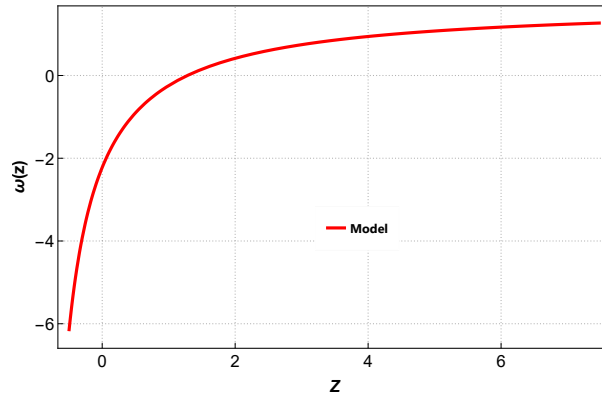


Figure 8. This figure shows the EoS $\omega(z)$.

In Fig. 8 we have plotted the equation of state parameter $\omega = p/\rho$ from equations (6.4), (32) and (31), using the parameter values $\alpha = 1.58, m = 4.03$ and $n = -1.71$ from our table. We notice that $\omega(z)$ is positive early on, signifying deceleration, and then flips signature to negative at the redshift $z_{tr} = 0.89 \pm 0.25$, indicating late-time acceleration as per observations.

In summary, the behavior of the energy density and pressure in cosmology is intimately tied to the composition of the universe. Matter, radiation and dark energy each have distinct behavior, and their contributions to the energy density and pressure evolve differently with cosmic time, influencing the overall dynamics of the expansion and acceleration of the universe. Understanding these behaviors is essential for constructing cosmological models and explaining the observed features of our universe.

In the context of the dark energy concept, if $\omega > -1$, then the DE model is dubbed quintessence and if $\omega < -1$, then the model is dubbed the phantom model. In our model, the EoS parameter is positive initially and continues its evolution with negative values after a certain time. It evolves into the phantom region, crossing the Λ CDM ($\omega = -1$) divide during late times.

7. ENERGY CONDITIONS

Energy conditions in the context of modified theories of gravity, such as those beyond Einstein’s General Theory of Relativity (GR), are somewhat different from the energy conditions in standard GR. These energy conditions are used to constrain and describe the behavior of energy and matter in these alternative theories of gravity. Below are some commonly used energy conditions in modified gravity theories, along with their physical interpretations:

Null Energy Condition (NEC):

Mathematical Form: $T_{ab}k^ak^b \geq 0$ for all null vectors k^a , where T_{ab} is the energy-momentum tensor.

Physical Interpretation: In modified gravity theories, the NEC is often retained. It signifies that the energy density, as measured along null geodesics (light rays), remains non-negative. This condition ensures that light rays do not focus or converge, similar to GR.

Weak Energy Condition (WEC):

Mathematical Form: $T_{ab}v^av^b \geq 0$ for all timelike vectors v^a .

Physical Interpretation: Like in GR, the WEC implies that the energy density, as measured by an observer at rest in any reference frame, must be non-negative. This condition helps to ensure that matter has positive energy and does not violate fundamental energy principles. We also expect the WEC to be obeyed in order to achieve a transition from deceleration to acceleration.

Strong Energy Condition (SEC):

Mathematical Form: $(T_{ab} - (1/2)g_{ab}T)v^av^b \geq 0$ for all timelike vectors v^a .

Physical Interpretation: In modified gravity theories, the SEC is expected to be violated corresponding the the late-time acceleration of the universe. It implies that the gravitational effects of matter must act as a source of attractive gravity, just as in GR.

Dominant Energy Condition The dominant energy condition stipulates that, in addition to the weak energy condition holding true, for every future-pointing causal vector field (either timelike or null) v^a , the vector field $-T_b^av^b$ must be a future-pointing causal vector, i.e, mass-energy can never be observed to be flowing faster than light. However, again with dark energy, the DEC is expected to be violated corresponding the the late-time acceleration of the universe.

It is important to note that modified gravity theories often introduce additional terms and degrees of freedom into the gravitational field equations compared to GR. These additional terms can affect the interpretation and validity of the energy conditions. Also we find the energy conditions in terms of the energy density and pressure:

Trace energy condition (TEC), now abandoned
 Null energy condition (NEC): $\rho + p \geq 0$,
 Weak energy condition (WEC): $\rho \geq 0$ and $\rho + p \geq 0$,
 Strong energy condition (SEC) $\rho + 3p \geq 0$ and $\rho + p \geq 0$,
 Dominant energy condition (DEC) $\rho \geq 0$ and $-\rho \leq p \leq \rho$

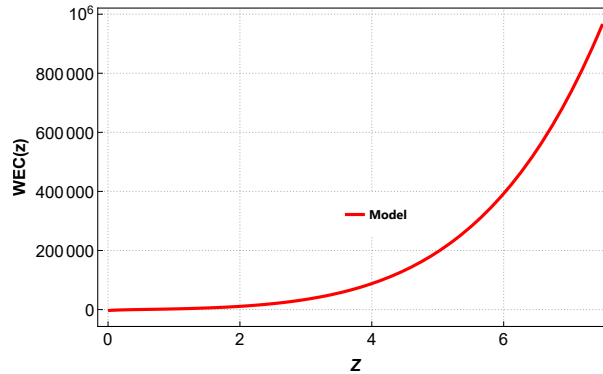


Figure 9. Figure of the *WEC*.

In Fig. 9, we have plotted the weak energy condition (WEC) against redshift z using equations (31) and (32) and the values of the parameters $\alpha = 1.58, m = 4.03$ and $n = -1.71$ as in our table. We see that the WEC is satisfied.

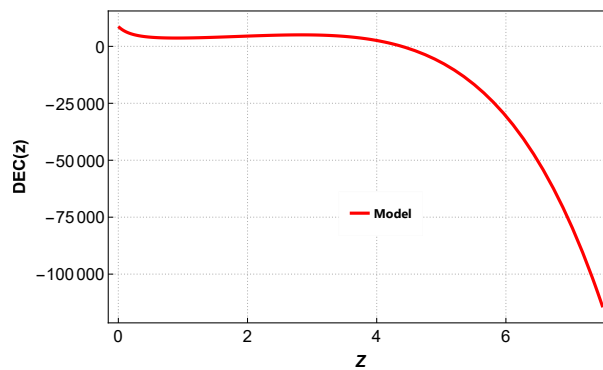


Figure 10. Figure of the *DEC*.

Fig. 10 plots the DEC against redshift using equations (31) and (32) and the values of the parameters $\alpha = 1.58, m = 4.03$ and $n = -1.71$ as in our table. It can be seen that the DEC is violated, in keeping with the requirements for a transition from deceleration to acceleration.

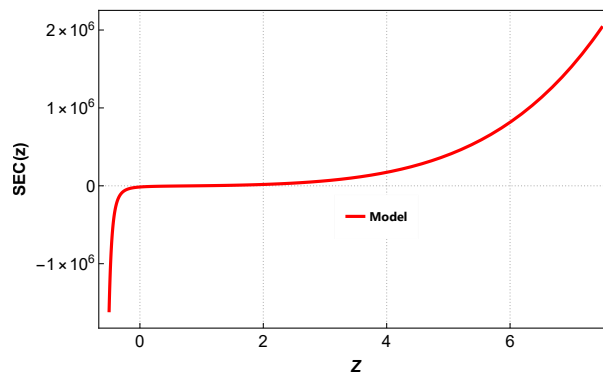


Figure 11. Figure of the *SEC*.

Fig. 11 plots the SEC against redshift using equations (31) and (32) and the values of the parameters $\alpha = 1.58, m = 4.03$ and $n = -1.71$ as in our table. It can be seen that the SEC is violated, in keeping with the requirements for a transition from deceleration to acceleration.

In summary, energy conditions in modified theories of gravity serve as a tool to understand the behavior of matter and energy in these theories. While some energy conditions may remain similar to GR, others can

be modified or relaxed, depending on the specific theory. These conditions help physicists analyze the implications of alternative gravity theories and their compatibility with observational data and fundamental physical principles. We note that in our model, the SEC and DEC are not satisfied, in keeping with a model with dark energy that has a transition from early deceleration to late-time acceleration.

8. CONCLUSION

In this work, we have studied an FLRW model in $f(\mathcal{R}, \mathcal{L}_m)$ gravity. After an introduction and background to the theory, we give a review in section 2. In section 3, we present our model. The extension presents a fresh perspective on understanding gravitational dynamics by simultaneously incorporating the geometric property of curvature and the energy distribution described by the matter Lagrangian density. Most studies involving Dark Energy in modified theories have to make some assumption on one of the parameters such as the scale factor, Hubble parameter or deceleration parameter. Here we assume a specific form for the EoS, viz., equation (19), which is not so common in the literature, and we study a solution which exhibits a transition from deceleration to acceleration. This is illustrated in Fig-3, showing that the deceleration parameter q changes sign from positive (deceleration) to negative (acceleration) at late-times.

We now make parallels with other similar works in the literature, pointing out the differences with our work. Jaybhaye et al [45] studied a model with a similar form of $f(\mathcal{R}, \mathcal{L}_m)$ as ours, but with the addition of a constant. However, their study was limited to the matter dominated universe only, i.e., $p = 0$. Hence, the energy conditions could not be discussed. Maurya [46] used a similar form for $f(\mathcal{R}, \mathcal{L}_m)$ as [45], but added a constant coefficient to the \mathcal{L}_m^α term. There was no discussion of the energy density, pressure and the energy conditions. The other paper that bears close resemblance to ours is that of Myrzakulov et al [47]. Those authors used the same form for $f(\mathcal{R}, \mathcal{L}_m)$, but they chose a different form for the EoS parameter. According to the deceleration parameter, there is a transition from deceleration to acceleration, but the pressure and EoS parameter remain negative throughout, indicating acceleration only. There is also no discussion of the energy conditions. In our work, the energy density is non-negative throughout. On the other hand, the deceleration parameter, pressure and EoS parameter show signature flips as required for a transition from deceleration to acceleration. We have provided a complete analysis of the energy conditions, showing that the WEC is satisfied, but both the DEC and SEC are violated. Again, this is in keeping with the change from deceleration to acceleration.

In section 4, we subjected the model to observational tests, and obtained the best fit values of the model parameters, viz., $H_0 = 69 \pm 0.012$, $\alpha = 1.58_{-0.35}^{+0.29}$, $m = 4.03_{-0.59}^{+0.29}$, and $n = -1.71_{-0.11}^{+0.11}$. In addition, we discussed the various cosmographic parameters in section 5 and illustrated by means of graphs. The deceleration parameter q , and the diagnostic pair (r, s) have been discussed in section 5, and illustrated by means of figures. Then, in section 6, the physical parameters ρ and p and the energy conditions are analysed. The energy density ρ is positive throughout, and the pressure p has a signature flip from positive (deceleration) to negative (acceleration). We have studied the energy conditions and showed that they are also compatible with the transition from deceleration to acceleration, i.e., the WEC is satisfied, but the DEC and SEC are not satisfied, and exhibit a signature flip associated with late-time acceleration.

In conclusion, we have studied an FLRW model in $f(\mathcal{R}, \mathcal{L}_m)$ gravity by utilising a form for the EoS. The model is compatible with observations, and is worthy of further study. In this work, we have chosen probably the most simple form for $f(\mathcal{R}, \mathcal{L}_m)$, i.e., $f(\mathcal{R}, \mathcal{L}_m) = R/2 + \mathcal{L}_m^\alpha$. However, it allows us to study the departure from general relativity, and what differences arise. Future prospects include extending to more complicated forms of $f(\mathcal{R}, \mathcal{L}_m)$, e.g., other functions of $f(R)$ since $f(R)$ theories have been well-studied in the literature [48]. In addition, one can consider other forms of \mathcal{L}_m^α .

ORCID

 **Bhupendra Kumar Shukla**, <https://orcid.org/0000-0002-4318-2356>;  **R.K. Tiwari**, <https://orcid.org/0009-0002-6931-3067>;  **D. Sofuoğlu**, <https://orcid.org/0000-0002-8842-7302>;  **A. Bee-sham**, <https://orcid.org/0000-0001-5350-6396>

REFERENCES

- [1] A.G. Riess, et al., *Astron. J.* **116**, 1009 (1998). <https://doi.org/10.1086/300499>
- [2] S. Perlmutter, et al., *Astrophys. J.* **517**, 565 (1999). <https://doi.org/10.1086/307221>
- [3] C.L. Bennett, et al., *Astrophys. J. Suppl.* **148**, 119-134 (2003). <https://doi.org/10.1086/377253>
- [4] R.R. Caldwell, and M. Doran, *Phys. Rev. D*, **69**, 103517 (2004). <https://doi.org/10.1103/PhysRevD.69.103517>
- [5] D.N. Spergel, et al., [WMAP Collaboration], *Astrophys. J. Suppl.* **148**, 175 (2003). <https://doi.org/10.1086/377226>
- [6] D.J. Eisenstein, et al., *Astrophys. J.* **633**, 560 (2005). <https://doi.org/10.1086/466512>

- [7] W.J. Percival, et al., *Mon. Not. R. Astron. Soc.* **401**, 2148 (2010). <https://doi.org/10.1111/j.1365-2966.2009.15812.x>
- [8] T. Koivisto, D.F. Mota, *Phys. Rev. D*, **73**, 083502 (2006). <https://doi.org/10.1103/PhysRevD.73.083502>
- [9] S.F. Daniel, *Phys. Rev. D*, **77**, 103513 (2008). <https://doi.org/10.1103/PhysRevD.77.103513>
- [10] S. Weinberg, *Rev. Mod. Phys.* **61**, 1 (1989). <https://doi.org/10.1103/RevModPhys.61.1>
- [11] E.J. Copeland et al., *Int. J. Mod. Phys. D*, **15**, 1753 (2006). <https://doi.org/10.1142/S021827180600942X>
- [12] A.A. Starobinsky, *Gravit. Cosmol.* **6**, 157 (2000). https://doi.org/10.1142/9789812793324_0008
- [13] R.R. Caldwell, *Phys. Lett. B*, **545**, 23 (2002). [https://doi.org/10.1016/S0370-2693\(02\)02589-3](https://doi.org/10.1016/S0370-2693(02)02589-3)
- [14] R.R. Caldwell, M. Kamionkowski, and N.N. Weinberg, *Phys. Rev. Lett.* **91**, 071301 (2003). <https://doi.org/10.1103/PhysRevLett.91.071301>
- [15] S. Capozziello, *Int. J. Mod. Phys. D*, **11**, 483 (2002). <https://doi.org/10.1142/S0218271802002025>
- [16] T. Harko, and F.S.N. Lobo, *Eur. Phys. J. C*, **70**, 373 (2010). <https://doi.org/10.1140/epjc/s10052-010-1467-3>
- [17] T. Harko, *Phys. Lett. B*, **669**, 376 (2008). <https://doi.org/10.1016/j.physletb.2008.10.007>
- [18] T. Harko, *Phys. Rev. D*, **81**, 084050 (2010). <https://doi.org/10.1103/PhysRevD.81.084050>
- [19] T. Harko, *Phys. Rev. D*, **81**, 044021 (2010). <https://doi.org/10.1103/PhysRevD.81.044021>
- [20] S. Nesseris, *Phys. Rev. D*, **79**, 044015 (2009). <https://doi.org/10.1103/PhysRevD.79.044015>
- [21] V. Faraoni, *Phys. Rev. D*, **76**, 127501 (2007). <https://doi.org/10.1103/PhysRevD.76.127501>
- [22] V. Faraoni, *Phys. Rev. D*, **80**, 124040 (2009). <https://doi.org/10.1103/PhysRevD.80.124040>
- [23] V. Faraoni, *Cosmology in Scalar-Tensor Gravity*, (Kluwer Academic, Dordrecht, 2004).
- [24] O. Bertolami, J. Paramos, and S. Turyshev, (2006). <https://doi.org/10.48550/arXiv.gr-qc/0602016>
- [25] J. Wang, and K. Liao, *Class. Quantum Grav.* **29**, 215016 (2012). <https://doi.org/10.1088/0264-9381/29/21/215016>
- [26] B.S. Goncalves, P.H.R.S. Moraes, and B. Mishra (2023). <https://doi.org/10.48550/arXiv.2101.05918>
- [27] R. Solanki, B. Patel, L.V. Jaybhaye, and P.K. Sahoo, *Commun. Theor. Phys.* **75**, 075401 (2023). <https://doi.org/10.1088/1572-9494/acd4aa>
- [28] L.V. Jaybhaye, R. Solanki, S. Mandal, and P.K. Sahoo, *Universe*, **9**, 163 (2023). <https://doi.org/10.3390/universe9040163>
- [29] M. Zeyauddin, A. Dixit, and A. Pradhan, *Int. J. Geom. M. Modern Phys.* (2023). <https://doi.org/10.1142/S0219887824500385>
- [30] N. Myrzakulov, M. Koussour, A.H.A. Alnadhief, A. Abebe, *Eur. Phys. J. P.* **138**, 852 (2023). <https://doi.org/10.1140/epjp/s13360-023-04483-3>
- [31] D.C. Maurya, *Grav. Cosm.* **29**, 315 (2023). <https://doi.org/10.1134/S020228932303012X>
- [32] R. Solanki, et al. *Commun. Theor. Phys.* **75**, 075401 (2023). <https://doi.org/10.1088/1572-9494/acd4aa>
- [33] J.K. Singh, et al., *New Astr.* **104**, 102070 (2023). <https://doi.org/10.1016/j.newast.2023.102070>
- [34] L.V. Jaybhaye et al., *Phys. Dark Univ.* **40**, 101223 (2023). <https://doi.org/10.1016/j.dark.2023.101223>
- [35] J.C. Fabris et al., *Eur. Phys. J. Plus*, **138**, 232 (2023). <https://doi.org/10.1140/epjp/s13360-023-03845-1>
- [36] A. Pradhan et al., *Int. J. Geom. M. Mod. Phys.* **20**, 1230105 (2023).
- [37] D.C. Maurya, *New Astr.* **100**, 101974 (2023). <https://doi.org/10.1016/j.newast.2022.101974>
- [38] G.A. Carvalho, et al., *Eur. Phys. J. C*, **82**, 1096 (2022). <https://doi.org/10.1140/epjc/s10052-022-11058-6>
- [39] R.V. Labato, G.A. Carvalho, and C.A. Bertulani, *Eur. Phys. J. C*, **81**, 1013 (2021). <https://doi.org/10.1140/epjc/s10052-021-09785-3>
- [40] T. Harko and S. Shahidi, *Eur. Phys. J. C*, **82**, 1003 (2022). <https://doi.org/10.1140/epjc/s10052-022-10891-z>
- [41] T. Harko and M.J. Lake, *Eur. Phys. J. C*, **75**, 60 (2015). <https://doi.org/10.1140/epjc/s10052-015-3287-y>
- [42] T. Harko and F.S.N. Lobo, *Galaxies*, **2014**(2), 410-465 (2014). <https://doi.org/10.3390/galaxies2030410>
- [43] M. Chevallier and D. Polarski, *Int. J. Mod. Phys. D*, **10**, 213 (2001). <https://doi.org/10.1142/S0218271801000822>
- [44] E.V. Linder, *Phys. Rev. Lett.* **90**, 091301 (2003). <https://doi.org/10.1103/PhysRevLett.90.091301>
- [45] Jaybhaye, et al., *Phys. Lett. B* **831**, 137148 (2022). <https://doi.org/10.1016/j.physletb.2022.137148>
- [46] D.C. Maurya, *Grav. Cosm.* **29**, 315-325 (2023) <https://doi.org/10.1134/S020228932303012X>
- [47] N. Myrzakulov, et al., *Eur. Phys. J. P.* (2023). <https://doi.org/10.1140/epjp/s13360-023-04483-3>
- [48] A. De Felice and S. Tsujikawa, *Living Rev. Rel.* **13**, 3 (2010). <https://doi.org/10.12942/lrr-2010-3>

ВСЕСВІТ FLRW У ГРАВІТАЦІЇ $f(\mathcal{R}, \mathcal{L}_m)$ З РІВНЯННЯМ ПАРАМЕТРА СТАНУБхупендра Кумар Шукла^a, Р.К. Тіварі^b, Д. Софуоглу^c, А. Бішем^{d,e,f}^a Департамент математики, Держ. Коледж Bandri Sagar, 470442 (М.Р.) Індія^b Департамент математики, Держ. Model Science College Rewa 486 001 (М.Р.) Індія^c Кафедра фізики Стамбульського університету Везнеджилер 34134, Фатіх, Стамбул, Туреччина^d Департамент математичних наук, Університет Зулуленду,

P Bag X1001, Ква-Dlangezwa 3886, Південна Африка

^e Факультет природничих наук, Технологічний університет Мангосуту,

PO Box 12363, Джейкобс, Південна Африка

^f Національний інститут теоретичних і обчислювальних наук, Південна Африка

Наявні дані спостережень щодо сучасних космологічних характеристик свідчать про те, що Всесвіт значною мірою є ізотропним і однорідним у великому масштабі. У цьому дослідженні наша мета полягає в аналізі просторового часу Фрідмана-Леметра-Робертсона-Уокера (FLRW) за допомогою ідеального розподілу рідини. Ми спеціально досліджуємо структуру $f(\mathcal{R}, \mathcal{L}_m)$ гравітації в межах певних обмежень. Щоб досягти цього, ми зосереджуємося на конкретній нелінійній моделі $f(\mathcal{R}, \mathcal{L}_m)$, представленій як $f(\mathcal{R}, \mathcal{L}_m) = \frac{\mathcal{R}}{2} + \mathcal{L}_m^\alpha$. Рівняння поля розв'язуються за допомогою рівняння параметра стану виду параметризації Шевальє-Полярського-Ліндера (CPL). Дослідження параметрів уповільнення виявляє прискорення Всесвіту в пізній час. Перехідне червоне зміщення виявлено $z_{tr} = 0,89 \pm 0,25$. Також ми обговорили фізичні та геометричні властивості моделі.

Ключові слова: $f(\mathcal{R}, \mathcal{L}_m)$ гравітація; темна енергія; прискорення Всесвіту; рівняння параметра стану

**ERRATUM: FIRST-PRINCIPLES CALCULATION OF STRUCTURAL, ELECTRONIC,
AND OPTICAL PROPERTIES OF CUBIC PEROVSKITE CsPbF₃**
[East European Journal of Physics. 3. 263-270 (2023)]

Zozan Y. Mohammed, Sarkawt A. Sami, Jalal M. Salih*

Department of Physics, College of Science, University of Duhok, Kurdistan Region-Iraq

**Corresponding Author e-mail: jalal@uod.ac*

The purpose of this Erratum is to correct a misprint presented in the original article.

In the published article, the sentence before the last of the third paragraph in page 268 reads:

“For incident photons having energies greater than 15.67 eV, the refractive index $n(\omega)$ becomes less than one which implies that the group velocity, $v_g = c/n$, is greater than the speed of light c .”

Here, “group velocity” is wrong; it is “phase velocity”. Thus, the mentioned sentence is to be read as follows:

“For incident photons having energies greater than 15.67 eV, the refractive index $n(\omega)$ becomes less than one which implies that the phase velocity, $v_{ph} = c/n$, is greater than the speed of light c .”

Original Article:

First-Principles Calculation of Structural, Electronic, and Optical Properties of Cubic Perovskite CsPbF₃
[East European Journal of Physics. 3. 263-270 (2023)]

<https://doi.org/10.26565/2312-4334-2023-3-23>

Zozan Y. Mohammed, Sarkawt A. Sami, Jalal M. Salih

Department of Physics, College of Science, University of Duhok, Kurdistan Region-Iraq

**ВИПРАВЛЕННЯ: ПЕРШОПРИНЦИПИ РОЗРАХУНКУ СТРУКТУРНИХ, ЕЛЕКТРОННИХ І ОПТИЧНИХ
ВЛАСТИВОСТЕЙ КУБІЧНОГО ПЕРОВСКІТУ CsPbF₃ [East European Journal of Physics. 3. 263-270 (2023)]**

Зозан Ю. Мохаммед, Саркау́т А. Самі, Джалал М. Саліх

Департамент фізики, Науковий коледж, Університет Духок, Курдистан, Ірак

Метою цієї помилки є виправлення друкарської помилки, представленої в оригінальній статті.

В опублікованій статті передостаннє речення третього абзацу на сторінці 268 звучить так:

«Для падаючих фотонів, які мають енергію понад 15,67 еВ, показник заломлення $n(\omega)$ стає меншим за одиницю, що означає, що групова швидкість, $v_g = c/n$, більша за швидкість світла c ».

Тут «групова швидкість» неправильна; це «фазова швидкість». Таким чином, зазначене речення викласти в такій редакції:

«Для падаючих фотонів, які мають енергію понад 15,67 еВ, показник заломлення $n(\omega)$ стає меншим за одиницю, що означає, що фазова швидкість, $v_{ph} = c/n$, більша за швидкість світла c ».

Оригінальна стаття:

**ПЕРШОПРИНЦИПИ РОЗРАХУНКУ СТРУКТУРНИХ, ЕЛЕКТРОННИХ І ОПТИЧНИХ ВЛАСТИВОСТЕЙ
КУБІЧНОГО ПЕРОВСКІТУ CsPbF₃**

[East European Journal of Physics. 3. 263-270 (2023)]

<https://doi.org/10.26565/2312-4334-2023-3-23>

Зозан Ю. Мохаммед, Саркау́т А. Самі, Джалал М. Саліх

Департамент фізики, Науковий коледж, Університет Духок, Курдистан, Ірак

INSTRUCTIONS FOR PREPARING MANUSCRIPT IN THE EAST EUROPEAN JOURNAL OF PHYSICS

Name A. Author^{a*}, Name B. Co-Author(s)^{b†}

^aAffiliation of first author

^bAffiliation of second author (if different from the first Author)

*Corresponding Author: corresponding_authors@mail.com, ^aORCID ID

[†]E-mail: co_authors@mail.com, ^bORCID ID

Received May 25, 2022; revised June 25, 2022 accepted July 5, 2022

Each paper must begin with an abstract. The abstract should be typed in the same manner as the body text (see below). Please note that these Instructions are typed just like the manuscripts should be. The abstract must have at least **25-300 words**, supplying general information about the achievements, and objectives of the paper, experimental technique, methods applied, significant results and conclusions. Page layout: the text should be printed on the paper **A4** format, at least **5 pages**, with margins of: **Top - 3, Bottom, Left and Right - 2 cm**. The abstract, keywords should be presented in **English** (only for foreign authors), and **Ukrainian**. The text should be prepared in **“doc” or “docx”** format.

Keywords: there, must, be, 5-10 keywords

PACS: specify PACS code(s) here

INSTRUCTIONS

The text should be typed as follows:

- **title:** Times New Roman, 12 pt, ALL CAPS, bold, 1 spacing, centred;
- **authors:** name, initials and family names; Times New Roman, 12 pt, bold, 1 spacing, centred;
- **affiliation(s):** Times New Roman, 9 pt, italic, 1 spacing, centred;
- **abstract:** Times New Roman, 9 pt, 1 spacing, justified;
- **body text:** Times New Roman, 10 pt, 1 spacing, justified; paragraphs in sections should be indented right (tabulated) for 0.75 cm;
- **section titles:** Times New Roman, 10 pt, bold, 1 spacing, centred, without numbering, one line should be left, blank above section title;
- **subsection titles:** Times New Roman, 10 pt, bold, 1 spacing, centred, without numbering in accordance to the section (see below), one line should be left blank above subsection title;
- **figure captions:** width of the figure should be 85 or 170 mm, Figures should be numbered (**Figure 1.**) and titled below Figures using sentence format, Times New Roman, 9 pt, 1 spacing, centred (if one line) or justified (if more than one line); one line should be left blank below figure captions;
- **table captions:** width of the table should be 85 or 170 mm, tables should be numbered (**Table 1.**) and titled above tables using sentence format, Times New Roman, 10 pt, 1 spacing, justified, Tables should be formatted with a single-line box around the outside border and single ruling lines between rows and columns; one line should be left blank below tables;
- **equations:** place equations centred, numbered in Arabic: (1), flush right, equations should be specially prepared in **MathType** or **“Microsoft Equation”**, Times New Roman, 10 pt, one line should be left blank below and above equation.

Additional instructions

Numerated figures and tables should be embedded in your text and placed after they are cited. Only sharp photographs and drawings are acceptable. Letters in the figures should be 3 mm high. The figures should be presented in one of the following graphic formats: jpg, gif, pex, bmp, tif.

REFERENCES

List of References must contain **at least 30% of articles published over the past 5 years** and **no more than 20% of links to their own work**. Cite References by number in AIP style (<https://aip.scitation.org/php/authors/manuscript>). Numbering in the order of referring in the text, e.g. [1], [2-5], etc. References should be listed in numerical order of citation in the text at the end of the paper (justified), Times New Roman, 9 pt, 1 spacing.

Journal Articles

- [1] T. Mikolajick, C. Dehm, W. Hartner, I. Kasko, M.J. Kastner, N. Nagel, M. Moert, and C. Mazure, *Microelectron. Reliab.* **41**, 947 (2001), [https://doi.org/10.1016/S0026-2714\(01\)00049-X](https://doi.org/10.1016/S0026-2714(01)00049-X).
- [2] S. Bushkova, B.K. Ostafiychuk, and O.V. Copenaev, *Physics and Chemistry of Solid State.* **15**(1), 182 (2014), <http://page.if.ua/uploads/pcss/vol15/1501-27.pdf>. (in Ukrainian)
- [3] M. Yoshimura, E. Nakai, K. Tomioka, and T. Fukui, *Appl. Phys. Lett.* **103**, 243111 (2013), <http://dx.doi.org/10.7567/APEX.6.052301>

E-print Resources with Collaboration Research or Preprint

- [4] M. Aaboud et al. (ATLAS Collaboration), *Eur. Phys. J. C*, **77**, 531 (2017), <http://dx.doi.org/10.1140/epjc/s10052-017-5061-9>
- [5] Sjöstrand et al., *Comput. Phys. Commun.* **191**, 159 (2015), <https://doi.org/10.1016/j.cpc.2015.01.024>
- [6] Boudreau, C. Escobar, J. Mueller, K. Sapp, and J. Su, (2013), <http://arxiv.org/abs/1304.5639>

Books

- [7] S. Inoue, and K.R. Spring, *Video Microscopy: The fundamentals*, 2nd ed. (Plenum, New York, 1997), pp. 19-24.
- [8] I. Gonsky, T.P. Maksymchuk, and M.I. Kalinsky, *Біохімія Людини [Biochemistry of Man]*, (Ukrmedknyga, Ternopil, 2002), pp. 16. (in Ukrainian)

Edited Books

- [9] Z.C. Feng, editor, *Handbook of Zinc Oxide and Related Materials: Devices and Nano Engineering*, vol. 2, (CRC Press/Taylor & Francis, Boca Raton, FL, 2012)

Book Chapters

- [10] P. Blaha, K. Schwarz, G.K.H. Madsen, D. Kvasnicka, and J. Luitz, in: *WIEN2K, An Augmented Plane Wave Plus Local Orbitals Program for Calculating Crystal Properties*, edited by K. Schwarz (Techn. Universität Wien, Austria, 2001).
- [11] M. Gonzalez-Leal, P. Krecmer, J. Prokop, and S.R. Elliot, in: *Photo-Induced Metastability in Amorphous Semiconductors*, edited by A.V. Kolobov (Wiley-VCH, Weinheim, 2003), pp. 338-340.
- [12] A. Kochelap, and S.I. Pekar, in: *Теорія Спонтанної і Стимульованої Хемілюмінесценції Газів [Theory of Spontaneous and Stimulated Gas Chemiluminescence]* (Naukova dumka, Kyiv, 1986), pp. 16-29. (in Russian)

Conference or Symposium Proceedings

- [13] C. Yaakov, and R. Huque, in: *Second International Telecommunications Energy Symposium Proceedings*, edited by E. Yow (IEEE, New York, 1996), pp. 17-27.
- [14] V. Nikolsky, A.K. Sandler, and M.S. Stetsenko, in: *Автоматика-2004: Матеріали 11 Міжнародної Конференції по Автоматичному Управлінню [Automation-2004: Materials of the 11th International Conference on Automated Management]* (NUHT, Kyiv, 2004), pp. 46-48. (in Ukrainian)

Patent

- [15] I.M. Vikulin, V.I. Irha, and M.I. Panfilov, Patent Ukraine No. 26020 (27 August 2007). (in Ukrainian)

Thesis / Dissertation

- [16] R.E. Teodorescu, Ph.D. dissertation, The George Washington University, 2009.

Special Notes

1. Use International System of Units (SI system). 2. It is undesirable to use acronyms in the titles. Please define the acronym on its first use in the paper. 3. Refer to isotopes as ¹⁴C, ³H, ⁶⁰Co, etc.